MIXING LIGHT AND MATTER WAVES: PRINCIPLES AND APPLICATIONS

By

YUPING HUANG

A DISSERTATION

Submitted to
Michigan State University
in partial fulfillment of the requirements
for the degree of

DOCTOR OF PHILOSOPHY

Physics and Astronomy

2009

ABSTRACT

MIXING LIGHT AND MATTER WAVES: PRINCIPLES AND APPLICATIONS

By

YUPING HUANG

The work of this dissertation is committed to theoretically explore rich physics involving quantum-mechanical mixing of light and matter waves, while specifically seeking applications in the fields of quantum interferometry, quantum information processing, and testing fundamental quantum mechanics. Towards this goal, the present research is guided by two lines. The first line is to study and manipulate collective behaviors of multi-atom systems at quantum-degenerate temperature, where the wave nature of atoms is maximized. Specifically, a variety of phase-coherent mixing processes of two macroscopic matter-waves, in the form of gaseous Bose-Einstein condensate (BEC), are investigated and engineered via i) tuning atomic collisional interaction and/or inter-wave tunneling rate; ii) mixing with optical waves of phase-locked lasers. By these means, a series of novel applications are proposed for generating highly nonclassical states, Heisenberg-uncertainty phase measurements and ultra-fast quantum state mapping between light and matter waves. The second line is to coherently mix single atoms with light beams in free space. It is well known that the free-space atom-photon interactions are weak, usually dominated by incoherent dissipation via spontaneous emission. Usable couplings between atoms and photons are routinely realized by confining them in high-finesse optical cavities in the strong coupling regime. The goal of the present work is to use ultrahigh-sensitivity quantum interferometry and the quantum Zeno effect to overcome the weak free-space atom-photon coupling, thus leading to implementations of quantum information processing in free space.

Along the first line of this dissertation, chapter II describes a dynamical approach

to create many-particle Schrödinger cat states, created in a Bose-Einstein condensate trapped in a double-well potential, via the technique of Feshbach resonance. A detection scheme for cat states is proposed via revivial of the initial state. Also particularly studied is the environmental decoherence due to laser-induced interaction between BEC atoms and the electromagnetic vacuum. Chapter III then presents an optimized Mach-Zender interferometry scheme with gaussian number-difference squeezed input states for sub-shot-noise phase resolution over a large phase-interval, also implemented in the double-well BEC system. We find utilizing adaptive measurement schemes allows any phase to be measured at Heisenberg-scaling precision within only a few measurements. The scheme can be readily implemented in a double-well BEC system. Chapter IV focuses on searching for the optimal operational strategy in a matter-wave amplification process, in order to facilitate potential applications in the fields of matter-wave interferometry and quantum information processing. In particular, the laser propagation effect inside two spatially overlapping spinor condensates is studied via the semiclassical multi-mode theory.

Along the second line, chapter V proposes to generate entanglement between single-atom qubits via a common photonic channel within the framework of quantum interferometry at ultrahigh phase sensitivities. Via this new approach, a scalable circuit element for quantum information processing is demonstrated at close-to-unity success probability and fidelity. Chapter VI employs environmental dissipation to implement on-demand interaction- and measurement-free quantum logic gates for hybrid quantum bits (qubits) of single atoms and single photons. By forcing qubits to stay in a decoherence-free subspace via the quantum Zeno effect, the problem of qubit decoherence, otherwise constituting a major challenge in implementing quantum computation and teleportation, is overcome counter-intuitively with the help of fast environmental dissipation.

Once described, it is modified

-by Laozi, $\sim$ 580 BC.

ACKNOWLEDGMENTS

First, I would like to take this chance to thank my Ph.D advisor, Michael Moore, for guiding me through the wonderland of quantum optics. He is a very "quantum" scientist, having his own unique viewpoints on quantum physics, most of which are simply brilliant and shining (perhaps except the everybody-being-a-robot idea). Having the fortune of being his first Ph. D student, I learned from him every operator, Hamiltonian and trick in quantum optics and beyond. To me, he has always been more than an advisor. I shall never forget that he let me stay with his family (Julie and Brian) for more than half a year, treated me innumerable dinners, and helped us whenever needed. I respect his personality, knowledgability, creativity and wisdom. I also appreciate his patience and understanding on me.

Second, I want to thank my wife for endless supports through my Ph.D study. While almost hating physics courses, she has been understanding and encouraging my devotion in this field. Literally, she married a poor physics student without an engagement ring, or even a wedding. I always understand that for me, she gave up too much of her own opportunities. I love her.

Third, I want to thank my mom for giving me the chance to experience this transient, but wonderful journey of life in this world, although not much has been achieved by her son yet. I also want to thank my and my wife's family members, especially our two grandmas who are now living elsewhere, for their loves on me.

Finally, I would like to thank all professors and friends who have helped me in various ways through my learning and researching. A few of them are L. Zhu, X. Liu, Z. Yuan, M. Böttcher, C. Piermarocchi, S. Mahanti, J. W. Liu, H. Lin, T. Yang and J. Kost.

Table of Contents

List of Figures

Chapter 1

Introduction

1.1 Bose-Einstein condensation

Bose-Einstein condensate (BEC) in dilute gases is a new form of matter that has revolutionized the subject of many-body physics at low temperature. This part of the introduction briefly reviews this relatively new subject and, particularly, discuss the rich connections with various subjects in many-body physics. We first address i) what a BEC is, ii) why gaseous BEC's are so unique and important, and iii) recent experimental progresses. Then, we focus on reviewing three important applications directly related to chapters II, III, and IV of this dissertation, including BEC in a double-well trapping potential, matter-wave interferometry and matter-wave amplification in dilute BEC gases.

1.1.1 The conception of Bose-Einstein condensation

Although the wave behavior of massless photons was observed by Young and Fresnel in the early 1800's, the wave nature of massive particles was not demonstrated until the year of 1927, when for the first time Davisson and Germer observed diffraction patterns of electrons analogous to that of photons [1]. The reason, now

well understood in quantum mechanics, is that the de Broglie wavelengthes of massive particles are normally much shorter than that of photons. Thus any observable diffractive phenomenon of massive particles would require much narrower slits. According to the de Broglie relation, a massive particle of momentum p has a wavelength λ_{dB} given by [2, 3]

$$\lambda_{dB} = \frac{h}{p} \tag{1.1}$$

where h is the Planck constant. For a noninteracting free gas in thermal equilibrium at temperature T, the average momentum p, according to Boltzmann distribution, is determined by the relation

$$\frac{p^2}{2m} = \frac{3}{2} k_B T, \tag{1.2}$$

with m the particle mass and k_B the Boltzman constant. This immediately leads to

$$\lambda_{dB} = \sqrt{\frac{h^2}{3mk_BT}}. \tag{1.3}$$

At room temperature (300 kelvin), the de Broglie wavelength for typical atoms of 10^{-26} Kg is $\sim 10^{-11}$m, which is of the order of the Bohr radius. To observe the wave behavior of room-temperature atoms in Young's double-slit experiment, it would require extremely narrow, almost inaccessible, slits of width close to atom size. They can thus be safely treated as microscopic billiard balls under most circumstances, exhibiting only the particle nature. If, however, we decrease the temperature to 1 mk, λ_{dB} will increase to 10 nm, providing more wave-like atomic behaviors. At the temperature of $T = 1$ μk, λ_{dB} is ~ 1 μm, which becomes comparable to a typical photon's wavelength in the infrared regime. By further cooling, the atomic de Broglie wavelength can eventually be made longer than the wavelength of visible light. For example, λ_{dB} is obtained at ~ 10 μm if further lowering the temperature to $T = 1$ nk.

As they get cooled, massive particles behave more and more wave-like. For bosonic atoms, when λ_{dB} reaches the inter-atom separation, a quantum phase transition occurs as an atom can no longer be distinguished from its neighbors due to wave-packet overlapping. For an ideal gas of bosonic atoms (with integer spins), a new type of matter forms at a critical temperature for which $n\lambda_{dB}^3 = 2.612$, with n the peak gas density. This new matter, characterized by a major portion of atoms occupying the same quantum-mechanical state, was predicted by S. N. Bose and A. Einstein in 1920s [4, 5], and has now come to be known as BEC.

The underlying physics of BEC is the quantum-mechanical phase transition in quantum statistics of bosonic particles. Consider an ideal gas of N noninteracting bosons confined in volume V, the number of particles in the quantum state of energy ϵ is given by Bose-Einstein statistics, as [6]

$$n_{BE}(\epsilon, \mu, T) = \frac{1}{\exp[(\epsilon - \mu)/k_B T] - 1}, \tag{1.4}$$

where μ is the chemical potential. In coordination with the fact $\epsilon \geq 0$, where $\epsilon = 0$ simply corresponds to the zero momentum state, μ must be less or equal to zero to keep n_{BE} positive. In practice, μ is determined by the number-sum condition, where the occupation sum of all energy levels is equal to the total particle number,

$$N = N_0(T) + V \int_0^\infty n_{BE}(\epsilon, \mu, T) g(\epsilon) d\epsilon, \tag{1.5}$$

where $g(\epsilon) \propto \sqrt{\epsilon}$ is the unit-volume density of states at energy ϵ in the three-dimension space. $N_0(T) \leq N$ is the atom number in the zero momentum state with $\epsilon = 0$. At high temperature, the number-sum condition (1.5), together with the Bose-Einstein distribution (1.4), requires μ to be a large negative number and $N_0 \ll N$. When cooling the gas while keeping the volume fixed, μ increases (decreases in magnitude) while N_0 stays small. Eventually, the phase transition occurs when T reaches a

critical point T_c where

$$N = V \int_0^\infty n_{BE}(\epsilon, \mu \approx 0, T_c) g(\epsilon) d\epsilon, \tag{1.6}$$

the condition of which leads to the critical parameter of $n\lambda_{dB}^3 = 2.612$. This corresponds to the point when the excited states can not accommodate most atoms any more. Further decreasing T to below T_c results in rapid building up of the population fraction in the ground state, while remaining atoms continue to occupy higher-energy levels according to the Bose-Einstein distribution for $\epsilon > 0$. Using equation (1.4) and taking $\mu = 0$, it is straightforward to obtain that

$$N_0(T < T_c) = N \left[1 - \left(\frac{T}{T_c} \right)^{3/2} \right]. \tag{1.7}$$

Clearly, in the limit of absolute zero temperature $T = 0$, then $N_0 = N$, and a pure BEC is obtained with all atoms occupying a single quantum mode, giving macroscopical quantum-degeneracy of translational states. It is noted that the above discussions have assumed non-interacting atoms. In practice, however, particles may be interacting with each other, in which case T_c will be shifted up or down, depending on the interaction being repulsive or attractive [7]. Further, in the above derivation, only statistical properties of the system are used, so that the phase transition condition of $n\lambda_{dB}^3 = x$ (x is a constant determined by the atom-atom interaction) applies to arbitrary systems consisting of spin-integer particles or quasi-particles. In fact, the most recognized phenomena associated with BEC, before the realization in dilute gases, was the superfluid Helium consisting of bosonic ^{4}He isotopes [8]. In these two examples, the critical temperatures are 2.17 kelvin for Helium and up to $\sim$ 100 kelvin for superconductors, both much higher than that for gaseous BEC, which is sub microkelvin.

1.1.2 Why Bose-Einstein condensates in dilute gases

The question is then why a BEC in dilute gases, if after all what we obtain is just *another* realization of Bose-Einstein condensation? There are multiple answers to this question, but perhaps the most convincing one is that compared to the liquid or solid systems, gaseous BEC's yield much lower densities, thus substantially reducing the inter-particle interaction. In practice, such interactions have been shown to significantly modify the nature of the BEC phase transition in liquid Helium and solid superconductors. In fact, due to strong interactions, only $\sim 10\%$ ^{4}He atoms in liquid Helium can be condensated. Yet, atoms in a gaseous BEC interact far more strongly than photons in a laser beam, the latter of which are generally considered as noninteracting unless mediated by nonlinear medias. These, together with the fact that the gases can be stably trapped and well isolated, make a gaseous BEC an extraordinarily pure and easily accessible platform for rich many-body physics.

From the prospective of fundamental quantum physics, BEC's in dilute gases provide a unique bridge connecting quantum theory and experiments. Perhaps the most distinctive feature of a gaseous BEC is that with hundreds of thousands of atoms occupying a single quantum state, a macroscopic matter wave is formed as a magnification of a single-atom wavefunction by a factor of the square root of the atom number. Imaging the BEC cloud by ordinary absorption or fluorescence method can directly visualize the shape of the single-particle wavefunction. Further, by overlapping two condensates, the relative phase between the two matter waves can be read out by simply imaging the resulting interference pattern [9]. In contrast, a similar phase is inferred by Josephson oscillations in superconductors [10], or through the motion of quantized vortices in the system of superfluid helium [11].

A second unique and very useful feature of gaseous BEC's is that the inter-atom interaction can be easily tuned by the technique of Feshbach resonance [12, 13]. This, provided with remarkable sensitivity of the system dynamics to such interactions, has

opened a door to a series of new quantum phenomena. A well justified example is the realization of BCS-BEC crossover in dilute gases of Fermions. The BCS-BEC crossover is important not only for studying superconductors, but also for testing many-body quantum theory, for it constituting one of few non-perturbative problems of N-body systems that are presently solvable. Previous studies on BCS-BEC crossover in superconductors have been hindered by strong interactions in such systems. In contrast, with tunable interactions via Feshbach resonance, gaseous BEC's can serve as a good platform for testing the fundamental many-body physics. Recently, the BCS to BEC crossover has been observed in a two-component gas of Fermionic atoms [14, 15].

An initial gaseous BEC can also serve primarily as a well-defined starting point for the generation of more exotic highly-correlated and/or entangled many-body states. Important applications include implementing the phase transition from superfluid to Mott-insulator in an optical lattice and the crossover to a 'fermionized' Tonks-Girardeau gas under quasi-one-dimensional confinement [16, 17, 18, 19, 20]. Also appealing is the crossover from a vortex-lattice to a nontrivial entangled many-body state in the ground state of a rapidly rotating BEC [21, 22]. In experiments, a reversible change from a superfluid to a Mott-insulator state was observed when crossing from tunneling-dominated to the collision-dominated regime, for atoms trapped in a lattice potential with repulsive atom-atom interactions. The analogous transition for the case of attractive interactions involves the crossover from a superfluid into a state often described as a 'Schrödinger cat state' where the atomic population collapses into a single lattice site, with the true ground state being a symmetric superposition over all possible lattice sites as the final occupied site. In addition to providing fundamental insights into the nature of the transition from the quantum to the classical descriptions of reality, such states may have important applications in precision measurement [23, 24, 25, 26, 27] and quantum information processing.

Another notable application is to use a disordered BEC system as a powerful "quantum emulator" for simulating complex behaviors in many-body physics. Disorder plays a critical role in condensed-matter physics as most materials inevitably contain defects, which, in solid systems, are often difficult to control, thus hindering our understandings. The disorder in BEC is usually provided by random potentials, and can be remarkably controlled by adjusting trapping as well as atomic scattering parameters. This, aided by the intrinsic cleanliness of the quantum-degenerate systems, offers unique opportunities to study disordered quantum behaviors [28, 29].

Lastly, with its well-established large degree of spatial and temporal coherence, the system of gaseous BEC has emerged as a viable candidate for matter-wave interferometry [30, 31, 32, 33, 34, 35, 36, 37]. Compared to optical systems, a BEC-based interferometer has the unique advantages of sensing inertial forces, measuring gravity gradient, and allowing measurements at the single-particle level with high-efficiency detectors [38, 39]. Furthermore, the feature of tunable interaction serves a natural source of dynamical nonlinearity which can lead to nonclassical many-particle states and eventually improved measurement precision [40]. Another remarkable application of gaseous BEC is the implementation of matter-wave amplification, which is a phase-coherent wave mixing processing between two matter-waves and two optical-waves. Further reviews on matter-wave interferometry and matter-wave amplification will be given in the later context.

1.1.3 Overview of experimental progresses

The first gaseous BEC was created by the group of Cornell and Wieman at JILA in 1995, where a dilute vapor of about 2000 ^{87}Rb atoms was cooled to below 170nk [41]. Then, about four months later, the group of Ketterle at MIT independently created a second BEC of ^{23}Na atoms [42], the size of which was about a hundred times greater than the one at JILA. Shortly following the seminal work at JILA

and MIT, gaseous BEC has been realized in many other atomic systems. By now, documented BEC gases include ^{7}Li produced in 1995 [43, 44], Hydrogen produced in 1998 [45], ^{85}Rb in 2000 [46], ^{41}K in 2001[47], metastable He* in 2001 [48, 49], ^{133}Cs in 2003 [50], ^{174}Yb in 2003 [51], and ^{52}Cr in 2005 [52].

Typical experimental procedures for creating gaseous BEC include two major stages, the laser cooling and evaporative cooling. In the laser cooling stage, a trapped thermal vapor is first cooled to Doppler temperature, typically $\sim 100\mu$k, by the means of Doppler cooling [53, 54]. The vapor is then further cooled to sub-Doppler temperature of $\sim 1\mu$k via a new type of cooling mechanism called Sisyphus cooling [55]. Then in the second stage, the cooling laser is turned off, and the trapping potential is lowered to further cool the vapor to below the BEC critical temperature. This cooling mechanism, proposed by Hess in 1986 [56], is called evaporative cooling, developed in an analogy to the cooling of a hot liquid by evaporation of energetic particles of higher momenta. It is noted the evaporative cooling is not the only cooling method to obtain a BEC. A demonstrated alternative approach is the sympathetic cooling, where a vapor is cooled by an ancillary BEC via mutual interactions [57, 47]. Finally, the existence of BEC is verified by time-of-flight measurements of the atoms' velocity distribution. That is, after the BEC is formed, atoms are released from the trapping potential and undergo free expansion for a preset time. The spatial density of the expanded vapor is then imaged by an absorption or phase-contrast method, from which the velocity distribution is reconstructed. A sharp peak in the velocity distribution announces the existence of a BEC.

A remarkable achievement in the field of experimental BEC is the development of atom laser. Just as optical lasers have led to revolutionary advancements in optical science, the realization of the atom laser has the potential to substantially impulse the subject of atom optics. The first atom laser in BEC was realized in 1997 by the Ketterle group [58]. In the experiment, a BEC vapor in, say, a spin-up state is

generated in a magnetic trapping potential. The magnetic trap is attractive to spin-up atoms, and repulsive to spin-down ones. By applying short pulses at radio-frequency (rf), the condensate is evolved into a two-state coherent state of spin up and spin down. The spin-down atoms are then ejected from the trap, and fall down due to gravity. In this way, an output coupler similar to that for optical lasers is realized. Since there is a matter-wave ejection for every beat of the rf pulse, a sequence of coherent matter pulses, or an atom laser, is produced. The pulse length and intensity can be controlled by tuning the rf pulse and the trapping potential. Such an atom laser serves as a prospective starting point for many applications in the field of atom optics [59].

Another notable experimental progress is loading, cooling and trapping BEC gases on microfabricated atom chips (for a review, see [60]). An atom chip is a microstructure consisting of ultrathin conductors electroplated on a substrate. The typical dimension of atom chips is of the order of millimeters or even smaller, and the typical conductor width is only several to tens of micrometers. These conductors allow high current densities of $\sim 10^6$ A/cm^2, and can thus produce strong magnetic micro-traps near the surface of atom chips [61]. Such traps are compared to conventional magneto-optic traps (MOT's) employing large-scale coils of table size. By arranging conductors, magnetic traps of arbitrary geometry can be produced, including strongly-confining ultra-long wave guides which are difficult with MOT's due to diffraction of the optical trapping beams. By varying applied currents, the trap size and potential barriers can be fine tuned, providing the feasibility to implement, for example, superfluid to Mott-insulator phase transition in on-chip lattices. All these give rise to the realizations of integrated atom-optics devices on miniaturized chip-cells, including portable and assemblable atom interferometers, quantum information processing units, Tonks-Girardeau gas cells and so on. In experiments, the first BEC gas on an atom chip was produced in 2001 by Ott *et al* [62] and by Hänsel *et al* [63].

In 2005, matter-wave interferometry of BEC gases was demonstrated on atom chips [64, 65, 37].

Other important experimental developments not elaborated here include the observations of vortices in a spinning BEC, superfluid to Mott-insulator transition in an optical lattice and the crossover to a 'fermionized' Tonks-Girardeau in 1D [16, 17, 18, 19, 20]. All these progresses give rise to implementations of rich many-body physics at ultra-low temperature and applications in the filed of quantum interferometry and quantum information processing. In the following, we will review three important applications related to the work of this dissertation, including double-well BEC, BEC-based matter-wave interferometry and matter-wave amplification.

1.1.4 Double-well Bose-Einstein condensates

For various applications, a gaseous BEC system consisting of two well-isolated yet weakly-coupled quantum components, generally referred to as a bimodal BEC, is recognized as a well-justified platform [66, 67, 68, 69, 70, 71]. Its power is from its exceptional simplicity and high controllability compared to competing systems such as Josephson-junction of superconductors. The two modes can be two internal hyperfine states or two external spatial modes. In the first case, the modes are spatially overlapped, and are connected by coupling lasers [72, 73]. In the second case, the two modes are spatially separated, each in one well of a double-well potential [74, 75]. Connection between the two modes is provided by weak inter-well tunneling. The main difference between the two models is the presence of inter-mode cross-phase modulation in the hyperfine system, as a consequence of mode overlapping. Its effect is nonetheless physically equivalent to an addition of self-phase modulation possibly together with a relative shift in chemical potentials of the two modes, and is thus unimportant for most applications. For concreteness, this dissertation is focused on the bimodal BEC system implemented in a double-well trapping potential, or the

so-called "double-well BEC".

At zero temperature, the system is conveniently described in the two-mode approximation, in which the annihilating field operator $\hat{\Psi}(\mathbf{r})$ for atoms at position $\mathbf{r}$ is delocalized into orthogonal localized left- and right- modes,

$$\hat{\Psi}(\mathbf{r},t) = \hat{c}_L(t)\psi_L(\mathbf{r}) + \hat{c}_R(t)\psi_R(\mathbf{r}), \tag{1.8}$$

where $\hat{c}_L$ and $\hat{c}_R$ are bosonic annihilation operators for the left and right modes, respectively. The localized modes correspond to the wavefunctions of atoms in left- and right- well, formally defined via a linear transformation of the ground and first-excited states. In this approximation, the system's dynamics are governed by a two-mode version of the Bose-Hubbard Hamiltonian, as [76]

$$\hat{H} = -\hbar\tau(\hat{c}_L^\dagger\hat{c}_R + \hat{c}_R^\dagger\hat{c}_L) + \hbar g(\hat{c}_L^{\dagger 2}\hat{c}_L^2 + \hat{c}_R^{\dagger 2}\hat{c}_R^2), \tag{1.9}$$

where τ describes the inter-mode tunneling, and g is the strength of nonlinear intra-mode interaction. The quantum state of this bimodal system is written in a superposition of number-difference states $|n\rangle$ [70]

$$|\hat{\Psi}\rangle = \sum_{n=-N/2}^{N/2} c_n|n\rangle, \tag{1.10}$$

where

$$|n\rangle \equiv \left|\frac{N}{2}+n, \frac{N}{2}+n\right\rangle = \frac{(c_L^\dagger)^{N/2+n}(c_R^\dagger)^{N/2-n}}{\sqrt{(N/2+n)!(N/2-n)!}}|\text{vacuum}\rangle. \tag{1.11}$$

Here, N is the total number of atoms in the condensate which, for convenience, is taken as a even number, and n denotes half number difference between the two modes. In practice, τ can be easily adjusted by varying the trapping potential, while g can be precisely tuned via the technique of Feshbach resonance [12, 13]. This extra freedom

of controllability has allowed a variety of important applications.

The first application is to implement a full range of Josephson-junction dynamics in a neutral-atom system, in an analogy to charged superconducting junctions. This includes the well-known dc, ac and Shapiro tunnelling phenomena, and most remarkably, the macroscopic quantum self-trapping (MQST) [67, 68]. MQST is a striking quantum-equilibrium phenomenon where the tunneling between the two modes is self-frozen with more atoms in one well than the other. It occurs when nonlinear atom interaction is sufficiently strong to shift the tunneling out of resonance. Thus by tuning g via Feshbach resonance, the system can be switched between Josephson oscillation and MQST regimes. All these effects give rise to new apparatuses in atom optics with interacting matter-waves, which have not been possible with conventional optics of noninteracting photons. Experimentally, the Josephson oscillation and self-trapping was first observed by the Oberthaler group in 2005 [71].

A second important application is to generate a variety of highly nonclassical states, including number squeezing, phase squeezing, and the macroscopic Schrödinger cat states. In the absence of intra-mode interaction, the system's ground state under Hamiltonian (1.9) is a two-mode coherent state, corresponding to a Gaussian distribution with $c_n \propto \exp(-n^2/\sigma^2)$, with the distribution width $\sigma = \sqrt{N}$. In presence of some repulsive interaction with $g > 0$, the ground state becomes number squeezed, corresponding to a Gaussian with a reduced width of $\sigma < \sqrt{N}$. This is because in order to minimize the interaction energy, atoms tend to be localized in each well. In the limit of large g, the system's ground state is a twin-Fock state with $c_n = \delta_{n,0}$. This state is characterized by an equal and definite number of atoms in two quantum modes. On the other hand, in the presence of attractive interaction with $g < 0$, the ground state becomes phase squeezed, characterized by a spreading in number distribution with $\sigma > \sqrt{N}$. In the limit of large attractive interaction, the ground state turns out to be a superposition of all atoms in the right and left well, which

is an N-atom realization of the famous Schrödinger-cat state [77]. Starting with a double-well BEC system in the ground state without interaction, a whole series of nonclassical states, ranging from number squeezing to phase squeezing, can be produced by adiabatically turning on interactions via Feshbach resonance. Such states are proven to be very useful in testing fundamental quantum mechanics [78, 79] and for applications in the fields of quantum interferometry and quantum information processing [37, 80, 81, 82, 83]. It is noted that in practice, Schrödinger cat states cannot be adiabatically generated by tuning g, hindered by the energy degeneracy of ground and first-excited states. Instead, it can be produced via a dynamical scheme, as will be discussed in Chapter II in this dissertation.

Furthermore, another well-justified application is to implement ultrahigh-sensitivity matter-wave interferometry in tunneling multi-mode BEC systems, as will be discussed in the next subsection.

1.1.5 Matter-wave interferometry

An interferometer is a measurement device which exploits the wave nature of photons and/or massive particles to explore inhomogeneities in probing environments. The first interferometry on file, which dated back to the 19th century, was implemented with interfering optical rays [84, 85, 86]. From then on, optical interferometers have been serving as primary tools for precise measurements in various fields. Only much later was the first matter-wave interferometry demonstrated, including that of employing electrons in 1952 [87], and neutrons in 1962 [88]. Today, matter-wave interferometers using electrons, neutrons and atoms as probes, have been widely recognized as invaluable tools for testing fundamental physics, precise measurements of physical constants, as well as a variety of important applications in astronomy, geometry and in the emerging field of quantum information processing (for reviews, see [89, 90, 91, 33]).

Compared to optical interferometry, interferometers built on matter waves have several immense advantages. In the first place, atoms are massive particles subjected to inertial-frame acceleration forces, such as gravitation. This makes matter-wave interferometers sensitive detectors for probing inertial effects, for instance, gravity gradients, since phase shifts induced by inertial forces increase with the mass of probing particles [92]. In practice, this feature has remarkably led to developments of atom-based accelerometers, gradiometers, rotation meters and gravimeters [93, 94]. Second, atoms are sensitive to the external electromagnetic (EM) force, making atom interferometers powerful devices for precisely measuring local fluctuations of EM fields. This is contrary to optical interferometers employing photons, which basically non-interact with external EM fields. A notable application is the measurement of the Aharonov-Casher phase via matter-wave interferometry in the middle of 1990's [95, 96]. Third and perhaps most importantly, matter-wave interferometers employing atoms have the most unique advantage that interfering atoms are rich in internal varieties such as hyperfine structure, excited levels, isotopes and so on. This provides the possibility of differential interactions of probing beams with local environments, providing selective measurements of external quantities. Using this feature, in practice, several important fundamental experiments were carried out, including testing the equivalence principle in general relativity [97] and measuring the Aharonov-Bohm effect [98].

This far, a variety of atom interferometers have been proposed, all of which rely on creating matter-wave gratings. For thermal atoms with short de Broglie wavelengthes, the gratings are formed either by a tight set of tiny apertures (e.g., narrow slits) in a solid membrane, or a tight standing-wave grating formed by interfering lasers. For ultra-cold atoms, such as BEC gases, the de Broglie wavelengths become much longer, allowing the use of a set of new, less-tight gratings at optical dimensions, such as tunneling optical lattices or micro-traps on an atom chip [35]. More

importantly, the contrast of the interference signal, which determines the measurement sensitivity, increases with the brightness of the source of probing particles, i.e., the number of particles per quantum mode. With macroscopic occupation of a single quantum mode, the advent of BEC gases holds promise to promote ultra-sensitive matter-wave interferometry, in a way that the invention of laser has revolutionized optical interferometry [30, 9, 32, 31, 33, 34, 35, 36, 37]. Another remarkable feature is that, the atom-atom interaction in gaseous BEC is adequately tunable by the method of Feshbach resonance. This provides the feasibility to implement some beneficial nonlinear interferometric procedures, as well generate number or phase squeezed input states. All these give rise to significant improvements on interferometry performances.

An archetypical, perhaps most notable BEC interferometer is implemented in a double-well system, the configuration of which was discussed in the above section. To implement a double-well interferometer, two phase-coherent condensates are prepared, usually by coherently splitting one condensate into two through adiabatically changing the shape of the trapping potential. The two condensates then separately interact with each's local environment, acquiring independent phase shifts. Finally, they are recombined to form interference pattern. The relative phase information is then extracted by measuring the interference pattern. In practice, a first proof-of-principle experiment was carried out by the Ketterle group in 1997, where two BEC's were prepared independently in a double-well potential [9]. The potential was then turned off, allowing the two gases to freely expand. As they overlapped, high-contrast interference fringes were observed. If, on the other hand, spatially-inhomogeneous dc and/or rf magnetic fields are applied to disturb the condensate phases during free-expansion, the fringe contrast is observed to be significantly reduced. This confirmed that fringes were determined by the relative phase of the overlapping matter-waves. Later in 2004, a whole procedure of double-well interferometric measurement was demonstrated by the same group [31]. In the experiment, a condensate was split

into two phase-locked condensates by deforming a single-well potential into two separated wells, thus realizing a coherent matter-well beamsplitter analogous to optical beamsplitters. The two separated condensates were then applied separately with ac Stark shifts, followed by recombination via free expansion. Phase information is then extracted from interference patterns, where good agreements are found between applied and measured phases. Recently, matter-wave interferometry was demonstrated on atom chips [64, 65, 37]. This holds the promise to build miniaturized, portable measurement devices for astronomy, geology and military uses.

1.1.6 Matter-wave Amplification in BEC

Matter-wave amplification (MWA) in BEC is a stimulated four-wave mixing (FWM) process in which two coherent matter waves, a pump mode and a signal mode, are mixed with a single pump laser [99, 100, 101, 102, 103, 104, 105, 106, 107, 108, 109, 110, 111, 112, 113, 114, 115, 116, 117]. The pump and signal waves are two BEC's in different momentum or hyperfine states, with a well-defined relative phase. During the MWA process, a photon from the pump laser is scattered by a pump atom, imparting a momentum kick of photon recoil. Due to the quantum stimulation effect, the kicked atom preferentially scatters into the populated signal wave. Consequently, a fourth coherent wave, namely the idler wave, is generated in the form of a light beam emitted along the phase-matching angle. Generated in a coherent process, the phase of the optical idler beam is locked to be the relative phase between the signal and pump matter-waves. As the amplification process preserves the relative phase between the two matter waves, MWA has been viewed as an active device with potential applications in matter-wave interferometry [118, 37, 81, 119, 83, 40]. This point of view, however, is limited by the fact that the signal matter-wave is amplified at the expense of the pump wave, whose depletion ultimately suppresses the MWA gain mechanism. In addition, since the idler light carries the relative

phase information between the two matter waves, MWA can in principle allow for the 'mapping' of an arbitrary quantum state from a two-mode atomic field onto a two-mode optical field [101, 100, 112]. This has the potential to revolutionize the field of matter-wave interferometry and quantum information processing. For example, the application of matter-wave interferometry is largely hindered by the fact that the relative phase between two matter-waves is read via the interference pattern between the two, upon spatially overlapping, which primarily restricts such measurements to be within short spatial range. However, by using a pair of phase-locked lasers to simultaneously drive two distant MWA systems, and then collecting and interfering the emitted idler lights, the relative phase information of the two matter-wave systems can be read out, without physically bringing them together. This leads to eliminating the short-range restriction in the matter-wave interferometry. Furthermore, the reverse process of MWA, in which an optical signal is amplified along with the generation of an atomic idler field, works equally well via the same mechanism [108]. Thus quantum information generated in a matter-wave field could be transferred to an optical field for detection or long-distance transfer to a second bimodal atomic system [120]. In some sense, MWA can be viewed as a dynamical counterpart to adiabatic electromagnetically-induced-transparancy (EIT) based quantum storage and retrieval techniques (for a review, see [121, 122]).

There are two theoretical models for the MWA systems. The first one, pioneered by the work of Moore and Meystre [103], is based on quantum treatment of light and matter coupling in Markovian approximation [123]. In this theory, the scattered light field is eliminated to form a closed set of dynamical equations for atomic fields only, which are then further simplified by assuming time-invariant momentum side modes [105, 124, 125]. We henceforth refer to it as the quantum coupled mode (QCM) model. Due to the elimination of scattered light, the MWA manifests itself as an atomic stimulation process, in which decaying into a particular side mode is

enhanced by a factor of the mode occupation number. In the second semiclassical picture, however, the MWA is viewed as an ordinary Bragg scattering process, in which atoms are diffracted by optical standing waves formed by the laser and scattered beam [126, 127, 128, 129, 130, 131, 132, 133, 117]. The superradiant enhancement is due to the diffraction efficiency being proportional to the square of the grating depth, and thus the atom number in the signal wave. Unlike QCM, the semiclassical model is capable of incorporating multi-mode treatment of the light-matter coupling in a more computationally accessible way, via the Maxwell-Schrödinger equations. We thus call it the semiclassical Maxwell-Schrödinger (SMS) model.

While the two show fair agreements in the weak driving regime, the QCM model is demonstrated to fail in interpreting several important observations in the strong driving regime [134, 108]. Such include the asymmetry between the forward and backward superradiance mode, and the subexponential growth of the scattered field [129, 131], both of which are, however, well explained in the SMS theory. It turns out that the invalidity of the QCM model is due to employing time-invariant spatial modes, thus excluding any spatial dynamics. Consequences of spatial mode evolution, usually referred to as spatial (or propagation) effects, are shown to be important in the strong driving regime when atomic motions can be neglected [127]. In this dissertation, we will explore the differences and connections between the QCM and SMS model in chapter IV.

In a close examination of the quantum approach employing master equations, we nonetheless find the spatial effect naturally arises as a consequence of the retardation effect of the collective atomic correlation via light medium, when appropriately treating the second-order perturbation. Physically, the retardation and thus the spatial effect is intuitively understood in a picture where along any light propagation direction, an atom in an ensemble only "sees" other atoms sitting behind it, but not those in front. Thus for light traveling along $\hat{\mathbf{z}}$, the strongest two-body nonlin-

ear effect occurs at far $+\hat{z}$, as having been observed [108, 135]. A master equation incorporating the spatial effect can then be viewed as a "quantum" version of the semiclassical Maxwell-Schrödinger equation, with the extra capability of describing the initialization of superradiance triggered by vacuum fluctuations, as well as the induced dipole-dipole interaction due atomic exchange of virtual photons. We note the dipole-dipole interactions would potentially spoil the MWA, by distorting the seed-mode phase via cross-phase modulation. In practice, however, this quantum approach is much more computationally complicated, when solving for the dynamics beyond few-mode approximation. In contrast, the Maxwell-Schrödinger method is more computationally accessible, especially within the slow-varying envelope approximation, and has been employed to successfully explain the asymmetric behavior observed in recent MWA experiments.

1.2 Quantum information processing

The technology of quantum information has emerged as a promising candidate for the next-generation information processing, having the potential to substantially advance our modern society. In this part of the introduction, I will give an overview of this emerging field, presenting i) the conception of quantum information processing; ii) the advantages over classical information processes; iii) implementations of quantum information processes; and iv) important recent experimental progresses.

1.2.1 The idea and advantages of quantum information processing

The technology of information processing has proven to be the key to recent immense advancements in civilization, in various aspects ranging from science, economics to industry. The past decades have witnessed tremendous developments of

information technology, mainly attributed to the exponential miniaturization of electronic elements, whose speed follows the famous Moore's law which sets the objective that the number of transistors on a chip doubles every one and a half year. To date, the advanced computational devices are now employing microchips with microscopic transistors linked with strip-conductors of $\sim$ 10 nm in width. This corresponds to a width of $\sim$ 1000 parallel atoms, providing the validity to describe the system with classical physics. If Moore's law persists, soon in ten years from now, the strip conductors will be miniaturized to a width of only tens of atoms. Under this scale, however, the classical laws break down, and quantum effects would unavoidably occur. In modern technologies, information is digitally coded in the form of sequential electric currents or light pulses. Entering the few-particle quantum regime would then lead to loss of information precision, due to inherent fluctuations caused by the Heisenberg uncertainty principle, as well as the probability nature of quantum measurements. The quantum effects thus put an ultimate limit on the maximal number of electronic elements on a unit microchip, and thus the achievable performance of corresponding information processing devices. Such a constraint is from physical laws, and thus cannot be conquered by technological advancements. This gives rise to the supposition that it is impossible to advance information technology soon as further miniaturization is prohibited by quantum effects.

So, is this the whole story? While quantum effects are unavoidable, why not just exploit them for information processing, possibly with a novel coding system other than the classical digitalization? If this is the case, then the miniaturization can be pushed to the minimal single-particle level, potentially improving information processing capabilities by many orders of magnitude [136, 137]. Even more appealing, can quantum effects expediently reduce the computational complexity associated with nowaday computers, for example, in searching large databases [138]?

These thoughts regarding processing information in quantum-mechanical systems

have led to a new information science, namely quantum information processing (QIP). Although the first ideas of QIP were proposed in the early 1980s [139, 140], only much later was it recognized as the next-generation information technique, thanks to several milestone experimental progresses (see [136] for a review). In the QIP, unit information, namely a quantum-bit (qubit) analogous to binary bits, is encoded in the quantum state of a quantum-mechanical object. Such an object can be a single particle, such as an isolated atom, nuclei or ion (approximately) occupying by two electronic or translational states, or a polarized photon traveling at the speed of light. Or it can be a mesoscopic object in collective states, such as an ensemble of atoms, or a light beam containing over thousands of photons. In any physical form, a qubit is described by a quantum superposition of two logic bases, namely $|0\rangle$ and $|1\rangle$, in a general density form of

$$\frac{1}{\sqrt{|c_0|^2 + |c_1|^2}}(c_0|0\rangle + c_1|1\rangle) \tag{1.12}$$

where c_0 and c_1 are arbitrary complex numbers. This is in contrast to a classical bit, where the state is either $|0\rangle$ or $|1\rangle$, but not the superposition of the two.

One of the most striking applications of the superposition principle is the quantum parallel computation, also widely referred to as quantum parallelism. In this algorithm, each basis state is treated as a single argument to a function and an operation on the quantum register is then simultaneously performed on all arguments. This allows generation of parallel outputs within only a single operation. In classical processing, in contrast, each argument must be addressed individually, so that a similar task would require an exponential number of steps. For example, suppose our goal is to compute all values of a function $g(\mathbf{x})$, where $\mathbf{x}$ is a binary vector of length N. In classical computation, this calculation requires either one copy of the calculation circuit and 2^N time steps, each with a different input. Or one time step but with 2^N copies of the circuit and 2^N different inputs. In either way, the computa-

tional complexity grows exponentially with N. In quantum parallelism, however, one can simply construct an operation defined by $|x\rangle \mapsto g(x)|x\rangle$. Preparing an N-qubit quantum register of an equally weighted superposition state

$$|\Psi_{in}\rangle = \frac{1}{\sqrt{2^N}}(|00\cdots0\rangle + |10\cdots0\rangle + \cdots |11\cdots1\rangle, \tag{1.13}$$

with the state basis $|ij\cdots k\rangle = |i\rangle_1|j\rangle_2\cdots|k\rangle_3$, and performing the operation $g(\mathbf{x})$ once, the register will evolve into an output state of

$$|\Psi_{out}\rangle = \frac{1}{\sqrt{2^N}}(g(00\cdots0)|00\cdots0\rangle + g(10\cdots0)|10\cdots0\rangle + \cdots g(11\cdots1)|11\cdots1\rangle. \tag{1.14}$$

In this way, all 2^N values of $g(\mathbf{x}_i)$ are obtained using a single quantum circuit and in a single time step. This literally corresponds to a dramatic reduction of computational complexity by a factor of 2^N from the classical algorithm.

The catch, or more precisely, the seeming catch, of this quantum parallelism is that while multiple outputs can be generated simultaneously, it is impossible to read them all out. In fact, according to the quantum measurement postulate, only the amplitude of $g(\mathbf{x}_i)$ can be statistically determined by the means of many repeated experimental runs. This supposedly makes quantum parallelism useless. What saves it is that in many cases only the aggregate properties of the $g(\mathbf{x}_i)$'s are of interest. Rather than reading out each individual $g(\mathbf{x}_i)$, one can instead use quantum parallelism as the intermediate calculation step, while not performing measurement until the end. Along this line of thought, there are now several important algorithms via quantum parallel computation, which are demonstrated to be much more efficient than via classical algorithms. The first one is the Deutsch algorithm proposed by David Deutsch in 1985 [140], where it was shown that the task to determine whether an unknown function is balanced or constant can be performed in a quantum computer in one call, while a classical computer requires two. The gist of the Deutsch

algorithm is to apply a single-qubit operation after the quantum parallel operation, a-priori to measurement. The net effect is to change the measurement basis from $\{|0\rangle, |1\rangle\}$ to $\{(|0\rangle \pm |1\rangle)/\sqrt{2}\}$. In this way, it is the relative phase between $|0\rangle$ and $|1\rangle$ after the parallel operation determines the measurement result, thus becoming an observable. Later in 1992, the Deutsch algorithm was generalized to an N-qubit version, namely the Deutsch-Jozsa algorithm [141], where the balance-constant problem, requiring $\sim 2^N$ evaluations in classical solution, is solved in a single evaluation with the quantum algorithm. This literally reduces the computational complexity by a factor of 2^N. Later in 1995, Peter Shor devised a landmark for efficiently finding the periodicity of a set of integer numbers using the discrete quantum Fourier transformation (DQFT), which is now widely known as Shor's algorithm [142]. The Shor's algorithm is particularly useful in factorizing large numbers, for example, into two prime numbers, for it reducing the exponential complexity in classical algorithm to only polynomial scaling. In practice, a proof-of-principle experiment was demonstrated with a NMR-based quantum computer in 2001 [143]. Another revolutionary quantum algorithm is the Grover algorithm proposed by Lov Grover in 1996, which concerns the problem of efficient searching in an unstructured and unsorted database of size $N \gg 1$ [144]. In classical algorithms, this task requires typically $\sim N/2$ operations. In the Grove algorithm, however, only $\sim \sqrt{N}$ operations are required, giving an improvement factor of $\sim 10^3$ for moderate $N = 10^6$.

A second remarkable application of QIP is quantum cryptography, also referred to as quantum secret-key distribution. The purpose of cryptography is to prevent information leakage to an unauthorized third party during long-distance communications. Quantum cryptography is a novel cryptographic protocol utilizing quantum properties to radically eliminate the possibility of eavesdropping by physical laws [136]. This is in contrast to classical cryptography approaches, where however programmed, secret codes are always subjected to the risk of eavesdropping. To explain

quantum cryptography, we first briefly review the principles of classical cryptography [137]. There are two major methods for classical cryptography. One is to use public-key encryption, the security of which relies on the fact that certain mathematical functions are extremely difficult to invert, for example, the factorization of a product of two large prime numbers. The problem is, however, there is no mathematical proof that an efficient algorithm does not exist; in fact, the aforementioned Shor's algorithm is designed for this exact purpose (which explains why Shor's algorithm has attracted so much military attentions). The second option is to use the so-called Vernam cipher [145], where the information sender and receiver share a random, unique pair of binary sequences, the secret key, for encoding each message. The Vernam cipher is absolutely secure because there are no patterns for cryptanalysts to recognize. The difficulty with this scheme is how to transfer these secret keys absolutely securely between the sender and receiver.

This question remained unanswered until 1984, when Bennett and Brassard proposed to use the quantum no-clone principle to detect the presence of eavesdropping [139]. In the scheme, the sender transmits a sequence of randomized keys in quantum superposition states to the receiver. If eavesdropping occurred, keys received by the receiver will be different from the original keys, due to the fact that 1) a superposition state can not be duplicated and 2) any measurement will immediately collapse it to one of the eigenstates according to measurement bases. By randomized measuring on the received keys and comparing some measurement results with the sender, the receiver and sender can tell if eavesdropping has occurred or not. If yes, the procedure is repeated. If no, then a secret key can be generated from the remaining key sequence. Another quantum cryptography method is built on quantum entanglement, using Bell's inequality to detect eavesdropping [146]. In this scheme, a sequence of entangled qubits are generated. For each pair, one is sent to the sender and the other to the receiver. The sender and receiver then each measure the qubits

they received on randomly chosen bases. Afterwards, they communicate the measurement bases through public keys. Then, they compare the measurement results via public keys for those measurements performed under orthogonal bases, based on which Bell-inequality analysis is performed. If Bell's inequality is violated, then the eavesdropping did not occur with certainty, so the secret keys are secure. In this case, measurement results performed on the same bases are used as secret keys. Otherwise, secret keys are considered eavesdropped, and the whole process is repeated. The theme of this protocol is that any measurement on the entangled pairs will inevitably destroy the entanglement, in which case the Bell inequality can not be violated.

1.2.2 How to process quantum information

Having seen its power, in this section, we present required elementary operations to execute QIP. To proceed, it is illustrative to recall that in classical information processing, there are two basic protocols, namely information computation and network. The information computation is operated with a series of basic logic gates, such as one-bit NOT and two-bit CNOT gates. The information network is accomplished by first converting the solid bits, e.g., coded in directed ferromagnetic materials, into propagating bits, e.g., in the form of sequential electronic or light pulses. The propagating bits are then transported via wires, optical fibers or free space. The processes of quantum information are very analogous, except that with qubits, the computation and network are executed with quantum logic circuits and quantum teleportation.

A quantum logic circuit consists of single-qubit and two-qubit gates. There are three kinds of widely-used single-qubit gates, the NOT gate, Z gate and Hadamard gate [147], which in the state basis $\{|0\rangle, |1\rangle\}$ are defined by matrices of

$$\text{NOT}: \begin{pmatrix} 0 & 1 \\ 1 & 0 \end{pmatrix}, \quad \text{Z}: \begin{pmatrix} 1 & 0 \\ 0 & -1 \end{pmatrix}, \quad \text{Hadamard}: \frac{1}{\sqrt{2}} \begin{pmatrix} 1 & 1 \\ 1 & -1 \end{pmatrix}. \quad (1.15)$$

In the Bloch-sphere representation of qubits [148], they each correspond to a π-rotation along the x-axis, π-rotation along the y-axis, and a π-rotation along z followed by a $\pi/2$-rotation along y axis. It's easy to verify that any single-bit operation can be decomposed into these three basic gates. Widely used two-qubit gates include the conditional phase gate, XOR gate and controlled-NOT (CNOT) gate, all of which are, however, inter-transformable with the aid of single-qubit operations. Among them, the CNOT gate corresponds to a transformation matrix of

$$\text{CNOT}: \begin{pmatrix} 1 & 0 & 0 & 0 \\ 0 & 1 & 0 & 0 \\ 0 & 0 & 0 & 1 \\ 0 & 0 & 1 & 0 \end{pmatrix}, \tag{1.16}$$

in the state basis of $\{|00\rangle, |01\rangle, |10\rangle, |11\rangle\}$. The CNOT operation thus switches the coefficients of the $|10\rangle$ and $|11\rangle$ state. It is noted that any gate operation can be constructed from the combination of three basic single-qubit gates and one two-qubit gate [136].

In quantum teleportation, the quantum states of information carriers (qubits), while not the physical carriers themselves, are transported from one computational device to another. Unlike in a classical information network, a qubit cannot transferred by measurement-reconstruction procedures due to the quantum measurement postulate. Instead, quantum teleportation is performed by making use of quantum entanglement and joint-state measurements. The first and also widely-used teleportation scheme was proposed by Bennett *et al.* back in 1993 [149]. In the scheme, the goal is to transfer a source qubit held by Alice to the target qubit held by Bob. The

source qubit is in an arbitrary state of

$$|\Psi\rangle_a = \frac{1}{\sqrt{|c_0|^2 + |c_1|^2}}(c_0|0\rangle_a + c_1|1\rangle_a). \tag{1.17}$$

To perform transportation, a pair of particles (usually photons), namely particle i and b, are generated in a Bell state of

$$|\Phi^+\rangle_{ib} = \frac{1}{\sqrt{2}}(|0\rangle_i|0\rangle_b + |1\rangle_i|1\rangle_b). \tag{1.18}$$

The particle i is then sent to Alice, while particle b is sent to Bob. The quantum state of the three qubits is then $|\Psi\rangle_a|\Phi^+\rangle_{ib}$. Alice then performs Bell-state measurement (BSM) on the joint state a and i, projecting it onto one of the four Bell bases,

$$|\Phi^\pm\rangle_{ai} = \frac{1}{\sqrt{2}}(|0\rangle_a|0\rangle_i \pm |1\rangle_a|1\rangle_i). \tag{1.19}$$

$$|\Psi^\pm\rangle_{ai} = \frac{1}{\sqrt{2}}(|0\rangle_a|1\rangle_i \pm |1\rangle_a|0\rangle_i). \tag{1.20}$$

After BSM, the final state of the b qubit $|\Psi\rangle_b$ is obtained by projecting the measured Bell basis onto the three-qubit state. It is straightforward to show that depending on the measurement result being $|\Phi^+\rangle$, $|\Phi^-\rangle$, $|\Psi^+\rangle$ or $|\Psi^-\rangle$, $|\Psi\rangle_b$ is collapsed to $\frac{1}{\sqrt{|c_0|^2+|c_1|^2}}(c_0|0\rangle_b + c_1|1\rangle_b)$, $\frac{1}{\sqrt{|c_0|^2+|c_1|^2}}(c_0|0\rangle_b - c_1|1\rangle_b)$, $\frac{1}{\sqrt{|c_0|^2+|c_1|^2}}(c_1|0\rangle_b + c_0|1\rangle_b)$ or $\frac{1}{\sqrt{|c_0|^2+|c_1|^2}}(c_0|1\rangle_b - c_1|0\rangle_b)$, respectively. Alice then sends the measurement result via a classical communication channel to Bob, who becomes aware of $|\Psi\rangle_b$. The last step is to apply appropriate single-qubit operations to recover the source qubit, thereby completing the transportation. It is worth noticing that the teleportation is not accomplished until Bob receives the measurement result from Alice, so that no information is transferred faster than speed light. Besides, upon the completion of teleportation, the original qubits are destroyed, so that the quantum

no-cloning theorem is not violated. Finally, while the aforementioned Bennett *et al.* scheme is now widely accepted as the standard approach, there exist other quantum teleportation protocols [150, 151, 40]. In this dissertation, we describe a new scheme via quantum interferometry.

1.2.3 Overcoming decoherence

Experimental implementation of QIP relies on the ability to precisely manipulate an isolated quantum object, which can be a single atom, ion, photon, or a collective atomic or photonic ensemble. For quantum computation and memory, it is of the general interest to use the atomic or quasi-atom qubits as stationary qubits, as they yield long coherence times and are easy manipulated by optical means. For quantum communication, it is optimal to use photons as information messengers, as they are robust carriers of quantum information that travel at the speed of light. The difficulties in implementing hybrid atom-photon QIP include preparing and storing an atomic qubit in a noisy background, creating strong atom-photon coupling, executing single- or two-qubit logic gates with high precision, transporting optical qubits over lossy channels, and so on, all of which are experimentally challenging. These difficulties are not only from the routine technical challenges in quantum control over microscopic objects, but also from decoherence of qubits due to interaction with surrounding environments. The underlying physics of the decoherence is the differential coupling of the qubits' basis states to orthogonal environmental degrees of freedom. The couplings are irreversible and dissipative, resulting in decoherence and thus the information loss. It is worth noting that the coupling may or may not be associated with energy dissipation, although a major decoherence source is through spontaneous decay of photons or phonons. A common decoherence source without energy dissipation is the Rayleigh or Raman scattering of lasers by atomic qubits, widely occurring during optical manipulations of atomic qubits.

In the presence of qubit decoherence, a successful quantum information process must be executed in a time interval shorter than the decoherence time scale. In practice, while the operation time is physically limited, great efforts are made to reduce the decoherence rate. As given by Fermi's Golden rule, the decoherence rate is proportional to the density of states in the bath at the transition energy. By providing a stronger isolation/confinement, the state density of the surrounding bath, and thus the decoherence rate, can be reduced. For example, due to coupling to the phonon bath, the lifetime τ of the exciton in an (In,As)Ga/GaAs quantum dot, usually of the order of 1 ns, can be significantly extended by embedding the system into an optical cavity, thus reducing the density of photon state it couples to [152]. In this way, a significantly extended lifetime of $\tau \sim 10$ ns has been demonstrated in a recent experiment [153]. Implementations of QIP in cavity-QED systems are operated on a similar principle. In free space, the atom-photon interaction is weak, so that generating useful atom-photon entanglement in this manner will generally fail due to incoherent Rayleigh/Raman scattering. By putting them in a high-finesse cavity in the strong-coupling regime, however, the interaction is enhanced due to the reduction in the photons' quantization volume. In the meanwhile, the spontaneous emission rate can be decreased by reducing the state density of the bath, using the Purcell effect [154]. In this way, the atom-photon coupling can overcome the spontaneous emission, allowing useful QIP in such sytems [155, 156].

While the cavity-QED approach is a well-justified method to create useful atom-atom and atom-photon entanglement at a single-particle level, it relies on confining each atomic qubit in a closed space, giving rise to the difficulty to manipulate these qubits by external electromagnetic fields. If, however, the spontaneous emission can somehow be overcome in free space, then the qubits can be easily manipulated by lasers and magnetic pulses. In principle, there are two ways to reduce the spontaneous emission rate of atomic qubits in free space.

The first one is to tune the interacting photon(s) to be far-off resonance with respective to atomic transitions. Let g be the bare atom-photon coupling constant in free space, Γ be the natural linewidth of the atomic transition, and Δ be the detuning of the photon from resonance, for $\Delta \gg g$, the effective atom-photon coupling strength is given by $|g|^2/2\Delta$, which scales as $1/\Delta$. The spontaneous emission rate of a single atom is $|g|^2\Gamma/4\Delta^2$, scaling as $1/\Delta^2$. The ratio between the two is $2\Delta/\Gamma$, which can be made $\gg 1$ by making the detunning Δ large. Thus in principle, the spontaneous emission can be overcome simply using far-off resonant photons. The problem is that in the far-off resonant regime, the effective atom-photon interaction is so weak that no useful entanglement can be created. One approach is to use many atoms, instead of a single atom, as an ensemble qubit. In this way, the interaction between the ensemble qubit and a photonic qubit is enhanced by a factor of the number of atoms in the ensemble. The inherent disadvantage in using ensemble qubits is, however, that they are subjected to collisional dephasing effects due to atom-atom interaction, thus a relative short quantum memory time. Instead, if one uses photonic-ensemble qubits of laser beams, this collisional dephasing problem can be eliminated, as photons are non-interacting. The difficulty is that, as well-known, while laser beams of many photons can strongly drive single-atom transitions, the back-action of a single atom onto a laser beam, in the form of phase shift, is very weak, so that generating useful entanglement between them will generally fail due to spontaneous emission. To overcome this difficulty, in this dissertation, we propose to use the extreme sensitivity of sub-shot-noise interferometers [157, 158, 119, 159, 160, 24, 25, 26, 27] to detect the weak phase imprinted on the forward scattered light in the regime where spontaneous emission is negligible, thus generating useful entanglements between isolated atomic qubits via a common photonic channel. This work is presented in chapter V.

In the second approach, it is observed that even if photons are resonant with atomic excitation, the spontaneous emission can still be suppressed by the quantum

Zeno effect. The quantum Zeno effect (QZE) occurs when a rapid sequence of measurements is performed on a slowly evolving quantum system, with the result that the system is frozen in its initial state [161]. Consider the coupling of a single atom and photon qubits, for $\Delta = 0$ and $g \ll \Gamma$, the effective spontaneous emission rate of a single-atom qubit is given by $\gamma_{eff} = |g|^2/\Gamma \ll \Gamma$. Counter-intuitively, γ_{eff} scales at $1/\Gamma$, meaning that the stronger natural linewidth, the slower the atomic qubit will decay. Unlike the off-resonance case, however, here the interaction is purely dissipative, in a sense that no phase-shift, thus no entanglement, is created between the atomic and photonic qubit. A possible protocol to generate entanglement out of this purely dissipative interaction is to introduce slow state-evolution of the atom or the photon using a weak driving laser or an optical rotator. The resonant atom-photon interaction is then used as a probe to monitor each other's quantum state during the evolution. If the driving is *sufficiently* weak, then the two qubits are forced to stay in decoherence-free subspace (DFS) [162, 163, 164], due to the quantum Zeno effect. As a result, the outcome state of one qubit is dependent on the other, leading to entanglement between them. What's appealing in this approach is that there is no direct interaction between the two qubits. Instead, the potential that such an interaction will lead to decoherence prevents the interaction to actually happen. In this sense, the entanglement is generated in an "interaction-free" manner. This helps to reduce the failure possibility due to decoherence when executing the QIP. In chapter VI of this dissertation, a series of universal, scalable QIP elements are proposed by making use of the quantum Zeno effect. The work of chapter V and VI can potentially lead to practical implementations of QIP in free space.

2.4 Recent experimental progresses

The past decade has witnessed steady experimental progress in the realization of quantum information processing protocols [136], including those for quantum com-

putation [165, 166, 167, 168, 169, 170, 171, 172, 173, 174], quantum communication [175, 176, 177], quantum cryptography [178], quantum dense coding [179] and optimal phase estimation [180]. The systems used in these experiments have involved purely photonic qubits [181], mixtures of atomic and photonic qubits [182, 183, 184, 185], or purely atomic qubits [186, 187, 188], where 'atomic' here refers to any massive particle or ensemble of massive particles.

From the quantum logical gate prospective, one-qubit gates can now be commonly realized by applying sequences of Rabi pulses. Implementing two-qubit gates are, however, much more difficult, mainly because they in general require strong qubit-qubit interaction. Several important proof-of-principle two-qubit gates are experimentally demonstrated in systems of 1) all-optical in 2000 [189]; 2) cavity-QED [182, 183, 184, 185]; 3) trapped ions in 2004 [186, 187]; 4) nuclear spin resonance of molecules in 1997 [190, 191]; 5) solid-state in 2009 [192]; and Rydberg atoms in 2009 [193]. A major difficulty in these schemes are, however, to maintain a strong interaction while avoiding decoherence. Such primarily limits the existing gate success probability to be only slightly above the threshold value of 66.7%, which is the upper-boundary of classical means. In order to overcome this difficulty, another emerging line of quantum computation is to use the quantum Zeno effect to replace the qubit-qubit interaction. In this scheme, the Zeno effect forces the system to remain in a decoherence free subspace (DFS) [162, 163, 164], and thus generating entanglement between two qubits. Several schemes for quantum entanglement manipulation and/or gate operation via a quantum Zeno gate have been recently proposed [194, 195, 196, 197, 198], including the work of chapter V in this dissertation.

Quantum teleportation, on the other hand, relies on the capability to generate correlated photon pairs and perform (Bell state measurement) BSM, both of which are considerably challenging due to the difficulty to pair photons and low-efficiency in photon detection. In the first series of experiments by the group of A. Zeilinger in

1997 [175] and Boschi *et al* in 1998 [199], qubits are encoded in the polarization state of photons. The ancillary photon pairs are generated from the so-called EPR source of type II parametric down-conversion device. The BSM is performed by first mixing the measuring photons with polarized beamsplitter (PBS) and then detecting the outcome photons. A second type of photonic quantum teleportation was demonstrated in 2003 by the Gisin group, where instead of polarization qubits, quantum information s coded in the form of a timed pulse sequence, thus improving sustainability against polarization relaxation in optical fibers [181]. Further, instead of qubit teleportation, he so-called entanglement teleportation, in which entanglement is swapped from Al-e with Bob to Alice with Charles, was also demonstrated in a 2001 experiment sing four photon entanglement [200]. However, all these schemes are probabilistic nd post-selection, where successful teleportation events are selected after comple-on of the experiment, by searching for a subset of experiments matching a preset econstruction operation. They are thus of little usability for practical QIP, which elies on unconditional teleportation of qubits. In contrast, deterministic quantum eleportation was demonstrated in 2004 by the Blatt group in Austria [186] and the Vineland group in NIST [187]. In these schemes, the quantum state of a trapped ion ubit is teleported to a target ion in a neighboring trap with the aid of an ancillary on qubit. The working principle is similar to the Zeilinger experiment [175]. That s, in the first step, the target and ancillary ions are prepared in Bell state by the neans of Raman gates. Then, the BSM is performed on the joint state of ancillary nd target qubits employing controlled phase gates. In both experiments, a fidelity of ~ 75% are achieved, thus demonstrating deterministic (non-post-selection) quantum eleportation with a fidelity exceeding the classical limit by $\sim 10\%$. The problem is, owever, the state transfer is restricted to within neighboring ion traps, correspond-ng to a length scale of ~ 0.1mm, and is thus not precisely "*tele*portation". A true lthough highly probabilistic teleportation over a 1m distance was demonstrated by

the Monroe group in JQI in Jan 2009 [201]. In their scheme, an arbitrary teleporting qubit is encoded in the ground hyperfine states of a trapped ion. The target qubit of another ion separated by 1m is prepared in a known superposition state. A laser pulse then excites each ion, leading to spontaneous emission. The spontaneous photons are then collected along certain directions and then interfere at a beamsplitter (BS). Conditioned on coincident detection of BS outcome, the entanglement of the two ion qubits are announced, upon which teleportation is accomplished with the addition of single-qubit operation. This scheme, while showing a heralded fidelity of $\sim$ 90%, relies on coincide spontaneous emission of the two ions into two preset direction (with a probability of $\sim 10^{-8}$), and is thus highly probabilistic.

To conclude, while steady experimental progresses have been demonstrated in various systems, realizing usable QIP remains a long-term effort. To date, the highest fidelity among all reported experiments is $\lesssim 90\%$, while a practical implementation of N-qubit QIP would require deterministic operations with a fidelity of $\gg 1/N \sim 0.999\cdots$. The gap between current achievements and practical requirements is thus considerably large. Committed to narrow this gap, two new implementations of QIP are proposed in chapter V and VI in this dissertation.

Chapter 2

Creation, detection and decoherence of Schrödinger cat states in double-well Bose-Einstein condensates

In this chapter, we study the possibility to create many-particle Schrödinger cat-like states by using a Feshbach resonance to reverse the sign of the scattering length of a Bose-Einstein condensate trapped in a double-well potential. To address the issue of experimental verification of coherence in the cat-like state, we study the revival of the initial condensate state in the presence of environmentally-induced decoherence. As a source of decoherence, we consider the interaction between the atoms and the electromagnetic vacuum, due to the polarization induced by an incident laser field. We find that the resulting decoherence is directly related to the rate at which spontaneously scattered photons carry away sufficient information to distinguish between the two atom-distributions which make-up the cat state. We show that for a 'perfect' cat-state, a single scattered photon will bring about a collapse of the su-

perposition, while a less-than-perfect cat-like state can survive multiple scatterings before collapse occurs. In addition, we study the dephasing effect of atom-atom collisions on the cat-like states. The major results of this chapter have been published in "Creation, detection, and decoherence of macroscopic quantum superposition states in double-well Bose-Einstein condensates", Y. P. Huang and M. G. Moore, in Phys. Rev. A **73**, 023606 (2006).

The organization of this chapter is as follows. In section 2.1, we give an introduction on the background of Schrödinger cat states and review previous implementations in BEC systems. In Section 2.2, the model of bimodal BEC in Double-well system is introduced and the cat states in such a system are defined; in Section 2.3, We propose generating a cat-like state through dynamic evolution following a sudden flipping of the sign of the atomic interaction, accomplished via Feshbach resonance. In Section 2.4, the method of detecting the cat-state via revival of the initial state is discussed in details. In Section 2.5, we investigate the decoherence of cat-states, via a master equation derived for laser-induced decoherence. In addition, the lifetime of cat-states in the presence of laser fields is determined. In Section 2.6, the dephasing effects due to the nonlinear two-body interaction is studied. And finally, we briefly summarize our results in Section 2.7.

2.1 Introduction

Interest in Schrödinger cat-like states, loosely defined as quantum superpositions of macroscopically distinguishable many-body states, goes back to the earliest days of quantum mechanics. In 1935, in oder to demonstrate the limitations inherent in using quantum mechanics to describe everyday phenomena, Erwin Schrodinger proposed a experiment in the macroscopic state of a cat is entangled with that of an unstable nuclei, allowing the cat to enter a coherent superposition of being dead and alive [77].

Such states were thought at the time to be logically untenable, although today we might consider only that they would not be observed due to rapid environmentally-induced decoherence [202]. To this day, this famous gedanken experiment illustrates the fundamental difficulties inherent in postulating a well-defined boundary between a 'classical' level of reality and an underlying level governed by quantum mechanics, one of the fundamental open questions in quantum theory.

Many of the early gedanken experiments, whose consideration led to the earliest understanding of quantum mechanics, are now being transformed into laboratory realities. One such effort has been the ongoing quest for Schrödinger-cat-like states, with the most striking experimental results to date being the observation of a superposition between clock-wise and counter-clock-wise currents in a superconducting quantum interference device [203] and the observation of double-slit diffraction for massive C_{60} molecules [204]. Additional efforts include work in trapped ions at low temperature [205, 206], nanoscale magnets[207], and superconductors [208, 209, 210]. This progress is generating deeper insight into the meaning of quantum theory, as well as potential applications in the fields of precision measurement and quantum information processing. Even with the current rapid rate of progress, the quest to obtain and utilize large cat-like states remains a serious experimental challenge, due primarily to the presumed scaling of fragility (with respect to environmentally-induced decoherence) with number of particles. For most appliciations, the utility of the cat-state increases with particle number [78, 79], so there is a strong need to find systems in which such maximally-entangled states of large numbers of particles can be generated without rapid collapse due to decoherence.

An atomic BEC [211, 212, 213] may be such a system, as its large degree of spatial and temporal coherence is well established by experiment [214]. The bimodal BEC, which is constructed by isolating a pair of weakly-coupled atomic-field modes, is one of the simplest quantum systems used in the study of entanglement physics and

has therefore been the subject of extensive theoretical study [69, 70]. In this system, N bosons are restricted to occupy one of two modes, and entanglement is established via two-body interactions between the bosons. For the case of an atomic BEC, the two modes can either be two potential-wells spatially separated by a potential barrier (so-called Double-well BEC's) [74, 75] or two spatially-overlapping modes in different hyperfine states [72, 73]. In addition, a recent paper proposes an analogous system in which a double-well 'potential' in momentum-space, formed from the band-structure in a lattice potential, can be used to create cat-states involving two momentum-states [215].

The quantum ground-state of the bosonic double-well system has been studied for the case of repulsive interactions in the context of the superfluid to Mott-insulator transition [216], as well as for the case of attractive interactions. For the latter, it has been shown under certain conditions that a Schödinger cat-like macroscopic superposition state, can be generated [217, 218]. In this cat-like many-body state, a large number of atoms are collectively either in one mode or in another. The dynamics of the bimodal system have also been investigated, both via a meanfield approach and a full many-body treatment within the two-mode approximation. In the mean-field treatment, the dynamic evolution is treated as a Bose Josephson Junction, which is complementary to that of a superconductor tunnel junction [219, 220]. This treatment predicts a degenerate ground-state, corresponding to all amplitude in one well or the other, but is not capable of predicting the dynamical evolution of cat-like states, as these states lie outside of the domain of mean-field theory. In the two-mode many-body treatment, the many-particle cat-like state is predicted to arise during the dynamical evolution of an initial minimally-entangled condensate state in the presence of repulsive interactions [72, 75], but with the sign of the tunneling coefficient reversed by imprinting a π-phase shift onto one well. In this chapter, we propose that such cat states can be realized for the case of an atomic BEC trapped

in a double-well potential by employing a magnetic Feshbach resonance to tune the atomic interaction from repulsive to attractive [12, 13]. It is found that for suitable parameters, the initial state will evolve into a cat-like state after a certain period of time, and then it will revive back to the initial state.

Despite these theoretical advances, there remain many challenges, some of which we address in the present manuscript. One challenge is the problem of experimental verification of the coherence between macroscopically distinguishable states, which is related to the challenge of understanding the role played by environmentally-induced decoherence in collapsing the cat-state onto a statistical mixture of the two macroscopically-distinguishable possibilities. In this chapter we focus in detail on the decoherence which will occur if laser-light is used for trapping and/or probing of the cat states. In addition the influence of atom-atom interactions on the proposed detection scheme is studied in some detail. We show the revival of the initial state can be used as an unambiguous signal that the supposed cat-state is indeed a coherent macroscopic superposition, as opposed to an incoherent mixture. We also demonstrate, however, that collisional de-phasing can mask the revival without a true loss of coherence.

The effects of decoherence on these cat-like states have primarily been discussed for the case of coupling to the thermal-cloud of non-condensate atoms. There is disagreement in the literature regarding whether or not this effect is significant [221, 222, 72]. We note, however, that these authors treat the non-condensate fraction as a Markovian reservoir, which implies an infinitely-short memory (relative to condensate evolution times) for correlations between the condensate and non-condensate terms. We question this assumption, primarily due to the fact that the non-condensate fraction typically has a very low temperature and density. In addition, the non-condensate atoms are trapped inside the condensate volume by the trapping potential, thus there is no irreversible loss of information due to propagation

of the entangled atoms outside of the system volume. Hence, we suspect that a non-Markovian treatment is necessary to accurately evaluate the thermal-cloud induced decoherence. However, modeling this is a difficult task that we do not address at present. Instead, we assume that this effect is negligible and concentrate primarily on an analysis of a new source of decoherence: that due to spontaneous scattering of far-off-resonant photons from laser fields which we presume are used in either the trapping and/or probing of the system. In this case, the correlation time of the reservoir is governed by the irreversible loss of the scattered photons from the system volume at the extremely fast rate of L/c where L is the atomic mode size and c is the speed of light. Hence, the Markov approximation works extremely well for describing the physics of photon-scattering. As is well known, this approach leads to effective interactions as well as decoherence, effects which include induced dipole-dipole interactions and collective spontaneous emission (superradiance) in the atomic ensemble.

When analyzing the effects of environmentally-induced decoherence, this chapter is devoted to answer two basic questions: (1) What limitations are imposed on the ability to create cat-states, and revive the initial condensate states by the presence of decoherence, and (2) how long can one 'hold' the cat-state by decreasing the tunnel-coupling to zero, without collapse of the cat-state onto a mixed state. The second question is raised in anticipation of applications in precision measurement and quantum information processing where the cat state is operated on and/or held ready for future operations during a complicated protocol. We therefore need to determine the lifetime of the cat states in the presence of decoherence, as well as the effect of decoherence on the dynamical evolution from the initial state into the cat-state.

2.2 The model

Our proposed scheme involves loading a BEC into a double-well potential and then employing a Feschbach resonance to vary the atomic scattering length in order to produce a Schrödinger cat-like state. For the present we consider only the case of a spatial double-well potential. However, an analogous system can be formed by using a Raman-scheme to couple two hyperfine states in a spinor BEC [72, 73]. The primary difference between this model and the double-well system lies in the presence of collisional interactions between the two modes, due to the spatial overlap of the hyperfine modes. Our model neglects these collisions, as they are negligible for the case of well-separated potential minima. Most of our results should apply to both systems.

We begin our analysis from the usual many-body Hamitonian describing atomic BEC,

$$\hat{H} = \int d^3r \hat{\Psi}^\dagger(\mathbf{r})[-\frac{\hbar^2}{2m}\nabla^2 + V_{trap}(\mathbf{r})]\hat{\Psi}(\mathbf{r}) + \frac{U_0}{2}\int d^3r\, \hat{\Psi}^\dagger(\mathbf{r})\hat{\Psi}^\dagger(\mathbf{r})\hat{\Psi}(\mathbf{r})\hat{\Psi}(\mathbf{r}), \quad (2.1)$$

where m is the atomic mass, V_{trap} is the trapping potential and $\hat{\Psi}$ is the annihilating field operator for the atoms in Heisenberg picture. The two-body interaction strength is given by $U_0 = 4\pi a\hbar^2/m$, with a denoting the $s-$wave scattering length. In our model, the BEC is assumed to occupy a symmetric double-well potential.

The single-atom ground state and first excited state for this system are denoted as $\psi_s(\mathbf{r})$ and $\psi_a(\mathbf{r})$, respectively, where $\psi_s(\mathbf{r})$ is symmetric with respect to the double-well symmetry and $\psi_a(\mathbf{r})$ is antisymmetric. We denote the energy gap between these states as $\hbar\tau$, which is typically much smaller than the gap between the first and second excited states. Because of this gap, we assume throughout that the atomic population is restricted to these two modes alone. It is convenient to introduce two

localized states ψ_L, ψ_R [223],

$$\begin{aligned}\psi_L(\mathbf{r}) &= \frac{1}{\sqrt{2}}\left[\psi_s(\mathbf{r}) + \psi_a(\mathbf{r})\right], \\ \psi_R(\mathbf{r}) &= \frac{1}{\sqrt{2}}\left[\psi_s(\mathbf{r}) - \psi_a(\mathbf{r})\right].\end{aligned} \tag{2.2}$$

Expanding the field operator $\hat{\Psi}(\mathbf{r})$ in forms of these two modes gives

$$\hat{\Psi}(\mathbf{r},t) = \hat{c}_L(t)\psi_L(\mathbf{r}) + \hat{c}_R(t)\psi_R(\mathbf{r}), \tag{2.3}$$

where $\hat{c}_L$ and $\hat{c}_R$ are bosonic atom-annihilation operators for the left and right modes, respectively. Inserting this expansion back into the many-body Hamiltonian (2.1), one recovers the two-mode version of the Bose-Hubbard model

$$\hat{H} = -\hbar\tau(\hat{c}_L^\dagger \hat{c}_R + \hat{c}_R^\dagger \hat{c}_L) + \hbar g(\hat{c}_L^{\dagger 2}\hat{c}_L^2 + \hat{c}_R^{\dagger 2}\hat{c}_R^2). \tag{2.4}$$

In deriving this expression, we have implicitly assumed that atomic collisions in the overlapping region of the two modes are negligible, valid under the assumption that the two modes are well separated. The intra-well two-body interaction strength is indicated by g, where $g = U_0/2\hbar \int d^3r |\psi_{L,R}(\mathbf{r})|^4$. Note that in deriving the bimodal Hamiltonian (2.4), the wavefunction for each mode is assumed to be independent of particle number in the trap, and terms proportional to the total atom number-operator have been dropped, as atom number is assumed to be a conserved quantity.

The N-particle quantum state of this bimodal system can be expressed as a superposition of Fock-states $|n\rangle$ [70]

$$|\hat{\Psi}\rangle = \sum_{n=-N/2}^{N/2} c_n |n\rangle, \tag{2.5}$$

where

$$|n\rangle = \frac{(c_L^\dagger)^{N/2+n}(c_R^\dagger)^{N/2-n}}{\sqrt{(N/2+n)!(N/2-n)!}}|0\rangle. \tag{2.6}$$

Here, N is the total number of atoms in the condensate which for convenience we take as an even number, and n denotes half the number difference between the two modes. The two corresponding operators are

$$\begin{aligned} \hat{N} &= \hat{c}_L^\dagger \hat{c}_L + \hat{c}_R^\dagger \hat{c}_R, \\ \hat{n} &= \frac{1}{2}(\hat{c}_L^\dagger \hat{c}_L - \hat{c}_R^\dagger \hat{c}_R). \end{aligned} \tag{2.7}$$

In this representation, the conventional Schrödinger cat state is defined as

$$|\mathrm{cat}\rangle = \frac{1}{\sqrt{2}}(|N/2\rangle + |-N/2\rangle), \tag{2.8}$$

where the N particles have equal probability to be all in the left or all in the right mode. This cat-state is an ideal maximally-entangled state, however it will be difficult to create such a state in this bimodal system. Instead, a more experimental accessible cat-like state is one containing two-well-separated wave-packets in the distribution of c_n. For example, a typical cat-like state can be of the form

$$c_n \propto e^{\frac{(n-n_0)^2}{2\sigma^2}} + e^{\frac{(n+n_0)^2}{2\sigma^2}}, \tag{2.9}$$

with $n_0 > \sigma$.

In the bimodal system we discuss below, the class of cat-like states is more general than the Gaussian form (2.9). A useful cat like state only needs to satisfy two conditions: (i) the probability distribution in Fock-space should be approximately symmetric; and (ii) the two wave-packets should be well separated in order to correspond to macroscopically distinguishable states. In the present model, condition (i) is

satisfied provided the initial state is symmetric, due to the symmetry of Hamiltonian (2.4). As we will see is Section 2.5, decoherence may break this symmetry. Nonetheless, to distinguish cat-like states from non-cat state, it is convenient to introduce a projection operator $\hat{P}_{cat}$

$$\hat{P}_{cat} = \sum_{n=n_c}^{N/2} (|n\rangle\langle n| + |-n\rangle\langle -n|). \tag{2.10}$$

This operator acts as a filter which picks up cat-states with a minimum wave-packet separation of $2n_c$, where n_c is preset parameter. The expectation value $\langle \hat{P}_{cat} \rangle$ can be a efficient way to determine whether a state is cat-like. It is straightforward to see that for a cat-like state we will have $\langle \hat{P}_{cat} \rangle \approx 1$, whereas for a non-cat state the trace will be noticeably less than unity.

2.3 Dynamical generation of cat states

As shown both theoretically and experimentally , the s-wave scattering length of cold atoms can be modulated by applying a varying magnetic field. In the vicinity of a Feshbach resonance, it takes the form [12]

$$a = a_0(1 - \frac{\Delta B}{B - B_0}), \tag{2.11}$$

where a_0 is the background value, B_0 is the resonant value of the magnetic field, and ΔB is the width of the resonance. By tuning the magnetic field B, the scattering length a can be efficiently tuned in an adequate range based on the Feshbach resonance, as demonstrated in a recent experiment [13]. Thus, the two body interaction term g in Hamiltonian (2.4), which is determined by scattering length a, is implicitly assumed to be an arbitrary adjustable number.

Before discussing the methods of generating cat-states, we note that attractive

BECs can collapse due to instability, as been demonstrated in experiments [224]. A trapped BEC, however, can be stable against collapse under the condition of low atomic density [225]. In terms of the BEC atom number N, the attractive interaction strength g and the energy gap between the first-excited state and ground state $\Delta\omega$, the stability condition can be written as

$$N < \frac{\Delta\omega}{|g|}. \tag{2.12}$$

In the present discussion one can increase the energy gap between the ground and excited state by adjusting the trapping potential, and in this way, we can ensure our system will not collapse when the sign of the scattering length is switched from positive to negative.

There were some efforts to generate Schrödinger cat states via adiabatic manipulation of the many-body ground state [217, 218], achieved by a continuous variation of the interaction strength g from a positive to a negative value. This approach, however, is extremely difficult to implement, due to the energy-degeneracy in the ground and first-excited state, as explained in appendix 2.8.1. An alternate approach to a Schrödinger cat state, based on dynamical evolution, has been studied for some time [72]. In this subsection, we show that it is feasible to dynamically create the cat state from a coherent state by using a Feshbach resonance to make a sudden change in the scattering length. Our proposed scheme is as follows. First, our system is prepared in the ground state with repulsive interactions and strong tunnelling between wells. This could be accomplished, e.g. by preparing a BEC in a single well, and then adiabatically raising a barrier to divide the well into two equal parts. Note here, the quantum state of this system is coherent in the sense that each atom in the condensate is independently in a superposition of the two localized states. The interaction parameters in this initial stage are chosen to satisfy $g = \frac{\tau}{0.9N}$ as this

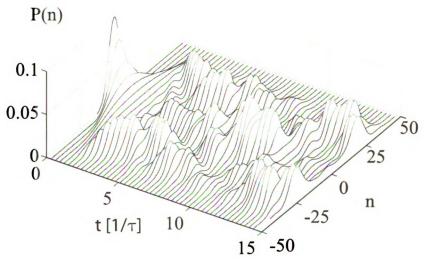

Figure 2.1: Evolution of the probability distribution $P(n) = |c_n|^2$ versus n, with $N =$ **100.** At $t = 0$, the initial state is taken as the ground state with$g = \tau/(0.9N)$. Then, **the** two body interaction is suddenly switched to the negative value $g = -\tau/(0.9N)$. **The** wavepacket then evolves, where it shows a collapse and revival process. It is **seen** that, at a time of $t = 14.5/\tau$, a well peaked cat state is obtained with two well **separated** wavepackets centers at around $n = 25, 75$, respectively.

will lead to the optimal cat-like state attainable in this scheme. Once this state is **estab**lished, the Feshbach resonance is used to achieve a sudden switch of the sign of **the** scattering length, i.e. we go from $g = \frac{\tau}{0.9N}$ to $g = -\frac{\tau}{0.9N}$. In order to avoid the **coll**apse of the condensate when scattering length a becomes negative, the amplitude **of** atomic interaction g should be small. At this point, with tunneling still on, the **initi**al state is no longer an eigenstate, thus it will start a dynamic evolution under **the** new Hamilton. The system dynamics is then calculated by numerically solving **the** underlying Schrödinger equations.

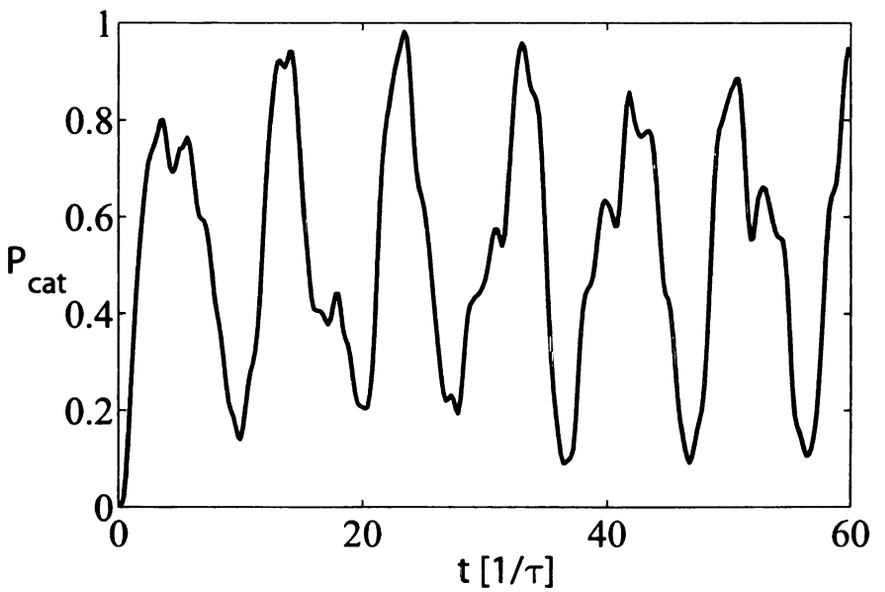

Figure 2.2: Time evolution of the expectation value of the projector P_{cat} with system **parameters** chosen as in Fig. (2.1) and a filtering window of width $n_c = 15$. A well **peaked** cat state is created at $t = 14.5/\tau, 24/\tau, 34/\tau....$ Note that P_{cat} reaches a **minimum** at $t \approx 10/\tau, 20/\tau, 30/\tau...$, which corresponds to the revival of the initial **coherent** state.

The evolution of the initial coherent state after the change in the sign of g is shown in Figure 2.1. It is seen that cat-like states are formed periodically, and between two consequent cat states the system approximately revives back to the initial coherent state. We have determined that the best cat state appears at time $t = 14.5/\tau$, which corresponds to the final state shown in Fig. 2.1. Once the cat state is formed, one needs to freeze the dynamic evolution at a time when the system is in the cat state. This can be accomplished by suddenly raising the barrier between the two modes to reduce the tunneling coeffient, τ, to zero.

Since the present proposal is based on a dynamic procedure, predicting the time when the cat state is produced t_{cat} is of critical importance. Due to the imposed constraint $\tau = 0.9Ng$, which is necessary to obtain an optimal cat-state, t_{cat} can be expressed solely in terms of the tunneling rate τ as

$$t_{cat} = \frac{\kappa}{\tau}, \tag{2.13}$$

where κ is determined from our simulations to be $\kappa \approx 14.5$.

In Figure 2.2, we show the dynamical evolution of projection operator P_{cat}. Again, it is shown that the optimum cat-like state forms at around $t = t_{cat} = 14.7/\tau$ and reappears again at intervals of $t = 10/\tau$. It is also noticed that between each cat state, there are valleys of P_{cat}, which correspond to revivals of the initial coherent state.

It is also of interest to study the relative phases between the Fock states in the cat-like state generated in this manner. The symmetry between left and right modes is automatically guaranteed in our model since our system Hamiltonian (2.4) and our initial state are both symmetric. In Figure 2.3, we see that the phase of created cat state is exactly symmetric around $n = 0$. In addition, we see that the phase flattens somewhat in the vicinity of $n = \pm 25$, where the peaks in the probability are located.

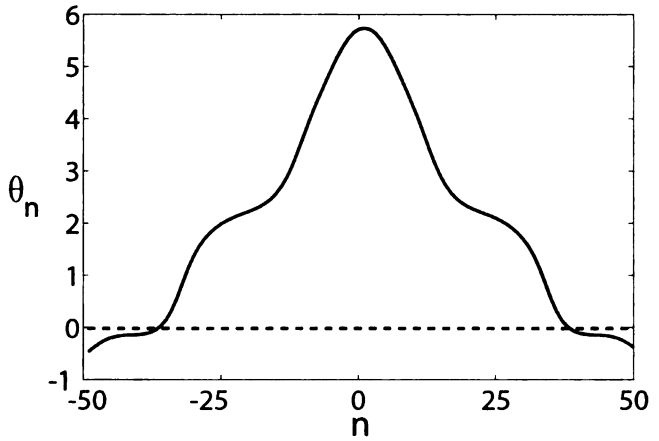

Figure 2.3: Phase distribution of the created Schrödinger cat state in Fock space. **The** y axis is the phase $\theta_n = Arg(c_n)$.

We have claimed that imposing the condition $\tau = 0.9Ng$ is necessary to produce **the** optimal cat state. It is worth pointing out that with other choices, left-right **symm**etric states can be created, but these are neither well-separated nor double **peaked**. This is shown in Figure 2.4, where we plot the expectation value of the **projector** P_{cat} versus δ_g, where we have taken $g = \frac{\tau}{0.9N}(1 + \delta_g)$. In this figure, we **see** the cat-like state is only created in the vicinity of $\delta_g = 0$ with an uncertainty of **approx**imately $\pm 5\%$. That means to create a cat state in the present system, a precise **control** of the atomic interaction g or tunneling rate τ is required. It is important **to** note that in generating Figure 2.4 we have varied the evolution time t_{cat} for each **parameter** choice, in order to maximize the projection P_{cat}. Thus Figure 2.4 can be **interpreted** as verifying the conditions $g = \frac{\tau}{0.9N}$ and $t_{cat} = 14.7/\tau$.

Finally, this method of generating a cat state is robust against noise in the initial **state**, which could be due to a finite temperature. On the other hand, it does require **a precise** knowledge of atomic interaction strength g to be within a deviation of about

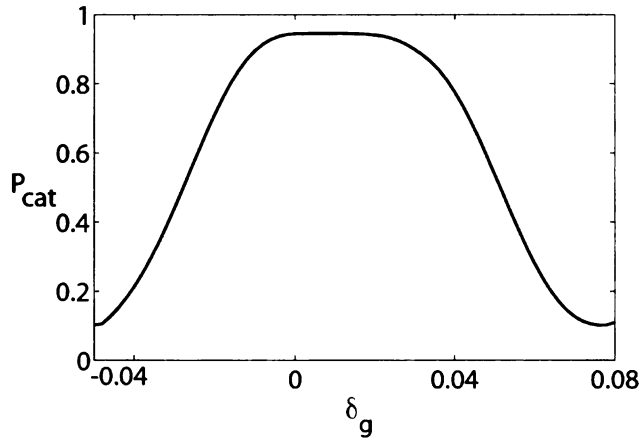

Figure 2.4: The measurement P_{cat} versus interaction strength variation, with $g = \frac{\tau}{0.9N}(1+\delta_g)$. Other system parameters and projection operators other identical to **Fig.** (2.2). It is shown that in the vicinity of $\delta_g = 0$, the cat state is created. Note **that** the projection is measured at different times for each δ_g, so that the value of P_{cat} is maximized.

2%. Detailed discussions are given in appendix 2.8.2.

2.4 Detection of cat state

Presuming a cat-like state can be created in the above manner, it remains a **chall**enge to experimentally verify the coherence between the macroscopically distin**guish**able states. Neverthless, a possible method to detect Schrödinger cat states in **this** bimodal BEC's lies in detecting the revival of the initial coherent state. In Fig. **2.5** we show the evolution of the cat state starting from $t = t_{cat}$ with the system **para**meters still satisfying $g = \frac{\tau}{0.9N}$. This shows that under the condition of no **deco**herence, the system will evolve back to a coherent state after a certain period **of ti**me, which we denote as t_{rev}. The revival time t_{rev} again is estimated from our **simu**lations, yielding $t_{rev} = 7/\tau$.

In the presence of decoherence, however, the system may not exhibit a distinct

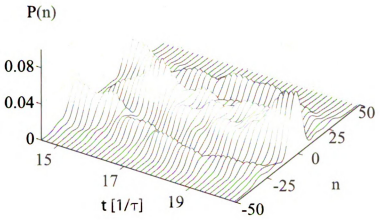

Figure 2.5: Revival dynamics from the cat state back to the coherent state. This figure shows the continued dynamical evolution following that shown in Fig.2.1 with $g = -0.01$. At $t = 14.5/\tau$, the quantum system is in a cat state, then at a time of $t \approx 21$, the initial coherent state is revived.

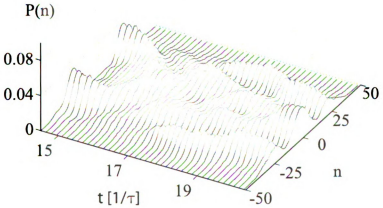

Figure 2.6: Dynamical evolution of a partially incoherent cat state. The parameters are chosen the same as Fig.2.5. At $t = 14.5/\tau$, the quantum system is in a mixed state with no coherence between the two wavepackets. Then as it evolves, the system exhibits oscillations, but will not evolve back to the initial state.

revival of the coherent state. To illustrate this we first consider two states which we define as the partially incoherent state and the totally incoherent state. These states are defined by the introduction of a coherence 'length' in Fock-space, I_{coh}, so that coherent superpositions between Fock-states $|n\rangle$ and $|m\rangle$ are destroyed for $|n-m| \gg I_{coh}$, while superpositions satisfying $|n-m| \lesssim I_{coh}$ are relatively unaffected by decoherence. The partially incoherent state is then defined in the sense that the coherence length I_{coh} is small compared to the distance between the two separated peaks of the cat state, but larger than the width of either wavepacket, i.e., $I_{coh} < n_0$ yet $I_{coh} > \sigma$ in Eq. (2.9). For the completely incoherent state, on the other hand, the cat state is taken to have collapsed to a single Fock state, i.e. a mixed state maintaining the probability distribution of the cat-state but with no coherence between Fock-states.

The evolution of those two states in time is shown in Fig.(2.6) and Fig.2.7, respectively. Unlike the cat state, the incoherent states will not exhibit a revival of the initial coherent state at $t = t_{rev}$. The partially incoherent state evolves instead into a disinct three-peaked state, whereas the completely incoherent state exhibits small oscillations with no discernable peaks after a very short collapse time.

Based on these considerations, one prospective method to verify the coherence of the cat state would involve: i) first, measuring the probability distribution, $P(n)$, which is accomplished by repeated measurements of the atom-number in each mode; ii) then after forming the cat-state, the state should be held for a time $t = t_{hold}$ and then with tunneling restored, the revival of the initial coherent state should be observed after a time t_{rev}; iii) a known source of decoherence should be added while holding the system in the cat state at $\tau = 0$ for a duration t_{hold}, after which a lack of revival should be observed. To add decoherence, one could simply add a laser field to the system. This will introduce decoherence due to spontaneous photon scattering, as described in Section 2.5. If the revival of the initial state can be observed in the

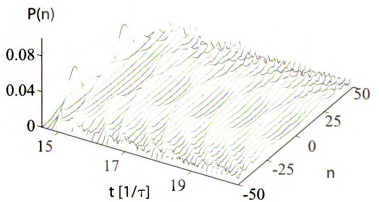

Figure 2.7: Dynamic evolution of completely decoherent cat state. At $t = 14.5/\tau$, we let the system collapse onto a statistical mixture of Fock-states. It is seen that the dynamic is completely disordered.

case of no additional decoherence, but disappears when the decoherence is added in a controlled way, than one should have a strong claim for the observation of coherence between macrscopically distinguishable states.

2.5 Laser-induced decoherence and losses

While trapped ultracold atoms are typically well-isolated from the environment, the presence of lasers for trapping and/or detection of atoms will polarize the atoms and thus couple them to the vacuum modes of the electromagnetic field. This coupling allows for spontaneous Rayleigh scattering and/or diffraction of laser photons, which can lead to losses and/or decoherence of the atomic system. If the scattered light field acquires sufficient information to determine the atom-number difference between the left and right wells, then this spontaneous scattering will lead to a dynamical collapse from the cat-state into a mixture of Fock states, an example of environmentally-

induced decoherence.

In order to model these effects, we derive the master-equation which governs the density operator of the atomic field ρ_s, where

$$\begin{aligned}\dot{\rho}_s(t) &= -iH_s\rho_s(t) - i\int d^3r\,\frac{|\Omega(\mathbf{r})|^2}{\Delta}\hat{\Psi}^\dagger(\mathbf{r})\hat{\Psi}(\mathbf{r}) \\ &\quad - \int d^3r\,d^3r'\Omega(\mathbf{r})\frac{L(\mathbf{r}-\mathbf{r}')}{\Delta^2}\Omega^*(\mathbf{r}')\hat{\Psi}^\dagger(\mathbf{r})\hat{\Psi}(\mathbf{r})\hat{\Psi}^\dagger(\mathbf{r}')\hat{\Psi}(\mathbf{r}')\rho_s(t) \qquad (2.14) \\ &\quad + \int d^3r d^3r'\Omega^*(\mathbf{r})\frac{L^*(\mathbf{r}-\mathbf{r}')}{\Delta^2}\Omega(\mathbf{r}')\hat{\Psi}^\dagger(\mathbf{r})\hat{\Psi}(\mathbf{r})\rho_s(t)\hat{\Psi}^\dagger(\mathbf{r}')\hat{\Psi}(\mathbf{r}') + H.c..\end{aligned}$$

A detailed derivation of this master equation is given in appendix 2.8.3. Here, $\hat{\Psi}(\mathbf{r})$ is the annihilation operators for atoms. $\Delta = \omega_e - \omega_L$ is the detunning of laser field from resonant excitation. The atom-laser interaction is governed by the Rabi-frequency $\Omega(\mathbf{r})$. $L(\mathbf{r}-\mathbf{r}')$ is the nonlinear two-body correlation coefficient defined in appendix 2.8.3, equation (2.60).

Underlying the dynamics governed by master equation (2.14) is the exchange of photons between atoms and between an atom and the EM vacuum. As such photon exchanges can involve significant momentum exchanges due to photon recoil, it is useful to first define elastic and inelastic regimes with respect to the initial atomic center-of-mass state. If the spatial size of the initial atomic mode is small compared to the laser wavelength, then one would be in the elastic regime, as photon-recoil would not be sufficient to carry the atom outside of the momentum distribution of the initial state. In the inelastic regime, on the other hand, the initial mode is large compared to the laser wavelength, which implies that it is narrow in momentum space compared to the photon momentum, so that the recoil from a single photon is sufficient to remove an atom from its initial mode and place it in an orthogonal mode.

In the strongly elastic regime, there will be negligible loss of atoms from their initial modes. As we shall demonstrate, the master equation (2.14) may still lead to decoherence/collapse of the two-mode cat-states. In the inelastic regime, on the

other hand, the predominant effect of the atom-field interaction will be scattering of atoms out of the initial modes and into a quasi-continuum of modes. This loss will be accompanied by a collapse of state of the remaining atoms into a mixture of states, which may or may not be cat-like in themselves. A quantitative discussion of atom loss via master equation is given in appendix 2.8.4.

2.5.1 Decoherence in elastic regime

In the present scheme, N atoms are trapped in a double-well potential with a finite spatial separation between the wells. Coupling of this system to the EM vacuum modes will result in decoherence only when scattered photons carry away sufficient information about the number of atoms in each well. It thus follows that if the separation between the two condensates, s, is less than the laser wavelength λ_L, no decoherence should occur, as the information contained in the photons is diffraction-limited to a resolution of no better than a wavelength. On the other hand, if s is larger than λ_L, the locations of the atoms can in-principle be determined from the phase-information contained in the scattered photons, this irreversible transfer of information to the environment will be reflected in decoherence of fock-space-superpositions of different atom-number distributions.

In the deeply elastic regime, the size of the left and right modes is the smallest length scale in the problem, so that we can replace the atomic density distributions with delta-functions, or equivalently we take

$$\hat{\Psi}(\mathbf{r}) = \sqrt{\delta(\mathbf{r} - \frac{\mathbf{s}}{2})}\hat{c}_L + \sqrt{\delta(\mathbf{r} + \frac{\mathbf{s}}{2})}\hat{c}_R, \tag{2.15}$$

where $\hat{c}_L$ and $\hat{c}_R$ are the annihilation operators for the left and right mode respectively. Inserting this expansion into the master equation (2.14) and assuming again

for simplicity $\Omega(\mathbf{r}) = \Omega e^{i\mathbf{k}_L \cdot \mathbf{r}}$, gives

$$\begin{aligned}
\dot{\rho}_s &= -\frac{|\Omega|^2\Gamma}{2\Delta^2}\Big[\hat{c}_L^\dagger \hat{c}_L \hat{c}_L^\dagger \hat{c}_L \rho_s + \hat{c}_R^\dagger \hat{c}_R \hat{c}_R^\dagger \hat{c}_R \rho_s \\
&\quad + 2\cos(\mathbf{k}_L \cdot \mathbf{s})\mu(\mathbf{s})\hat{c}_L^\dagger \hat{c}_L \hat{c}_R^\dagger \hat{c}_R \rho_s - \hat{c}_L^\dagger \hat{c}_L \rho_s \hat{c}_L^\dagger \hat{c}_L \\
&\quad - \hat{c}_R^\dagger \hat{c}_R \rho_s \hat{c}_R^\dagger \hat{c}_R - \cos(\mathbf{k}_L \cdot \mathbf{s})\mu(\mathbf{s})\hat{c}_L^\dagger \hat{c}_L \rho_s \hat{c}_R^\dagger \hat{c}_R \\
&\quad - \cos(\mathbf{k}_L \cdot \mathbf{s})\mu(\mathbf{s})\hat{c}_R^\dagger \hat{c}_R \rho_s \hat{c}_L^\dagger \hat{c}_L)\Big] + H.c
\end{aligned} \tag{2.16}$$

where again the imaginary parts are absorbed via a transformation to the appropriate rotating frame. The resulting decoherence is governed by the parameter $\mu(\mathbf{s})$, defined as

$$\begin{aligned}
\mu(\mathbf{s}) &\equiv 2\Re[L(\mathbf{s})]/\Gamma \\
&= \frac{3}{2}[\sin^2\theta_{\mathbf{s}}\frac{\sin\zeta}{\zeta} + (1 - 3\cos^2\theta_{\mathbf{s}})(\frac{\cos\zeta}{\zeta^2} - \frac{\sin\zeta}{\zeta^3})].
\end{aligned} \tag{2.17}$$

where $\zeta = 2\pi s/\lambda_L$ and $\theta_{\mathbf{s}}$ is the angle between the induced polarization direction $\mathbf{d}$ and the relative coordinate $\mathbf{s}$.

From this master equation (2.16), we derive the equation of motion for the fock-space matrix elements $\rho_{nm} = \langle n|\rho_s|m\rangle$, yielding

$$\dot{\rho}_{nm} = -\Gamma\frac{|\Omega|^2}{\Delta^2}(n-m)^2(1 - \cos(\mathbf{k}_L \cdot \mathbf{s})\mu(\mathbf{s}))\rho_{nm}. \tag{2.18}$$

This shows that the diagonal matrix elements (m=n) do not decay, reflecting the absence of condensate losses in the elastic regime. The off-diagonal elements, on the other hand, decay as at a rate proportional to $(1 - \cos(\mathbf{k}_L \cdot \mathbf{s})\mu(\mathbf{s}))(n-m)^2$.

The dependence of $\mu(\mathbf{s})$ on the mode separation is shown in Fig. 2.8, which plots $\mu(\mathbf{s})$ versus s/λ_L and $\theta_{\mathbf{s}} = \arg\mathbf{s}$. We see that under the condition of $s \ll \lambda_L$ we have $\cos(\mathbf{k} \cdot \mathbf{s})\mu(\mathbf{s}) \approx 1$, and therefore no decoherence. As s increases, $\mu(\mathbf{s})$ will decrease and the decoherence rate will increase. In the limit of $s \gg \lambda_L$, we have $\mu(\mathbf{s}) \approx 0$,

and the decoherence converges to the rate $\gamma_{nm} = \frac{|\Omega|^2}{\Delta^2}\Gamma(n-m)^2$. It is interesting to note that $\mu(\mathbf{s})$ is angle-dependent, as seen in Fig.2.8.

To understand the reason for this decoherence rate(2.18) we will consider the limiting cases $s \gg \lambda_L$ and $s \ll \lambda_L$, corresponding to a mode separation much larger than or much smaller than the laser wavelength, respectively. For the case where the mode separation is large compared to the laser wavelength, we have $\mu(\mathbf{s}) \rightarrow 0$ so that the decoherence rate is $\gamma_{nm} = \frac{|\Omega|^2}{\Delta^2}\Gamma(n-m)^2$. Our goal is thus to explain the peculiar $(n-m)^2$ dependence in this expression. We begin by noting that in this regime the phase information in the scattered photon wavefronts can in principle determine whether the photon scattered from the L or R mode. Thus the question becomes: on what timescale, T, does the radiation field scattered by L or R acquire sufficient information to distinguish the state $|n\rangle$ from the state $|m\rangle$. This timescale will then determine the decay rate for the off-diagonal elements ρ_{nm}, which give the degree of coherence between the states $|n\rangle$ and $m\rangle$. The rate at which photons will scatter from the left mode is $\frac{|\Omega|^2}{\Delta^2}\Gamma n_L^2$, where n_L is the number of atoms in the left mode. The reason for the n_L^2 dependence, rather than the usual n_L, is due to Bose stimulation, as the atoms remain in their initial mode after elastic scattering.

The actual scattering of photons is a random process, so that the number of L scattered photons n_p over a time interval t is drawn from a distribution function $P_L(n_p, n_L, t)$. It is reasonable to assume that $P_L(n_p, n_L, t)$ is at least approximately Poissonian, with a center at $\bar{n}_p(n_L, t) = \frac{|\Omega|^2}{\Delta^2}\Gamma n_L^2 t$, and a width $\Delta n_p(n_L, t) = \sqrt{\bar{n}_p(n_L, t)} = \frac{|\Omega|}{\Delta}\sqrt{\Gamma t}\, n_L$. Based on this assumption, the criterion for distinguishing state $|n\rangle$ from state $|m\rangle$ is that the distributions $p_L(n_p, n_L, t)$ and $p_L(n_p, m_L, t)$ should be distinguishable, so that the scattered photon number can be attributed to one distribution or the other. In this expression n_L is the number of atoms in mode L for state $|n\rangle$. This requires minimal overlap between the two distributions, which

can be approximately formulated as

$$\bar{n}_p(n_L,T) + \Delta n_p(n_L,T) = \bar{n}_p(m_L,T) - \Delta n_p(m_L,T), \tag{2.19}$$

where we have temporarily assumed $m_L > n_L$. Solving this equation for the decoherence rate $\gamma_{nm} = 1/t_d$ yields

$$\gamma_{nm} = \frac{|\Omega|^2}{\Delta^2}\Gamma\frac{\left[m_L^2 - n_L^2\right]^2}{[m_L + n_L]^2}. \tag{2.20}$$

From eq. (2.7) it follows that

$$\begin{aligned} n_L &= \frac{N}{2} - n \\ n_R &= \frac{N}{2} + n, \end{aligned} \tag{2.21}$$

which also hold for m_L and m_R with a simple substitution $n \rightarrow m$. Inserting this into (2.20) yields

$$\gamma_{nm} = \frac{|\Omega|^2}{\Delta^2}\Gamma(n-m)^2. \tag{2.22}$$

We note that the result for mode R instead of L can be found via $n \leftrightarrow -n$ and $m \leftrightarrow -m$, while the result for $m_L < n_L$ can be found via $n \leftrightarrow m$, all of which leave the result (2.22) unchanged. Thus we have verified our interpretation that the decay of the ρ_{nm} coherence is governed by the timescale on which the information carried by the scattered light becomes sufficient to distinguish between the states $|n\rangle$ and $|m\rangle$.

If we consider the opposite case $s \ll \lambda_L$ we can no longer assume that scattered photons carry information concerning which mode they scattered from, due to the standard diffraction limit. In this case one might be tempted to assume that the total scattering rate is proportional to $n_L^2 + n_R^2 = N^2/2 + 2n^2$, as photons must still

scatter from one mode or the other and each mode will experience Bose-stimulation of the recoiling atom. This would imply that the total scattering rate would be different for the states $|n\rangle$ and $|m\rangle$, so that given sufficient time the environment could learn which state is scattering the light and thus destroy the coherence. This effect, however, is compensated for by superradiance [226] so that the scattering rate is proportional simply to N^2, which is the same for both $|n\rangle$ and $|m\rangle$. Superradiance is a many-body quantum-interference effect whereby atoms within a distance less than one optical wavelength of emitted photons experience enhanced decay, identical to Bose stimulation, even for distinguishable atoms.

To verify this interpretation one can calculate the scattered light intensity and see precisely how it scales with n_L and n_R. This can be accomplished by using Eqs (2.51) and (2.52) to obtain the Heisenberg equation of motion for $\hat{a}_{\mathbf{k}\lambda}$,

$$\begin{aligned}\frac{d}{dt}\hat{a}_{\mathbf{k}\lambda} &= -i\omega_k \hat{a}_{\mathbf{k}\lambda} \\ &- i\frac{\Omega}{\Delta} g^*_{\mathbf{k}\lambda} e^{-i\omega_L t} \int d^3r\, e^{i(\mathbf{k}_L - \mathbf{k})\cdot\mathbf{r}} \hat{\Psi}^\dagger(\mathbf{r})\hat{\Psi}(\mathbf{r}),\end{aligned} \tag{2.23}$$

where we have substituted the adiabatic solution $\hat{\psi}_e(\mathbf{r}) = \frac{\Omega}{\Delta}\hat{\Psi}(\mathbf{r})$. Substituting the mode expansion (2.15) and noting that $\hat{n}_L$ and $\hat{n}_R$ are constants of motion in the absence of tunneling gives upon time integration

$$\begin{aligned}&\hat{a}_{\mathbf{k}\lambda}(t) = \hat{a}_{\mathbf{k}\lambda}(0)e^{-i\omega_k t} - i\frac{\Omega}{\Delta} g^*_{\mathbf{k}\lambda} e^{-i(\omega_k+\omega_L)t/2} \\ &\times \frac{\sin[(\omega_k-\omega_L)t/2]}{(\omega_k-\omega_L)/2}\left[e^{i(\mathbf{k}-\mathbf{k}_L)\cdot\frac{\mathbf{s}}{2}}\hat{n}_L + e^{-i(\mathbf{k}-\mathbf{k}_L)\cdot\frac{\mathbf{s}}{2}}\hat{n}_R\right].\end{aligned} \tag{2.24}$$

From this expression we can compute the mean number of scattered photons via $n_p(t) = \sum_{\mathbf{k}\lambda}\langle \hat{a}^\dagger_{\mathbf{k}\lambda}\hat{a}_{\mathbf{k}\lambda}\rangle$, yielding

$$n_p(t) = \frac{|\Omega|^2}{\Delta^2}\Gamma\left[n_L^2 + n_R^2 + 2\cos(\mathbf{k}_L\cdot\mathbf{s})\mu(\mathbf{s})\, n_L n_R\right] t \tag{2.25}$$

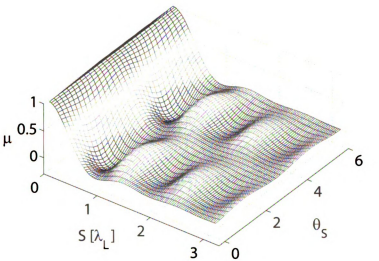

Figure 2.8: The decoherence parameter $\mu(\mathbf{s})$ as a function of $\theta_{\mathbf{s}}$ and s/λ_L. From the diagram, $\mu(\mathbf{s})$ is approximately 1 when the separation of two modes s is much smaller than the laser wavelength λ_L. As s increases, $\mu(\mathbf{s})$ decreases at a speed of $1/s$ and eventually approaches zero as s goes much larger than λ_L. Note that $\mu(\mathbf{s})$ is also dependent on $\theta_{\mathbf{s}}$, where at large s, $\mu(\mathbf{s}) \sim \sin^2\theta_{\mathbf{s}}$.

where we have converted the sum to an integral in the limit of infinite quantization volume and made the approximation $\sin^2(xt)/x^2 \approx \pi t\,\delta(x)$ when integrating over k. This expression reveals an additional component to the scattering rate proportional to $\cos(\mathbf{k}_L \cdot \mathbf{s})\mu(\mathbf{s})n_L n_R$. This term is only significant when $\mu(\mathbf{s}) \sim 1$, which requires that the mode separation be comparable to or less than the optical wavelength. In addition it depends on the exact spacing and orientation of the modes with respect to the polarization of the lasers, via the implied dependence of $\mu(\mathbf{s})$ on $\mathbf{s}$. We interpret this additional scattering as superradiance, as it arises from the imaginary part of the two-body dipole-dipole interaction. We see that in the limit as $s/\lambda_L \to 0$ we have $\cos(\mathbf{k}_L \cdot \mathbf{s})\mu(\mathbf{s}) \to 1$ so that the total scattering rate is proportional to N^2. As stated previously, this means that the radiation field never acquires sufficient information to distinguish the states $|n\rangle$ and $|m\rangle$, therefore no decoherence occurs.

We now focus on the tunneling dynamics in presence of elastic decoherence, where the total atom number can be treated as a constant of motion. In addition, we will assume that the separation of condensates are much larger than the laser wavelength, so that the dynamics is determined Eq. (2.18) but with $\mu_{\mathbf{S}} = 0$. Under those assumptions, it is straightforward to guess the coherence time t_{coh} as

$$t_{coh} = \frac{4\Delta^2}{N^2|\Omega|^2\Gamma}, \tag{2.26}$$

by observing that the peaks of the dynamically created cat-state are separated by $n_0 = \pm N/4$. This is the time-scale on which coherence between states separated by $N/4$ should decay based on the decoherence rate (2.22). During the generation of the cat state, it is expected that if the coherence time t_{coh} is large compared to t_{cat}, the cat state can still be produced. Otherwise, the system should evolve into a mixed-state rather than a pure cat-state.

The effects of decoherence on the dynamical evolution of cat-states is shown in Figures 2.9-2.11. In Fig. 2.9 we show the magnitude of the density-matrix elements for the initial coherent state at $t = 0$. Under the condition of no decoherence, this state evolves into a cat-state at $t = t_{cat}$, which is shown in Fig. 2.10. In Figures 2.11 (a) and (b) we show the resulting state for the cases of weak and strong decoherence, respectively. In Fig. 2.11(a) the decoherence strength is chosen such that $t_{coh} = 5t_{cat}$, while for the strong decoherence of Fig. 2.11 (b), we have $t_{coh} = t_{cat}$. It is seen that with $t_{coh} = 5t_{cat}$ we can still create cat-like states, while as the decoherence strength increases up to $t_{coh} = t_{cat}$, the outcome state is a mixed state with no coherence between macroscopically distinguishable distributions. Therefore, to successfully produce cat state, the coherence time t_{coh} should be much longer than the time need to produce cat state t_{cat}.

It is also quite interesting to observe from Fig. 2.11 that not only the off diagonal,

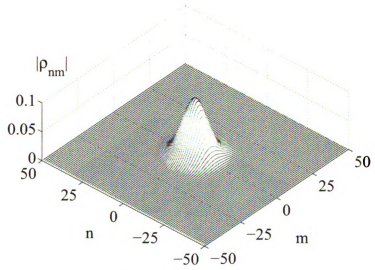

Figure 2.9: Magnitude of the density matrix elements for the initial coherent state.

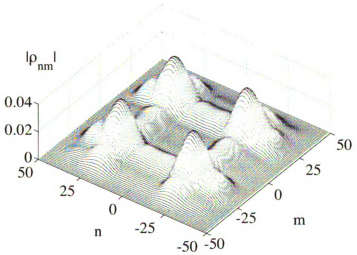

Figure 2.10: Magnitude of the density matrix elements of the dynamical created cat state at $t = t_{cat}$ with no decoherence.

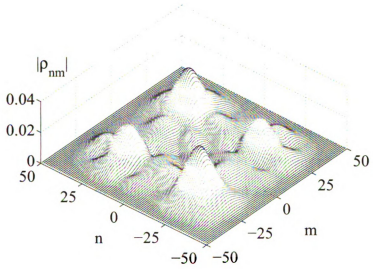

(a)

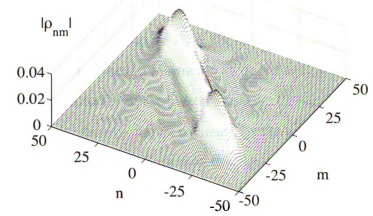

(b)

Figure 2.11: Magnitude of density matrix elements of the resulting state under weak decoherence (a) and strong decoherence (b). System parameters are chosen the same as in Fig.(2.1), and the resulting states (a) (b) are measured at a time of $t_{cat} = 14.5/\tau$.

but also the diagonal of density matrix of the final states are affected by decoherence effect. In Figure 2.12, we plot the probability distribution $P(n) \equiv \rho_{nn}$ of several resulting states corresponding to different coherence times. In the figure we see that the probability distribution of the mixed states formed under strong decoherence is significantly different from that of the pure cat state. This is because under strong decoherence, the coherences between different number basis states are continuously destroyed during the dynamics, so that the population dynamics are modified. In other words, if decoherence dominates the system dynamics, it will not yield the same $P(n)$. Thus the probability distribution alone supplies a direct way to verify the existence of cat state at time t_{cat}, without the need to detect revivals. We note that we have so far only established this result for the elastic regime. We suspect that the elastic regime will be much more difficult to achieve experimentally than the inelastic regime, due to the necessity of sub-wavelength confinement.

In Figure 2.13 we examine the effects of decoherence on the revival process, under the assumption that $t_{cat} < t_{coh}$, but assuming that the system is held at $\tau = 0$ for a time t_{hold}, which may be longer than the coherence time. These figures show the magnitude of the density-matrix elements at time $t = t_{cat} + t_{hold} + t_{rev}$, calculated by direct numerical solution of the master equation (2.16). In Figure 2.13 (a) we show the magnitude of the density-matrix elements for the case $t_{hold} = 0$ and for $t_{coh} = \infty$, i.e. no decoherence is present. Note that this figure corresponds to $t = 21$ in Fig. 2.5. In Figure 2.13 (b) we plot the magnitude of the resulting density matrix for the case $t_{hold} = t_{coh} = 10t_{cat}$. This choice gives sufficient time to destroy coherence between fock states where n differs by $N/2$, corresponding to the distance between peaks in the initial cat state. This shows that the revival is effectively destroyed by decoherence on the the timescale governed by the coherence time (2.26). This figure corresponds to the 'partially incoherent state' shown in Fig. 2.6 at time $t = 21$, in the sense that the choice $t_{hold} = t_{coh}$ implies the condition $\sigma < I_{coh} < n_0$. Lastly, Figure 2.13

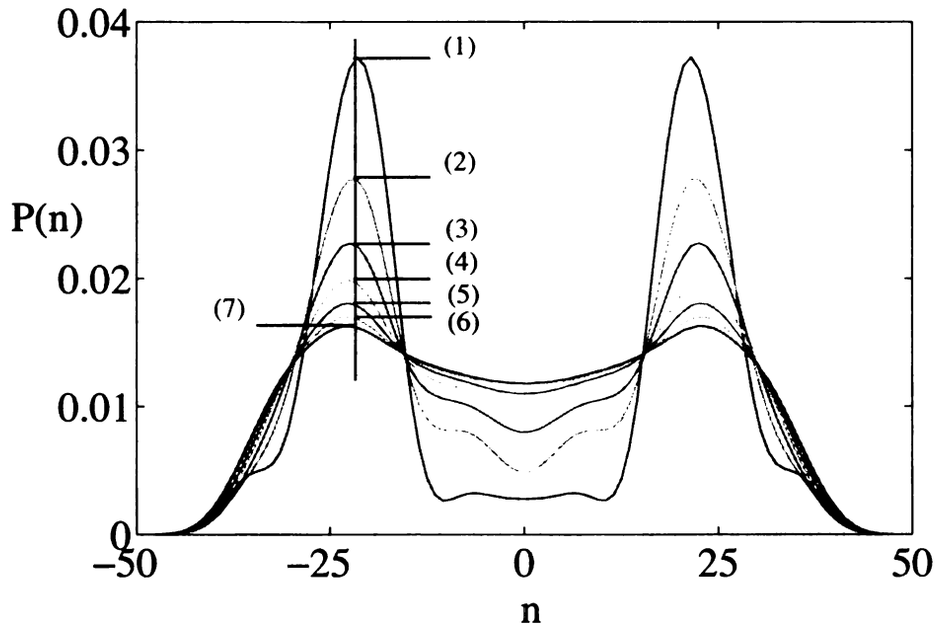

Figure 2.12: Probability distribution $P(n)$ of the resulting states corresponding to different coherence times. Parameters are choose as in Fig. (2.11), while from line (1) to (7), the coherent time t_{coh} is chosen as ∞, $3t_{cat}$, $3t_{cat}/2$, t_{cat}, $3t_{cat}/4$, $3t_{cat}/5$, $t_{cat}/2$, respectively.

(c) shows the case $t_{hold} = \frac{N^2}{4} t_{coh}$ with $t_{coh} = 10 t_{cat}$ which gives sufficient time to destroy coherence between any fock states. We see this case that the system has collapsed onto an almost pure mixture of fock-states, and it is clear that no revival occurs. This figure corresponds to the totally incoherent state of Fig. 2.7.

2.5.2 Loss and Decoherence in the inelastic regime

In this subsection we turn to the inelastic regime, which takes into account the finite size of the atomic modes, so that the scattering of laser photons is not entirely elastic due to photon recoil effects. The resulting losses from the two initially occupied modes should necessarily be accompanied by decoherence, which may or may not be sufficient to 'collapse' the two-mode cat state. We focus solely on the case where the mode separation is large compared to the wavelength, so that we can safely ignore the cross terms in Eq. (2.16). The master equation in this situation is found by substituting the two-mode expansion $\hat{\Psi}(\mathbf{r}) = \phi_L(\mathbf{r})\hat{c}_L + \phi_R(\mathbf{r})\hat{c}_R$, yielding

$$\begin{aligned} \dot{\rho}_s(t) &= -\frac{|\Omega|^2\Gamma}{2\Delta^2}[N\rho_s(t) + \xi[n_L^2 + n_R^2 - N]\rho_s(t) \\ &+ \xi[n_L\rho_s(t)n_L + n_R\rho_s(t)n_R]] + H.c., \end{aligned} \tag{2.27}$$

with ξ defined in Eq. (2.79). Deriving the equation of motion for the density matrix elements is then straightforward, giving

$$\dot{\rho}_{nm}(t) = -\Gamma\frac{|\Omega|^2}{\Delta^2}[(1-\xi)N + \xi(n-m)^2]\rho_{nm}(t). \tag{2.28}$$

Under the condition of spatially broad (relative to λ_L) condensates, $\xi \approx 0$, as seen if Figure 2.24, and this equation is reduced to

$$\dot{\rho}_{nm}(t) = -\Gamma\frac{|\Omega|^2}{\Delta^2}N\rho_{nm}(t), \tag{2.29}$$

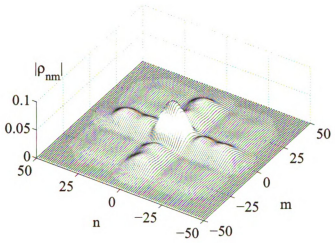

(a)

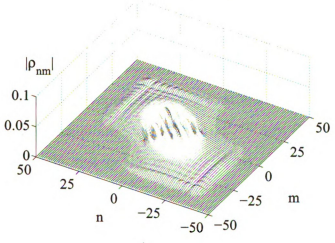

(b)

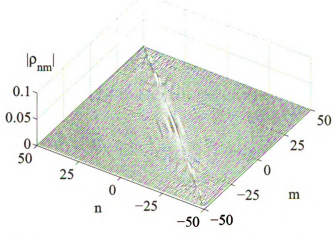

(c)

Figure 2.13: Effects of decoherence on the revival of the initial coherent state. Shown is the magnitude of the density matrix elements of the system at time $t = t_{cat}+t_{hold}+t_{rev}$ under no decoherence (a), the decoherent resulting state with $t_{hold} = t_{coh}$ (b), and $t_{hold} = N^2 t_{coh}/4$ (c). System parameters are chosen the same as in Fig. 2.1.

which shows that the decoherence rate is exactly equal to the atomic loss rate (2.78). The reason for this is that the loss of an atom takes us from the manifold with N atoms to that with $N-1$ atoms. This is equivalent to $n \rightarrow n \pm 1$ where the choice of $\pm$ depends on whether the atom was lost from the L or R mode (- for L and + for R). Thus one might suspect that a careful treatment of the scattering of the atom into the quasi-continuum of recoil modes would reveal that the loss of coherence on the matrix element ρ_{nm} could be accompanied by a corresponding appearance of coherence on the matrix element $\rho_{n\pm1,m\pm1}$ which lies in the $N-1$ manifold.

A complete quantum description of this inelastic process should include both the initial cat-state modes as well as a quasi-continuum of recoil modes.We can therefore describe the initial unscattered systems with a density of product $\rho_{sr}^{N} = \rho^{N} \otimes \rho_{r}$, where ρ_{sr}^{m} is the full density operator having m atoms in the initial modes and $N-m$ atoms in the quasi-continuum, and ρ^{m} and ρ_{r}^{N-m} are the corresponding reduced density matrices for the system and reservoir. After one photon is scattered, the full density matrix goes from ρ_{sr}^{N} to ρ_{sr}^{N-1}, due to the transfer of one atom from the initial modes into the quasi-continuum. As the modes are well-separated, the scattered photon carries sufficient phase information into the environment to determine whether the atom recoils from the L or the R mode. Assuming that atoms from L and R modes scatter into different manifolds of recoil modes, the reduced density operator of the two-mode system, obtained by tracing out the quasi-continuum modes, becomes

$$\rho^{N-1} = \frac{1}{\mathcal{N}}(c_L \rho^{N} c_L^{\dagger} + c_R \rho^{N} c_R^{\dagger}) \tag{2.30}$$

with $\mathcal{N}$ the normalization factor. In other words the system collapse onto an incoherent mixture of the state with one atom lost from mode L and the state with one atom lost from mode R.

As an example, we now consider a N particle cat state of

$$\rho^N = |\Psi_c\rangle\langle\Psi_c|. \tag{2.31}$$

and to distinguish cat states with different total atom numbers, here we use a new notation

$$|\Psi_c\rangle = \frac{1}{\sqrt{2}}(|N/4, 3N/4\rangle + |3N/4, N/4\rangle), \tag{2.32}$$

where $|n_L, n_R\rangle$ stands for a Fock basis with n_L atoms in left mode and n_R in the right. This cat state is collapsed after one photon-detection into a statistical mixture of two $N-1$ particle states,

$$\rho^{N-1} = \frac{1}{2}(|\Psi_1\rangle\langle\Psi_1| + |\Psi_2\rangle\langle\Psi_2|) \tag{2.33}$$

where

$$|\Psi_1\rangle = \frac{1}{\sqrt{2}}(|N/4 - 1, 3N/4\rangle + |3N/4 - 1, N/4\rangle), \tag{2.34}$$

$$|\Psi_2\rangle = \frac{1}{\sqrt{2}}(|N/4, 3N/4 - 1\rangle + |3N/4, N/4 - 1\rangle). \tag{2.35}$$

The important point here is that each of these states is still a good cat-like state, so that while we don't know which one the system has collapsed into, we do know that the system remains in a good cat-like state. The means that the effect of scattering a photon and losing an atom may not have a significant detrimental effect on cat-like states. Similarly, after a second photon is scattered, the system will collapse into a statistical mixture of four $N-2$ particle cat states, and so on. We note, however, that for the 'perfect' cat state $[|N0\rangle + |0N\rangle]/\sqrt{2}$ a single scattering results in a mixture of the states $|(N-1)0\rangle$ and $|0(N-1)\rangle$, neither of which is itself a cat-state. This means that while the ideal cat state is so fragile that a single scattered photon is

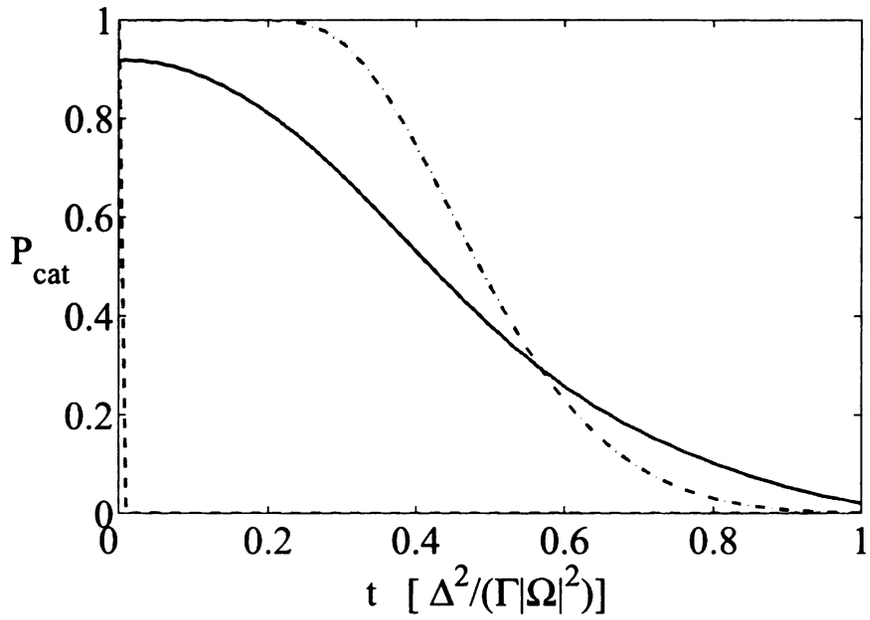

Figure 2.14: The evolution of the projector P_{cat} under decoherence due to inelastic atom loss. The curves correspond to the dynamically-created cat state (Blue solid line), the perfect cat state (Red dashed line) and less extreme cat state (2.32) (Green dashed-dotted line). The figure plots the estimated probability to remain in a cat-like state versus time. Starting from 100 atoms, it is estimated that 63 atoms are lost by the final time $t = \frac{\Delta^2}{|\Omega|^2\Gamma}$.

sufficient to collapse that cat onto all-left or all-right states, the cat-like states we are considering should be significantly more robust, giving them a significant advantage provided they are still suitable for whatever application is desired.

To show the dynamics under decoherence induced by these inelastic condensate losses, in Fig. 2.14, we plot the time evolution of the expectation value of the projector P_{cat}, defined in (2.10). Three initial states are shown, the extreme cat state $[|N,0\rangle + |0N\rangle]/\sqrt{2}$, the less extreme cat state, $\left[|\frac{N}{4}\frac{3N}{4}\rangle + |\frac{3N}{4},\frac{N}{4}\rangle\right]/\sqrt{2}$ and the wave-packet cat-states produced via dynamical evolution as in Section 2.3.

Figure 2.14 is obtained by assuming a single photon is detected in each time interval $\Delta t = \frac{\Delta^2}{|\Omega|^2\Gamma N(t)}$, where $N(t)$ is the number of remaining atoms at time t. After each scattering a new density matrix is obtained by applying Eq. (2.30). We

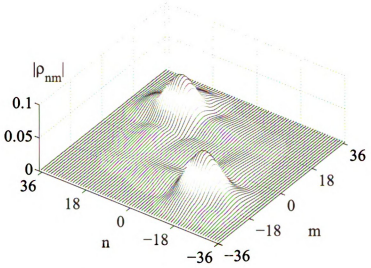

Figure 2.15: Magnitude of the resulting density matrix elements corresponding to Fig. 2.14 at time $t = 0.3\frac{\Delta^2}{|\Omega|^2\Gamma}$.

note that the use of (2.30) automatically weighs the probabilities that the scattering occurs from the L or R mode due to the action of the annihilation operators being proportional to the square root of the mode occupation. The resulting density matrix is then diagonalized and written

$$\rho = \sum_i P_i |\Psi_i\rangle\langle\Psi_i|, \tag{2.36}$$

where $|\Psi_i\rangle$ denotes the ith eigenmode, with P_i its statistical weights over the mixture state. The resulting eigenmodes $|\Psi_i\rangle$'s are then analyzed to determine whether or not they are sufficiently cat-like. This is accomplished by first assigning a value of zero to any state where $\sum_{n>0} |c_n|^2 \neq \sum_{n<0} |c_n|^2$, where c_n is again the probability amplitudes for the state $|n\rangle$. The states which survive this test are then assigned a value equal to the expectation value of the projector P_{cat}. The assigned values for each eigenmode of the density matrix at time t are then averaged together and the results are plotted versus time.

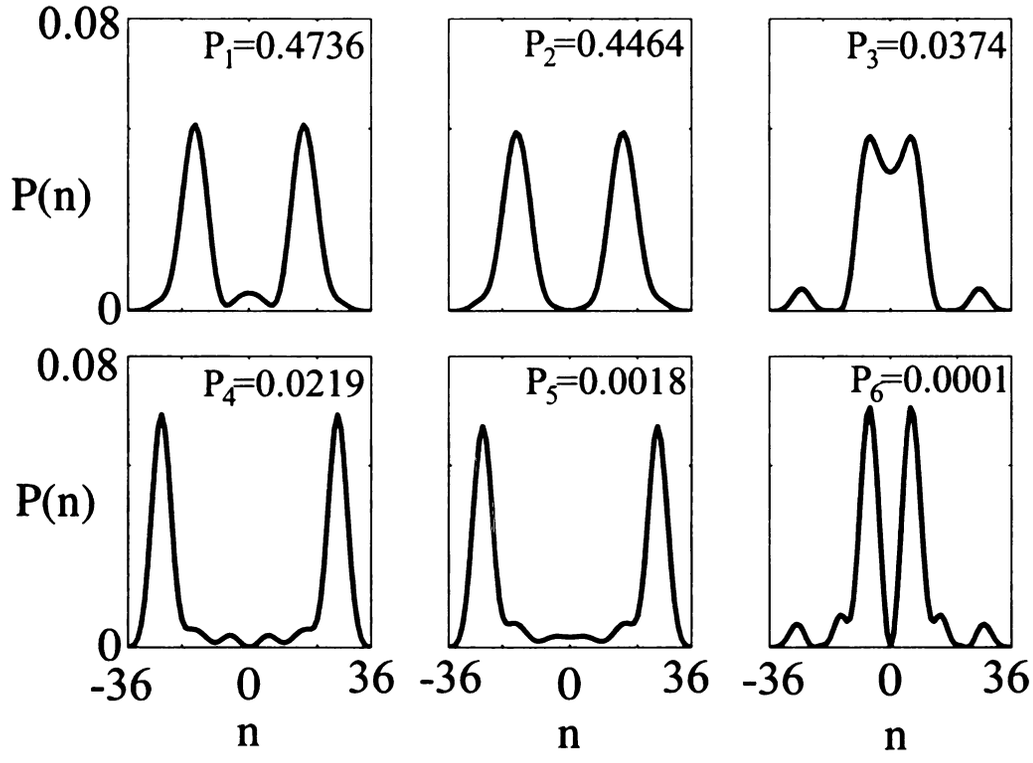

Figure 2.16: Probability distributions $P(n)$ of the six leading eigenmodes $\{|\Psi_i\rangle\}$ of the density matrix shown in Fig. (2.15), where P_i is the eigenvalue for eigenmode $|\Psi_i\rangle$.

From the figure, we verify that the perfect cat state is completely collapsed immediately after one photon scattering. In contrast, the less extreme cat states has a high probability to remain in a cat-like state even after many scatterings, and, the dynamically created cat-states are similarly robust against decoherence. We note that in the figure out of an initial population of $N = 100$ atoms, $N = 37$ remain at the end-time $t = \frac{\Delta^2}{|\Omega|^2\Gamma}$.

In Fig. 2.15, we plot the magnitude of the density matrix after a time of $t_{hold} = 0.3\frac{\Delta^2}{|\Omega|^2\Gamma}$ as in Fig. (2.14) (Blue solid line). In this figure, an initial cat state is formed at time t_{cat} via dynamic evolution with no decoherence. The state is then held with $g = 0$ and $\tau = 0$ for time t_{hold} with photon-scattering acting as a gradual source of decoherence. The figure shows a collapse of the reduced density matrix onto a statistical mixture of left-centered and right-centered peaks, and thus the collapse of cat state. This conclusion is, however, in seeming contradiction to the result via numerical diagonalization of this matrix, which reveals that that the system is in fact in a mixture of different cat states, as shown in Fig. 2.16, we plot the major eigenmodes $|\Psi_i\rangle$ of this density matrix. From the picture, some of these resulting eigenmodes, such as $|\Psi_i\rangle$'s with $i = 1, 2, 4, 5$ are still cat-like, in a sense that separation between two peaks are larger than the width of either peak. While for some others, like $|\Psi_3\rangle$ and $|\Psi_6\rangle$, the separation between peaks are not larger than the width of each peak, and thus they are not cat-like. It is noted $|\Psi_1\rangle$ and $|\Psi_2\rangle$ are symmetric and antisymmetric states around $n = 0$, respectively. From here, one might think that such a collapsed state, being a mixture of cat-like states, can still exhibit the macroscopic property of a *pure* cat state. The flaw in this argument is that the two major eigenmodes $|\Psi_1\rangle$ and $|\Psi_2\rangle$ are nearly degenerate, and would then simultaneously response to any measurements or operations, instead of individually. As a consequence, they always act as an incoherence mixture of left-centered and right-centered Fock-states. This is understood in the simplest case of a single qubit

in a mixture state of

$$\rho_{\text{qubit}} = \frac{1}{2}\left(|0\rangle\langle 0| + |1\rangle\langle 1|\right). \tag{2.37}$$

Due to the degeneracy of $|0\rangle$ and $|1\rangle$, this density can be rewritten in the form of

$$\rho_{\text{qubit}} = \frac{1}{2}\left(|+\rangle\langle +| + |-\rangle\langle -|\right), \tag{2.38}$$

where $|+\rangle$ and $|-\rangle$ are superposition states of

$$|+\rangle = \frac{1}{\sqrt{2}}(|0\rangle + |1\rangle), \tag{2.39}$$

$$|-\rangle = \frac{1}{\sqrt{2}}(|0\rangle - |1\rangle). \tag{2.40}$$

An arbitrary operation on state basis $|0\rangle$ and $|1\rangle$ would unavoidably act on both $|+\rangle$ and $|-\rangle$. The system then responses as a mixture of $|0\rangle$ and $|1\rangle$, without exhibiting coherence between the two.

2.6 Dephasing induced by atomic collisions

In this section we consider the effects of atom-atom collisions on a cat-state which is 'frozen' by reducing the tunneling strength, τ, to zero. If during this hold state the atomic interaction strength, g, is nonzero, the system will undergo a dephasing process [227, 216], whose dynamics is determined by Hamiltonian (2.44). The main effect of this dephasing process is that, while it will not collapse the coherence of the cat-state, once the state is dephased, it cannot evolve back to the initial coherent state. In this way, a detection scheme based on revivals will incorrectly create the appearance of collape. Therefore, in general, the dephasing effect needs to be suppressed by making the atomic interaction strength g, and/or the hold time small.

In studying the dephasing effect, first, we note that at each period of π/g, the

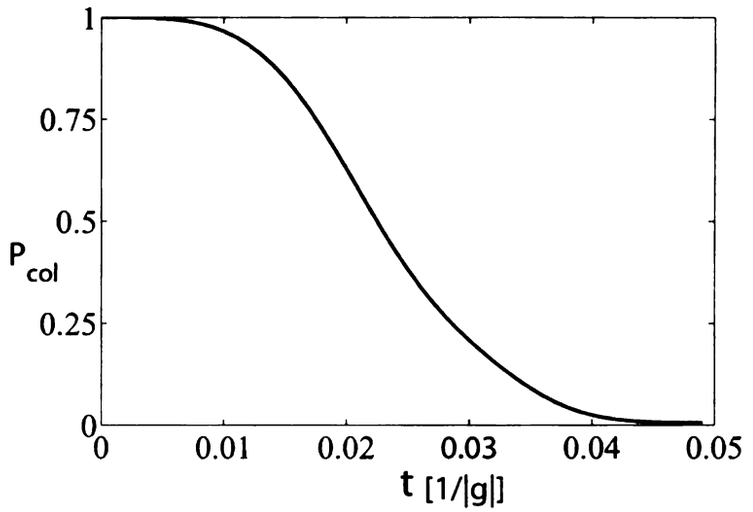

Figure 2.17: Dephasing process of cat state with nonzero atomic interaction. The collapse is measured by $P_{col} = tr\{\rho_c \rho(t)\}$, where ρ_c and $\rho(t)$ are the densities of the initial cat state and dephased state after a hold time t_{hold} respectively. Parameters are given the same as in Fig. 2.1 while t_{hold} has units of $1/|g|$.

relative phase of each c_n is exactly restored and thus the many-body states is revived. While between two consequent revivals, nonzero relative phases are introduced to Fock basis, and the cat state will collapse. In Fig. 2.17, we show such a rapid dephasing process, where the cat-state decays with a collapse time around $t_{col} = 0.02/|g|$, determined from numerical simulations.

To obtain an analytic estimate of the collapse time scale, we assume that our system is prepared in a Gaussian-like cat state (2.9), which is a good approximation of the realistic cat state in our system. And then, we associate the collapse and revival of our bimodal system with the evolution of one-body two-mode correlation function Λ,

$$\Lambda = \langle \mathtt{cat} | \hat{a}_L^\dagger \hat{a}_R | \mathtt{cat} \rangle. \tag{2.41}$$

At short time scale, the correlation function (2.41) is obtained, under the condition of

that the Gaussians are well peaked around $n = \pm n_0$, to a good approximation [227],

$$\Lambda(t) = \Lambda(0)e^{-(g\sigma t)^2} \tag{2.42}$$

And therefore, the collapse time t_{col} can be estimated by

$$t_{col} = \frac{1}{2g\sigma}. \tag{2.43}$$

As discuss above, the collisional dephasing will affect the revival process. Generally speaking, if the holding time t_{hold} is less than collapse time t_{col}, the system can still evolve back to the initial state as shown in Fig. 2.18 (a). But under the condition of $t_{hold} > t_{col}$, the cat state is dephased, and the coherent state can not be restored. Rather it will evolve to a disordered state as shown Fig. 2.18 (b). Therefore, for the success of the detection scheme, one should make sure that the dephasing collapse time is longer than the hold time and the revival process is only affected by decoherence.

2.7 Conclusion

We have considered the double-well BEC system and proposed that cat-like states can be formed by switching the sign of the interaction strength from positive to negative using a Feshbach resonance. We examined the possibility of either adiabatic or sudden switching with the following results. In the adiabatic case, the ground state evolves into a macroscopic superposition state with all of the atoms collectively occupying either the left or right well. However, by examining the degeneracy of the ground state, we conclude that the cat state is unstable against small perturbations and may readily evolve into a localized state. For the case of a sudden change in the scattering length, we find that an initial condensate state evolves dynamically

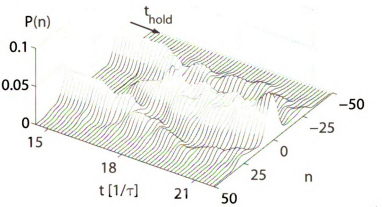

(a)

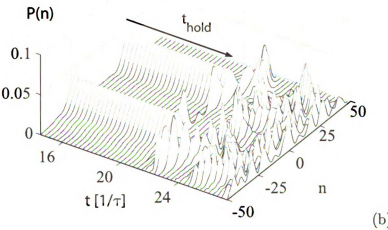

(b)

Figure 2.18: Dynamic evolution of dephased cat state after tuning on the tunneling. The parameters are chosen as in Fig. 2.1 with a collapse time of $t_{col} = 1.5/\tau$. In the first picture (a), the hold time is set to be $t_{hold} = t_{col}$, while for (b), we set $t_{hold} = 5t_{col}$. It is shown that for (a), the system still revives to the initial state, while in (b), the initial state can not be restored.

into a double-peaked superposition of number states, with one peak corresponding to the majority of atoms being in one well, and the other peak corresponding to the majority being in the opposite well.

We have shown that this process is stable against perturbations in the initial state, as well as in the control parameters. For this reason we believe that the dynamical evolution scheme is more likely to be demonstrated experimentally. In addition, we have demonstrated that continuing the evolution after the cat-state formation results in a nearly complete revival of the initial state. However, this revival does not occur if the cat-state has collapsed into an incoherent mixed state, so that this revival can be taken as proof of coherence of the initial cat-state. We note that the states formed via adiabatic switching are maximum 'all or nothing' cat states, while those formed dynamically are less distinct cat-like states corresponding to a double-peaked distribution in Fock-space.

The effects of decoherence due to spontaneous scattering of laser photons have also been studied in detail. We have determined that decoherence is strongest for the case where the single-photon momentum recoil is not sufficient to remove the atom from its initial state, due to Bose-stimulation as the atom remains in an strongly-occupied atomic-field mode. In the opposite regime, where the scattering rate is smaller by a factor of N, N being the atom number, we find that the maximally entangled 'all or nothing' cat states are destroyed by the scattering of a single photon, while the dynamically-formed less-extreme cat-like states can survive multiple scatterings without leaving the subspace of cat-like states, in analogy to the effect of atomic collision losses studied in [72]. Because of this enhanced survivability, the less-extreme cat-states may be more useful for applications, providing they are suitable for the desired protocol.

In this context of 'freezing' the cat states for a prolonged time, we have also considered the de-phasing effects of atom-atom interactions during this stage, and

conclude that collisions can mimic the effects of decoherence with regard to a revival-type measurement, however with regard to applications, they may or may not be detrimental, depending on the type of interaction and/or measurements involved.

We note that in the present proposal, there are three different time scales which we have established: the time need to create cat state t_{cat}, the coherence time t_{coh} and the collisional dephasing time t_{col}. First, to generate the cat state, the coherence time scale t_{coh} must be longer than t_{cat}. While later, in order to hold the cat state for later use in an application, a hold time t_{hold} shorter than t_{coh} is required to maintain the macroscopic superposition state. And finally, another condition $t_{col} > t_{hold}$ should be satisfied to avoid the dephasing quasi-collapse, if such dephasing is detrimental to the desired application. The coherence time, t_{coh}, is tunable by adjusting the laser intensity and detuning, while the dephasing time $t_{dephase}$ can be adjusted if the interaction strength g is modified during the hold stage.

2.8 Derivations and further discussions

2.8.1 Adiabatic generation of cat states: why impractical

In this subsection, we explain the difficulty to generate cat-states via adiabatic manipulation of the system's ground state. In order to better understand the adiabatic evolution of the ground state, we first examine the ground state under certain parameter values for which it can be determined exactly. First, in presence of zero tunneling, the bimodal Hamiltonian (2.4) is reduced to

$$\hat{H} = 2\hbar g\,\hat{n}^2. \tag{2.44}$$

The ground state of this Hamiltonian is determined solely by the parameter g. For $g > 0$, corresponding to repulsive interactions, the ground state will be $|0\rangle$ in our number-

difference representation (2.6), i.e., an insulator state. While in the case of $g < 0$, the ground state is doubly degenerate, corresponding to any arbitrary superposition of the two extreme states $|N/2\rangle$ and $|-N/2\rangle$, and its orthogonal counterpart. These states can be written as

$$\frac{1}{\sqrt{\alpha^2+\beta^2}}(\alpha|N/2\rangle + \beta|-N/2\rangle), \tag{2.45}$$

with α, β being arbitrary complex numbers. Note when $\alpha = \beta$, one recovers the Shrödinger cat state (2.8).

In the other extreme case, if there is no atomic interaction but only the tunneling term, the ground state of Hamiltonian (2.4) becomes the two-site analogue of the superfluid phase [70]

$$|g\rangle = 2^{-N/2} \sum_{-N/2}^{N/2} \sqrt{\binom{N}{n}} |n\rangle, \tag{2.46}$$

which is a binomial distribution of Fock states, and thus approximately Gaussian when N is a large number. Henceforth we shall refer to this class of states as a 'coherent state', meaning that each atom is in a coherent superposition of both modes and there are no atom-atom correlations or many-body entanglement.

The more general ground state of our model, with the presence of both collisions and tunneling, can be understood as a smooth cross-over between these two extremes. First, under the condition of a repulsive atomic interaction, the ground states of this system can be well approximated by a single Gaussian-like distribution of c_n peaked at $n = 0$

$$c_n \propto e^{-n^2/(2\sigma^2)}, \tag{2.47}$$

where the relative atom number dispersion σ is obtained by minimizing by the mean-energy of Hamiltonian. Second, under the condition of attractive two-body interaction, the ground state of this system will be split into two separated wave-packets.

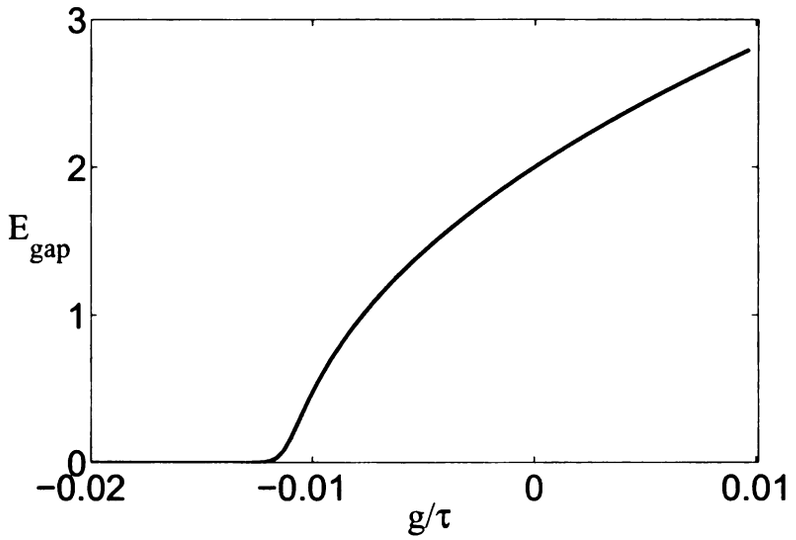

Figure 2.19: The energy gap E_{gap} as a function of ratio g/τ. Here, $E_{gap} = E_1 - E_0$, with E_0, E_1 being the eigen energies of the ground and first excited state respectively.

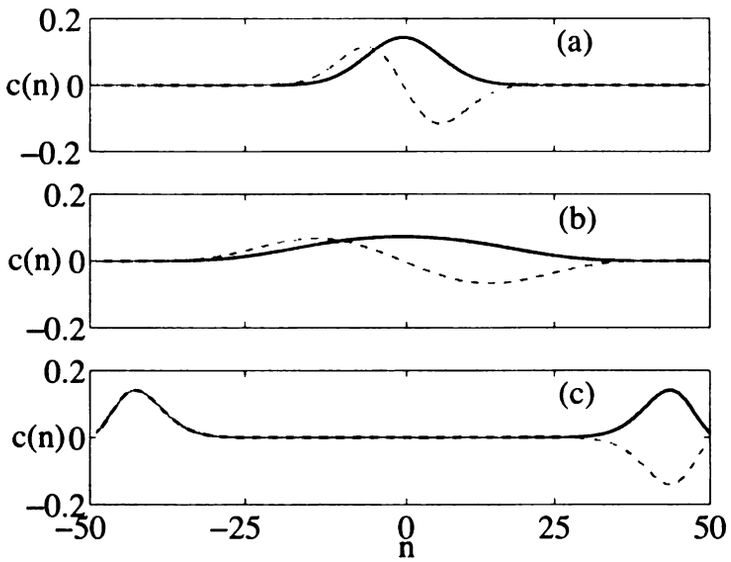

Figure 2.20: The wave-packet $c(n)$ of the ground state (Blue solid) and first excited sate (Green dashed) with (a) $g/\tau = 0.01$, (b) $g/\tau = -0.01$ and (c) $g/\tau = -0.02$ respectively.

Thus instead of (2.47), a good approximation of this state turns out to be a superposition of two Gaussian distributions (2.9) [218], where again the minima center n_0 and spread width σ are obtained by minimizing the mean-energy. For repulsive atomic interactions, the energy minima is found at $n_0 = 0$, which indicates that the atom number distribution does not split. For attractive interactions, $n_0 \neq 0$, and under the condition of $n_0 > \sigma$, the wavepacket of ground state will split and become a superposition of two well-separated components, i.e. it becomes a cat-like state (2.9). Note for this state, the relative phase for any Fock basis pair $|n\rangle$ and $|-n\rangle$ is zero.

Based on these considerations, it is of theoretical interest to determine whether or not the Shrödinger cat state in this bimodal BEC system can be generated by an adiabatic process [218, 217]. As a basic scheme, the system would be first prepared in the many-body ground state with positive g, corresponding to a coherent state centered at $n = 0$. Then by slowly tuning g to be negative, the distribution will split and finally end up with a Shrödinger cat like state under the condition of $n_0 > \sigma$.

There is a significant difficulty with this proposal, however, in that when the two wavepackets in Fock space are well separated, the ground state, which is the desired cat state, is nearly degenerate with the first excited state, as shown in Fig.(2.19). It is observed that when g is positive, there is a relatively large energy gap between the ground and first excited states. Then as g decreases, the energy gap decreases so that at some point the energy gap becomes exponentially small. In Fig. 2.20, we show the corresponding wavefunctions of the ground and first excited states $c(n)$ with different ratios g/τ. It is clear that the ground state does not evolve into cat state until the bimodal system enters the degenerate regime. In the degenerate regime, any small perturbation can mix the two states. As the first excited state is nearly identical with the ground state, but with a π phase-shift between the left and right wave-packets, an arbitrary superposition of these two states could easily correspond to a localized state, which is equivalent to a collapse of the Schrödinger cat wave-

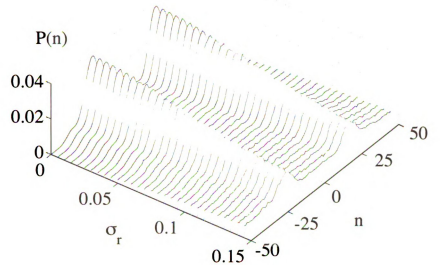

Figure 2.21: The probability distribution $P(n)$ at time $t = t_{cat}$ is plotted versus the level of random noise in the initial state σ_r. We see that even at $\sigma_r = 0.05$ the output state is still a good cat-state. This corresponds to random fluctuations in the initial c_n's at about 5% of their exact ground state values

function. Strictly speaking, this degeneracy implies that to adiabatically create the cat state, the process requires an exponentially long time. Thus experimental realization appears impractical, particularly when considering the inevitable exposure of the system to noise.

2.8.2 Experimental Feasibility

In section 2.3, we have only considered the ideal situation where the initial state is exactly prepared in the ground state and the atomic scattering length can be tuned in a precise way. This may not necessarily hold true under experimental conditions, where random fluctuations in system parameters may affect the formation of the cat-state. Here, to test the susceptibility of the present proposal to such fluctuations, we study the dependence of final cat-state on the precision of the initial state by adding

random noise to the exact ground state. Thus, the initial state becomes $c_n + \delta_r$. The random noise, δ_r, is a complex with an amplitude drawn from a Gaussian distribution, and a completely random phase. The probability distributions for the amplitude and phase are therefore

$$\begin{aligned} P(|\delta_r|) &= \frac{1}{\sqrt{\pi}\sigma_r} e^{-|\delta_r|^2/\sigma_r^2}, \\ P(\theta) &= \frac{1}{2\pi}. \end{aligned} \tag{2.48}$$

Figure 2.21 shows the resulting cat-state as a function of σ_r. We see that a well peaked cat state can be produced up to $\sigma_r \approx 0.05$, which is about $c_0(t = 0)/6$, i.e, the peak of initial coherent state we make the cat state from. Thus this method of generating a cat state appears robust against noise in the initial state, which could be do to a finite temperature.

Another possible source of error in creating the cat state is from the inaccuracy in control of the atomic interaction strength g and/or the tunneling rate τ. This effect is simulated by adding a Gaussian-distributed random number to negative g. We note that this is not equivalent to time-dependent fluctuations in g and τ, but rather represents imprecision in the control over the values of the parameters. The result is shown in Fig. 2.23, where it is seen that the evolution system is sensitive to the noise of the atomic interaction g, with only about $\pm 2\%$ deviation being tolerable. However, it does not necessarily mean that one can not create a cat-state without the well defined g. Instead, when g is shifted, the time need to create cat state t_{cat} is also shifted, and one can still obtain the cat-state on another time. The primary difficulty here is that if the variation in g is unknown for a given run, then the precise time to stop the dynamics, t_{cat} is not known a-priori.

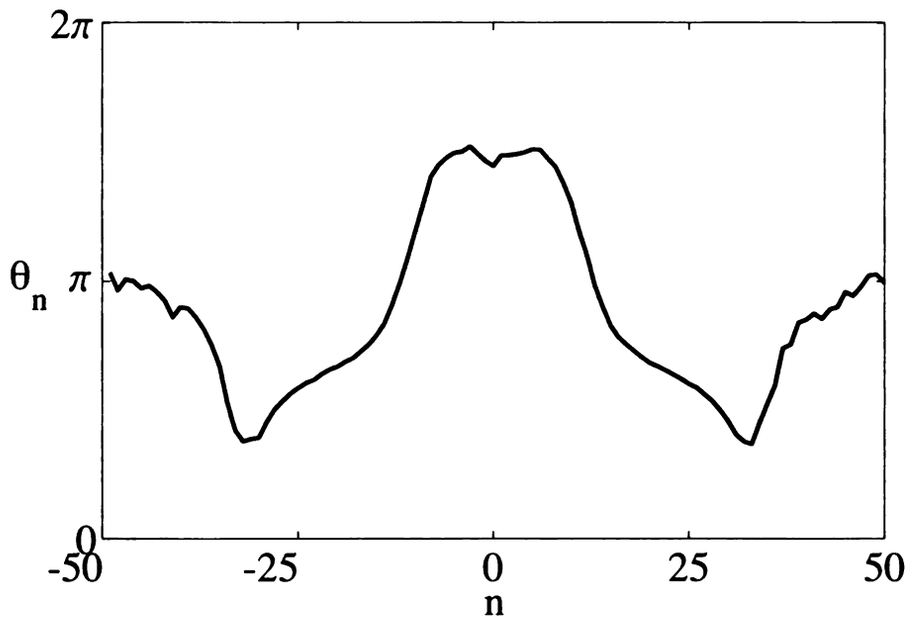

Figure 2.22: The phase distribution $\theta_n = \arg(c_n)$ at $t = t_{cat}$ is plotted for the case of random noise in the initial state with $\sigma_r = 0.05$. We see that the phase distribution agrees well with Fig. 2.3 up to a non-physical overall phase-shift. The disagreement occurs only in the regions where the amplitude of c_n is small.

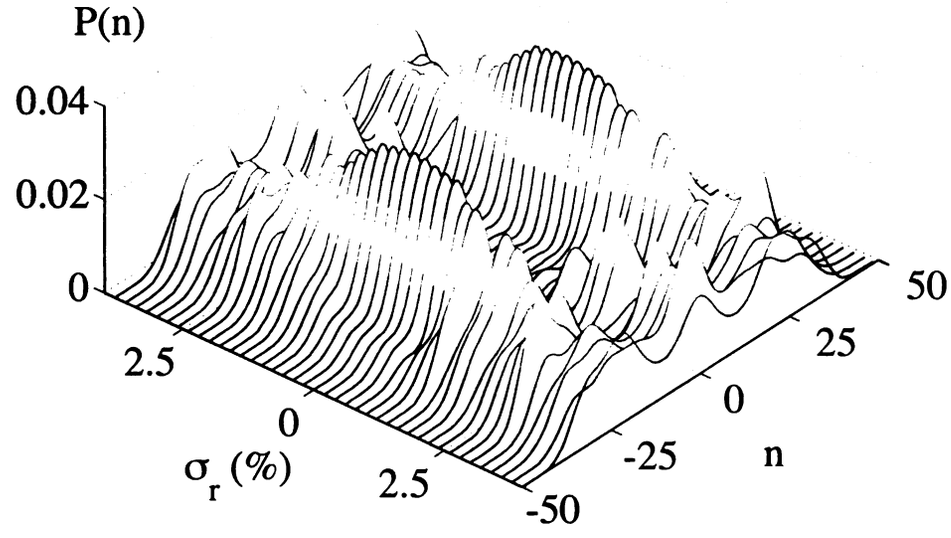

Figure 2.23: The effect of imprecise control over the atomic interaction strencth g. The noise of g is introduced by adding a real random number, where σ_r is the width of the corresponding Gaussian distribution, to the value of g in Hamiltonian (2.4). The cat state is measured at a time of $t = 14.5/\tau$ and plotted as a function of σ_r. It is shown that uncertanties in g up to 3% can be tolerated.

2.8.3 Derivation of Master equation

In the presence of laser coupling to a BEC system, the total Hamiltonian for the system, which includes the Hamiltonian for the atoms in condensate H_s, the reservoir of vacuum electromagnetic field H_r and the interaction between them V_{sr} can be written as

$$H = H_s + H_r + V_{sr}, \tag{2.49}$$

$$H_s = \int d^3r \Delta \hat{\Psi}_e^\dagger(\mathbf{r})\hat{\Psi}_e(\mathbf{r}) + \int d^3r \Omega(\mathbf{r})\hat{\Psi}_e^\dagger(\mathbf{r})\hat{\Psi}_g(\mathbf{r}), \tag{2.50}$$

$$H_r = \sum_{k\lambda} \omega_k \hat{a}_{\mathbf{k}\lambda}^\dagger \hat{a}_{\mathbf{k}\lambda}, \tag{2.51}$$

$$V_{sr} = \sum_{k\lambda} \int d^3r\, g_{k\lambda} e^{i\mathbf{k}\cdot\mathbf{r}} e^{i\omega_L t} \hat{\Psi}_e^\dagger(\mathbf{r})\hat{\Psi}_g(\mathbf{r})\hat{a}_{\mathbf{k}\lambda} + H.c., \tag{2.52}$$

where $\hat{\Psi}_e(\mathbf{r})$ and $\hat{\Psi}_g(\mathbf{r})$ are the annihilation operators for atoms in the excited and ground state respectively, and $\hat{a}_{\mathbf{k}\lambda}$ is the photon annihilation operator for momentum $\hbar\mathbf{k}$ and polarization state λ. In addition, ω_e, ω_L and ω_k denote the frequency of atomic excited state, laser field, and the reservoir photons respectively, while $\Delta = \omega_e - \omega_L$ is the detunning of laser field from the excited state. The atom-laser interaction is governed by the Rabi-frequency $\Omega(\mathbf{r})$, while the atom-reservoir interaction is governed by $g_{k\lambda} = \sqrt{\frac{\omega_k}{2\hbar\epsilon_0 V_e}}\mathbf{d}\cdot\epsilon_{k\lambda}$, with $\mathbf{d}$ being the atomic dipole moment in mks units. We note that for the purpose of deriving the master equation it is not necessary to include terms in H_s governing the free evolution of the ground state, as this involves very slow time scales relative to the dynamics of the excited-state/EM-vacuum system. These terms can be added to the system Hamiltonian at the end of the calculation, as any energy-shifts they introduce will be negligible compared to the natural line-width of the excited state.

The quantum state of the system+reservoir is described by the density operator ρ_{sr}. An effective equation of motion for the reduced system density operator,

$\rho_s = tr_r\{\rho_{sr}\}$, can be derived via second-order perturbation theory by following the standard approach (see for example [59]). For the case of a zero-temperature bath this leads to the master equation of

$$\begin{aligned}\dot{\rho}_s(t) &= -iH_s\rho_s(t) - \frac{i}{\tau}\int_0^\tau d\tau' \, tr_r\{V_I(\tau')P_{sr}(t)\} - \\ &\frac{1}{\tau}\int_0^\tau d\tau' \int_0^{\tau'} d\tau'' \, tr_r\{V_I(\tau')V_I(\tau'')P_{sr}(t) - V_I(\tau')P_{sr}(t)V_I(\tau'')\} + H.c.,\end{aligned} \tag{2.53}$$

where P_{sr} is the system-reservoir density ρ_{sr} in interaction picture,

$$P_{sr}(t) = e^{i(H_s+H_r)t}\rho_{sr}e^{-i(H_s+H_r)t}. \tag{2.54}$$

The interaction picture system-reservoir interaction, V_I is defined as

$$V_I(\tau) = e^{i(H_s+H_r)\tau}Ve^{-i(H_s+H_r)\tau} \tag{2.55}$$

$$= \sum_{k\lambda}\int d^3r \, g_{k\lambda}e^{i\mathbf{k}\cdot\mathbf{r}}e^{-i(\omega_k-\omega_L)t}\hat{\Psi}_e^\dagger(\mathbf{r})\hat{\Psi}_g(\mathbf{r})\hat{a}_{\mathbf{k}\lambda} + H.c. \tag{2.56}$$

where we assume that τ is sufficiently small that $\exp[iH_s\tau] \approx 1$, yet large compared to the relaxation time of the reservoir so that $\rho_{sr}(t-\tau) \approx \rho_s(t) \otimes \rho_r^{[eq]}$, where $\rho_r^{[eq]}$ is the density matrix for the equilibrium state of the reservoir. For a thermal reservoir we would have $\rho_r^{[eq]} = e^{-\beta\hat{H}_r}/\mathcal{Z}_r$, where β is the inverse temperature and $\mathcal{Z}_r$ is the partition function. In the tracing over reservoir of vacuum modes, we assume that the all modes are unoccupied, i.e. zero temperature, so that

$$\begin{aligned}\langle\hat{a}_{\mathbf{k}\lambda}\rangle &= \langle\hat{a}_{\mathbf{k}\lambda}^\dagger\rangle = 0, \\ \langle\hat{a}_{k\lambda}\hat{a}_{\mathbf{k}'\lambda'}\rangle &= \langle\hat{a}_{\mathbf{k}\lambda}^\dagger\hat{a}_{\mathbf{k}'\lambda'}^\dagger\rangle = 0, \\ \langle\hat{a}_{\mathbf{k}\lambda}^\dagger\hat{a}_{\mathbf{k}'\lambda'}\rangle &= 0, \\ \langle\hat{a}_{\mathbf{k}\lambda}\hat{a}_{\mathbf{k}'\lambda'}^\dagger\rangle &= \delta_{kk'}\delta_{\lambda\lambda'},\end{aligned} \tag{2.57}$$

Invoking the Markoff approximation for the radiation field of the atoms,

$$\frac{1}{\tau}\int_0^\tau dt' \int_0^{t'} dt'' \, e^{-i(\omega_k-\omega_L)(t'-t'')} \approx \pi\delta(\omega_k-\omega_L) + \frac{i\mathcal{P}}{\omega_k-\omega_L}, \tag{2.58}$$

The resulting master-equation is then

$$\begin{aligned}
\dot{\rho}_s(t) &= -iH_s\rho_s(t) \\
&- \int d^3r d^3r' \Big[L(\mathbf{r}-\mathbf{r}')\hat{\Psi}_e^\dagger(\mathbf{r})\hat{\Psi}_g(\mathbf{r})\hat{\Psi}_g^\dagger(\mathbf{r}')\hat{\Psi}_e(\mathbf{r}')\rho_s(t) \\
&- L^*(\mathbf{r}-\mathbf{r}')\hat{\Psi}_g^\dagger(\mathbf{r})\hat{\Psi}_e(\mathbf{r})\rho_s(t)\hat{\Psi}_e^\dagger(\mathbf{r}')\hat{\Psi}_g(\mathbf{r}')\Big] + H.c.,
\end{aligned} \tag{2.59}$$

where

$$L(\mathbf{r}-\mathbf{r}') = \sum_{k\lambda} |g_{k\lambda}|^2 e^{i\mathbf{k}\cdot(\mathbf{r}-\mathbf{r}')}\{\pi\delta(\omega_k-\omega_L) + \frac{i\mathcal{P}}{\omega_k-\omega_L}\}, \tag{2.60}$$

with $\mathcal{P}$ indicating a principal value. In the limit of infinite quantization volume, the summation becomes an integral, which can be done analytically [228], yielding

$$L(\mathbf{r}-\mathbf{r}') = \frac{3\Gamma}{4}e^{-i\zeta}\left[\sin^2\theta\frac{i}{\zeta} + (1-3\cos^2\theta)\left[\frac{1}{\zeta^2}-\frac{i}{\zeta^2}\right]\right] \tag{2.61}$$

where $\Gamma = \omega_L^3 d^2/(3\pi\epsilon_0\hbar c^3)$ is the single-atom spontaneous emission rate, $\zeta = k_L|\mathbf{r}-\mathbf{r}'|$ and θ is the angle between the dipole moment $\mathbf{d}$ and $\mathbf{r}-\mathbf{r}'$. The real part of $L(\mathbf{r}-\mathbf{r}')$ will contribute to decoherence in the master equation (2.59), while the imaginary part contributes an energy shift due to photon exchange between atoms. In the limit $|\mathbf{r}-\mathbf{r}'| \to 0$ we find

$$L(0) = \frac{\Gamma}{2} + i\delta, \tag{2.62}$$

where the imaginary part, δ is an infinite quantity, reflecting the fact that the standard two-level atom-field interaction model is not properly renormalized. Physically, this term is a Lamb-type shift in the energy of the excited-state due to interaction with

the vacuum modes of the EM field. In our system we can always choose a rotating frame to absorb this shift, so that we can take $\delta = 0$ without loss of generality.

For most optical traps, the laser is detuned very far from the atomic resonance frequency, so that the excited state occupation number is $\ll 1$. In this regime it is useful to perform an adiabatic elimination of the excited-state operators. To eliminate the excited state in the master equation (2.59), we note that for a far-off-resonant laser field, the excitation rate in BEC is extremely low, which enables us to expand the density matrix to a good approximation as

$$\rho \approx \rho_{00} + \rho_{01} + \rho_{10} + \rho_{11}, \tag{2.63}$$

where ρ_{00} and ρ_{11} stand for the density matrix of zero-excitation and one excitation state respectively, while ρ_{01} and ρ_{10} describe coherence between these two manifolds. In fact, it is convenient to define a projection operator $\hat{P}_j$, which is a projection into a subspace with j atomic excitations of the BEC system, such that

$$\rho_{ij} = \hat{P}_i \rho \hat{P}_j. \tag{2.64}$$

With this expansion, one obtains

$$\begin{aligned} \dot{\rho}_{00} &= -i \int d^3r\, \Omega(\mathbf{r}) \hat{\Psi}_g^\dagger(\mathbf{r}) \hat{\Psi}_e(\mathbf{r}) \rho_{01} + \\ &\quad \int d^3r d^3r'\, L(\mathbf{r}-\mathbf{r}') \hat{\Psi}_g^\dagger(\mathbf{r}) \hat{\Psi}_e(\mathbf{r}) \rho_{11} \hat{\Psi}_e^\dagger(\mathbf{r}') \hat{\Psi}_g(\mathbf{r}') + H.c., \end{aligned} \tag{2.65}$$

$$\begin{aligned} \dot{\rho}_{10} &= -i \int d^3r\, \Omega^*(\mathbf{r}) \hat{\Psi}_e^\dagger(\mathbf{r}) \hat{\Psi}_g(\mathbf{r}) \rho_{00} \\ &\quad + i \int d^3r\, \Omega^*(\mathbf{r}) \rho_{11} \hat{\Psi}_e^\dagger(\mathbf{r}) \hat{\Psi}_g(\mathbf{r}) \\ &\quad - \int d^3r d^3r'\, L(\mathbf{r}-\mathbf{r}') \hat{\Psi}_e^\dagger(\mathbf{r}) \hat{\Psi}_g(\mathbf{r}) \hat{\Psi}_g^\dagger(\mathbf{r}') \hat{\Psi}_e(\mathbf{r}') \rho_{10} - i\Delta\rho_{10}, \end{aligned} \tag{2.66}$$

$$\dot{\rho}_{01} = \dot{\rho}_{10}^{\dagger}, \tag{2.67}$$

and

$$\begin{aligned}
\dot{\rho}_{10} &= -i \int d^3r\, \Omega^*(\mathbf{r}) \hat{\Psi}_e^{\dagger}(\mathbf{r}) \hat{\Psi}_g(\mathbf{r}) \rho_{01} \\
&\quad - \int d^3r d^3r'\, L(\mathbf{r}-\mathbf{r}') \hat{\Psi}_e^{\dagger}(\mathbf{r}) \hat{\Psi}_g(\mathbf{r}) \hat{\Psi}_g^{\dagger}(\mathbf{r}') \hat{\Psi}_e(\mathbf{r}') \rho_{11} \\
&\quad + H.c.. \qquad (2.68)
\end{aligned}$$

In the assumption of low excitation rate, one can adiabatically eliminate ρ_{01} and ρ_{10} by demanding $\dot{\rho}_{01} \approx 0$ and $\dot{\rho}_{10} \approx 0$ respectively, yielding

$$\begin{aligned}
\rho_{10} &= -\int d^3r \frac{\Omega^*(\mathbf{r})}{\Delta} \hat{\Psi}_e^{\dagger}(\mathbf{r}) \hat{\Psi}_g(\mathbf{r}) \rho_{00} + \\
&\quad + \int d^3r \frac{\Omega^*(\mathbf{r})}{\Delta} \rho_{11} \hat{\Psi}_e^{\dagger}(\mathbf{r}) \hat{\Psi}_g(\mathbf{r}) \\
&\quad i \int d^3r d^3r' \frac{L(\mathbf{r}-\mathbf{r}')}{\Delta} \hat{\Psi}_e^{\dagger}(\mathbf{r}) \hat{\Psi}_g(\mathbf{r}) \hat{\Psi}_g^{\dagger}(\mathbf{r}') \hat{\Psi}_e(\mathbf{r}') \rho_{10} \qquad (2.69)
\end{aligned}$$

Solving this equation perturbatively up to the order $\frac{1}{\Delta^2}$, one obtains

$$\begin{aligned}
&\rho_{10} = -\int d^3r \frac{\Omega^*(\mathbf{r})}{\Delta} \hat{\Psi}_e^{\dagger}(\mathbf{r}) \hat{\Psi}_g(\mathbf{r}) \rho_{00} + + \int d^3r \frac{\Omega^*(\mathbf{r})}{\Delta} \rho_{11} \hat{\Psi}_e^{\dagger}(\mathbf{r}) \hat{\Psi}_g(\mathbf{r}) \qquad (2.70) \\
&-i \int d^3r d^3r' d^3r'' \frac{L(\mathbf{r}-\mathbf{r}') \Omega^*(\mathbf{r}'')}{\Delta^2} \hat{\Psi}_e^{\dagger}(\mathbf{r}) \hat{\Psi}_g(\mathbf{r}) \hat{\Psi}_g^{\dagger}(\mathbf{r}') \hat{\Psi}_e(\mathbf{r}') \hat{\Psi}_e^{\dagger}(\mathbf{r}'') \hat{\Psi}_g(\mathbf{r}'') \rho_{00} \\
&+i \int d^3r d^3r' d^3r'' \frac{L(\mathbf{r}-\mathbf{r}') \Omega^*(\mathbf{r}'')}{\Delta^2} \hat{\Psi}_e^{\dagger}(\mathbf{r}) \hat{\Psi}_g(\mathbf{r}) \hat{\Psi}_g^{\dagger}(\mathbf{r}') \hat{\Psi}_e(\mathbf{r}') \rho_{11} \hat{\Psi}_e^{\dagger}(\mathbf{r}'') \hat{\Psi}_g(\mathbf{r}''),
\end{aligned}$$

and $\rho_{01} = \rho_{01}^{\dagger}$. Inserting this result for ρ_{01}, ρ_{10} back into Eq. (2.68), we find

$$\begin{aligned}
&\dot{\rho}_{11} = i \int d^3r d^3r' \frac{\Omega^*(\mathbf{r}) \Omega(\mathbf{r}')}{\Delta} \hat{\Psi}_e^{\dagger}(\mathbf{r}) \hat{\Psi}_g(\mathbf{r}) \rho_{00} \hat{\Psi}_g^{\dagger}(\mathbf{r}') \hat{\Psi}_e(\mathbf{r}') \\
&-i \int d^3r d^3r' \frac{\Omega^*(\mathbf{r}) \Omega(\mathbf{r}')}{\Delta} \hat{\Psi}_e^{\dagger}(\mathbf{r}) \hat{\Psi}_g(\mathbf{r}) \hat{\Psi}_g^{\dagger}(\mathbf{r}') \hat{\Psi}_e(\mathbf{r}') \rho_{11} + \int d^3r d^3r' d^3r'' d^3r'''
\end{aligned}$$

$$\frac{L^*(\mathbf{r}''-\mathbf{r}')\Omega^*(\mathbf{r})\Omega(\mathbf{r}^{'''})}{\Delta^2}\hat{\Psi}_e^\dagger(\mathbf{r})\hat{\Psi}_g(\mathbf{r})\rho_{00}\times$$
$$\hat{\Psi}_g^\dagger(\mathbf{r}^{'''})\hat{\Psi}_e(\mathbf{r}^{'''})\hat{\Psi}_e^\dagger(\mathbf{r}^{'})\hat{\Psi}_g(\mathbf{r}^{'})\hat{\Psi}_g^\dagger(\mathbf{r}'')\hat{\Psi}_e(\mathbf{r}'')$$
$$-\int d^3r d^3r^{'} d^3r^{''} d^3r^{'''}\,\frac{L^*(\mathbf{r}''-\mathbf{r}')\Omega^*(\mathbf{r})\Omega(\mathbf{r}^{'''})}{\Delta^2}\hat{\Psi}_e^\dagger(\mathbf{r})\hat{\Psi}_g(\mathbf{r})\hat{\Psi}_g^\dagger(\mathbf{r}^{'''})\hat{\Psi}_e(\mathbf{r}^{'''})\times$$
$$\rho_{11}\hat{\Psi}_e^\dagger(\mathbf{r}^{'})\hat{\Psi}_g(\mathbf{r}^{'})\hat{\Psi}_g^\dagger(\mathbf{r}'')\hat{\Psi}_e(\mathbf{r}'')$$
$$+i\int d^3r d^3r^{'}\,L(\mathbf{r}-\mathbf{r}')\hat{\Psi}_e^\dagger(\mathbf{r})\hat{\Psi}_g(\mathbf{r})\hat{\Psi}_g^\dagger(\mathbf{r}')\hat{\Psi}_e(\mathbf{r}')\rho_{11}+H.c.. \tag{2.71}$$

Next, we apply a similar adiabatic elimination process eliminate the excited state matrix ρ_{11}. To do that, first we normal order the ground state operators in above equation, and then by setting $\dot{\rho}_{11}\approx 0$, obtains

$$\rho_{11}=i\int d^3r d^3r^{'}\,\frac{\Omega^*(\mathbf{r})\Omega(\mathbf{r}')}{2\Delta\Gamma}\hat{\Psi}_e^\dagger(\mathbf{r})\hat{\Psi}_g(\mathbf{r})$$
$$\times\rho_{00}\hat{\Psi}_g^\dagger(\mathbf{r}')\hat{\Psi}_e(\mathbf{r}')$$
$$-i\int d^3r d^3r^{'}\,\frac{\Omega^*(\mathbf{r})\Omega(\mathbf{r}')}{2\Delta\Gamma}\hat{\Psi}_e^\dagger(\mathbf{r})\hat{\Psi}_g^\dagger(\mathbf{r}')\hat{\Psi}_g(\mathbf{r})\hat{\Psi}_e(\mathbf{r}')\rho_{11} \tag{2.72}$$
$$-i\int d^3r\frac{|\Omega(\mathbf{r})|^2}{2\Delta\Gamma}\hat{\Psi}_e^\dagger(\mathbf{r})\hat{\Psi}_e(\mathbf{r})\rho_{11}$$
$$-\int d^3r d^3r^{'}\,\frac{L(\mathbf{r}-\mathbf{r}')}{2\Gamma}\hat{\Psi}_e^\dagger(\mathbf{r})\hat{\Psi}_g^\dagger(\mathbf{r}')\hat{\Psi}_g(\mathbf{r})\hat{\Psi}_e(\mathbf{r}')\rho_{11}$$
$$+\int d^3r d^3r^{'} d^3r^{''}\,\frac{L^*(\mathbf{r}''-\mathbf{r}')\Omega^*(\mathbf{r})\Omega(\mathbf{r}^{'})}{2\Delta^2\Gamma}\hat{\Psi}_e^\dagger(\mathbf{r})\hat{\Psi}_g(\mathbf{r})\times$$
$$\rho_{00}\hat{\Psi}_g^\dagger(\mathbf{r}')\hat{\Psi}_g(\mathbf{r}')\hat{\Psi}_g^\dagger(\mathbf{r}^{''})\hat{\Psi}_e(\mathbf{r}^{''})$$
$$-\int d^3r d^3r^{'} d^3r^{''} d^3r^{'''}\,\frac{L^*(\mathbf{r}''-\mathbf{r}')\Omega^*(\mathbf{r})\Omega(\mathbf{r}^{'''})}{2\Delta^2\Gamma}\hat{\Psi}_e^\dagger(\mathbf{r})\hat{\Psi}_g(\mathbf{r})\hat{\Psi}_g^\dagger(\mathbf{r}^{'''})$$
$$\times\hat{\Psi}_e(\mathbf{r}^{'''})\rho_{11}\hat{\Psi}_e^\dagger(\mathbf{r}^{'})\hat{\Psi}_g(\mathbf{r}^{'})\hat{\Psi}_g^\dagger(\mathbf{r}'')\hat{\Psi}_e(\mathbf{r}'')$$
$$+H.c.,$$

Again, we solve this equation perturbatively up to order $\frac{1}{\Delta^2}$, and arrive at

$$\begin{aligned}
\rho_{11} = & \int d^3r d^3r' d^3r'' \frac{L^*(\mathbf{r}''-\mathbf{r}')\Omega^*(\mathbf{r})\Omega(\mathbf{r}')}{2\Delta^2\Gamma}\hat{\Psi}_e^\dagger(\mathbf{r})\hat{\Psi}_g(\mathbf{r}) \\
& \times\rho_{00}\hat{\Psi}_g^\dagger(\mathbf{r}')\hat{\Psi}_g(\mathbf{r}')\hat{\Psi}_g^\dagger(\mathbf{r}'')\hat{\Psi}_e(\mathbf{r}'') \\
& - \int d^3r d^3r' d^3r'' d^3r''' d^3r'''' \frac{L(\mathbf{r}-\mathbf{r}')L^*(\mathbf{r}''''-\mathbf{r}''')\Omega^*(\mathbf{r}'')\Omega(\mathbf{r}''')}{2\Delta^2\Gamma^2}\times \\
& \hat{\Psi}_e^\dagger(\mathbf{r})\hat{\Psi}_g^\dagger(\mathbf{r}')\hat{\Psi}_g(\mathbf{r})\hat{\Psi}_e(\mathbf{r}')\hat{\Psi}_e^\dagger(\mathbf{r}'')\hat{\Psi}_g^\dagger(\mathbf{r}'')\rho_{00}\hat{\Psi}_g^\dagger(\mathbf{r}''')\hat{\Psi}_g(\mathbf{r}''')\hat{\Psi}_g^\dagger(\mathbf{r}'''')\hat{\Psi}_e(\mathbf{r}'''') \\
& - \int d^3r d^3r' d^3r'' d^3r''' d^3r'''' \frac{L(\mathbf{r}-\mathbf{r}')L^*(\mathbf{r}''''-\mathbf{r}''')\Omega^*(\mathbf{r}''')\Omega(\mathbf{r}'')}{2\Delta^2\Gamma^2}\times \\
& \hat{\Psi}_e^\dagger(\mathbf{r})\hat{\Psi}_g^\dagger(\mathbf{r}')\hat{\Psi}_g(\mathbf{r})\hat{\Psi}_e(\mathbf{r}')\hat{\Psi}_e^\dagger(\mathbf{r}'''')\hat{\Psi}_g^\dagger(\mathbf{r}'''')\hat{\Psi}_g^\dagger(\mathbf{r}''')\hat{\Psi}_g(\mathbf{r}''')\rho_{00}\hat{\Psi}_g^\dagger(\mathbf{r}'')\hat{\Psi}_e(\mathbf{r}'') \\
& + H.c..
\end{aligned} \tag{2.73}$$

This expression for ρ_{11} can be simplified by normal ordering. Finally, we insert the normal ordered $\rho_{01}, \rho_{01}, \rho_{11}$ back into Eq. (2.65), and keep only terms up to $\frac{1}{\Delta^2}$. Meanwhile, since the number density of atoms in BEC is small, we drop any 3-body and above terms. With these two assumptions, we obtain the resulting master equation (2.14),

$$\begin{aligned}
\dot{\rho}_s(t) = & -iH_s\rho_s(t) - \frac{|\Omega|^2}{\Delta^2}\Gamma\int d^3r\hat{\Psi}_g^\dagger(\mathbf{r})\hat{\Psi}_g(\mathbf{r})\rho_s(t) - \\
& \int d^3r d^3r' \frac{\Omega(\mathbf{r})L(\mathbf{r}-\mathbf{r}')\Omega^*(\mathbf{r}')}{\Delta^2}\hat{\Psi}_g^\dagger(\mathbf{r})\hat{\Psi}_g^\dagger(\mathbf{r})\hat{\Psi}_g(\mathbf{r}')\hat{\Psi}_g(\mathbf{r}')\rho_s(t) + \\
& \int d^3r d^3r' \frac{\Omega^*(\mathbf{r})L(\mathbf{r}-\mathbf{r}')\Omega(\mathbf{r}')}{\Delta^2}\hat{\Psi}_g^\dagger(\mathbf{r})\hat{\Psi}_g(\mathbf{r})\rho_s(t)\hat{\Psi}_g^\dagger(\mathbf{r}')\hat{\Psi}_g(\mathbf{r}') + H.c..
\end{aligned}$$

where we have written $\rho_s \equiv \rho_{00}$.

2.8.4 Atom loss dynamics: elastic and inelastic regime

To derive the atom decay rate of a single atomic-field mode, we will need to make use of the commutation relation

$$[\hat{c}^\dagger \hat{c}, \hat{\Psi}^\dagger(\mathbf{r})\hat{\Psi}(\mathbf{r})] = -\phi(\mathbf{r})\hat{c}^\dagger\hat{\Psi}(\mathbf{r}) - \phi^*(\mathbf{r})\hat{\Psi}^\dagger(\mathbf{r})\hat{c}, \tag{2.74}$$

where $\hat{c}$ is the annihilation operator for atoms in mode $\phi(\mathbf{r})$. Then, from the master equation (2.14), it is straight forward to obtain the evolution of the mean mode occupation $n_0 = \langle \hat{c}^\dagger \hat{c} \rangle$ as

$$\begin{aligned} \dot{n}_0 &= -\int d^3r d^3r' \frac{G(\mathbf{r},\mathbf{r}')}{\Delta^2} \Big[\phi^*(\mathbf{r})\delta^3(\mathbf{r}-\mathbf{r}')\langle \hat{c}^\dagger \hat{\Psi}(\mathbf{r}')\rangle \\ &- \phi(\mathbf{r})\phi^*(\mathbf{r}')\langle \hat{\Psi}^\dagger(\mathbf{r})\hat{\Psi}(\mathbf{r}')\rangle + \phi^*(\mathbf{r})\langle \hat{c}^\dagger\hat{\Psi}^\dagger(\mathbf{r}')\hat{\Psi}(\mathbf{r})\hat{\Psi}(\mathbf{r}')\rangle \\ &- \phi(\mathbf{r})\langle \hat{\Psi}^\dagger(\mathbf{r})\hat{\Psi}^\dagger(\mathbf{r}')\hat{\Psi}(\mathbf{r}')\hat{c}\rangle \Big], \end{aligned} \tag{2.75}$$

where $G(\mathbf{r},\mathbf{r}') = \Omega(\mathbf{r})L(\mathbf{r}-\mathbf{r}')\Omega^*(\mathbf{r}')$. Making a single mode approximation,

$$\hat{\Psi}(\mathbf{r}) = \phi(\mathbf{r})\hat{c}, \tag{2.76}$$

one obtains

$$\dot{n}_0 = -\frac{2}{\Delta^2}\int d^3r d^3r' \,\Re\left[G(\mathbf{r},\mathbf{r}')\right] |\phi(\mathbf{r})|^2 \times \left[\delta^3(\mathbf{r}-\mathbf{r}') - |\phi(\mathbf{r}')|^2\right] n_0. \tag{2.77}$$

To better understand the physics described by this equation, we make the simplifying assumption $\Omega(\mathbf{r}) \approx \Omega e^{i\mathbf{k}_L\cdot(\mathbf{r}-\mathbf{r}')}$, where $\mathbf{k}_L$ is the laser wave-vector, satisfying $\mathbf{k}_L \cdot \mathbf{d} = 0$. This leads to

$$\dot{n}_0 = -\frac{|\Omega|^2}{\Delta^2}\Gamma(1-\xi)n_0, \tag{2.78}$$

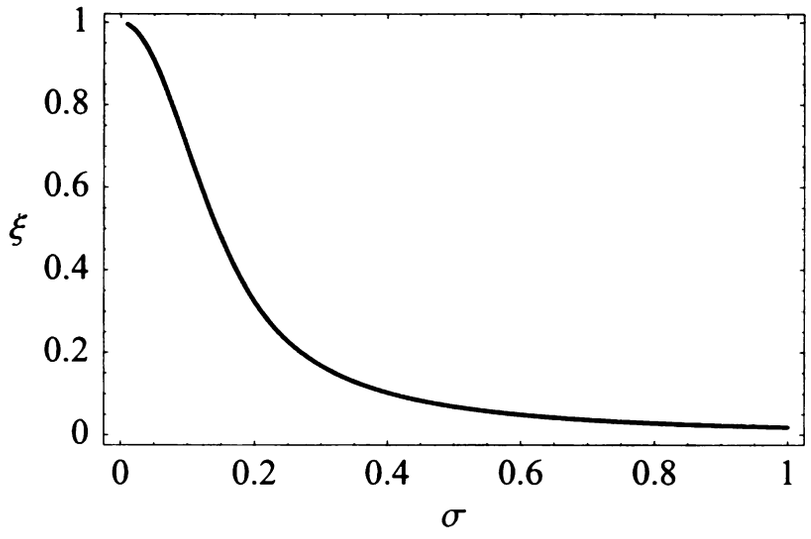

Figure 2.24: Dependence of the inelastic loss parameter ξ on the spatial size of condensate, which is indicated by the dimensionless parameter σ as shown in Eq. (2.80). It is seen that ξ is approximately unity when the size of condensate is much less than the laser wavelength, i.e. $\sigma \ll 1$, which means there is negligible atom loss. As the condensate size approaches half λ_L, ξ decreases to around 0, corresponding to the maximum loss rate.

where

$$\xi = \frac{2}{\Gamma}\int d^3r d^3r' \Re[e^{i\mathbf{k}_L\cdot(\mathbf{r}-\mathbf{r}')}L(\mathbf{r}-\mathbf{r}')]|\phi_g(\mathbf{r})|^2|\phi_g(\mathbf{r}')|^2. \tag{2.79}$$

In the elastic regime we have $|\phi(\mathbf{r})|^2 \approx \delta(\mathbf{r})$ relative to $L(\mathbf{r}-\mathbf{r}')$, which leads to $\xi = 1$ so that there is no atomic loss, as expected. As the size of condensate grows, ξ will decrease, as shown in Fig. 2.24, which plots ξ versus condensate size for the case of a spherically symmetric Gaussian condensate wavefuction

$$\phi(\mathbf{r}) = \frac{1}{(\sigma\lambda_L)^{3/2}\pi^{3/4}}e^{-r^2/(2\sigma^2\lambda_L^2)}, \tag{2.80}$$

where σ is the ratio of the condensate size to the laser wavelength, λ_L. From the figure, we see that the decay rate of the condensate can be neglected under the condition $\sigma \ll 1$, while for a mode whose size is comparable to or larger than the laser wavelength, we have $\xi \to 0$ so that the population will decay at the expected rate

$|\Omega|^2\Gamma/\Delta^2$, which is simply the electronically-excited state fraction times the excited state lifetime.

Chapter 3

Optimized Double-well interferometry with Gaussian-squeezed states

In this chapter, we show that a Mach-Zender interferometer with a gaussian number-difference squeezed input state can exhibit a sub-shot-noise phase resolution over a large phase-interval. We obtain the optimal level of squeezing for a given phase-interval $\Delta\theta_0$ and particle number N, with the resulting phase-estimation uncertainty smoothly approaching $3.5/N$ as $\Delta\theta_0$ approaches $10/N$, achieved with highly squeezed input state near Fock regime. We then analyze an adaptive measurement scheme which allows any phase on $(-\pi/2, \pi/2)$ to be measured with a precision of $3.5/N$ requiring only a few measurements, even for very large N. We obtain an asymptotic scaling law of $\Delta\theta \approx (2.1+3.2\ln(\ln(N_{tot}\tan\Delta\theta_0)))/N_{tot}$, resulting in a final precision of $\approx 10/N_{tot}$, with N_{tot} the total particle number used in adaptive measurements. This scheme can be readily implemented in a double-well Bose-Einstein condensate system, as the optimal input states can be obtained by adiabatic manipulation of the double-well ground state. The major results of this chapter have been published in

"Optimized Double-Well Quantum Interferometry with Gaussian Squeezed States", Y. P. Huang and M. G. Moore in Phys. Rev. Lett. **100**, 250406 (2008).

The organization of this chapter is as follows. In section 3.1, we provide a background on quantum interferometry and briefly review previous apparatus to achieve measurement precisions beyond the classical limit. In section 3.2, we present the model of Mach-Zehnder (MZ) interferometer and a realization in a double-well BEC system. In section 3.3, we introduce the Bayesian analysis as a reliable method to evaluate the interferometers' performance. The major result of this work is presented in section 3.4, where we show that ultrahigh-sensitivity phase measurements can be realized by feeding a Mach-Zehnder interferometer with optimally number-squeezed input states. Such states are obtained in a double-well BEC system as the ground state in presence of repulsive atomic interaction, providing experimental feasibility in present or near-future laboratories. We then briefly conclude this chapter in 3.5. For a comparison, in appendix 3.6, using the Bayesian analysis, we analyze the performances of two existing interferometers, one employing number-squeezed input states while the other based on quantum discrete Fourier transformation.

3.1 Introduction

The goal of quantum interferometry is to overcome inherent limitations of classical interferometers, thereby significantly improving the phase measurement precision provided with similar amounts of resources [229]. Due to the nonexistence of a well-defined Hermitian phase operator [230], a phase eigenstate in general does not exist, so that the standard quantum measurement postulate does not apply. Instead, a phase shift θ can only be *estimated* by measuring some phase-dependent observables. The accuracy of this estimation, measured by a phase uncertainty $\Delta\theta$, is then a critical parameter in evaluating the interferometer's performance. Ultimately, the minimal

obtainable $\Delta\theta$ is constrained by the inherent quantum fluctuation in the interferometer output, which, unlike classical noises, can not be suppressed by improving measurement precision. In a Mach-Zehnder (MZ) interferometer with coherent input states [231], the participating particles are uncorrelated with each other. The output fluctuation is then limited by the shot noise, corresponding to a $\sqrt{N_{tot}}$ uncertainty in the number difference between the two output ports of the interferometer (N_{tot} is the total particle number). The phase uncertainty, determined by the signal to noise ratio, is then $\Delta\theta \sim \sqrt{N_{tot}}/N_{tot} = 1/\sqrt{N_{tot}}$. This precision is widely recognized as the standard quantum limit (SQL), also referred to as "shot noise". If the particles are correlated, the output fluctuation can be suppressed, leading to a reduced phase uncertainty from SQL [232, 233, 157]. The minimal phase uncertainty allowed by quantum-mechanics, given in a analogy to the Heisenberg-uncertainty, is $\Delta\theta_{min} = 1/N_{tot}$. Such is the so-called Heisenberg limit. Interferometric devices yielding phase uncertainties at or near the Heisenberg limit, with $\Delta\theta = \beta/N_{tot}$ and $\beta \gtrsim 1$, are considered efficient, generally referred to as Heisenberg scaling (HS) interferometers. Given the same amount of resources N_{tot}, a HS interferometer tremendously reduces the phase uncertainty from SQL by an immense factor of $\sqrt{N_{tot}}$.

The improvement from SQL to HS turns out to be very useful, mainly due to two reasons. The first is to overcome the physical limitation on resources available for interferometry uses. For example, the maximally attainable N_{tot} for an optical interferometry is limited by the achievable laser intensity. Eventually, this limitation can be overcome as technology develops. The second, perhaps more crucial reason is that in various applications requiring non-demolition measurements, HS interferometers are the only feasible candidates, as is usually the case in the field of quantum information processing. For example, in a MZ-interferometric approach to generate entanglement between isolated single-atom qubits, the allowed photon number N_{tot} is primarily restricted by the need to avoid the spontaneous emission

of atomic qubits. It turns out that under such a constraint, a HS phase-sensitivity is a required, unless optical resonators are used [234]. All these give rise to the importance of HS interferometry, as reflected by the continuous interdisciplinary efforts to construct HS interferometers in the past decades. Thus far, particular efforts have been made in elevating the performance of MZ interferometry with nonclassical squeezed/entangled input states [232, 157, 158, 30, 235, 236, 237, 238, 239]. Recently, a range of non-MZ interferometries employing nonlinear beamsplitters and/or novel measurement protocols have been proposed [26, 240, 27, 180, 241, 242, 243], among which the maximally-entangled N-particle NOON state, in a superposition of $\frac{1}{\sqrt{2}}(|N,0\rangle + |0,N\rangle)$, has attracted intensive attentions [24, 25, 26, 27].

According to their usages, interferometers can be generally categorized into two classes, namely *phase switches* and *phase meters*. A phase switch is built for the purpose of detecting the presence of a phase imbalance induced by environmental inhomogeneities, for example, the gravity gradient. A phase meter, on the other hand, is used to quantitatively read out an unknown phase shift. In general, constructing a phase meter at a sub-SQL precision is much more challenging than building a phase switch at the same precision. This is because the quantum fluctuation in an interferometer output is usually dependent on the value of phase shift θ, and thus cannot be congruously suppressed with the a-priori information on θ [229]. For example, for a MZ interferometer, at a small phase imbalance, the quantum fluctuation at the interferometer output can be efficiently suppressed by number-squeezing the input state. This mechanism has allowed a series of phase switches operating at HS sensitivity [230, 232, 157, 158, 24, 235, 236, 119]. For not-so-small phases, however, a strong number-squeezing would adversely increase the output fluctuation. As a matter of fact, a MZ interferometer with maximally-squeezed input states has been shown to yield a worse-than-SQL phase resolution for $|\theta| \gg 1/N_{tot}$ [244].

To evaluate the performance of an interferometer, or precisely, to determine the

phase uncertainty $\Delta\theta$, there exist two major statistical methods. The first is the linearized error propagation analysis, where assuming $n(\theta)$ is a θ-dependent output observable, $\Delta\theta$ is linearly related to the quantum fluctuation Δn in $n(\theta)$ by $\Delta\theta = (\frac{\partial n}{\partial\theta})^{-1}\Delta n$. This method, being extremely intuitive and easy to apply, has been very popular among scientists in this field. Only recently was it found to be valid only if the probability distribution of $n(\theta)$ is a singly-peaked Gaussian, which is, however, seldom the case in the quantum interferometry [245, 244, 246, 119]. A second, more general method is the Bayesian analysis applying to quantum statistics [247]. In this approach, the conditional probability of estimating a physical phase θ to be ϕ, namely $P(\phi|\theta)$, is evaluated utilizing the classical Bayesian theorem. The phase uncertainty $\Delta\theta$ is estimated at the confidence interval, which can be $68\%, 95\%$ or 99%. By this analysis, quite a few of existing interferometers, which were previously predicted by the error propagation method to be HS, turn out to yield a near or worse-than SQL phase resolution when measuring nonzero phases [230, 232, 157, 24, 235, 236, 26, 240, 27, 180, 241, 242, 243].

This far, it has been shown in theory that the Twin-Fock (TF) state and related Pezze-Smerzi (PS) state can achieve HS precision when measuring a zero phase, thus implementing HS phase switches [248, 244, 119, 131]. The TF state is a maximally number-squeezed state of $|N/2, N/2\rangle$, i.e., having an equal and definite number of particles in the two input modes, whereas the PS state is a two-mode superposition of $\frac{1}{\sqrt{2}}|N/2+1, N/2-1\rangle + |N/2-1, N/2+1\rangle$. We find, however, that for $|\theta| > 1/N$ the phase precisions of both TF and PS interferometry quickly degrade to worse-than-SQL. Eventually in the limit of large N, the phase uncertainty saturates at a constant, N-independent value. This saturation behavior for the TF state was first observed by Kim *et al* in 1998, where they found the phase uncertainty $\Delta\theta \sim 1/N_{tot}$ for $\theta < 1/N$, and growing rapidly thereafter [248]. The work of this chapter similarly finds that TF and PS states become worse than shot-noise for $|\theta| \gg 1/N$. On the

other hand, we verify that a truly HS phase meter, i.e., $\Delta\theta \propto 1/N$ for any θ, can be implemented with quantum discrete fourier transformation (QDFT). The drawback is, however, that implementing QDFT in practice requires the extremely-challenging capability to perform quantum computation over a large number of qubits, making it experimentally unfeasible in the present or even near-future laboratories.

Recently, with the well-established large degree of spatial and temporal coherence, the system of Bose-Einstein condensate (BEC) has emerged as a viable candidate for matter-wave interferometry [30, 31, 32, 33, 34, 35, 36, 37]. Compared to optical systems, a BEC-based interferometer has the unique advantages of sensing inertial forces, measuring gravity gradient, and allowing measurements at single-particle level with high-efficiency detectors [38, 39]. Furthermore, unlike photons, atoms are strongly interacting particles. This feature serves a natural source of nonlinearity which can lead to nonclassical many-particle states [249]. In particular, in BEC, the strength of inter-atom interaction via s-wave scattering is conveniently tunable by Feshbach resonance technique, providing the ease to engineer the system's quantum state [31, 118]. A most accessible, archetypical BEC interferometer is realized in a double-well BEC system. The beamsplitter, in an analogue to MZ interferometers, is implemented by manipulating the potential barrier between the two trapping wells [37, 80, 81, 82, 83]. For this system, the squeezed-vacuum protocols are not applicable, while the NOON state is not suited to determine an unknown phase due to the periodicity of the phase-distribution [250, 244]. This leaves number-difference squeezed states as a viable candidate, although to date there has been no systematic study of how to measure arbitrary phases at HS precision in the large-N limit. In this chapter, we perform such an analysis and show that an asymptotic scaling of $(\ln(\ln N_{tot}))/N_{tot}$ can be achieved via multiple adaptive measurements with Gaussian number-squeezed states, which can be readily created in a double-well BEC.

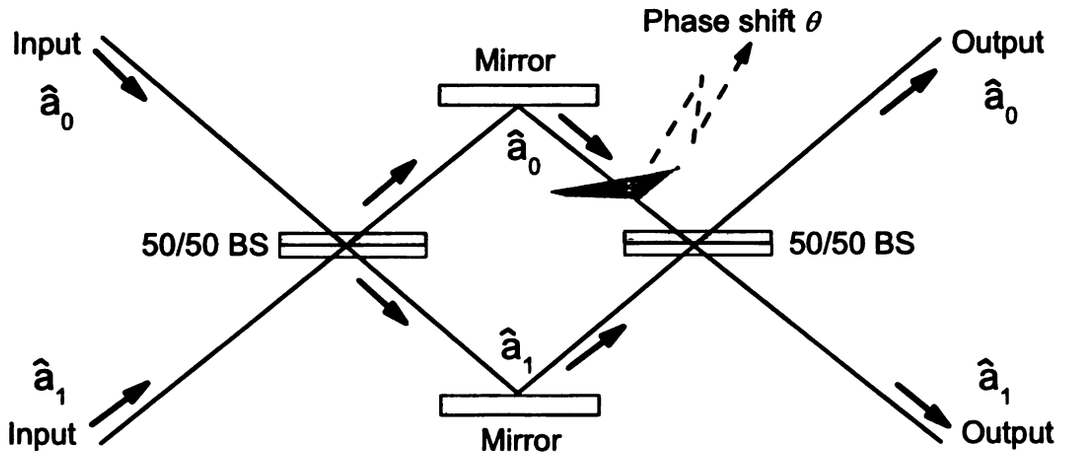

Figure 3.1: The schematic graph of a MZ interferometer.

3.2 Double-well MZ interferometer

3.2.1 MZ interferometer

A MZ interferometer is a balanced homodyne measurement device consisting of two 50/50 beamsplitters (BS), as shown in figure 3.1. It has two input and output ports. During a phase measurement, the input beam, entering the interferometer via one or two input ports, passes through the first 50/50 BS, thereby coherently bifurcating into two beams traveling in the upper and lower arms. As it propagates, each beam independently acquires local phase shift of the arm it travels in. The two beams are then recombined at the second 50/50 BS to give the interferometer output in the form of interference pattern. The output state is determined by the relative phase shift of the two arms, which is inferred by measuring the number difference of particles coming from the two output ports.

Describing the upper and lower arm with bosonic annihilators $\hat{a}_0$ and $\hat{a}_1$, it is

convenient to introduce the following momentum operators [157]

$$\hat{J}_x = \frac{1}{2}(\hat{a}_0^\dagger \hat{a}_1 + \hat{a}_1^\dagger \hat{a}_0), \tag{3.1}$$

$$\hat{J}_y = \frac{1}{2i}(\hat{a}_0^\dagger \hat{a}_1 - \hat{a}_1^\dagger \hat{a}_0), \tag{3.2}$$

$$\hat{J}_z = \frac{1}{2}(\hat{a}_0^\dagger \hat{a}_0 - \hat{a}_1^\dagger \hat{a}_1), \tag{3.3}$$

and the particle number operator

$$N = \hat{a}_0^\dagger \hat{a}_0 + \hat{a}_1^\dagger \hat{a}_1. \tag{3.4}$$

It is straightforward to verify that $\hat{J}_x, \hat{J}_y, \hat{J}_z$ constitute a SU(2) group. The total spin $\hat{J}$ satisfies

$$\hat{J}^2 = \frac{N}{2}\left(\frac{N}{2} + 1\right) \tag{3.5}$$

The function of 50/50 BS is then represented by a $\hat{J}_x$ rotation for a $\pi/2$ angle, with the propagator

$$\hat{U}_{BS} = \exp\left(i\frac{\pi}{2}\hat{J}_x\right). \tag{3.6}$$

The phase shift is a θ-rotation along $\hat{J}_z$ axis, described by the propagator

$$\hat{U}_{phase}(\theta) = \exp\left(i\theta\hat{J}_z\right). \tag{3.7}$$

In the above spin-rotation formalism, the interferometer input and output state are connected by a passage propagator $\hat{U}$, given by

$$|\Psi_{out}\rangle = \hat{U}(\theta)|\Psi_{in}\rangle, \tag{3.8}$$

where

$$\hat{U}(\theta) = \hat{U}_{BS}\hat{U}_{phase}(\theta)\hat{U}_{BS}. \tag{3.9}$$

During the transformation, the total spin of the system $\hat{J}$ is conserved. Using the commutation relations (3.1)-(3.3) and that $e^{\hat{A}}e^{\hat{B}} = e^{\hat{B}}e^{\hat{A}}e^{[\hat{A},\hat{B}]}$, the propagator $\hat{U}(\theta)$ is reduced to

$$\hat{U}(\theta) = \exp(-i\theta\hat{J}_y)\exp(i\pi\hat{J}_x). \tag{3.10}$$

Thus for a symmetric interferometer input, the output state is merely a $-\theta$ rotation along the $\hat{J}_y$ axis.

Due to the conservation of total spin, the state transformation of the MZ interferometry can be visualized in the Bloch sphere picture [237]. In this picture, a state $|\Psi\rangle$ corresponds to a quasi-probability on Bloch sphere of radius $\sqrt{\hat{J}^2} \approx N/2$, defined as

$$P(\theta,\phi) = |\langle N/2|e^{i\hat{J}_y(\pi/2-\theta)}e^{i\hat{J}_z\phi}|\Psi\rangle|^2, \tag{3.11}$$

where the Fock state $|N/2\rangle = \frac{1}{\sqrt{N!}}(\hat{a}_0^\dagger)^N|\text{vacuum}\rangle$. Note any N-atoms state for which all atoms are in the same single-particle state can be written in the form $e^{-i\hat{J}_z\phi}e^{-i\hat{J}_y(\pi/2-\theta)}|N/2\rangle$, which has eigenvalue $N/2$ with respect to the projection of $\hat{J}$ onto the axis defined by θ,ϕ. In this picture, the two-mode coherent state corresponds to a round of radius $\sqrt{N}/2$ on the sphere centered at $\langle\hat{J}_z\rangle = \langle\hat{J}_y\rangle = 0$. Number squeezing corresponds to compressing the round along the J_z-direction, resulting in an ellipse, as shown in figure 3.2 (a). Phase squeezing, on the hand, corresponds to compressing along the J_x direction. Specifically, a maximally-squeezed TF state is a thin equatorial ring on the sphere.

In the Bloch-sphere picture, the process of MZ interferometric measurement is intuitively described by a set of rotations, as shown in figure 3.2. For a number-squeezed input state, the first BS rotate the state along J_x axis for an angle of $\pi/2$, transforming it to a phase-squeezed state, as shown in figure (b). The phase acquisition corresponds to a J_z rotation for an angle of θ, as seen in figure (c). The second BS, performing another J_x rotation, transforms the state into the output state

shown in figure (d). Clearly from the figure, the total effect of rotations corresponds to a J_y rotation for an angle of $-\theta$. Phase information is obtained by measuring the number difference between the two interferometer modes, which projects the output state onto a $\hat{J}_z$ eigenstate. Quantum fluctuations in this measurement are governed by the projection of the output distribution onto the J_z-axis. Due to the rigid rotation, the width of the projection will be determined by a θ-dependent combination of the J_z and J_x noise of the input distribution.

3.2.2 Double-well BEC as MZ interferometer

Matter-wave interferometers have emerged as powerful tools for ultra-precise detection of gravitational waves and inertial forces [232, 251]. Among them, the double-well BEC system has manifested itself as a promising candidate, with its established large degree of spatial and temporal coherence and the recent progress towards single-atom counting. As discussed in chapter one, a double-well BEC can be consisted of atoms in two internal spin states, or in two spatially-separated trapping potentials. In either case, the system can be approximately described on the state basis of two localized modes. The modes are mapped onto the upper and lower channel in a MZ interferometer as shown in figure 3.1, and are similarly described by annihilation operators of $\hat{a}_0$ and $\hat{a}_1$. In this two-mode approximation, the double-well BEC system is described by the Hamiltonian,

$$\hat{H}(\chi) = -2\tau \hat{J}_x + \delta \hat{J}_z + U \hat{J}_z^2, \tag{3.12}$$

where τ is the inter-well tunneling rate, U is the atom-atom interaction strength, and δ is the asymmetric tilt of the double-well, presumably due to the external perturbation being measured. For repulsive atom-atom interaction and $\delta \approx 0$, the ground state is

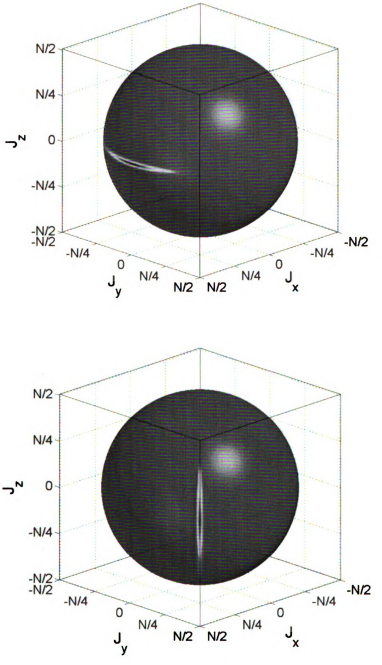

Figure 3.2: State engineering for MZ interferometry in the Bloch-sphere picture, where (a) plots the interferometer input of number squeezed state, (b) shows the state after the first BS.

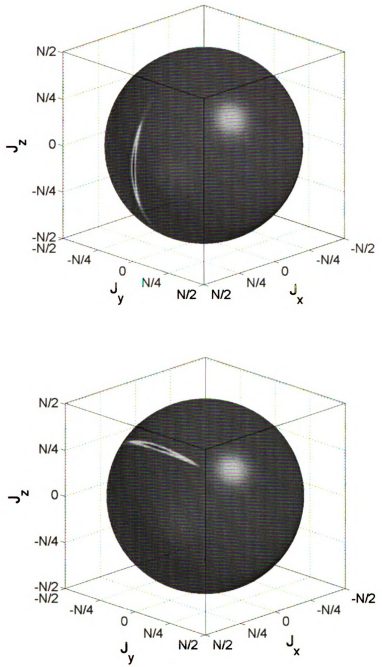

Figure 3.3: State engineering for MZ interferometry in the Bloch-sphere picture, where (a) shows the state after phase acquisition, and (b) plots the final output state obtained after the second BS.

very close to a Gaussian squeezed (GS) state of the form

$$|\sigma\rangle \propto \sum_{n=-N/2}^{N/2} e^{-n^2/4\sigma^2}|n\rangle, \tag{3.13}$$

where $|n\rangle$ is a number-difference eigenstate satisfying $\hat{J}_z|n\rangle = n|n\rangle$. The width σ, depends on the parameter $u = U/\tau$, and is given by $\sigma^2 = N/4\sqrt{1+uN}$ [227]. This formula turns out to be a good approximation to exact for a wide range of system parameters, as shown in figure 3.4. We note that u can be tuned by varying U/τ via a Feshbach resonance and/or changing the shape of the double-well potential, and allows σ to be varied between 0 and $\sqrt{N}/2$, corresponding to maximal number-difference squeezing and no squeezing, respectively.

To implement a MZ interferometer, we set $U = 0$ and allow tunneling for $t = \pi/4\tau$ duration, thus realizing a linear 50/50 beamsplitter, described by the propagator $e^{i\frac{\pi}{2}\hat{J}_x}$. This is followed by a sudden raising of the potential barrier to turn off tunneling and allow phase acquisition due to the small but non-vanishing δ. Holding the system for a measurement time T, a phase shift of $\theta = -\delta T$ will be acquired, described by the propagator $e^{i\theta\hat{J}_z}$. The barrier is then lowered again to implement a second beamsplitter. The evolution of the system is shown in figure 3.5, where we plot the probability packet dynamics for a phase shift of $\theta = \pi/4$, with a moderately number-squeezed state and the PS input state in figure (a) and (b), respectively. In both figures, the probability-packet of the system, initially centered at $n = 0$, is shifted from the center at the end of measurement by a distance determined by θ. Measuring the number difference of output state then provides information on θ. In figure 3.5 (a) with an input of some number-squeezing, the final probability-packet of the system exhibits a sharp peak, suggesting a high signal to noise ratio, thus a small phase uncertainty. In contrast, using the highly-squeezed PS input state as shown in figure (b), the system evolves into two peaks, each peak yielding large

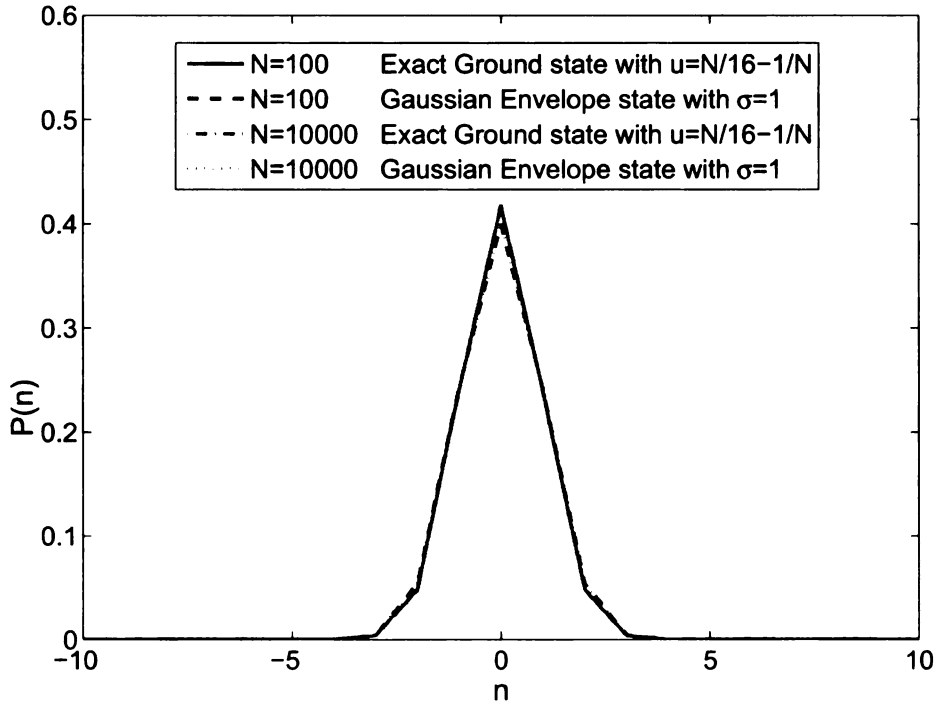

Figure 3.4: A comparison of the exact ground state of a double-well BEC and the Gaussian envelope (3.13).

oscillatory tails. This indicates a strong quantum fluctuation, which gives rise to a large phase uncertainty. From here, we can preliminarily conclude that too much number squeezing acts adversely in minimizing phase uncertainty.

3.3 Bayesian analysis of phase uncertainties

As discussed earlier, a phase shift θ can only be estimated indirectly by measuring some θ-dependent observables [230]. The estimation accuracy, measured by the phase uncertainty $\Delta\theta$, is commonly estimated either by the linearized error propagation method or by the Bayesian analysis [252, 232, 253, 82, 158, 244, 119]. In the error

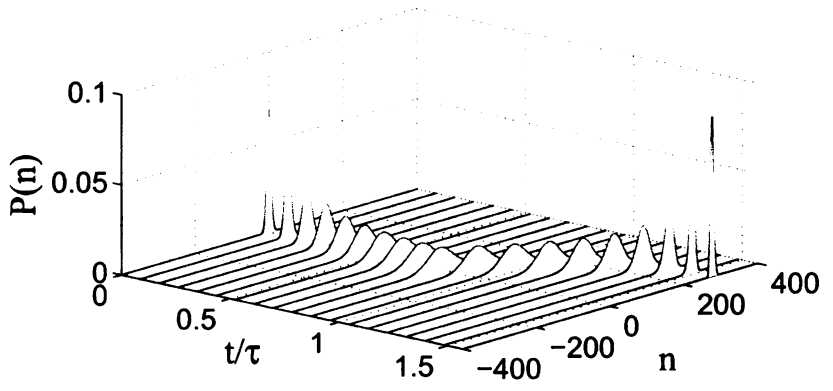

(a)

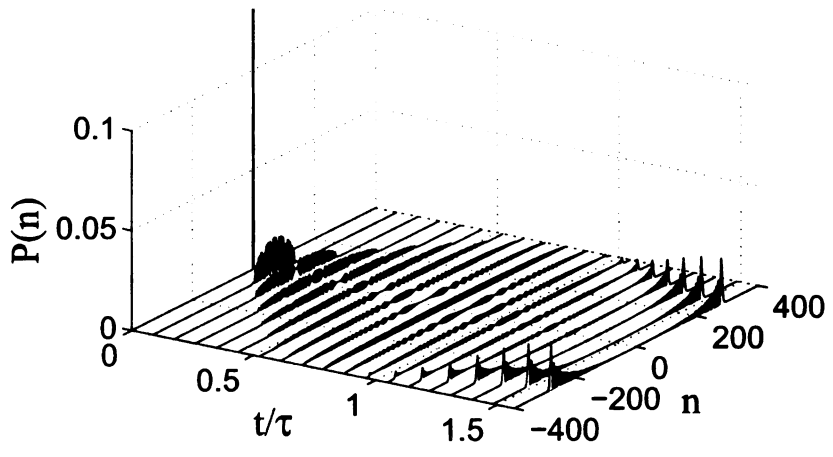

(b)

Figure 3.5: Probability packet dynamics of the double-well BEC system undergoing MZ interferometric measurement with $N = 800$ and a phase shift of $\theta = \pi/4$. Figure (a) and (b) are shown for an moderately number-squeezed and the PS input state, respectively. In figure, the process of phase imprinting, occurring at $t = \pi\tau/4$, is not shown.

propagation method, with a θ-dependent observable $\hat{\mu}(\theta)$, $\Delta\theta$ is estimated to be [252]

$$\Delta\phi = \left|\frac{d\mu(\theta)}{d\theta}\right|^{-1} \Delta\mu, \tag{3.14}$$

where $\mu(\theta) = \langle\hat{\mu}(\theta)\rangle$ is the expected value of $\hat{\mu}(\theta)$, and $\Delta\mu$ is the variance, given by

$$\Delta\mu = \sqrt{\langle\hat{\mu}^2\rangle - \mu^2}. \tag{3.15}$$

This method, while widely used in the field of quantum interferometry, turns out to be valid only if the output distribution is a single Gaussian [244, 246, 119]. In more general cases where the output is not a Gaussian, the error propagation method gives imprecise, sometimes incorrect, predictions. For example, the NOON-state interferometer, employing the maximally-entangled two-mode state of $\frac{1}{\sqrt{2}}(|N,0\rangle\rangle + |N,0\rangle)$, is predicted to yield a HS phase resolution for any θ by the error propagation method [24, 26, 254, 240, 241, 180, 242]. Yet as lately revealed [250, 244], for such a interferometer, phase shifts of θ and $\theta + 2k\pi/N$ (k is a nonzero integer) always lead to identical experimental outcomes, due to the existence of N-periods in the interference pattern. Thus, phase shifts of this class are then indistinguishable, giving rise to a phase uncertainty of 2π. An arbitrary phase θ can be determined within an uncertainty $\Delta\theta \sim 1/N$ only if θ is already known to be within a interval of period $2\pi/N$, an evident paradox.

A improved measure of phase uncertainty, applying to arbitrary interferometer outputs, is provide by the Bayesian analysis [247]. In this approach, we seek to determine the conditional phase probability $P(\phi|\mu_i)$, for a given measurement result μ_i. $P(\phi|\mu_i)$ is indirectly obtained using Bayes theorem, via

$$P(\phi|\mu_i) = \frac{P(\mu_i|\phi)P(\phi)}{P(\mu_i)}, \tag{3.16}$$

where $P(\mu_i|\phi)$ is the probability distribution of interferometer output in presence of a phase shift ϕ, and can be calculated directly using input-output formalism (3.8). $P(\mu_i)$ and $P(\phi)$ represent priori information on the distributions of μ_i and ϕ, *before* the phase measurement. Restricting the unknown phase to be in $[-\pi/2, \pi/2]$, in the case of no priori information, $P(\phi) = H(\pi/2 - |\theta|)$, where $H(x)$ is the Heaviside step function for x. $P(\mu_i)$ is then determined by normalization to satisfy $\int_{-\pi/2}^{\pi/2} P(\phi|\mu_i)P(\mu_i)d\phi = 1$, resulting in

$$P(\phi|\mu_i) = \frac{P(\mu_i|\phi)P(\phi)}{\int P(\mu_i|\phi')P(\phi')d\phi'}. \tag{3.17}$$

With $P(\phi|\mu_i)$, an experimenter can then perform phase estimation upon a measured result μ_i. For example, the unknown phase θ can be estimated to be the most likely value $\phi_{\max}$, for which $P(\phi|\mu_i)$ is maximized. The phase uncertainty $\Delta\theta$ is then given by confidence interval. Or if $P(\phi|\mu_i)$ is singly peaked, θ can also be estimated by the mean value of $\bar{\phi}$, where $\bar{\phi} = \int P(\phi|\mu_i)\phi d\phi$. The uncertainty can then be given by the RMS variance, with $\Delta\theta = \sqrt{\int P(\phi|\mu_i)\phi^2 d\phi - \bar{\phi}^2}$.

In order to theoretically evaluate the performance of an interferometer, however, we must take into account the fact that the measurement result, μ_i, is a random outcome obeying the quantum probability $P(\mu_i|\theta)$. This requires to average over all possible outcomes to obtain a statistical mean phase distribution. For a phase θ, such a distribution, namely the phase density, is given by

$$\begin{aligned} P(\phi|\theta) &= \sum_i P(\phi|\mu_i)P(\mu_i|\theta), \\ &= \sum_i \frac{P(\mu_i|\phi)P(\phi)P(\mu_i|\theta)}{\int P(\mu_i|\phi')P(\phi')d\phi'} \end{aligned} \tag{3.18}$$

Clearly, this phase density characterizes the probability of estimating a *true* phase θ to be ϕ. From here, the phase uncertainty can be estimated by the confidence

interval,

$$\int_{\mathrm{Max}(0,\theta-\Delta\theta)}^{\mathrm{Min}(\pi/2,\theta+\Delta\theta)} P(\phi|\theta)d\phi = \epsilon, \tag{3.19}$$

where $\epsilon = 0.68, 0.95, 0.99$ correspond to a phase uncertainty at the confidence level of $68\%, 95\%$ and 99%, respectively.

In appendix 3.6, we use Bayesian analysis to evaluate two existing interferometric apparatuses emerging as prospective HS interferometers. One is the MZ interferometer with the PS input state. The other is a non-MZ interferometer built on QDFT. We find for the PS-state interferometer, while exhibiting HS sensitivity for a zero phase, the phase uncertainty blows up to worse than SQL when measuring a nonzero phase. Besides, such a state, in a superposition of two next-neighbor TF states, shall be difficult to be produced in experiments. In contrast, the QDFT-interferometer yields a phase uncertainty $\leq 7.47/N$ for any θ, and hence justifies itself as a HS phase meter. Yet, experimental implementations would require performing quantum computation over a large number of qubits, which is extremely challenging at present or even in a foreseeable future.

3.4 Optimized Double-well interferometer

In observation of the lack of an efficient phase meter to measure arbitrarily unknown phases, in this section, we propose to optimize the level of number-squeezing level of input states for MZ interferometers, thus significantly elevating the measurement resolution to near HS for any nonzero phase. For experimental obtainability, the input states are restricted to be the ground state of the double-well BEC system, given in the form of GS state (3.13).

3.4.1 Squeezing optimization

As discussed in section 3.2.1, in the Bloch-sphere picture, a GS input state corresponds to an ellipse located at $J_z = J_y = 0$. The output state is obtained by a $-\theta$ rotation along J_y. In figure 3.6 (a), we give the quasi-probability distributions of a typical GS input and output state. Before we present numerical results from a rigorous Bayesian analysis, we first use linearized error propagation to provide an approximate analytical description of the interferometer performance. Such analysis shall be approximately valid given only moderate squeezing. We note that an analytical result is important for predicting the behavior at large N, where a numerical result is inaccessible. In the case of MZ interferometry, the phase uncertainty is estimated by evaluating $\Delta\theta = [\partial\langle\hat{J}_z\rangle/\partial\theta]^{-1}\Delta J_z$ at the interferometer output. For input states symmetric around $n = 0$, the expectation values at the output are related to those at the input via $\langle\hat{J}_z\rangle = \sin\theta\langle\hat{J}_x^i\rangle$ and $\Delta J_z = \sqrt{\cos^2\theta\Delta J_z^{i\,2} + \sin^2\theta\Delta J_x^{i\,2}}$. For GS states, $\langle\hat{J}_x^i\rangle \approx N/2$, and $\Delta J_z^i = \sigma$, which immediately leads to $\langle\hat{J}_z\rangle = N(\sin\theta)/2$. In figure 3.6 (c) we see that $\Delta J_x^i \approx N/2 - \sqrt{N^2/4 - \Delta J_y^{i\,2}}$. Since GS state is a minimum uncertainty state with $\Delta J_y^i \Delta J_z^i = \langle\hat{J}_x^i\rangle/2$, we see that $\Delta J_y^i = N/4\sigma$. This leads to $\Delta J_x^i = \alpha N/\sigma^2$, with $\alpha \approx 0.06$. Exact numerical calculations verify this analytic form for $1 \ll \sigma \ll \sqrt{N}/2$, as shown in figure 1(d), but with $\alpha = 0.09$. Inserting these results into the error-propagation formula, we find

$$\Delta\theta \approx \frac{2\sigma}{N}\sqrt{1 + \left[\frac{0.09N\tan\theta}{\sigma^3}\right]^2}. \tag{3.20}$$

The TF and PS states roughly correspond to a fixed $\sigma \lesssim 1$, resulting in $\lim_{N\to\infty}\Delta\theta = .18\tan\theta/\sigma^2$, which quickly becomes saturated to an N-independent constant for $\theta \gg 1/N$, a result we have verified numerically with exact Bayesian calculations in above section. On the other hand, if holding u fixed so that $\sigma \sim N^{1/4}$, the phase uncertainty scales as $\Delta\theta \sim 1/N^{3/4}$ for $\theta = 0$, as discussed in [255], and would even-

tually saturate to $\sim 1/\sqrt{N}$ for $\theta \neq 0$. Rather than holding σ or u fixed, we propose varying u and thus σ with N in order to minimize the phase variance. By setting $d\Delta\theta/d\sigma = 0$ we find

$$\sigma_{min}(\theta, N) \approx .503(N \tan|\theta|)^{1/3}, \tag{3.21}$$

$$\Delta\theta_{min}(\theta, N) \approx 1.23(\tan|\theta|)^{1/3}/N^{2/3} \tag{3.22}$$

From self-consistency, these expressions are valid only when

$$10/N \lesssim |\theta| \lesssim \tan^{-1}(.137\sqrt{N}) \approx \pi/2. \tag{3.23}$$

In figure 3.6 (b), we show the output states for optimized input states with various phases θ. From the figure, as θ increases in amplitude, less squeezing is optimal.

We now employ rigorous Bayesian analysis to quantify the phase uncertainty and validate our approximate analytic results, again assuming that $|\theta|$ is not too close to $\pi/2$. The error-propagation result (3.22) is close to the 68% confidence interval of $P(\phi|n)$ because the underlying number distribution of the optimized GS output state is approximated by the gaussian distribution

$$P(n|\theta) \approx \frac{1}{\sqrt{2\pi}\Delta n} \exp\left(-\frac{(n - N\sin\theta/2)^2}{2\Delta n^2}\right), \tag{3.24}$$

where

$$\Delta n = \sqrt{1 + \frac{\tan^2\theta}{2\tan^2\theta_a}}\sigma_{min}(\theta_a, N), \tag{3.25}$$

with θ being the unknown phase, and θ_a being the assumed phase used for optimization. This ansatz roughly agrees with the exact numerics, as shown in figure 3.8. Provided that $|\theta| \sim |\theta_a|$, the dependence on θ is weak, and we have $\Delta n \approx \sqrt{3/2}\sigma_{min}(\theta_a, N)$. This shows that the most-probable outcome is $\bar{n} = N\sin\theta/2$, which is sensitive to the sign of θ. Because Δn is only weakly dependent on θ, the

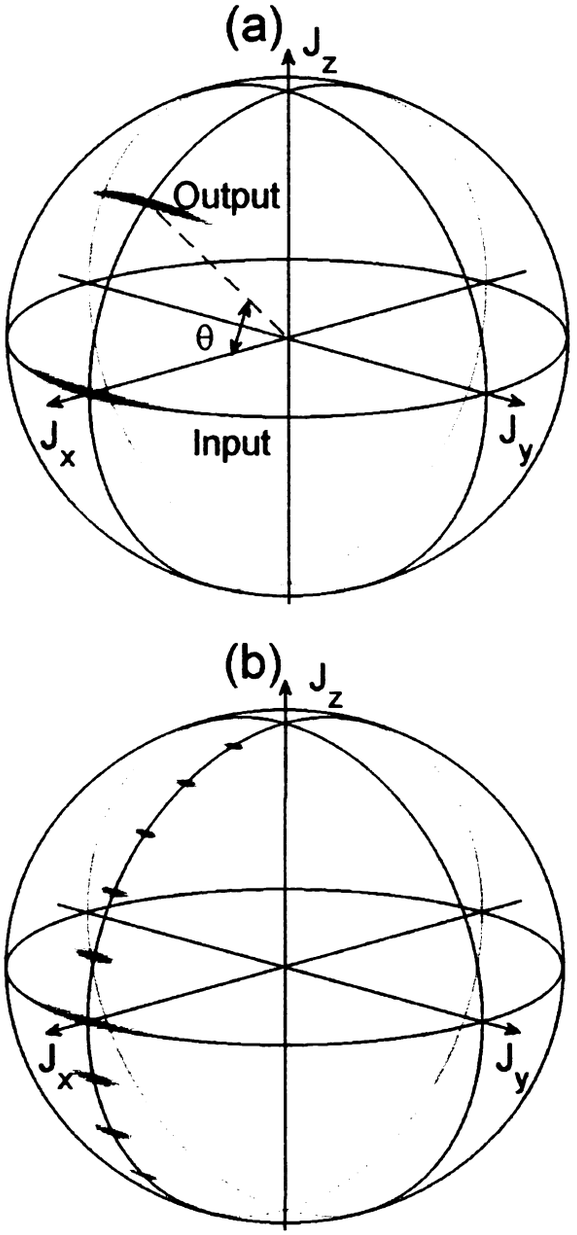

Figure 3.6: Bloch-sphere analysis of the MZI with a GS input state: (a) A typical GS state at input and output stages; (b) output states for optimized input states with $\theta = 0, \pm\frac{\pi}{12}, \pm\frac{\pi}{6}, \pm\frac{\pi}{4}, \pm\frac{\pi}{3}, \pm\frac{5\pi}{12}$; (c) (continued on the next page) geometric origin of the J_x input noise, ΔJ_x^i; (d) (continued on the next page) numerical results plotting $\Delta J_x^i/N$ versus σ on a log-log scale for three different N-values, validating the functional form of ΔJ_x^i derived geometrically from (c). The dashed vertical lines correspond to $\sigma = \frac{\sqrt{N}}{2}$, where ΔJ_x^i drops to zero.

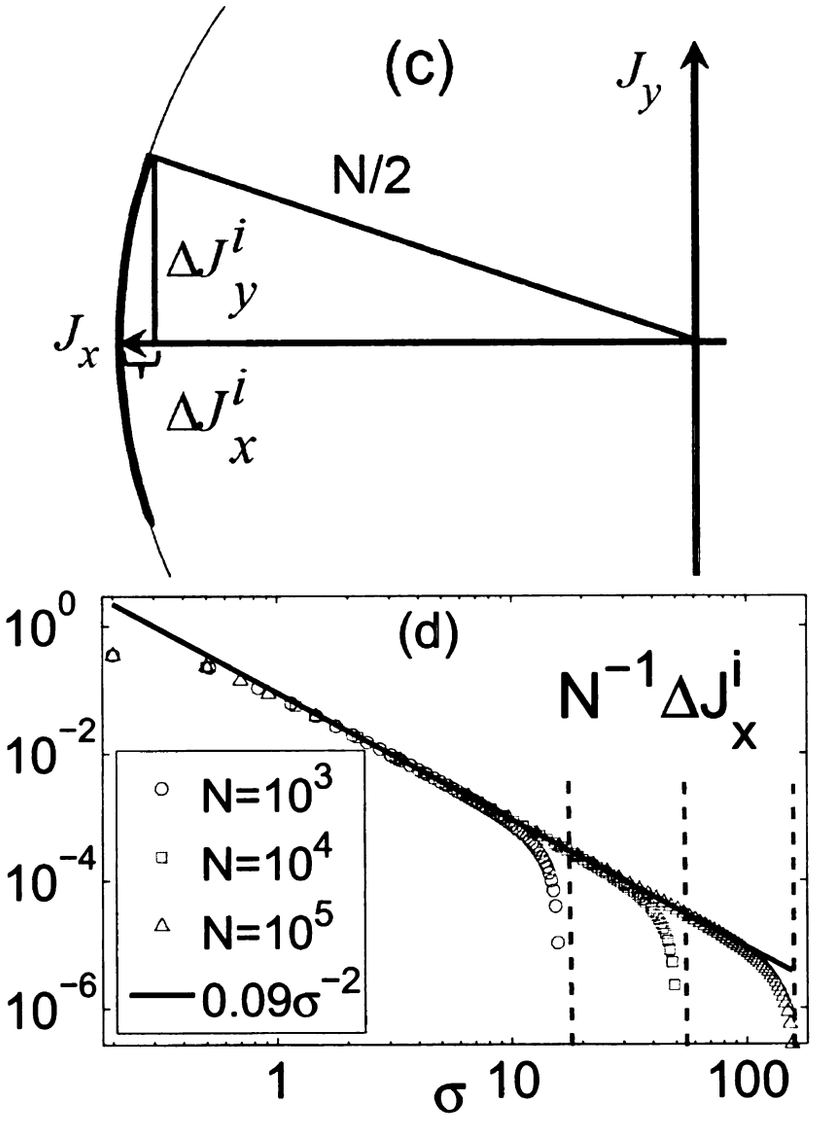

Figure 3.7: A continuation of Fig.3.6.

inverted distribution $P(\phi|n)$ will also be close to Gaussian in the small-angle regime, with width given by (3.22).

Using the Bayesian-analysis approach, together with the exact double-well ground-state, we numerically find u_{min}, the value of U/τ which minimizes the phase uncertainty. In figure 3.9 (a) and (b), we plot phase densities of optimized double-well interferometer for $\theta = 0$ and $\pi/4$. In both cases, the phase density exhibits a narrow and sharp peak, indicating a small phase uncertainty. Moreover, as N increases from 100 to 1000, the peak is significantly narrowed, leading to a significant reduction in the phase uncertainty. This is in contrast to the MZ interferometer with a PS input showing in figure 3.13 in the appendix, where the phase density almost keeps unchanged as N increases, which eventually gives rise to a constant, N-independent phase uncertainty. In figure 3.10 (a), we plot the corresponding $\sigma_{min} = \sigma(u_{min})$ as a function of N for several θs. Also shown is a least-squares fit to the $N > 10^3$ data (including many data points not shown explicitly) to the analytic form (3.21), giving

$$\sigma_{min}(\theta, N) = \begin{cases} 1.00, & |\theta| < 10/N; \\ 0.45(N \tan|\theta|)^{1/3}, & |\theta| > 10/N, \end{cases} \tag{3.26}$$

in good agreement with our analytical result. Inverting Eq. (3.26) leads to

$$u_{min}(\theta, N) = \begin{cases} \frac{N}{16} - \frac{1}{N}, & |\theta| < 10/N; \\ \frac{1.52}{(\tan|\theta|)^{4/3} N^{1/3}} - \frac{1}{N}, & |\theta| > 10/N. \end{cases} \tag{3.27}$$

In Fig. 3.10 (b) we plot the corresponding minimized $\Delta\theta_{min}$ versus N for several phases, achieved by setting $\sigma = \sigma_{min}(\theta, N)$. Again fitting the $N > 10^3$ data to the

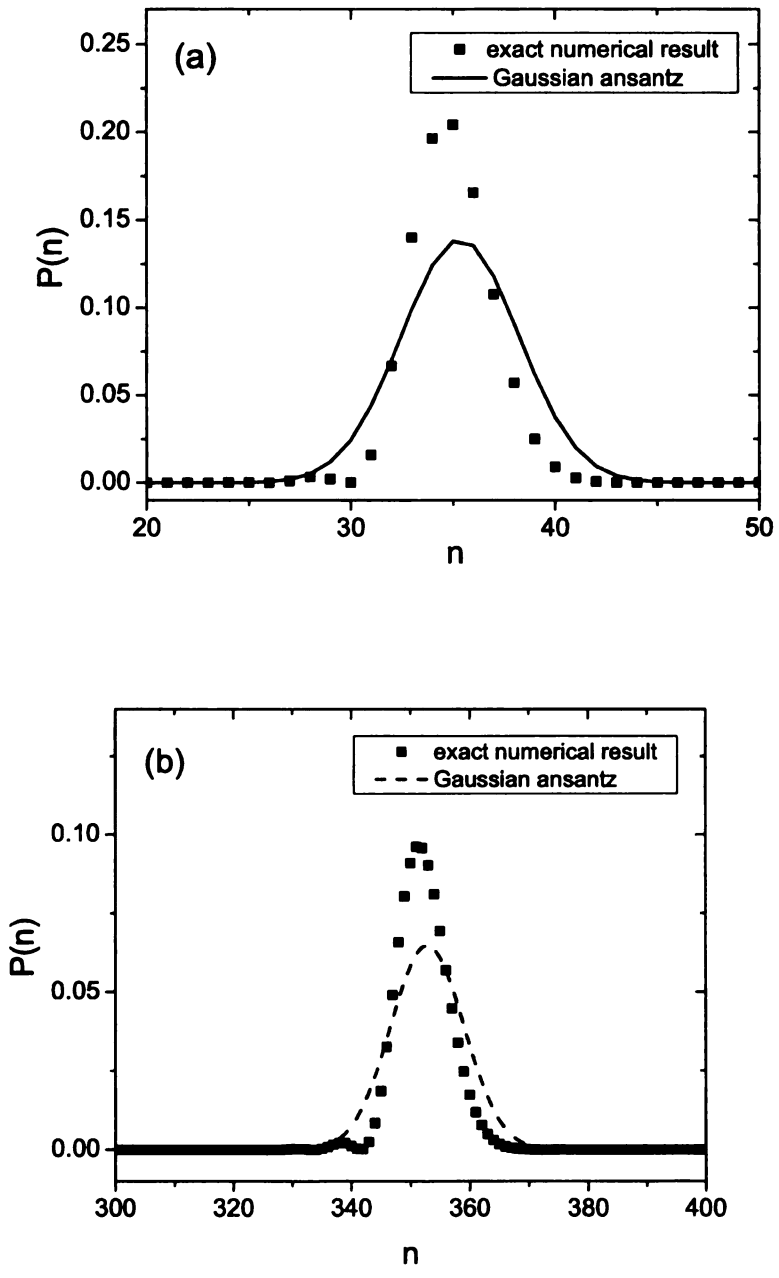

Figure 3.8: The probability distribution of optimized double-well interferometer output for $\theta = \theta_a = \pi/4$, where figure (a) and (b) are for $N = 100$ and 1000, respectively. In both figures, scatters are exact results from numeric calculation, while solid lines represent the Gaussian distribution (3.24).

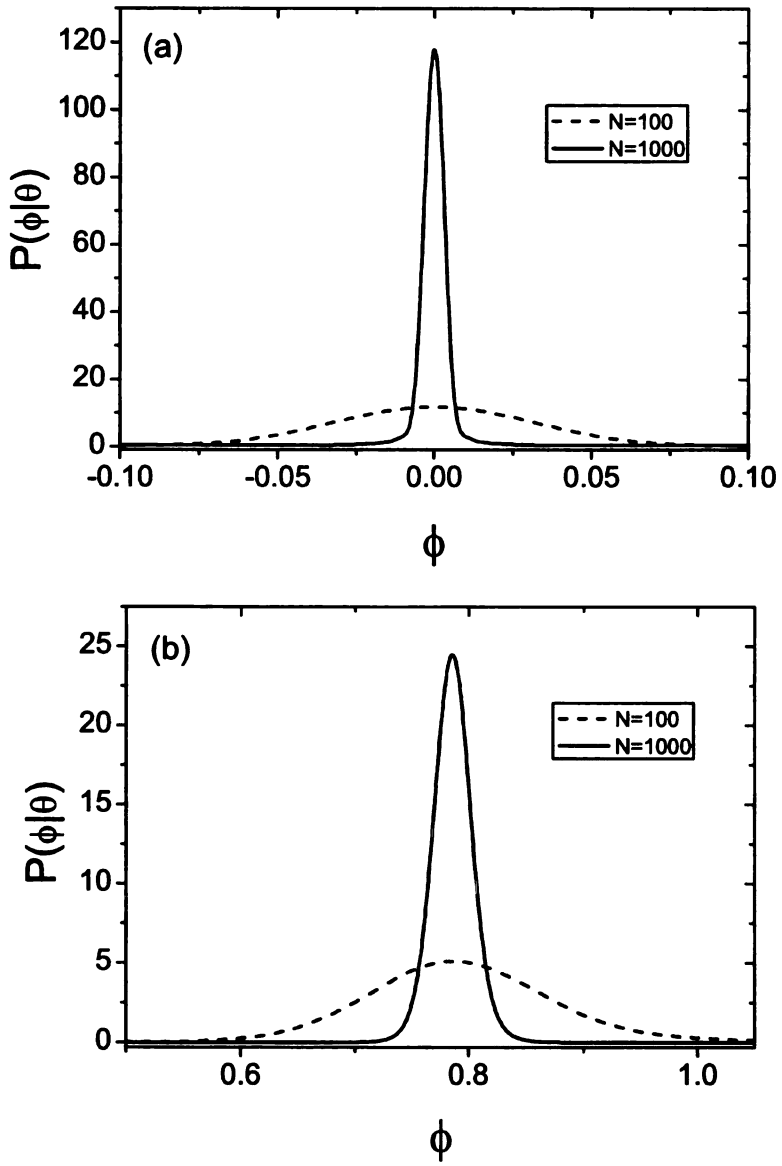

Figure 3.9: The phase density of optimized double-well interferometer, where figure (a) and (b) are for $\theta = 0$ and $\pi/4$, respectively. In both figures the dashed and solid lines are each for $N = 100$ and $N = 1000$.

analytic form of (3.22), we find

$$\Delta\theta_{min}(\theta, N) = \begin{cases} 3.50/N, & |\theta| < 10/N; \\ 1.63(\tan|\theta|)^{1/3}/N^{2/3}, & |\theta| > 10/N. \end{cases} \tag{3.28}$$

The difference between the prefactor here and (3.22) is primarily due to a factor of approximately $\sqrt{2}$ which comes from the definition of $P(\phi|\theta)$.

In practice, θ is not known a-priori, hence it is not clear what value for θ to use in determining $\sigma_{min}(\theta, N)$ via Eq. (3.26). If we assume prior knowledge of the form $P(\theta) \propto \exp[-(\theta - \theta_0)^2/2\Delta\theta_0^2]$, we should first remove θ_0 by adding θ_0/T to the tilt δ during phase acquisition, and then use $\sigma_{min}(\Delta\theta_0, N)$. After obtaining a measurement result n_1, the estimated uncertainty $\Delta\theta_1$ is then be determined via $\int_{\theta_1-\Delta\theta_1}^{\theta_1+\Delta\theta_1} d\theta' P(\theta'|n_1)$, with $P(\theta'|n_1)$ being given by Bayes theorem. This will result in $\Delta\theta_1 \sim \Delta\theta_{min}(\Delta\theta_0, N)$. Based on Eq. (3.28), this uncertainty appears to scale only as $N^{-2/3}$, only a slight improvement of $N^{1/6}$ over the SQL. However, in many applications requiring high precision, the phases are very small, in which case the phase uncertainty can be reduced considerably due to the explicit phase dependence in (3.28). This is in contrast to a shot-noise-limited interferometer, where $\Delta\theta = 1/\sqrt{N}$ for all θs not too close to $\pm\pi/2$. The explicit theta-dependence in the optimized scheme is due to the fact that stronger number-squeezing can be tolerated at smaller angles before the $\hat{J}_x^i$ noise becomes detrimental. For example, if the phase is known to be smaller than $1/\sqrt{N}$, we have $\Delta\theta_{min} \leq 1.63/N^{5/6}$, which is now an $N^{1/3}$ improvement over the SQL. As can be seen from Eq. (3.28), a maximum sensitivity of $3.5/N$ can be achieved for $|\theta| < 10/N$, which is true Heisenberg scaling.

3.4.2 Adaptive measurements

In fact, almost any phase between $-\pi/2$ and $\pi/2$ can be measured at the maximum precision of $3.5/N$ if the present scheme is combined with multiple adaptive

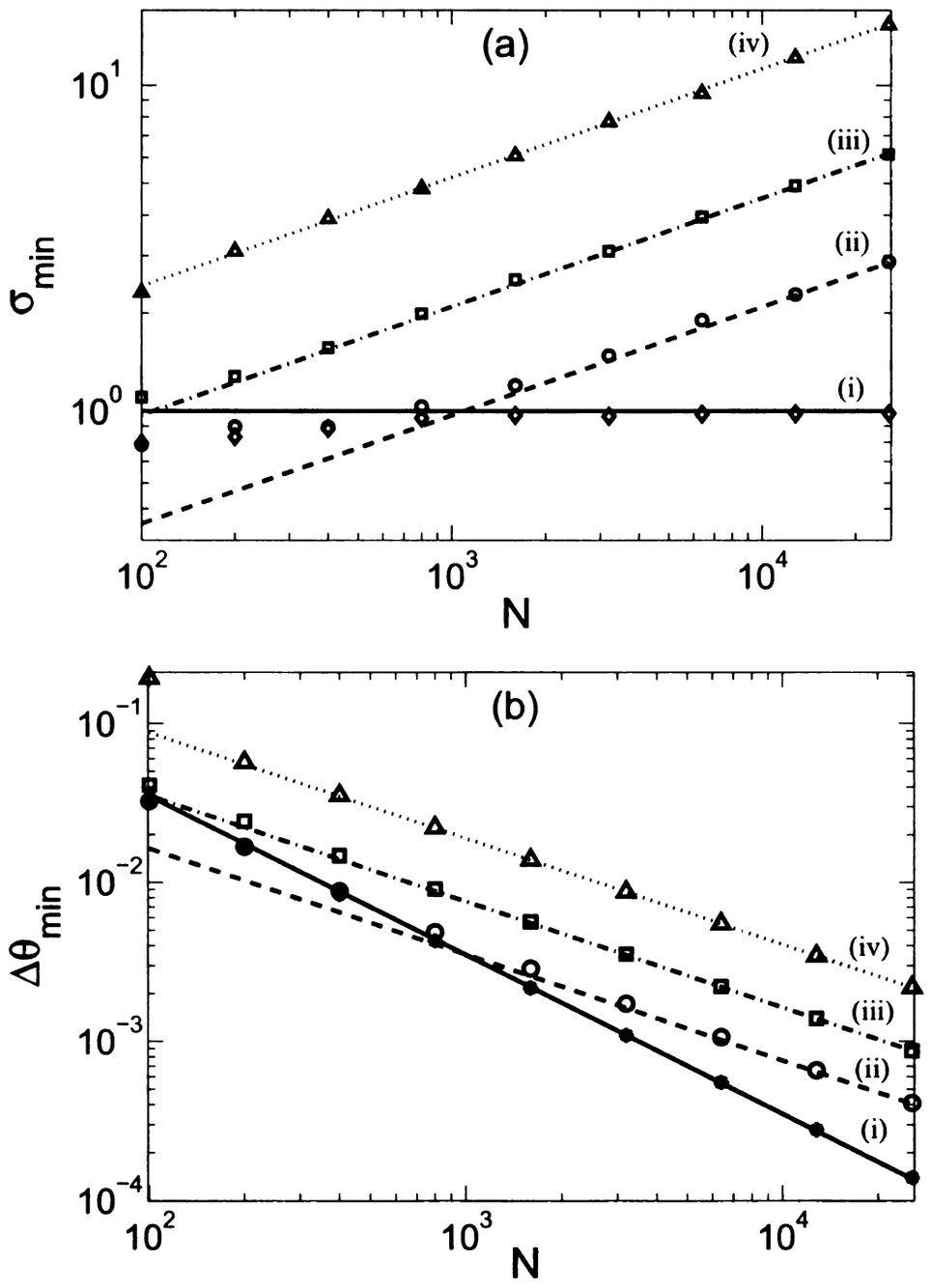

Figure 3.10: Figure (a): Optimal width σ_{min} versus N for different θ; (b): corresponding minimized phase uncertainty $\Delta\theta_{min}$. In both figures, from (i) to (iv) the interferometer phases are $\theta = 0,\ 0.01,\ 0.1$ and 1. The data points represent numerical results from strict Bayesian analysis using the exact ground states of a double-well BEC, while the straight lines represent the asymptotical forms of Eq.(3.26) and Eq.(3.28), respectively.

measurements [157, 238]. After the first measurement as described above, we can again rebalance the interferometer by adding θ_1/T to the tilt, followed by a second measurement with $\sigma_2 = \sigma_{min}(\Delta\theta_1, N)$, with result n_2. The Bayesian distribution for θ_2 will then be approximately

$$P(\theta_2|n_2, n_1) \propto \exp[-(\theta_2 - \bar{\theta}_2)^2/2y_2^2], \tag{3.29}$$

where $\bar{\theta}_j = \sin^{-1}(2n_j/N)$ and $1/y_j^2 = \sum_{k=0}^{j} 1/\Delta\theta_k^2$. Since $\Delta\theta_j$ is much smaller than $\Delta\theta_{j-1}$ we can say $y_j \approx \Delta\theta_j \sim \Delta\theta_{min}(\Delta\theta_{j-1}, N)$. In other words, since the distribution after a measurement is much narrower than the previous distribution, multiplying the distributions has little effect, so that the final uncertainty is effectively determined by the resolution of the final measurement alone. After M iterations, with $\sigma_j = \sigma_{min}(\Delta\theta_{j-1}, N) \approx 0.57\,(N \tan\Delta\theta_0/2.1)^{3^{-j}}$, we find

$$\Delta\theta_M \sim \frac{2.1}{N}\left(\frac{N\tan\Delta\theta_0}{2.1}\right)^{3^{-M}}. \tag{3.30}$$

While the above expressions are good estimates of the expected behavior, in practice each σ_j and $\Delta\theta_j$ would be computed exactly by applying Bayes theorem after each measurement. This procedure should be repeated only until $\Delta\theta_M \lesssim 10/N$, after which an addition measurement will push the phase uncertainty to $3.5/N$. The final measurement is then made using the GS state with $\sigma = 1$, which lies at the edge of the maximally-squeezed Fock regime defined by $\sigma \ll 1$. Thus an arbitrary phase can be measured at $3.5/N$ precision with $M + 1$ measurements in total. Setting $\Delta\theta_M = 10/N$, and solving for M gives

$$M \approx 0.9\ln(\ln(N\tan\Delta\theta_0/2.1)) - 0.4, \tag{3.31}$$

where again this is just an estimate subject to run-to-run fluctuations. For $\theta_r = \pi/3$ and $N = 10^4$, $M = 1.6$, i.e. only 2 or 3 total measurements will be required. For $N = 10^{12}$, $M = 2.6$, requiring 3 or 4 measurements. Even for $\Delta\theta_0$ extremely close to $\pi/2$, M remains small, for example, $\Delta\theta_0 = \pi/2 - 10^{-10}$ gives $M \approx 2.7$ for $N = 10^4$, and $M \approx 3.1$ for $N = 10^{12}$. Hence, for arbitrary phases in $(-\pi/2, \pi/2)$, our interferometer converges quickly to the $3.5/N$ precision within a few measurements, regardless of N. The final experimental value for the initial unknown phase is then $\theta = \sum_{j=1}^{M+1} \theta_j$ with a quantum-limited uncertainty of $\Delta\theta = 3.5/N$. The total number of atoms used to obtain this precision is $N_{tot} = (M+1)N$. For large enough N, we can approximate $\ln(N_{tot}/2(M+1)) \approx \ln(N_{tot})$, so that $M + 1 \approx 0.9 \ln(\ln(N_{tot} \tan \Delta\theta_0)) + 0.6$, which leads to the asymptotic scaling law

$$\Delta\theta \approx (2.1 + 3.2 \ln(\ln(N_{tot} \tan \Delta\theta_0)))/N_{tot}. \tag{3.32}$$

That the scaling law should depend on the initial phase interval has been previously pointed out [256]. As our final approximation effectively overestimates N_{tot}, the uncertainty approaches (3.32) from *below* as N increases.

In order to verify the accuracy of Eq. (3.31), as well as determine the magnitude of the run-to-run fluctuations, we have carried out exact Monte-Carlo simulations of many measurements of the phase $\pi/6$, with an initial uncertainty $\Delta\theta_0 = \pi/3$. During each simulation run, the measurement outcome was randomly selected according to the output distribution, and the phase information was determined numerically via Bayes theorem. The prescribed measure-rebalance process was iterated until the estimated phase uncertainty reaches $3.5/N$. Figure 3.11 shows the percentage of runs which attain the desired resolution on the $(M + 1)$th iteration, for two different N values, with 10^4 runs each. The averages are $\overline{M+1} = 2.2$ for $N = 500$, and 2.5 for 5000. Equation (3.31) gives 2.2 and 2.5 as well. The corresponding variances

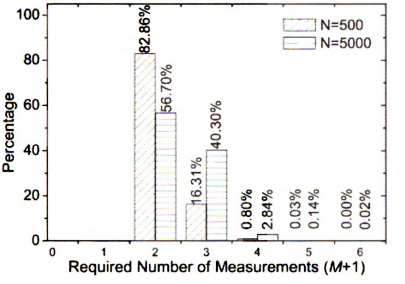

Figure 3.11: Monte-Carlo simulation results showing the percentage of runs which achieved the maximum precision of $3.5/N$ after $(M+1)$ measurements, plotted versus $(M+1)$.

$\Delta(M+1)$ are 0.4 and 0.6. We note that as the average approaches a half-integer value, the minimum possible variance approaches 0.5, because M is constrained to integer values. Thus the fluctuations are close to minimum allowed values.

For TF and PS states, adaptive measurement schemes are extremely inefficient. This is due in part to their inability to distinguish positive from negative phases, which makes rebalancing impossible. But even if this were overcome, the primary difficulty is that the phase-uncertainty is N-independent for large phases, so that $\sim N^2$ measurements are required to obtain $1/N$ precision. This results in $1/N_{tot}^{1/3}$ scaling, worse than SQL. To verify this, we perform pseudo Monte-Carlo simulation of a repeated adaptive measurements with the TF and PS state, with the following adaptive algorithm: repeated measurements are made at the phase θ, as well as $\theta + \pi/4$, with results for each measurement randomly drawn from a gaussian distribution with $\Delta\theta_{LB}(\theta)$ given by the fitting curves shown in figure 3.15 in the appendix. For each measurement, a phase distribution was generated, given by a gaussian centered at

the measurement with width $\Delta\theta_{fit}(\theta)$. The phase distributions for the θ and $\theta+\pi/4$ measurements are separately multiplied to generate two final distributions. Sufficient measurements are performed so that these distributions are separated by a distance larger than their widths. The order of the two peaks determines the sign, and the phase can be determined from the center of the θ distribution. This resulting phase is subtracted from the tilt, and the process is then repeated until a phase uncertainty of $3.5/N$ is obtained. We note that errors in determining the sign due to bad luck are self-corrected by the algorithm. This happens frequently and increases the number of measurements required. This error can be reduced by taking more measurements at each step to further separate the θ and $\theta+\pi/4$ peaks, with the result that the prefactor changes, but the scaling with N stays the same. The results are shown in figure 3.12, where we plot the average number of measurements versus particle number N, based on 10^4 simulations for each N-value. A least-squares fitting results in a scaling as N^2 for the TF state, $N^{1.94}$ for the PS state. For a comparison, a similar pseudo Monte Carlo simulation for the GS state is also shown, using instead the alternative algorithm described in last paragraph, as a GS interferometer is capable of distinguishing positive and negative phases. The agreement with Eq. (3.31) is shown to be fairly good. Exact simulations are shown for $N = 500$ and $N = 5000$, showing even better agreement with Eq. (3.31).

3.4.3 Experimental stability

The above discussions have assumed that the input state is optimally squeezed to width σ_{min}. A realistic input state, however, may deviate from σ_{min}, due to imprecise control over u and/or imprecise knowledge of N. A straightforward error analysis shows that our scheme is extremely robust against such uncertainties. The increase in the single-measurement phase uncertainty $\delta\Delta\theta$ due to fluctuations in u

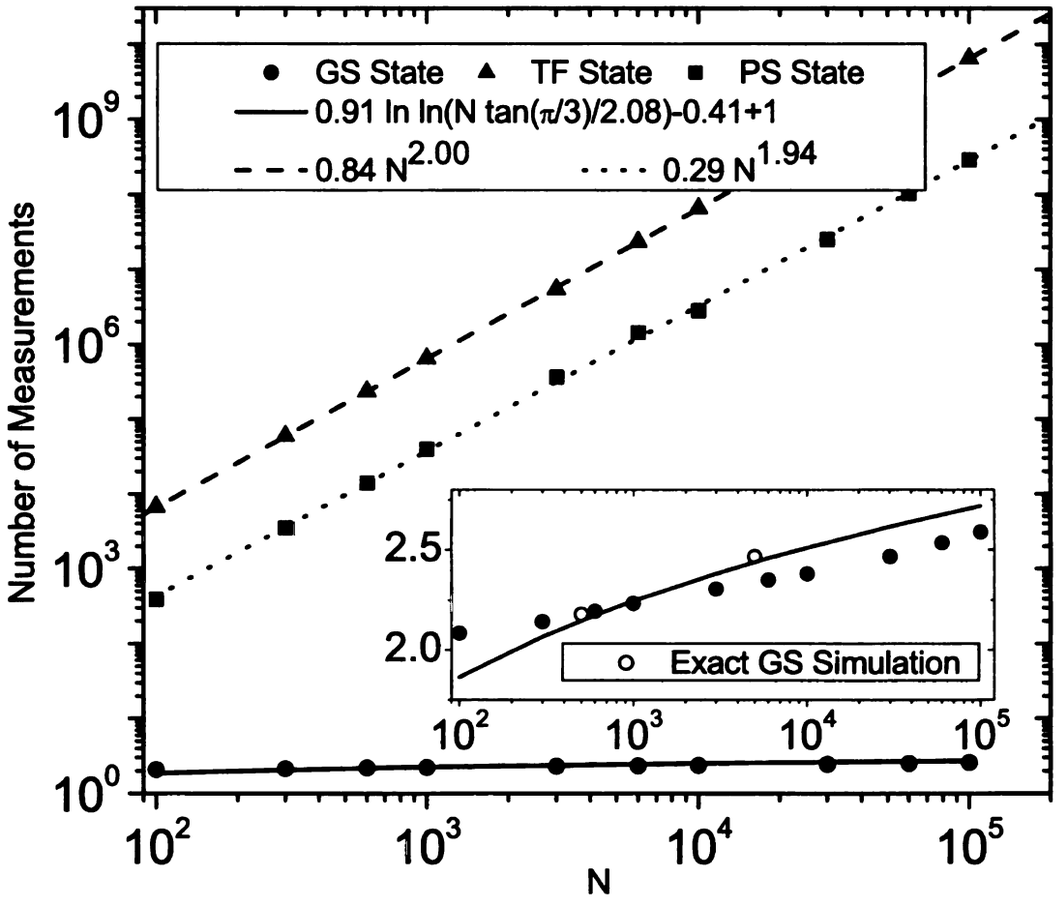

Figure 3.12: Pseudo Monte-Carlor simulation results of 10^4 runs. The true initial phase is $\pi/6$, and the a-priori phase interval is $[-\pi/3, \pi/3]$. Results are shown for the TF, PS, and GS states. In the inset, we see that the formula from Eq. (3.31) (with one added for the final measurement to go from $10/N$ to $3.5/N$) agrees fairly well with pseudo simulation results.

and N, using formula (3.20), is found to be

$$\delta\Delta\theta = \left|\frac{\partial\Delta\theta(N,u)}{\partial N}\right|\delta N + \left|\frac{\partial^2\Delta\theta(N,u)}{\partial^2 u}\right|\frac{1}{2}\delta u^2 \tag{3.33}$$

evaluated at $u = u_{min}$. The scaling with δu^2 reflects the fact that $u = u_{min}$ is a local minimum with respect to the phase uncertainty. This gives

$$\frac{\delta\Delta\theta}{\Delta\theta_{min}} = \frac{2}{3}\frac{\delta N}{N} + \frac{1}{8}\left(\frac{\delta u}{u_{min}}\right)^2, \tag{3.34}$$

so that a 10% variation in N leads to a 7% variation in the phase uncertainty, while even a 100% uncertainty in u only results in a 13% variation. For our purposes, these increases are essentially negligible, and are independent of the values of N or θ. Of course there are many other potential sources of error, e.g. the precision with which the tilt can be rebalanced, and the precision with which the scattering length can be set to zero during interferometer operation. Reaching the Heisenberg limit in a double-well BEC interferometer will clearly require major technological advances in many areas. Assuming that a level of precision significantly below the SQL is eventually obtained, the scheme we have developed will be the optimal method to obtain this precision, whether or not it is close to the Heisenberg limit.

3.5 Conclusion

To conclude this chapter, we have used the Bayesian analysis to evaluate the performance of important existing interferometers for measuring non-zero phases. The MZ interferometer employ highly number-squeezed TF or PS state is shown to be worse than SQL, due to large quantum fluctuations in the interferometer output. The QDFT-based interferometer, on the other hand, can measure arbitrary phases at Heisenberg scaling. Yet the experimental implementation is extremely challenging.

Instead, we propose to use an adaptive GS-state scheme, which has three advantages over previously discussed MZ interferometry schemes. It (1) can readily be implemented in a double-well BEC system, (2) can achieve a resolution well beyond the SQL for a wide range of phases with a single measurement, and (3) quickly converges to a final precision $\approx 10/N_{tot}$ within only a few adaptive measurements. In this way, we have realized a Heisenberg-scaling interferometer for measuring arbitrary phase, which could be realized in nowaday or near-future laboratories.

3.6 Extension: Bayesian analysis of PS and QDFT interferometers

3.6.1 MZ interferometer with PS input

Using Bayesian analysis, Hradil *et.al* first examined the sensitivity of a MZ interferomter with twin Fock state $|N/2, N/2\rangle$ as input [244]. Surprisingly, such interferometry turned out to have a phase sensitivity that is even worse than the shot noise. The reason is that while the phase density distribution $P(\phi|\theta)$ does have a narrow, N-sensitive central peak,the probability is majorly distributed among broad, N-insensitive tails outside the central peak region. As a consequence, its phase uncertainty, as determined by confidence interval (3.19), will exceed that of a SQL interferometer with coherent input, which yields a wider central peak but no such tails. To address this problem, Pezzé *et.al* proposed to use an input state of the form $(|N/2+1, |N/2-1\rangle + |N/2-1, |N/2+1\rangle)/\sqrt{2}$, in order to destructively cancel out those tails [119]. Indeed, the tails are successfully eliminated at $\theta = 0$ and a Heisenberg-limited *phase switch* is discovered. For a single measurement, such is among the best sensitivities of a MZ interferometer having been reported so far.

The problem with PS-state interferometry is, in the first place, that it is ex-

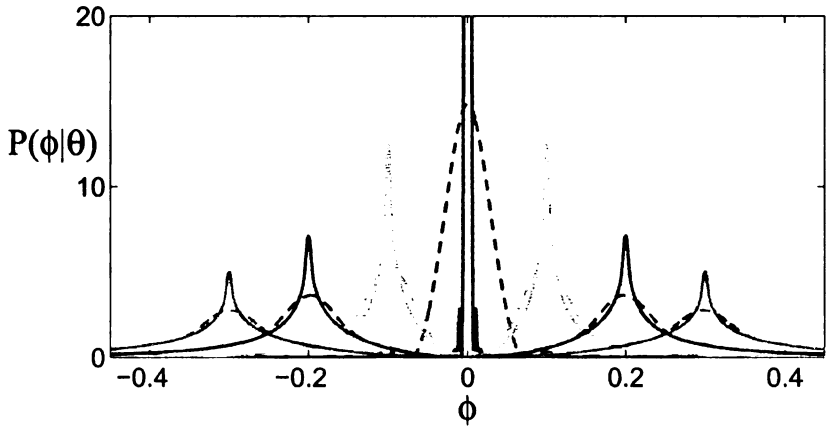

Figure 3.13: Phase density distribution $P(\phi|\theta)$ for Mach-Zehnder interferometer with the PS input. Here $P(\phi|\theta = 0)$ is a single peak located at $\phi = 0$, whereas, for $\theta = 0.1, 0.2, 0.3$, $P(\phi|\theta)$ is split into twin peaks at around $\phi = \pm 0.1, \pm 0.2, \pm 0.3$, respectively. For each θ, solid lines and dashed lines are corresponding to $N = 1000, 100$, respectively.

perimentally challenging to create such a PS input state. More importantly, even provided that the PS state can be prepared, it turns out that such a interferometer, while proven to be a HS phase switch, is in fact a worse-than-SQL *phase meter*. That's, as soon as θ deviates from zero, its phase density $P(\phi|\theta)$ behaves significantly differently from that of $\theta = 0$, as shown in Fig. 3.13. In figure, the phase density distribution at $\theta = 0$ is sharply peaked and N-sensitive, i.e., it dramatically shrinks as N increases. For nonzero θ, however, $P(\phi|\theta)$ is split into two symmetric packets around $\theta = 0$, each of which consists of dominating background bases. The symmetric pattern makes it unable to distinguish between positive and negative phases. The dominating bases are N-insensitive, resisting large even as N increases. Consequently, the phase uncertainty for nonzero phases, determined from confidence interval of $P(\phi|\theta)$, is expected to be bonded by a fixed, N-independent lower limit. This is shown clearly in Fig. 3.14, where we plot $\Delta\phi$ calculated from the absolute phase density distribution $P(|\phi| \; |\theta)$. In figure, at $\theta = 0$ the log-log show of $\Delta\phi$ v.s. N is a exact straight line, where we recover the previous result $\Delta\theta = 2.67/N$ reported in [119]. For nonzero phases, the behavior is significantly different. For instance, for small Ns, $\Delta\phi$ as of

$\theta = 0.01$ coincides with that of $\theta = 0$. Whereas as soon as N exceeds a critical value $N_{cr} = 100$, it deviates from the straight line and saturates to be flat. Similar phase-transition behaviors are found for $\Delta\phi$s at $\theta = 0.1, 0.001$, but at $N_{cr} = 10, 1000$ correspondingly. This phase transition is understood as follows. For $N < N_{cr}$, $P(\phi|\theta)$ is broad and dominated by peaks, resulting in a $\Delta\phi$ that is N-sensitive. While as N exceeds N_{cr}, although the peaks continue to shrink, the background bases remain constant and hence become dominating. The N-insensitivity of the bases gives rise to the saturation of $\Delta\phi$.

In Fig.3.15 we show the asymptotical value $\Delta\theta_{LB}$ as N goes infinity for various values of θ. At $\theta = 0$, $\Delta\theta_{LB} = 0$, due to that $\Delta\phi$ is infinitesimal as N increase. For $\theta \neq 0$, a good fit of $\Delta\theta_{LB}$ is found to be

$$\Delta\theta_{LB} = -0.45 + \exp(-0.8(\theta - 1)^2), \tag{3.35}$$

which in the small θ limit approaches 0.72θ. Also shown in figure is the asymptotical phase uncertainty for the TF state, which constantly lies above the PS curve.

Hence, for the PS interferometer the highest possible signal-to-noise ratio for a nonzero θ is given by $\Delta\theta_{LB}/\theta = 0.72$, regardless of N. In practice, in order to distinguish between two phases θ_1, θ_2, it requires in general

$$\theta_1 - \theta_2 > \Delta\theta_1 + \Delta\theta_2, \tag{3.36}$$

where we assume $\theta_1 > \theta_2 > 0$. For any N, this gives $\theta_1 > 6.1\theta_2$. That's, a phase shift can at the best be distinguished from ones whose amplitudes are at least six times greater. Evidently, such interferometer is unsuitable to measure an arbitrary phase.

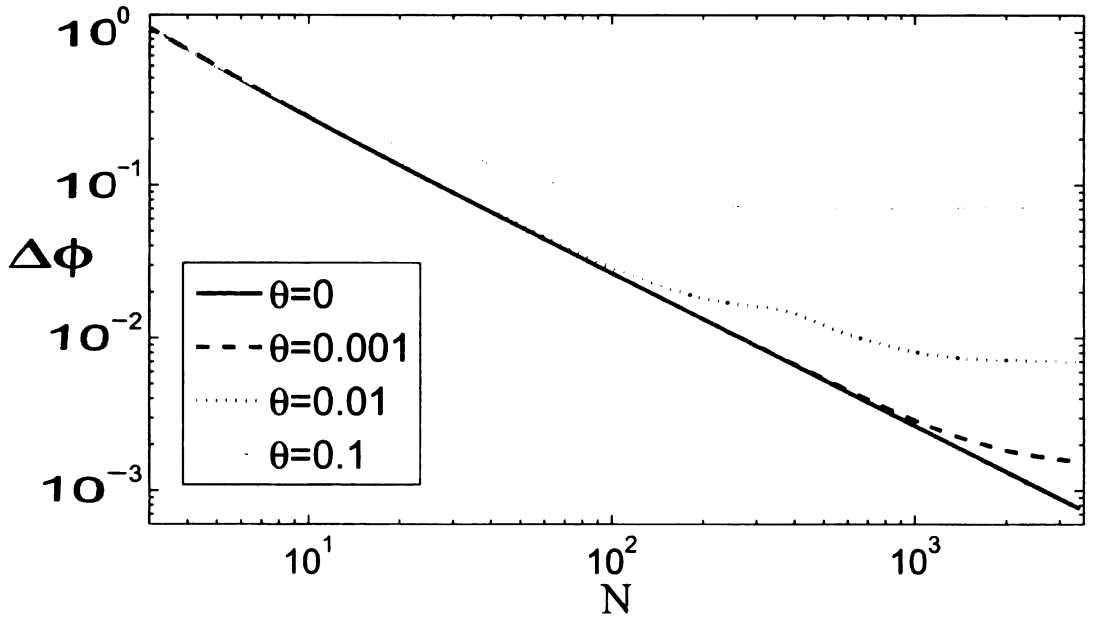

Figure 3.14: Phase uncertainty $\Delta\phi$ versus N for several θ. Here, because of the symmetric nature of the phase density, $\Delta\phi$ is determined by 68% confidence interval of the *absolute* phase distribution of $P(|\phi|\ |\theta)$.

3.6.2 QDFT-based interferometer

To the author's best knowledge, the QDFT-interferometer is so far the only truly HS phase meter under Bayesian analysis. To proceed with describing this interferometer, it is recalled that the action of a QDFT is a unitary mapping between two, say, $N+1$-dimension Hilbert spaces of basis $\{|k\rangle\}$ and $\{|\ell\rangle\}$, with the projection defined by $\langle \ell | k \rangle = \frac{1}{\sqrt{N+1}} e^{-i2\pi lk/(N+1)}$. That's, a QDFT operates on $|k\rangle$ via

$$QDFT : |k\rangle \longmapsto \frac{1}{\sqrt{N+1}} \sum_{l=0}^{N} e^{-i2\pi lk/(N+1)} |\ell\rangle. \tag{3.37}$$

A reverse QDFT, denoted as QDFT†, is defined in a conjugate manner. During a measurement, a single-Fock input state of $|0\rangle$ is first transformed to a superposition state of $\frac{1}{\sqrt{N+1}} \sum_{l=0}^{N} |\ell\rangle$ via QDFT. Then, the measuring phase θ is acquired, resulting in

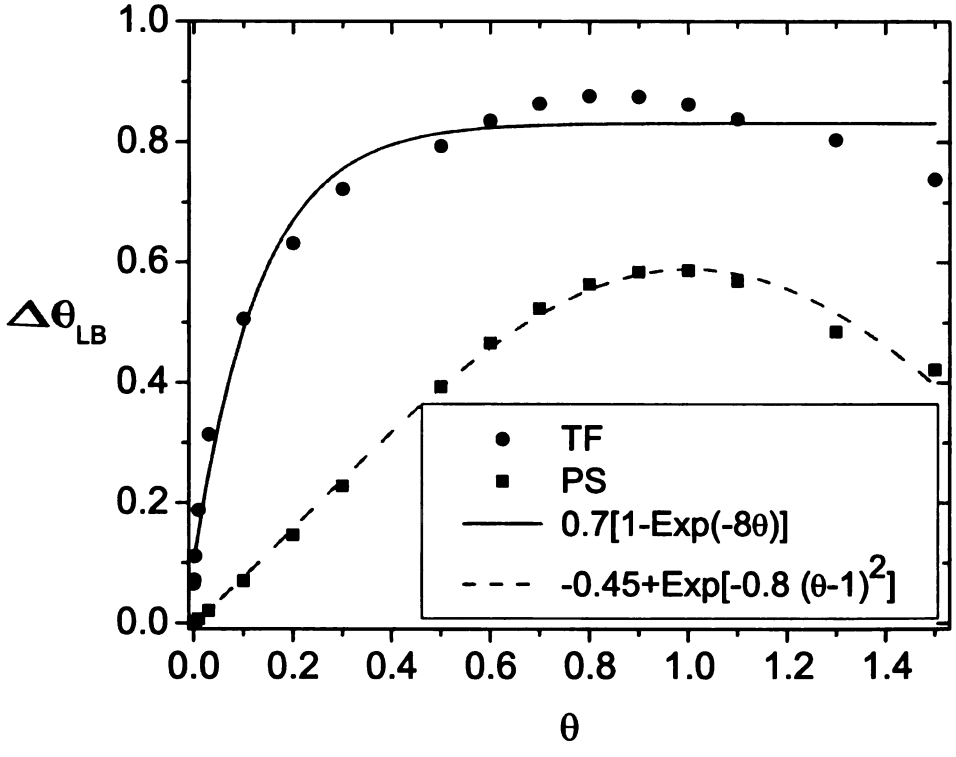

Figure 3.15: The phase uncertainty versus true phase in the limit $N \to \infty$, as determined by exact Bayesian analysis for large, but finite N. Results are shown for TF and PS states based on a single measurement. Approximate fitting functions are also shown.

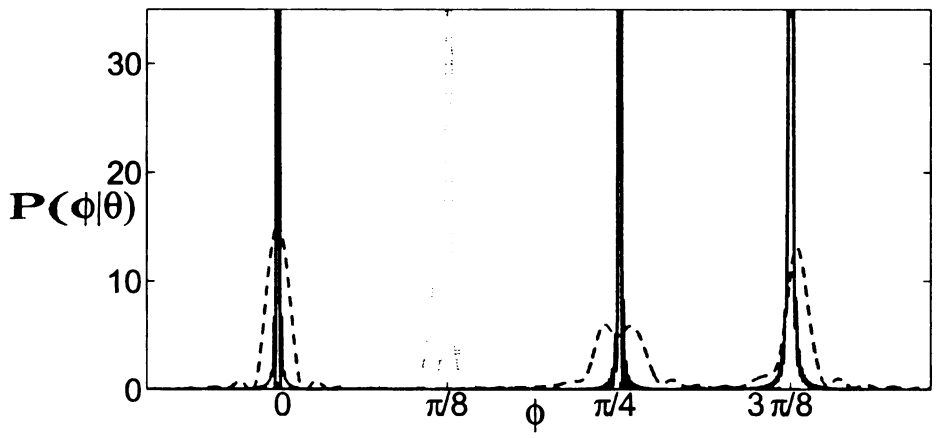

Figure 3.16: Phase distribution $P(\phi|\theta)$ for different θs in QDFT-based interferometer. **From** left to right, the peaks correspond to $\theta = 0, \pi/8, \pi/4, 3\pi/8$, where for each θ, **solid lines** and dashed lines are corresponding to $N = 1000, 100$, respectively.

$\frac{1}{\sqrt{N+1}} \sum_{l=0}^{N} e^{-i\theta l}|\ell\rangle$. Finally, a QDFT† is applied, upon which the interferometer **output** is obtained as

$$|\Psi_f\rangle = \sum_{k=0}^{N} c_k(\theta)|k\rangle, \tag{3.38}$$

where

$$c_k(\theta) = \frac{1}{\sqrt{N+1}} \frac{1 - e^{-i(N+1)\theta}}{1 - e^{i[2\pi k/(N+1)-\theta]}}. \tag{3.39}$$

The output probability distribution is then $P(k|\theta) = |c_k(\theta)|^2$. By measuring the **output** state on $\{|k\rangle\}$ basis, the phase density $P(\phi|\theta)$ is calculated via Bayesian ap**proach**. In Fig.3.16, we plot the obtained $P(\phi|\theta)$ for several θs. Compared to the PS **interferometry** in Fig. 3.13, here $P(\phi|\theta)$ is singly peaked for arbitrary θ, so that posi**tive and** negative phase shifts are now distinguishable. Further, all background bases **are eliminated**, and as N increases, the distribution width is dramatically reduced. **This** is a clear sign of HS phase precision.

To show that the phase uncertainty indeed yields $1/N$ scaling, in Fig. 3.17, we **plot** $\alpha = N\Delta\phi$ versus N. For any θ, for zero phase, $\alpha = 2.61$. While for nonzero

phases, α yields a periodical N-dependent value oscillating between $\alpha = 2.61$ and 7.47, as shown in figure (a). Such is a characteristic HS behavior. It is recalled that the PS interferometer yields a very close sensitivity of $\Delta\phi = 2.67/N$. To explain the oscillatory behavior of α, it is noticed that the probability distribution $P(k|\theta)$ in Eq.(3.38) is a periodical function of N, with a period of $T = 2\pi/\theta$. For N at $N_1 = 2k_0\pi/\theta - 1$ (assume both N_1 and k_0 are integers), $P(k|\theta)$ is reduced to

$$P(k|\theta) = \delta_{k,k_0}, \tag{3.40}$$

corresponding to a maximally sharped distribution. In contrast, at $N_2 = (2k_0 + 1)\pi/\theta - 1$, the probability distribution,

$$P(k|\theta) = \frac{2}{N+1}\cot[\frac{(k - k_0 - 1/2)\pi}{(N+1)}], \tag{3.41}$$

is maximally broadened. As a consequence, the phase density distribution is sharply peaked at $N = N_1$, but much wider at $N = N_2$. This leads to the periodicity of α as a function of N, with a period of $T = 2\pi/\theta$. This periodicity is clearly shown in a close view of figure (b), where for a nonzero phase θ, α exhibits a Sine-like behavior in N, with a period of $T = 16, 8, 16/3$ for $\theta = \pi/8, \pi/4, 3\pi/8$, as predicted by the formula (3.41).

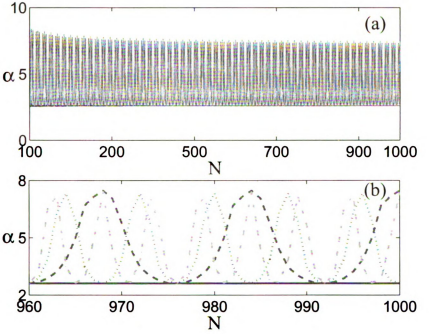

Figure 3.17: Plot of $\alpha = N\Delta\phi$ versus N for QDFT-interferometry, with N from 100 to 1000. Here figure (b) is a close view of figure (a) with $N \in [960, 1000]$. The solid, dashed, pointed and dashed-pointed lines in both figures correspond to $\theta = 0, \pi/8, \pi/4, 3\pi/8$, respectively.

Chapter 4

Resonant Matter Wave Amplification in Mean Field Theory

In this chapter, we study the four-wave mixing process involving two matter-waves of gaseous BEC's and two phase-locked lasers, widely recognized as the matter-wave amplification (MWA). We focus on searching for an optimal operational strategy for MWA, motivated by the goal to facilitate applications in the fields of matter-wave interferometry and quantum information processing. Specifically, we compare three different dynamical regimes, namely the off-resonance, overdamping and Rabi regime. Our results show that for a given laser intensity, the fastest amplification process is achieved when tuning the driving laser to be on-resonance, whereas previous studies are focused on the far-off resonance regime. In the meanwhile, the total atom loss is nearly identical in all dynamical regimes. Furthermore, due to the phase distortion by the ac-Stark shift, it turns out an off-resonance three-level system is unsuitable for state mapping between light and matter waves, while a resonant system is not subject to this problem. All these give rise to superiorities of resonant MWA processes. We

identify the laser depletion and spatial effect by comparing the quantum coupled-mode and semiclassical multi-mode theory.

The organization of this chapter is as follows. After an overview of the present work in section 4.1, we present the level scheme of the three-level Raman MWA system in section 4.2, . In section 4.3, we use the quantum few-mode theory to give a pellucid picture of the MWA dynamics. We then employ the semiclassical multi-mode theory in section 4.4, to develop a more 'physical' model incorporating the laser depletion and spatial effect. We finally conclude in section 4.5.

4.1 Introduction

To employ MWA for coherent amplifiers or as quantum information protocols, a major challenge, commonly existing with any quantum devices, is to overcome fast dephasing and/or decoherence whose rates usually scale as the square of matter-wave sizes. This naturally requires processing MWA in a shortest time window. In a prototypical three-level system, for N_1 and N_2 being atom numbers in pump 1 and the signal wave, the instant amplification rate is $P_e\Gamma_s N_1 N_2$. Here, Γ_s is the superradiance emission rate into the signal mode, and P_e is the fraction of pump atoms in the excited state, approximately given by $P_e = \frac{|\Omega|^2}{2|\Omega|^2+\Gamma_s^2+4\Delta^2}$, with Ω and Δ the Rabi frequency and detuning of the driving laser pump 2. In most MWA or superradiance experiments carried out with BECs, the driven laser is tuned far off-resonance with $\Delta \gg |\Omega|\Gamma_s$, so that the amplification rate is $\propto \frac{|\Omega|^2}{4\Delta^2}\Gamma_s$ [102, 101, 108, 112, 135]. If instead going on resonance, the rate then becomes $\propto \frac{|\Omega|^2}{2|\Omega|^2+\Gamma_s^2}\Gamma_s$, which is always higher than that the off-resonance case for any driving strength Ω. This suggests to employ resonant, rather than off-resonance, driving laser for a fast MWA process. Specifically, in case of $|\Omega| < \Gamma_s$, the system is in the overdamping dynamical regime with $P_e \ll 1$, for an amplification rate of $\propto \frac{|\Omega|^2}{\Gamma_s}$. The ultimately maximal rate

of $\propto \frac{1}{2}\Gamma_s$ is obtained in the Rabi regime with $|\Omega| > \Gamma_s$, where the excited state is macroscopically populated.

Ultimately, the source of the nonlinearity in the MWA dynamics is the atom-field dipole interaction, which becomes a quadratic nonlinearity in terms of atomic operators upon second-quantization of the matter-wave field. In the far-off resonance or overdamping regime, the electronically excited atomic state can be adiabatically eliminated, resulting in an effective cubic nonlinearity whereby MWA behaves as a standard four-wave mixing process. In the Rabi regime, however, the excited state is macroscopically populated, so that a fifth wave of the excited atomic state is required in order to describe the system dynamics. Thus asides from practical point of view, it is also of interest of fundamental nonlinear optics to study the collective response of atomic ensembles to a resonant driving. Physically, treating the excited level dynamically is equivalent to extending nonlinear susceptibility to infinite orders. In practice, the increased nonlinearity will potentially lead to nontrivial profiles of both light and matter waves, as having been observed in a recent Rayleigh superradiance experiment under near-resonant driving [117]. Besides, the scattered light in the Rabi regime yield a characteristic spectrum with two side bands, whose linewidth depends only on the optical depth of the samples [257]. On the other side, due to a larger amplification rate, the MWA under resonant driving can be processed in a time window shorter than any time scales related to atomic motion, environmental decoherence, or meanfield dephasing. This leaves the resonant MWA a relatively "pure" quantum system whose dynamics is solely determined by the light and matter coupling, thus providing the ease to engineer it as a useful quantum device. Theoretically, the problem of forward-light scattering of a BEC illuminated by resonant and short pulses has been addressed, under single-mode and undeleted pump approximations [258]. The work of this chapter is to go beyond these approximations and study important dynamical consequences.

Following these considerations, in this chapter, we study the MWA process under various dynamical circumstance ranging from the off-resonance, overdamping to Rabi regimes. For purposes of illustrating important underlying physics, we will focus on a simplest, prototypical three-level Raman system. For comparison, we employ both the quantum and semiclassical theories, the former of which adopts a common time-invariant spatial mode of the matter waves, while the later uses multi-mode treatment. Our results show that the two models predict similar population transfer dynamics in the beginning MWA stage, but then become divergent as the matter-wave modes, evaluated via semiclassical Maxwell-Schrödinger (SMS) equations, grow out of their initial shapes. The divergence turns out to be due to a combination of the laser depletion and spatial effect, both not included in the quantum coupled-mode (QCM) model. Interestingly, both the spatial mode evolution and the population transfer dynamics are found to be qualitatively similar in the off-resonance and Rabi regimes, only for the later occurring on a much short time scale. The population dynamics in both regimes is shown to agree well with QCM results before the time when half of pump 1 atoms are depleted, but undergoes a sudden slowdown afterwards. This suggests identical spatial effects on the two regimes. In the overdamping regime, however, the sudden slowdown does not appear, and the population dynamics is constantly following the quantum results. We attribute this behavior as a consequence of strong laser depletion effect. In addition, the relative phase between between pump 1 and the signal wave turns out to undergo ac-Stark shift and π-switching in the off-resonance and Rabi regime, but is preserved in the overdamping regime. This result provides the feasibility of using the present MWA system in the overdamping or Rabi regimes, but not in the off-resonance regime, as a quantum state-mapping device. Finally, the atom loss dynamics is shown to be inversely proportional to the optical depth, and is nearly independent of dynamical regimes.

4.2 The Model

A MWA process can be implemented with Raman or Rayleigh transitions, corresponding to the pump 1 and signal matter waves in different electronic or translational momentum states. Comparatively, while functioning on similar principles, the former requires spatial overlap of two spinor condensates in different hyperfine states, while the latter relies on forming a density grating of single-spin condensates. Thus a MWA employing Raman transitions is the only scheme that can generate an idler wave copropagating with pump 2. Besides, in a Rayleigh MWA process, multiple atomic recoil modes, aside from the seeded pump 1 and signal modes, would unavoidably appear due to a higher-order process involving the reabsorption of idler beam and stimulated re-emission into pump 2 [108, 127, 129]. In a Raman MWA, however, such processes can in general be efficiently suppressed by using appropriate level configuration [124, 131]. In this way, the Raman system can serve as a simplest, prototypical implementation of MWA, with clear physical interpretations of experimental observations. In practice, due to a higher controllability, a Raman MWA system is a better candidate for potential quantum information processes using light and matter waves. Based on the above considerations, in this chapter we will focus our discussions on the Raman MWA system.

The 'Λ' level diagram and schematic setup of a typical Raman MWA system is drawn in Fig. 4.1. Figure (a) shows a toy-model of the Λ level scheme, where spatially-overlapped pump 1 and signal waves, in ground $|1\rangle$ and $|2\rangle$ states, are coupled to the excited $|3\rangle$ level by pump 2 and idler light beams, respectively. Pump 2 can be off-resonance or on-resonance, depending on whether or not the detuning Δ is greater than both its Rabi-frequency Ω and the linewidth of $|3\rangle$ level. Both pump 1 and the signal wave are initially populated. During the MWA process, atoms in $|1\rangle$ are first driven to $|3\rangle$ by pump 2. Due to the quantum stimulation effect, $|3\rangle$ atoms will preferentially decay to the seeded $|2\rangle$ state, resulting in phase-coherence amplification

of the signal wave. This process is imparted by emitting an idler light beam along the phase matching direction, carrying phase information of the system.

A realistic example of the Λ-level scheme configured on the D1 transition in ^{137}Cs atoms is shown in Fig. 4.1 (b). The states $|1\rangle$ and $|2\rangle$ correspond to the ground hyperfine levels of $|F = 3, m_F = -3\rangle$ and $|F = 4, m_F = -3\rangle$, with a level spacing of 9.2 GHz between them. The excited $|3\rangle$ level corresponds to the $|F = 4, m_F = -4\rangle$ hyperfine level. Both pump 2 and the idler beam are σ^- polarized, and are different in frequency by the ground hyperfine splitting of 9.2 GHz. Two possible side transitions in this level scheme, including exciting $|1\rangle$ atoms by the idler beam or exciting $|2\rangle$ atoms by pump 2, are plotted in figure (b) with dashed lines. They are off-resonance by amounts of $9.2 - \Delta$ GHz and $9.2 + \Delta$ GHz, and can thus be strongly suppressed, leaving an effective Λ MWA system. Within Alkaline atoms, a feasible configuration is similarly found in Rubidium, but not in Sodium due a smaller ground hyperfine splitting.

The schematic setup employing $\hat{z}$-copropagating pump 2 and idler beams is shown in figure 4.1 (c). Both beams are σ^--polarized along the $\frac{1}{\sqrt{2}}(\hat{x} - i\hat{y})$ direction. They are distinguishable in that their frequency difference is greater than each's linewidth, as is the case for Cs and Rb atoms. This co-propagation arrangement is different from the commonly used end-fire configuration where pump 2 and idler beams are along perpendicular propagating directions [102, 108, 112]. Comparatively, the laser depletion effect is thus expected to be stronger in our scheme. On the other hand, here the recoil momentum of $|2\rangle$ atoms, which is of the order of 10 m^{-1}, is effectively zero in that it is much smaller than the typical momentum dispersion of $\sim 10^4$ m^{-4} for condensates. This unique feature allows performing MWA with stationary matter waves, which may benefit applications such as state mapping between light and matter waves.

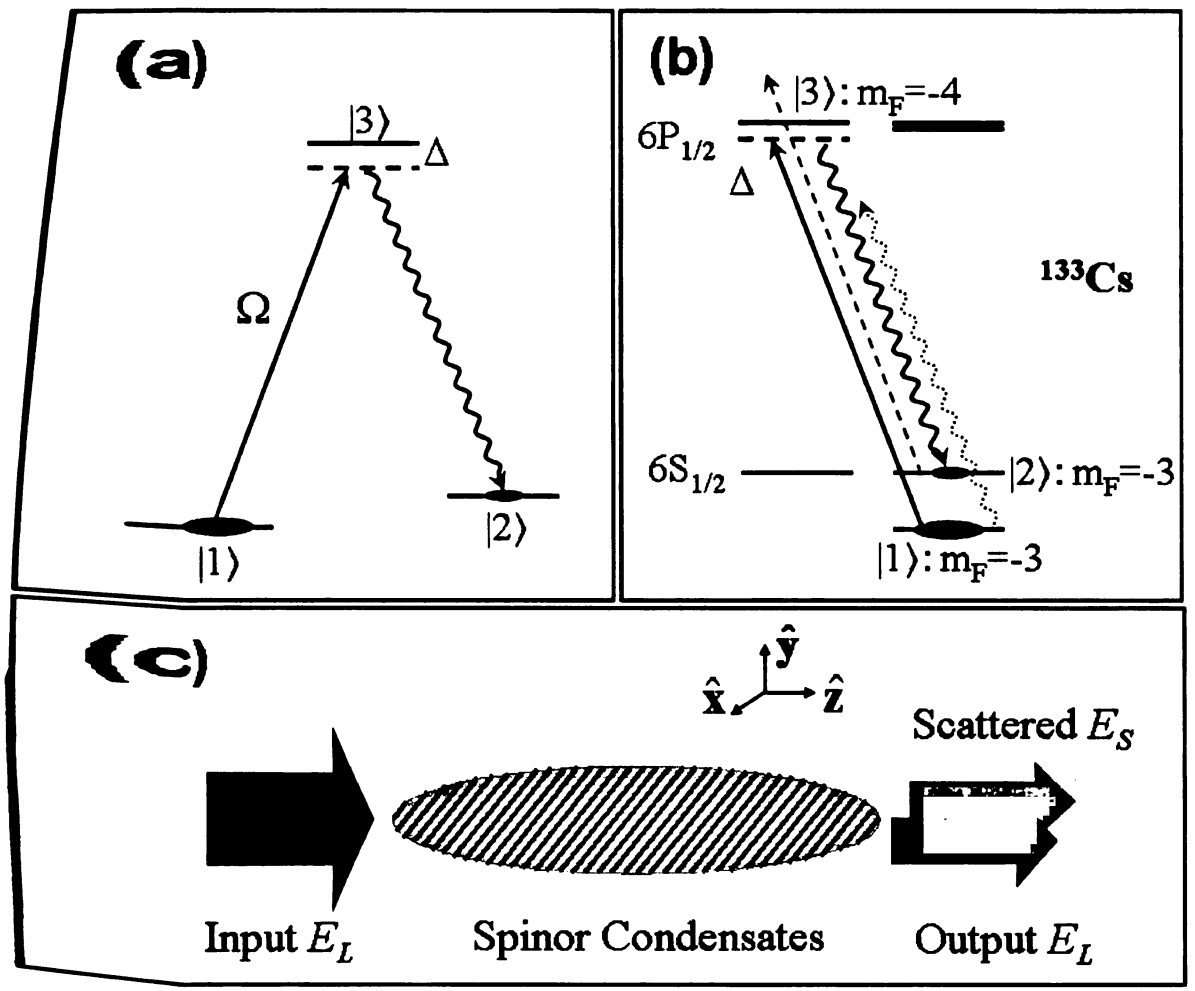

Figure 4.1: A MWA system configured on Raman transitions. Figure (a) plots a toy **mode** showing the Λ-level scheme. Figure (b) shows a physical implementation using **Cesium**'s D1-line transition. Figure (c) draws the schematic setup using copropagat-**ing** beams.

4.3 Quantum Coupled-Mode theory

4.3.1 The meanfield dynamics

We now build the mean-field model of atomic dynamics via the master-equation approach where the light-matter coupling is treated in the Markovian approximation. A detailed discussion on this approach is given in appendix 4.6.1. From the master equation 4.45, the mean-field dynamics for each level is determined by

$$\frac{d}{dt}\psi_1(\mathbf{r}) = -i\frac{\Omega^*(\mathbf{r})}{2}\psi_3(\mathbf{r}) + \int d^3r' L_1^*(\mathbf{r}-\mathbf{r}')\psi_3^\dagger(\mathbf{r}')\psi_1(\mathbf{r}')\psi_3(\mathbf{r}) \tag{4.1}$$

$$\frac{d}{dt}\psi_2(\mathbf{r}) = \int d^3r' L_2^*(\mathbf{r}-\mathbf{r}')\psi_3^\dagger(\mathbf{r}')\psi_2(\mathbf{r}')\psi_3(\mathbf{r}) \tag{4.2}$$

$$\frac{d}{dt}\psi_3(\mathbf{r}) = -i\frac{\Omega(\mathbf{r})}{2}\psi_1(\mathbf{r}) - \left(\frac{\gamma}{2}+i\Delta\right)\psi_3(\mathbf{r}) \tag{4.3}$$

$$+\int d^3r' \sum_{j=1,2} L_j(\mathbf{r}-\mathbf{r}')\psi_j^\dagger(\mathbf{r}')\psi_3(\mathbf{r}')\psi_j(\mathbf{r}). \tag{4.4}$$

Here the Schrödinger fields are defined as $\psi_j(\mathbf{r}) = tr\{\hat{\Psi}_j(\mathbf{r})\rho\}$ tracing over the whole atomic Hilbert space, with $\hat{\Psi}_j(\mathbf{r})$ $(j = 1,2,3)$ the field annihilate operator for level $|j\rangle$. Δ is the detuning of pump 2 from resonance, Ω the Rabi frequency, and γ is the spontaneous relaxation rate of $|3\rangle$ level. $L_j(\mathbf{r}-\mathbf{r}')$ $(j = 1,2)$ is the nonlinear two-body cooperative coefficient for transitions $|3\rangle \rightarrow |j\rangle$, defined in equation (4.47) in appendix 4.6.1. In getting this result, a mean-field factorization of field operators has been applied. While directly solving the meanfield dynamics (4.1)-(4.3) is in principle feasible, in practice, however, is extremely hard due to the presence of $1/|\mathbf{r}-\mathbf{r}'|$ and $1/|\mathbf{r}-\mathbf{r}'|^2$ terms in $L_j(\mathbf{r}-\mathbf{r}')$. Instead, we expand the Schrödinger fields onto momentum quasi-modes,

$$\psi_j(\mathbf{r},t) = \sqrt{N}c_j(t)\phi(\mathbf{r}), \quad j = 1,2 \tag{4.5}$$

$$\psi_3(\mathbf{r},t) = \sqrt{N}c_3(t)\phi(\mathbf{r})e^{i\mathbf{k}_L\cdot\mathbf{r}},$$

where $\phi(\mathbf{r})$ is the time-invariant spatial profile, and $\mathbf{k}_L$ the wavevector of pump 2. In this expansion, both pump 1 and signal wave are assumed to have zero momenta. This is the case for the Cesium example shown in Fig. 4.1, where the momentum mismatch between pump 1 and signal wave due to the hyperfine splitting is negligible compared to the Fourier-transferred momentum dispersion of condensates. The atomic population in the $|j\rangle$ state ($j = 1, 2, 3$) is then given by $N_j = N|c_j|^2$.

In the above expansion, we have assumed a single momentum mode for each internal atomic state. In practice, however, the system is simultaneously coupled to other modes, via spontaneous or superradiance emission. To the leading dynamical order, however, coupling to other modes does not interfere with the MWA process, since they deal with orthogonal electromagnetic modes. The net effect is the atom loss from the c_1, c_2, c_3 manifold. Thus the single-mode expansion (4.5) is valid as long as the atom loss fraction is small. Taking the coupling to other modes into account, the total atom loss can be described by an effective relaxation rate of $\chi_s\gamma$. Here χ_s is the superradiance enhancement factor on atom loss, which is obtained by solving a toy multi-mode system, as in section 4.6.4. γ is spontaneous emission rate of the excited level $|3\rangle$. Using moderately elongated condensates, we find $\chi_s \approx 1$, so that the enhancement effect is not significant and the atom loss is dominated by spontaneous decay.

Inserting the mode expansion (4.5) and incorporating the atom loss enhancement, the equation set (4.1) is now reduced to

$$\frac{d}{dt}c_1 = -\frac{i\Omega^*}{2}c_3 + \frac{1}{2}\Gamma_1 f_1^* N|c_3|^2 c_1 \tag{4.6}$$

$$\frac{d}{dt}c_2 = \frac{1}{2}\Gamma_2 f_2^* N|c_3|^2 c_2 \tag{4.7}$$

$$\frac{d}{dt}c_3 = -\left(\frac{\chi_s\gamma}{2}+i\Delta\right)c_3 - \frac{i\Omega}{2}c_1 - \frac{1}{2}\sum_{j=1,2}\Gamma_j f_j N|c_j|^2 c_3, \tag{4.8}$$

with the cooperative parameter f_j $(j = 1, 2)$ given by

$$f_j = \frac{2}{\Gamma_j}\int d^3r d^3r' |\phi(\mathbf{r})\phi(\mathbf{r}')|^2 L_j(\mathbf{r}-\mathbf{r}')e^{-i\mathbf{k}_L\cdot(\mathbf{r}-\mathbf{r}')} \tag{4.9}$$

with Γ_j the spontaneous relaxation rate from level $|3\rangle$ to $|j\rangle$. An evaluation of f_j for condensates of Thomas-Fermi profile is given in appendix 4.6.2.

The real part of f_j is often referred to as optical depth for an atomic cloud, while the imaginary part contributes to the atomic mean-field shift due to dipole-dipole interaction. For simplicity, we take $\Gamma_1 = \Gamma_2 = \gamma/2$ in the following discussions. In practice, for the level scheme configured on Cs's D1-line transitions shown in figure 4.1 (b), we find $\Gamma_1 = \gamma/12$, $\Gamma_2 = 7\gamma/12$, while for a similar level scheme on Rb's D1-line, $\Gamma_1 = \gamma/6$, $\Gamma_2 = \gamma/2$. Generalizing present conclusions and discussions to specific level schemes shall be straightforward. Finally, because of the employment of single-mode expansion, any spatial dynamics of mode functions is excluded in this model. Thus the QCM theory is valid only if variations of the mode functions remain insignificant. As we will show in the second part of the chapter, this is the case through the point where half of pump 1 atoms are depleted.

We now investigate the atomic dynamics of the Raman MWA system by solving the QCM equations (4.6)-(4.8). To characterize population transfer behaviors, we define a differential population fraction n, as

$$n = \frac{N_2 - N_1 - N_3}{2(N_1 + N_2 + N_3)}. \tag{4.10}$$

This quantity measures the relative population distribution between the $|1\rangle\&|3\rangle$ and $|2\rangle$ manifold, for atoms remaining in the condensates. For negligible atom loss, it is reduced to $n \approx \frac{1}{2}(|c_2|^2 - |c_1|^2 - |c_3|^2)$. To measure the speed of MWA, we intro-

duce the transfer time τ, defined as the evolution duration for which the differential population is inverted, i.e., $n(\tau) = -n(0)$. We note τ is meaningful only if the initial size of pump 1 is much greater than the signal wave. The transfer rate R can then be defined as the inverse of transfer time, with $R = \frac{1}{\tau}$.

For a back-of-the-envelope estimation of τ, we assume that the fraction of excited population, $P_e = N_3/(N_1 + N_3)$, is constant during the dynamics, given by

$$P_e = \frac{|\Omega|^2}{2|\Omega|^2 + (\chi_s\gamma + \Gamma_s)^2 + 4\Delta^2}. \tag{4.11}$$

Here $\Gamma_s = \Gamma_2 f_R N$ is the superradiant emission rate. The validity of this formula is in that it provides correct asymptotical results for whichever parameter much lager than the rest.

Under extreme considerations, the system can be classified into off-resonance, overdamping and Rabi regime, depending on pump 2. For $\Delta \gg |\Omega|, \chi_s\gamma + \Gamma_s$, the system is in the off-resonance regime, with $P_e = \frac{|\Omega|^2}{4\Delta^2}$. For Δ smaller than $|\Omega|$ or $\chi_s\gamma + \Gamma_s$, the system is (effectively) in the resonant regime. Depending on $|\Omega|$ smaller or greater than $\chi_s\gamma + \Gamma_s$, the system undergoes overdamping dynamics with $P_e = \frac{|\Omega|^2}{(\chi_s\gamma+\Gamma_s)^2}$, or Rabi oscillations with the time-averaging $P_e = \frac{1}{2}$. Neglecting atom loss, we have $N = N_2 + \frac{N_3}{P_e}$ and thus $n = \frac{N_2}{N} - \frac{1}{2}$, so that

$$\frac{d}{dt}n = -P_e\Gamma_s\left(n^2 - \frac{1}{4}\right). \tag{4.12}$$

This equation of motion can be analytically solved to give

$$n(t) = \frac{1}{2}\coth\left(\frac{1}{2}P_e\Gamma_s t + \coth^{-1}\left(\frac{1-\nu}{1+\nu}\right)\right). \tag{4.13}$$

where $\nu = \frac{N_1(0)}{N_2(0)}$ is the initial population ratio. The gain factor of the signal wave,

defined as $G_Q = \frac{N_2(t)}{N_2(0)}$, is then

$$G_Q = \frac{1+\nu}{2}\left[\coth\left(\frac{1}{2}P_e\Gamma_s t + \coth^{-1}\left(\frac{1-\nu}{1+\nu}\right)\right)+1\right]. \tag{4.14}$$

Further, the transfer time τ is given by

$$\tau_1 = \frac{2}{P_e\Gamma_s}\ln\nu, \tag{4.15}$$

Clearly, for any given Ω and Γ_s, the least transfer time is always achieved at $\Delta = 0$, i.e., when using a resonant driving laser. The ultimate shortest transfer time of $\tau = \frac{4}{\Gamma_s}\ln\nu$ is achieved when $|\Omega| \gtrsim \Gamma_s, \Delta$, for which P_e reaches its maximum of 1/2.

In the following subsections, we analyze in detail the three dynamical regimes, using adiabatical elimination or coarse-graining method. We then compare our analysis to exact numerics.

Off-resonance Regime

In this regime, $\Delta \gg |\Omega|, \chi_s\gamma+\Gamma_s$, so that state $|3\rangle$ can be adiabatically eliminated to give $c_3 = -\frac{\Omega}{2\Delta}c_1$. Neglecting atom loss, the equations of motion (4.6) are reduced to

$$\begin{aligned}\frac{d}{dt}c_1 &\approx i\frac{|\Omega|^2}{4\Delta}c_1 - \frac{|\Omega|^2}{8\Delta^2}\Gamma_2 f^* N|c_2|^2 c_1, \\ \frac{d}{dt}c_2 &\approx \frac{|\Omega|^2}{8\Delta^2}\Gamma_2 f^* N|c_1|^2 c_2.\end{aligned} \tag{4.16}$$

In the equation of motion for c_1, the first term is the ac-Stark shift induced by the far-off resonance driving. Since $f = f_R + if_I$, the second term contains real and imaginary part, respectively corresponding to population decay and cross-phase

modulation by c_2. Analytically solving these equation finds

$$n_0(t) = \frac{1}{2}\coth\left(\frac{|\Omega|^2}{8\Delta^2}\Gamma_s t + \coth^{-1}\left(\frac{1-\nu}{1+\nu}\right)\right), \tag{4.17}$$

and a transfer time of

$$\tau_o = \frac{8\Delta^2}{|\Omega|^2\Gamma_s}\ln\nu. \tag{4.18}$$

These results are asymptotes of the back-of-the-envelope formula (4.13) and (4.15) in the limit of $\Delta \gg |\Omega|, \chi_s\gamma + \Gamma_s$.

To study the dynamics of relative phase between c_1 and c_2, we write

$$c_j = \sqrt{n_j}e^{i\theta j} \tag{4.19}$$

for $j = 1,2,3$. The relative phase between c_1 and c_2, defined as $\theta_{12} = \theta_1 - \theta_2$, is then given by

$$\begin{aligned}\frac{d}{dt}\theta_{12} &= \frac{|\Omega|^2}{4\Delta} + \frac{|\Omega|^2}{4\Delta^2}\Gamma f_I N n, \\ &\approx \frac{|\Omega|^2}{4\Delta}.\end{aligned} \tag{4.20}$$

This is because $\frac{|\Omega|^2}{4\Delta^2}\Gamma f_I N n \ll \frac{|\Omega|^2}{4\Delta^2}\Gamma_s n \ll \frac{|\Omega|^2}{4\Delta}$, so that the phase dynamics is dominantly attributed to ac-Stark shift of pump 1 atoms, driven by pump 2. Assuming initially $\theta_{12} = 0$, upon population inverting, the accumulated relative phase is

$$\theta_{12}(\tau_o) = \frac{2\Delta}{\Gamma_s}\nu \gg 1. \tag{4.21}$$

Clearly, the relative phase between pump 1 and signal wave is not preserved during the MWA dynamics. Consequently, the phase of emitted idler beam is distorted, in which sense an off-resonant MWA can not be used as a hybrid state-mapping device between light and matter waves. On the other hand, the phase distortion of the signal wave,

due to cross-phase modulation c_2, is $< \frac{f_I}{f_R}\nu \ll 1$ for typical elongated condensates. Hence, while not suitable for quantum state mapping between matter and light waves, an off-resonance MWA system can be used to phase-coherently amplify a signal matter wave.

Overdamping Regime

In this regime, $\Delta = 0$ and $|\Omega| \ll \Gamma_s$, so that the excited level is only weakly pumped due to the quantum Zeno effect. Neglecting atom loss and adiabatically eliminating c_3 lead to

$$\begin{aligned} \frac{d}{dt}c_1 &\approx -\frac{|\Omega|^2}{2\Gamma f N}|c_2|^2 c_1, \\ \frac{d}{dt}c_2 &\approx \frac{|\Omega|^2}{2\Gamma f N}|c_1|^2 c_2. \end{aligned} \tag{4.22}$$

Again, these equations can be analytically solved to give

$$n_w(t) = \frac{1}{2}\coth\left(\frac{|\Omega|^2}{2\Gamma_s}t + \coth^{-1}\left(\frac{1-\nu}{1+\nu}\right)\right), \tag{4.23}$$

and

$$\tau_w = \frac{2\Gamma_s}{|\Omega|^2}\ln\nu. \tag{4.24}$$

Here we have used the fact that $f_R \gg f_I$ so that $\frac{|\Omega|^2 f_R}{\Gamma|f|^2 N} \approx \frac{|\Omega|^2}{\Gamma_s}$. Again, these results are consistent with the back-of-the-envelop formula (4.13) and (4.15) in the resonant weak driving limit, in which $P_e = \frac{|\Omega|^2}{\Gamma_s^2}$.

The motion of relative phase θ_{12} is given by

$$\frac{d}{dt}\theta_{12} = \frac{|\Omega|^2}{\Gamma_s}\frac{f_I}{f_R}n. \tag{4.25}$$

The magnitude of accumulated phase shift upon population inversion is then

$$|\theta_{12}(\tau_w)| < \frac{f_I}{f_R} \ln \nu, \tag{4.26}$$

which is negligibly small given $f_I \lesssim 0.01 f_R$, if using a typical cigar-shape condensate. Unlike in the off-resonance regime, here the relative phase between pump 1 and signal wave is preserved, due to the elimination of ac Stark shift using resonant driving. This provides the feasibility to use a overdamped MWA as a quantum device for state mapping between light and matter waves, in addition to a matter wave amplifier.

Rabi Regime

For a strong and resonant driving with $|\Omega| \gg \Gamma_s$, the dynamics is saturated in the Rabi regime, characterized by rapid Rabi oscillations between $|1\rangle$ and $|3\rangle$. Averaging over multiple Rabi oscillations, the mean atom number occupying $|1\rangle$ and $|3\rangle$ are approximately equal. To solve the mean-field dynamics 4.6, we separate two distinct time scales of Rabi oscillation and population transfer, using coarse-graining approach. This leads to

$$\frac{d}{dt} n = -\frac{\Gamma_s}{8}(4n^2 - 1). \tag{4.27}$$

with a solution of

$$n_s(t) = \frac{1}{2} \coth\left(\frac{\Gamma f_R N}{4} t + \coth^{-1}\left(\frac{1-\nu}{1+\nu}\right)\right). \tag{4.28}$$

and hence a transfer time of

$$\tau_2 = \frac{4}{\Gamma_s} \ln \nu. \tag{4.29}$$

Both match with (4.13) and (4.15) in strong driving regime where $P_e = \frac{1}{2}$. Similarly, the phase c_2 nearly does not change in time, so that the evolution of relative phase θ_{12} is due to the Rabi oscillation of c_1. Via a straightforward iterative analysis, the

dynamic solution for c_1 is

$$c_1(t) = \sqrt{\frac{1}{2} - \frac{n(t)}{2}} \cos \frac{\Omega t}{2}. \tag{4.30}$$

This gives rise to the relative phase

$$\theta_{12}(t) = \frac{\pi}{2}(1 - \text{Sign}\left[\cos\left(\frac{\Omega t}{2}\right)\right]). \tag{4.31}$$

The relative phase between pump 1 and signal wave is thus an oscillatory square function in time with an amplitude of $\pi/2$ and a period of $2\pi/\Omega$. The MWA in this regime is therefore not a phase-preserving process, so that it is in general unsuitable for applications of state mapping. Nonetheless, in contrast to complete phase randomization as in the off-resonance regime, here θ_{12} is switching between $\theta_{12}(0)$ and $\theta_{12}(0) + \pi$ during the dynamics, so does the phase of emitted idler beam. In an interferometry measurement, a phase θ can not be distinguished from its π-conjugate of $\theta + \pi$. In this way, the initial phase $\theta_{12}(0)$ can still be read out via interferometrical measurements of idler beams, thus providing the feasibility of using Rabi MWA for the state mapping purposes.

Numerical Results

To verify the preceding analysis, we numerically solve the mean-field equations (4.6)–(4.8), using the following parameters: $\Gamma_1 = \Gamma_2 = \gamma/2$, $N = 3 \times 10^6$, $W = 100/k_L$ and $A = 10$. The optical depth Nf_R, given in (4.72), is then 105. We choose the initial occupation fraction to be $c_1(0) = \sqrt{0.9}$, $c_2(0) = \sqrt{0.1}$ and $c_3(0) = 0$.

In figure 4.2, we plot the dynamics of differential population fraction $n(t)$, where (a), (b) and (c) are showing for $\Delta = 10\Gamma_s$ &, $\Omega = \Gamma_s$, $\Delta = 0$ & $\Omega = 0.1\Gamma_s$ and $\Delta = 0$ & $\Omega = 10\Gamma_s$. They are then each corresponding to the off-resonance, overdamping and Rabi regime. In all regimes, the analytical formula are found to agree well with

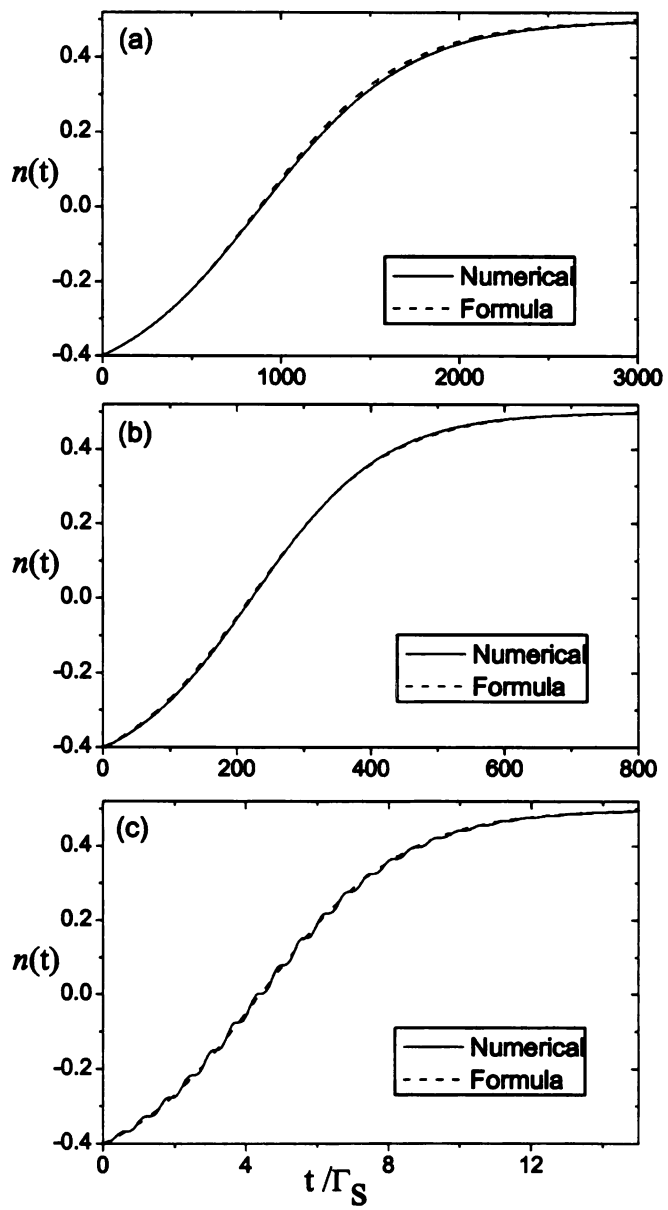

Figure 4.2: Figures (a), (b) and (c) show the dynamics of differential population **fraction** in the off-resonance, overdamping and Rabi regimes. In all figures, solid lines **are** numerical results, while dashed lines represent formulas (4.17), (4.23) and (4.28), **respectively**.

exact numerical results, thus validating our analysis. From figure 4.2, the transfer times for each case are determined to be $1800\Gamma_s^{-1}$, $436.8\Gamma_s^{-1}$ and $8.96\Gamma_s^{-1}$, compared to analytical results of $1757\Gamma_s^{-1}$, $439.4(\Gamma_s)^{-1}$ and $8.79\Gamma_s^{-1}$, respectively given by formula (4.18), (4.24) and (4.29) in each dynamical regime.

As discussed before, the least transfer time and thus the maximum transfer rate is obtained when the dynamics is saturated in Rabi regime with strong resonant driving. To study the saturation behavior, in Fig. 4.3 we plot the transfer rate R, as a function of $|\Omega|$ for $\Delta = 0$. The analytical formula (4.15) is shown to agree well with numerical results. For $|\Omega|$ smaller than Γ_s, the transfer rate R grows quadratically as $|\Omega|$ increases. This is because in this overdamping regime, $R \propto P_e \propto |\Omega|^2$, due to quantum Zeno effect. As $|\Omega|$ grows to be comparable with Γ_s, R is saturated to $R \propto \Gamma_s/4$, as $P_e \approx 1/2$ in this Rabi regime. The phase transition between overdamping and Rabi regimes occurs when $|\Omega| \approx \Gamma_s$. In practice, it is thus optimal to set $|\Omega| \sim \Gamma_s$ for a fastest amplification process.

On the other hand, the transfer rate as a function of optical thickness Γ_s for a fixed $|\Omega|$ is shown in figure 4.3 (b). Again, formula (4.15) agrees well with the numerical data. For $\Gamma_s < |\Omega|$, the system is in the Rabi regime, so that R increases linearly with Γ_s. The maximum R is achieved at the phase transition point with $\Gamma_s \approx |\Omega|$. As Γ_s continues to increase, R decreases linearly in Γ_s^{-1}, as the system enters the overdamping regime. The fact that R reaches its peak value when Γ_s and $|\Omega|$ are comparable indicates that given a finite laser intensity, the fastest MWA process is obtained by matching Γ_s to $|\Omega|$, via manipulating the trapping potential. We note for $\Gamma_s \ll |\Omega|$, the formula result is divergent from numerics. Such is because in that region, the atom loss becomes significant, so that the formula is invalid.

The relative phase evolution $\theta_{12}(t)$ for the three dynamical regimes is shown in Fig. 4.4 (a),(b) and (c). In the off-resonance regime, $\theta_{12}(t)$ oscillating at a period of $\frac{8\pi\Delta}{|\Omega|^2}$, as expected. In the weak resonant regime, $\theta_{12}(t)$ increases only slowly. The ac-

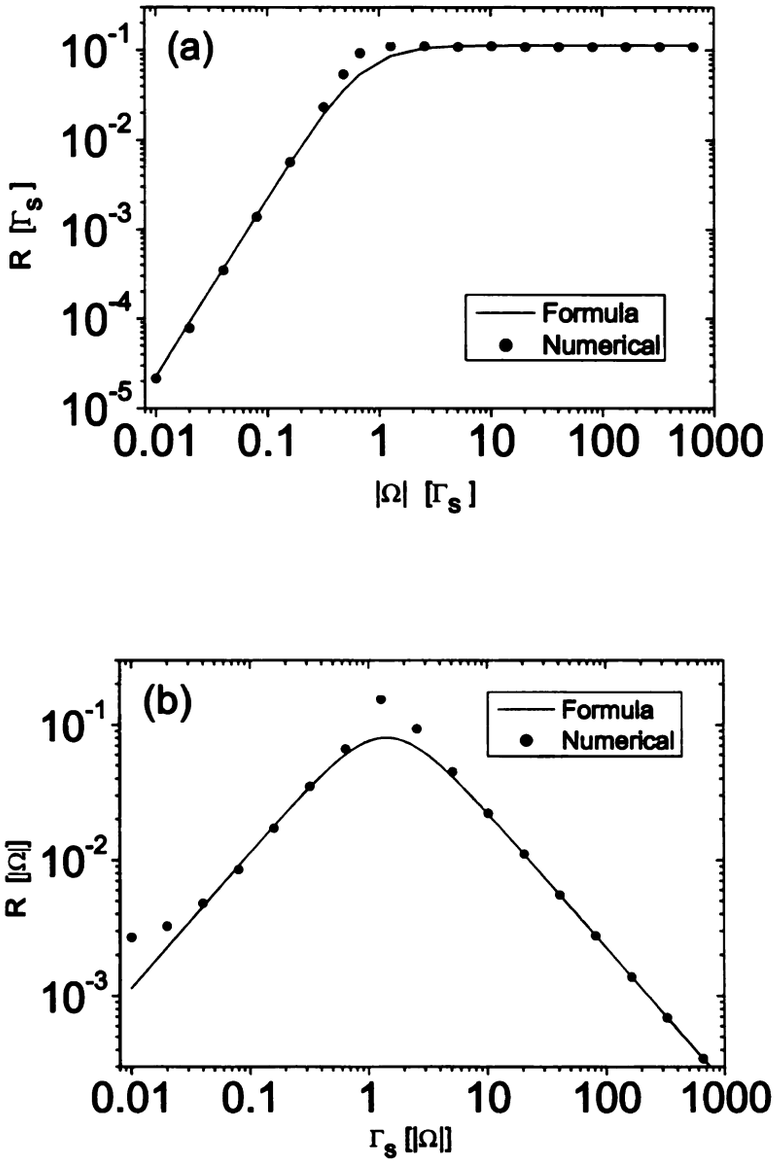

Figure 4.3: Figure (a) shows the transfer rate R as a function of Rabi-frequency $|\Omega|$ of a resonant driving field, where Γ_s is fixed, given the same as in 4.2. Figure (b) shows R as a function of Γ_s for a fixed $|\Omega| = 105\gamma$. In both figures, solid points are numeric results obtained by solving the meanfield equations (4.6), while solid lines are plotted for the back-of-the-envelope formula (4.15).

cumulated phase drift upon population inverting is about ~ 0.24, which is marginally consistent with the estimated value of 0.13. In practice, further suppression of the phase drift is easily achievable by increasing the condensate width W or reducing the aspect ratio A. In the Rabi regime, θ_{12} flips between 0 and π at a period of $2\pi/|\Omega|$, as predicted.

4.3.2 Further Discussions

In this section, we have developed the QCM theory for the three-level Raman MWA system, whose dynamics is treated with single-mode approximation. We studied the dynamical behaviors according to the off-resonance, overdamping and Rabi regimes, respectively driven by off-resonance, weak resonant, and strong resonant lasers. For any given laser intensity, the largest amplification rate is achieved with resonant driving. The ultimate maximum rate is obtained in the Rabi regime, when the Rabi frequency of driving laser is comparable to or greater than the superradiance emission rate. The atom loss fraction upon completing population transfer, as discussed in details in appendix 4.6.4, is a universal quality independent of dynamical regime the system is in.

In all regimes, the phase of signal wave is preserved, except for a small meanfield shift by cross phase modulation, which can be suppressed by adjusting the condensate geometry, for example, changing the aspect ratio of the condensate. Thus MWA in all regimes is qualified as a matter-wave amplification device. In the off-resonance regime, due to the ac-Stark shift of pump 1 atoms by the driving, the relative phase between pump 1 and signal wave is completed distorted, making it unsuitable for the application of state mapping between light and matter waves. In Rabi regime, the relative phase switches between its initial value $\theta_{12}(0)$ and $\theta_{12}(0) + \pi$. While this randomizes the relative phase, the initial phase value $\theta_{12}(0)$ can still be read out via interferometrically measurement of the emitted idler beam. Thus to some extent, a

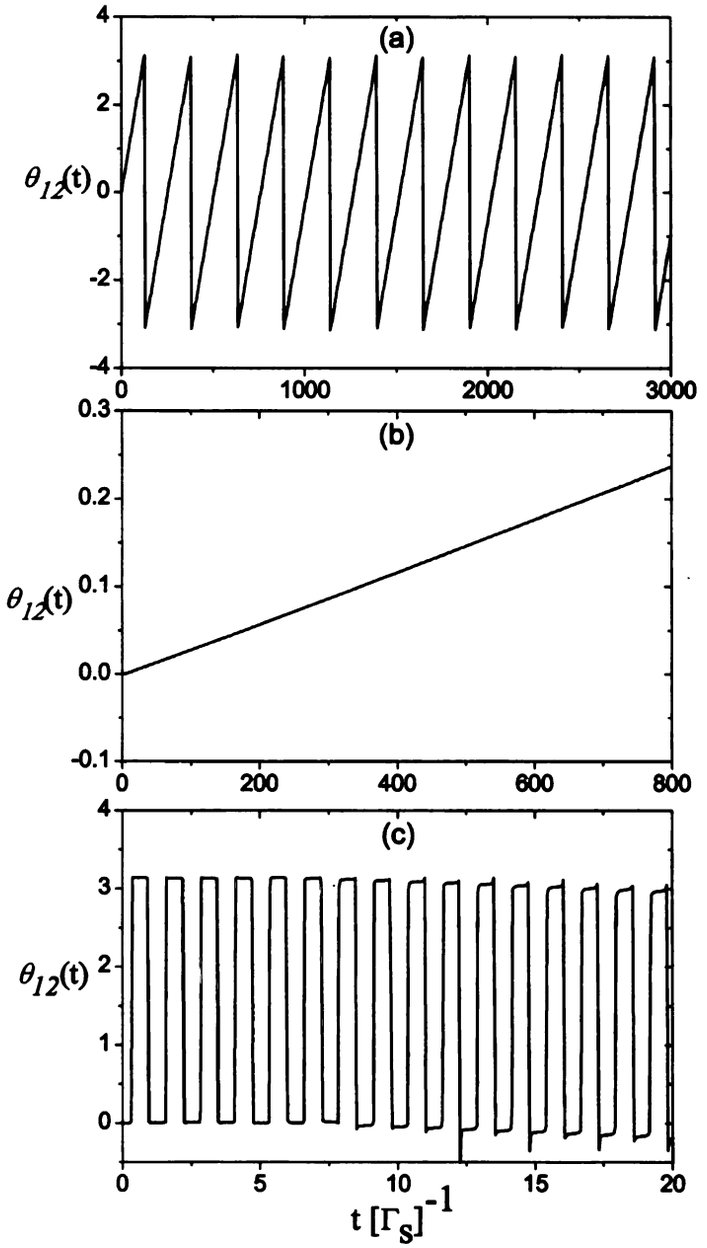

Figure 4.4: Figures (a), (b) and (c) show the evolution of relative phase $\theta_{12}(t)$ in the off-resonance, overdamping and Rabi regimes. Parameters are the same with corresponding figures in Fig. 4.2.

Rabi MWA system can be still used as a state mapping device, for the benefit of a shortest operation time. In contrast, the phase distortion is strongly suppressed in the overdamping regime, thus establishing a viable candidate for quantum information purposes.

On the other hand, the phase distortion can alternatively be overcome in a four-level Rayleigh MWA system in the so-called 'weak pulse' regime [100, 108, 129]. It is characterized by $P_e\Gamma_s \ll \omega_R$, with the atom recoil frequency $\omega_R = \frac{\hbar k_L^2}{2m}$ (m is the atomic mass). Such is imposed in order to inhibit further coupling of the matter waves to other modes by phase mismatching. Otherwise, the MWA process will be spoiled because coupling to other modes is turned out to occur on a similar time scale with MWA, since they are stimulated by the emitted idler light field. In this four-level Rayleigh system, pump 1 and the signal wave, corresponding to identical electronic states, are simultaneously driven by pump 2. They therefore experience similar phase shifts, so that the phase distortion is eliminated. Typically, $\Gamma_s \sim 10^9$ Hz and $\omega_R \sim 10^5$ Hz, so that it requires $P_e < 10^{-4}$. This requires the use of off-resonance driving with $|\Omega| \lesssim 10^{-2}\Delta$ or resonant driving with $|\Omega| \lesssim 10^{-2}\Gamma_s$. Under similar conditions, however, the transfer rate is orders of magnitude smaller than that allowed in the present Raman system, in overdamping or Rabi regimes.

4.4 Semiclassical Multi-mode Theory

In the previous part, we have developed quantum coupled-mode theory at the meanfield level for the three-level Raman MWA system, employing time-invariant spatial modes. Such a theory, while extremely intuitive and easy to access, does not take into account any effects accommodating propagation of light fields inside the condensates. In practice, such effects have been shown to account for several important experimental observations [113, 127, 129, 131]. For a more physically

accurate model, we now develop the semiclassical Maxwell-Schrödinger (SMS) theory, via semiclassical treatments of dipole coupling between light and matter waves via Maxwell-Schrödinger (MS) equations.

4.4.1 Spatial-Mode Evolution

The semiclassical MS equations for this system are derived from a generic set of nonlinear coupling equations for lights propagating inside a polarized atomic medium, as given in appendix 4.6.3. In terms of the following dimensionless units and variables

$$\begin{aligned}
\tilde{t} &= \Gamma_s t, \\
\tilde{\mathbf{r}} &= k_L \mathbf{r}, \\
\tilde{\psi}_i(\tilde{\mathbf{r}}, t) &= k_L^{-3/2} \psi_i(\mathbf{r}, t), \quad i = 1, 2, 3 \\
\zeta_{L,S}(\mathbf{r}, t) &= \frac{2d_{1,2}}{\hbar \Gamma_s} E^{(+)}_{L,S}(\mathbf{r}, t)
\end{aligned}$$

the equation of motion can be is found to be

$$\frac{d}{d\tilde{t}}\tilde{\psi}_1(\tilde{\mathbf{r}}, \tilde{t}) = \frac{i}{2}\zeta_L^*(\tilde{\mathbf{r}}, t)\tilde{\psi}_3(\tilde{\mathbf{r}}, \tilde{t}) \tag{4.32}$$

$$\frac{d}{d\tilde{t}}\tilde{\psi}_2(\tilde{\mathbf{r}}, \tilde{t}) = \frac{i}{2}\zeta_S^*(\tilde{\mathbf{r}}, t)\tilde{\psi}_3(\tilde{\mathbf{r}}, \tilde{t}) \tag{4.33}$$

$$\frac{d}{d\tilde{t}}\tilde{\psi}_3(\tilde{\mathbf{r}}, \tilde{t}) = -\frac{2i\Delta + \chi_s\gamma}{2\Gamma_s}\tilde{\psi}_3(\tilde{\mathbf{r}}, \tilde{t}) + \frac{i}{2}\left[\zeta_L(\tilde{\mathbf{r}}, \tilde{t})\tilde{\psi}_1(\tilde{\mathbf{r}}, \tilde{t}) + \zeta_S(\tilde{\mathbf{r}}, \tilde{t})\tilde{\psi}_2(\tilde{\mathbf{r}}, \tilde{t})\right] \tag{4.34}$$

$$\frac{\partial\zeta_L(\tilde{\mathbf{r}}, \tilde{t})}{\partial\tilde{z}} = i\frac{3\pi}{f_R}\tilde{\psi}_1^*(\tilde{\mathbf{r}}, \tilde{t})\tilde{\psi}_3(\tilde{\mathbf{r}}, \tilde{t}) \tag{4.35}$$

$$\frac{\partial\zeta_S(\tilde{\mathbf{r}}, \tilde{t})}{\partial\tilde{z}} = i\frac{3\pi}{f_R}\tilde{\psi}_2^*(\tilde{\mathbf{r}}, \tilde{t})\tilde{\psi}_3(\tilde{\mathbf{r}}, \tilde{t}) \tag{4.36}$$

In deriving these equations, we have neglected translational degrees of freedom, using the fact that the MWA is processed within a time scale of $1 \sim 10^3$ns, much shorter than any time scales related to atomic motions. Also, we have neglected the retardation effect associated with light propagating inside the condensate, which yields a

time scale of $\lesssim 10^{-12}$s, much shorter than atomic dynamics time scales of $\sim 10^{-9}$s. These equations are then numerically solved via Runge-kutta method to simulate the multi-mode MWA dynamics.

First, we investigate the dynamical evolution of the spatial modes for both matter and light waves. We take similar parameters as used in section 4.3.1, where $\Gamma_1 = \Gamma_2 = \gamma/2$, $N = 3 \times 10^6$ and an initial population ratio of $\nu = 9$. Initially, the matter waves are in Thomas-Fermi profile (4.54) with $W = 100/k_L$, $L = 10W$. In Fig. 4.5, we plot the signal wave density integrated over the transverse dimension, defined as

$$P_2(\tilde{z}, \tilde{t}) = \int d\tilde{x} d\tilde{y} |\tilde{\psi}_2(\tilde{\mathbf{r}}, \tilde{t})|^2. \tag{4.37}$$

The driving parameters are $\Delta = 10\Gamma_s$, and $\Omega = \Gamma_s$ for figure (a), $\Delta = 0$ and $\Omega = 0.1\Gamma_s$ for figure (b), and $\Delta = 0$, $\Omega = 10\Gamma_s$ for figure (c). Here $\Omega = 2\hbar^{-1} d_1 E_L(-\infty, t)$ is the Rabi frequency of the applied driving laser. Thus each of the figures are respectively corresponding to the off-resonance, overdamping and Rabi regimes in the QCM model discussed in section 4.3.1.

In figure 4.5 (a) for the off-resonance regime, the signal wave is seen to be amplified firstly in the back with respect to the beam propagation direction, i.e., the $+\tilde{z}$ region. In the front, signal-wave amplification becomes significant only when $t > \tau/2$. Thus initially in spatially symmetric, the mode function of the signal wave firstly evolves to an asymmetric profile weighted in the back. Without reabsorption of the idler beam, an atom transferred to the signal wave stays there, so that the symmetry is gradually restored as the front is lately amplified. A very similar dynamical behavior is seen in the Rabi regime in figure (c), but on the much shorter time scale. In contrast, in figure (c) for the overdamping regime, the dynamical asymmetry is reversed, where the amplification firstly occurs in the front and then subsequently extends to the back.

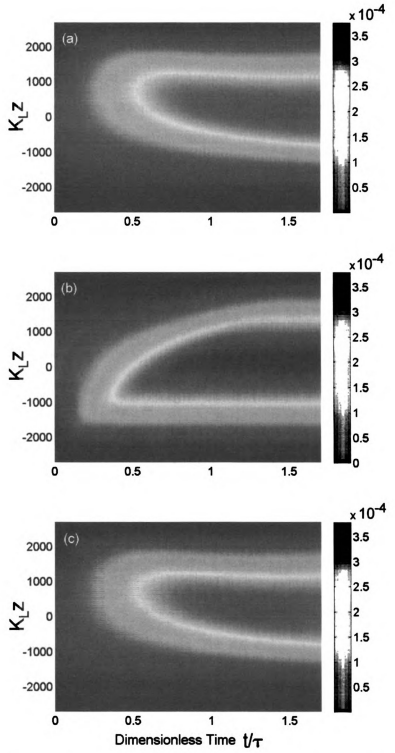

Figure 4.5: (Color online) Figures (a)-(c) are the surface plots of $P_2(\tilde{z}, \tilde{t})$ in the off-resonance, overdamping and Rabi dynamical regimes. In each figure, the evolution time has been rescaled by the corresponding transfer time τ obtained via QCM model, which for (a), (b) and (c) is $8.96\Gamma_s^{-1}$, $436.8\Gamma_s^{-1}$ and $1800\Gamma_s^{-1}$, respectively.

The dynamical asymmetry is due to two competing factors of laser depletion of pump 2 and spatial effect of the idler beam [127, 129, 131, 117]. The depletion of pump 2 is due to photon absorption by pump 1 atoms, resulting in intensity attenuation as it travels inside the medium. Atoms in the signal wave, however, are not coupled with the pump 2 due to a large detunning, and are thus effectively 'dark' to the driving. Hence, the depletion effect is strongest in the early stage, becoming weaker as atoms are transferred to the signal wave, and is eventually gone upon depletion of pump 1. A rough method to measure the significance of the laser depletion is to compare the photon number in driving pump N_p and atom number N in the medium. This method is very intuitive: because an atom can at most absorb one photon, the depletion is significant only if there are more atoms than photons. For a time duration of Δt, it is straightforward to find

$$\begin{aligned} N_p &= \frac{\epsilon_0 W^2 c \Delta t E_L^2(-\infty)}{\hbar \omega_L}, \\ &= \frac{\Omega^2 N \Delta t}{64\pi \Gamma_s} \end{aligned} \tag{4.38}$$

assuming a beam focal area of W^2. Taking Δt to be the transfer time τ given in (4.15), this gives

$$\frac{N_p}{N} = \frac{2\Omega^2 + \Gamma_s^2 + 4\Delta^2}{32\pi \Gamma_s^2} \ln \nu. \tag{4.39}$$

Thus, for $|\Omega|, \Delta \gg \Gamma_s$, $N_p > N$, so that the laser depletion effect is expected to small in off-resonance and Rabi regimes. For $|\Omega| < \Gamma_s$, on the other hand, $N_p < N$, indicating a strong depletion effect in overdamping regime. For parameters for figure 4.5 (a), (b) and (c), we have $\frac{N_p}{N} = 8.8, 0.02$ and 4.3, so that the laser depletion is significant only for figure (b). This analysis agrees with the exact numerics shown in figure 4.6, where the amplitude of pump 2 across the medium at $\tilde{x} = \tilde{y} = 0$ is plotted as a function of time. In figure (a) and (c) for the off-resonance and Rabi regimes, pump 2 is almost constantly uniform in amplitude across the condensate. While in

figure (b) for the overdamping regime, there appears two distinct front and back regions, with a tiny laser amplitude in the back, exhibiting a strong laser depletion. In the early stage, pump 2 is only able to penetrate into the shallow of the atomic medium. The penetration becomes deeper as atoms are subsequently transferred out of pump 10.

The second factor is attributed to the so-called spatial effect, a characteristic phenomenon where the simulation effect for the scattering process is stronger in the back region than in the front [108, 127, 129, 131]. In the picture of Bragger scattering, such is due to a higher intensity of idler beam in the back. As seen in equation (4.36), propagating along $+\tilde{z}$, the idler beam at $\tilde{z}$ is proportional to the integration of $\tilde{\psi}_2^*\tilde{\psi}_3$ from $-\infty$ to $\tilde{z}$. Given that $\tilde{\psi}_2$ and $\tilde{\psi}_3$ are spatially homogeneous in phases, its intensity monotonically builds up in the $\tilde{z}$ direction. According to equation (4.33), the amplification rate of the signal wave is higher in the back, i.e., the area of of large idler field. As an example, in figure 4.11, we plot the amplitude of idler beam $|\zeta_s|$ as a function of $\tilde{z}$ and $\tilde{t}$ at $\tilde{x}, \tilde{y} = 0$. In figure (a) for the off-resonance regime, $|\zeta_s|$ is shown to be much greater in the front than in the back, which is a clear sign of the spatial effect. The idler field at the $+\tilde{z}$ edge exhibits a characteristic 'ringing' behavior, where a second peak appears after the main pulse [129, 131]. The 'ringing' is due to reabsorption of the idler beam in the back, in which atoms in the signal wave are excited by the idler field, and then repumped to pump 1 by stimulated emission back to the laser. Due to the reabsorption, a small outcome idler field does not necessarily imply a equally small field inside the sample. In fact, at around $t = \tau$, the density of idler beam is peaked close to the center, not the edge. Ultimately, the reabsorption is due to the relative phase between pump 1 and the signal wave evolving into mismatched front and back patterns, as we will plot later in figure 4.11 (a). On the other hand, the reabsorption effect is nonetheless insignificant in the present system, in that only a small portion of signal-wave atoms are repumped. This is

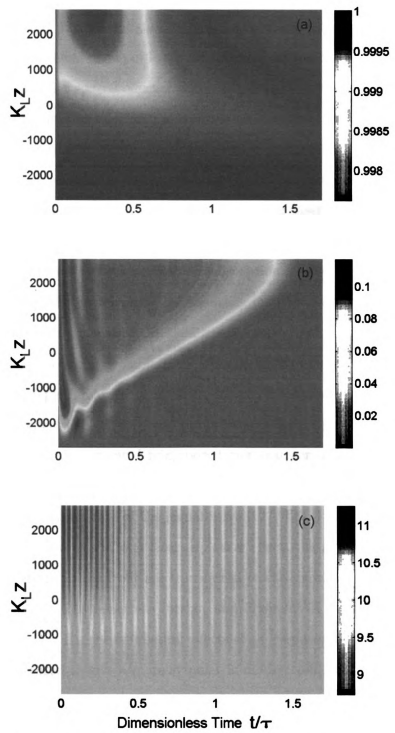

Figure 4.6: Figures (a)-(c) are the surface plots of $\left|\zeta_L(\tilde{z},\tilde{t})\right|$ at $\tilde{x},\tilde{y}=0$ for corresponding regimes in figure 4.5. The evolution time is similarly rescaled according to the transfer time. Notice the distinct scales of color bar in each figure.

clearly seen in figure 4.5 (a), where the density of signal wave is nearly monotonically built up in all areas. Shown in figure (c), similar envelope behaviors are found for the Rabi regime, with the addition of fast Rabi oscillations. Such is expected, since both are exposed to similar spatial effects.

Interestingly, in figure (c) for the overdamping regime, the idler beam is shown to yield uniform intensity from a time-variant edge to the back. The edge is initially at the front of condensates and then gradually shrinks towards back. This seemingly counterintuitive behavior is in fact due to the strong laser depletion effect in this regime, because of which the MWA occurs firstly in the front. The uniform distribution from edge to back reflects negligible reabsorption of idler beam. Physically, this is due to the preservation of phase homogeneity in the area of strong idler field, as we will show later in figure 4.11 (a).

To this end, we can now explain the dynamical asymmetry seen in figure 4.5 in context of laser depletion and spatial effect. In the off-resonance and Rabi regime, the laser depletion effect is negligible, and pump 2 is capable of propagating through the condensate and simultaneously driving population transfer. Due to the spatial effect, atoms in the back experience a stronger simulation effect by the idler beam, resulting in a larger amplification rate of the signal wave [127, 129, 131]. In the overdamping regime, however, due to a strong laser depletion effect, the MWA is driven firstly in the front. As atoms in the front are transferred to the signal wave, the driving laser pump 2 is allowed it to penetrate further and drive MWA in the back. We found that for $\Delta = 0$, $\Omega = \Gamma_s$, the competing effects of propagation and laser depletion are somehow neutralized to give a more symmetric mode profile during the dynamic.

4.4.2 Population Transfer

In this section, we study the population transfer dynamic via the SMS model, taking into account the laser depletion and spatial effect. The population fraction in

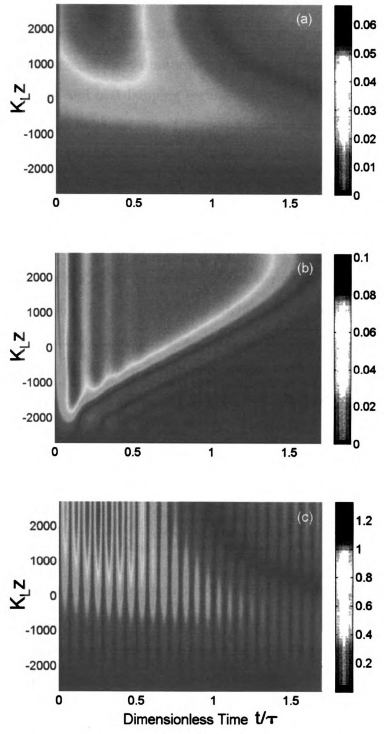

Figure 4.7: Figures (a)-(c) are similar surface plots but for $\left|\zeta_S(\tilde{z},\tilde{t})\right|$.

the each matter-wave mode is given by $n_j = \int d^3\tilde{\mathbf{r}}\ \varrho_j(\tilde{\mathbf{r}})$, for $j = 1, 2, 3$. In figure 4.8 (a)-(c), we plot the evolution of differential population fraction n, defined in (4.10), in the three dynamical regimes, using the same parameters as for figure 4.5. From figure (a) and (c), although on distinct time scales, qualitatively similar behaviors are found for the off-resonance and overdamping regime. For $t < \tau/2$, both closely follow the QCM dynamics. Soon as t reaches $\tau/2$, corresponding to about half of pump 1 atoms being depleted, $n(t)$ obviates from the QCM results, downgrading to a slower growth rate. The population inverting occurs at $t = 5.4\tau$ for both cases, which is about five times longer than the QCM transfer time in corresponding regimes. The behavior is dramatically different in the overdamping regime, as shown in figure (b), where $n(t)$ roughly follows the QCM curve throughout the whole dynamics. Surprisingly, for $t < \tau/2$, the population transfer is even slightly faster than via the QCM model. Such a behavior is counterintuitive, since both the laser depletion and spatial effect are expected to slow down the population transfer.

To explain these behaviors, we define a relative collectivity parameter ξ_{eff} with respect to f_R, as

$$\begin{aligned} \xi_{eff}(t) &= \frac{6\pi^2}{f_R n_2 n_3} \int_{-\infty}^{\infty} d\tilde{\mathbf{z}} \int_0^{\infty} d\tilde{\rho}\ \tilde{\rho} \sqrt{\varrho_2(\tilde{\rho}, \tilde{\mathbf{z}}) \varrho_3(\tilde{\rho}, \tilde{\mathbf{z}})} \\ &\quad \times \int_{-\infty}^{\tilde{\mathbf{z}}} d\tilde{\mathbf{z}}' \sqrt{\varrho_2(\tilde{\rho}, \tilde{\mathbf{z}}') \varrho_3(\tilde{\rho}, \tilde{\mathbf{z}}')}. \end{aligned} \tag{4.40}$$

Here, the angular integration has been performed analytically to give 2π, by using the azimuthal symmetry. For condensates initially prepared in azimuth-symmetric modes, such as the Thomas-Fermi profile (4.54), the azimuthal symmetry is preserved during the dynamics since atoms are uncoupled in transverse dimensions, as a consequence of single $\mathbf{k}$-vector approximation for the idler beam. We note that because the mode functions evolve in time, ξ_{eff} is a time-variant quantity. The equation of motion for

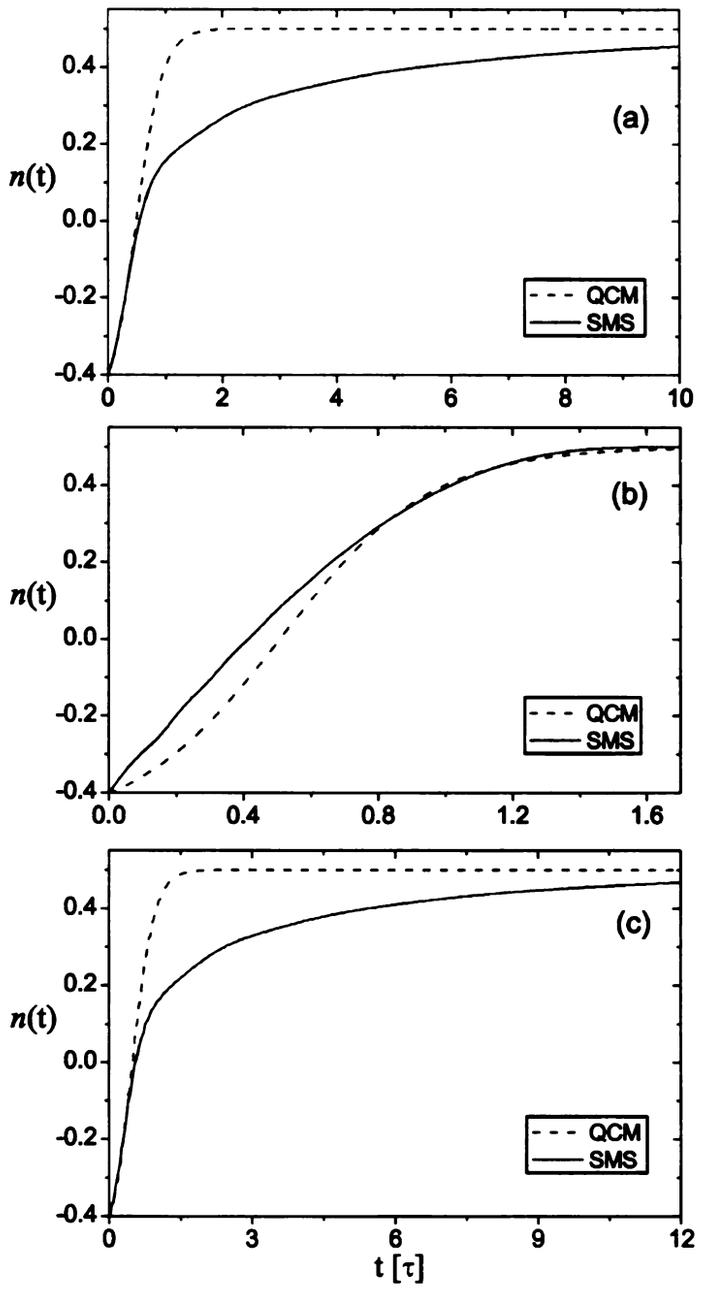

Figure 4.8: Dynamical evolution of the differential population fraction $n(t)$, where (a), (b) and (c) are plotted for the off-resonance, overdamping and Rabi regimes, respectively. All parameters are the same as for corresponding figures in Fig 4.5, with the evolution time similarly rescaled.

n_2 can then be written in a compact form of

$$\frac{d}{dt}n_2 = \xi_{eff} n_2 n_3. \tag{4.41}$$

assuming spatially homogeneous phases for matter waves, i.e., $\theta_j(\tilde{\mathbf{r}}) = \theta_j(\mathbf{r}')$, for $j = 1, 2, 3$. In the QCM model, $\frac{d}{dt}n_2 = n_2 n_3$, so that the deviation of ξ_{eff} from 1 is a measure of the significance of the spatial effect.

In figure 4.10, we plot the time evolution of ξ_{eff} for the three dynamical regimes shown in figure 4.5. In all regimes, $\xi_{eff} = 1$ at $t = 0$, indicating the physical equivalence of the semiclassical Maxwell-Schrödinger equation and quantum master equation. In the off-resonance regime, ξ_{eff} smoothly downgrades from 1 to around 0.5, as t increases from 0 to $\tau/2$. It then slowly oscillates around 0.5 in a small amplitude. A similar envelop function of ξ_{eff} is found for the Rabi regime, but with the additions of sharp oscillations. Because the laser depletion effect is weak in these two regimes, the slowdown of population transfer at the half-depletion time is mainly due to the downgrade of ξ_{eff}. Essentially, the descending of ξ_{eff} is a consequence of the spatial effect, due to which the mode functions of the matter waves evolve to asymmetric profiles. This is seen in equation (4.40), where ξ_{eff} is determined by the overlapping of ϱ_2 and ϱ_3, or equivalently the densities of pump 1 and the signal waves. In the early stage, pump 1 and the signal wave are spatially matched. Due to the spatial effect, the depletion of pump 1 occurs firstly in the back, imparting with the amplification of the signal wave also in the back. This leads to a spatial mismatch of ϱ_2 and ϱ_3, thus a reduced relative collectivity ξ_{eff}.

Comparatively, in the overdamping regime, ξ_{eff} sharply decays to 0.2, and then quickly regains to around 0.5. After $t = 2\tau$, it gradually decreases to 0. Due to quantum Zeno effect, the transfer rate in this regime is inversely proportional to the optical thickness, and thus ξ_{eff}. That's, the spatial effect, while resulting in a

reduced optical thickness, in fact leads to a enhanced transfer rate. This exact reason accounts for the counterintuitive phenomenon seen in figure 4.8 (b), where population transfer is slightly faster in the SMS model. Of course, in the overdamping regime, the laser depletion effect is strong, acting adversely on the population transfer. The two competing factors somehow annihilate with each other, resulting in roughly agreeing SMS and QCM population dynamics.

As discussed above, the downgrade of ξ_{eff} is due to the matter waves evolving into spatially mismatched modes, and is not directly related to the population distribution among different modes. Thus the spatial effect would similarly affect the population dynamics for various initial population ratio ν. To verify this, in figure 4.9 we present the population dynamics for $\nu = 1$, i.e., with evenly feeded pump 1 and signal waves. All other parameters are the same as for figure 4.8. In figure (a) and (c) for the off-resonance and overdamping regimes, the SMS dynamics coincides with the QCM results for $n < 0.25$, before pump 1 is half depleted. Afterwards, the transfer rate is then significantly reduced, exhibiting similar divergent behaviors with figure 4.8 (a) and (c) where $\nu = 9$. In figure (b) for the overdamping regime, however, $n(t)$ only moderately follows the QCM curve. The transfer speed in the SMS model is shown to be slower than that via QCM.

4.4.3 Phase dynamics

In section 4.3.1, we studied the phase coherence property of the three-level Raman MWA system within the QCM model. A strong phase distortion effect is found in the off-resonance regime, due to the ac-Stark shift by the pump 2 laser. In the Rabi regime, the relative phase between pump 1 and signal wave is switched between its initial value $\theta_{12}(0)$ and $\theta_{12}(0) + \pi$ rapidly. The only phase preserving process is, however, realized in the overdamping regime, yet with a small drift due to cross phase modulation via atomic dipole interaction.

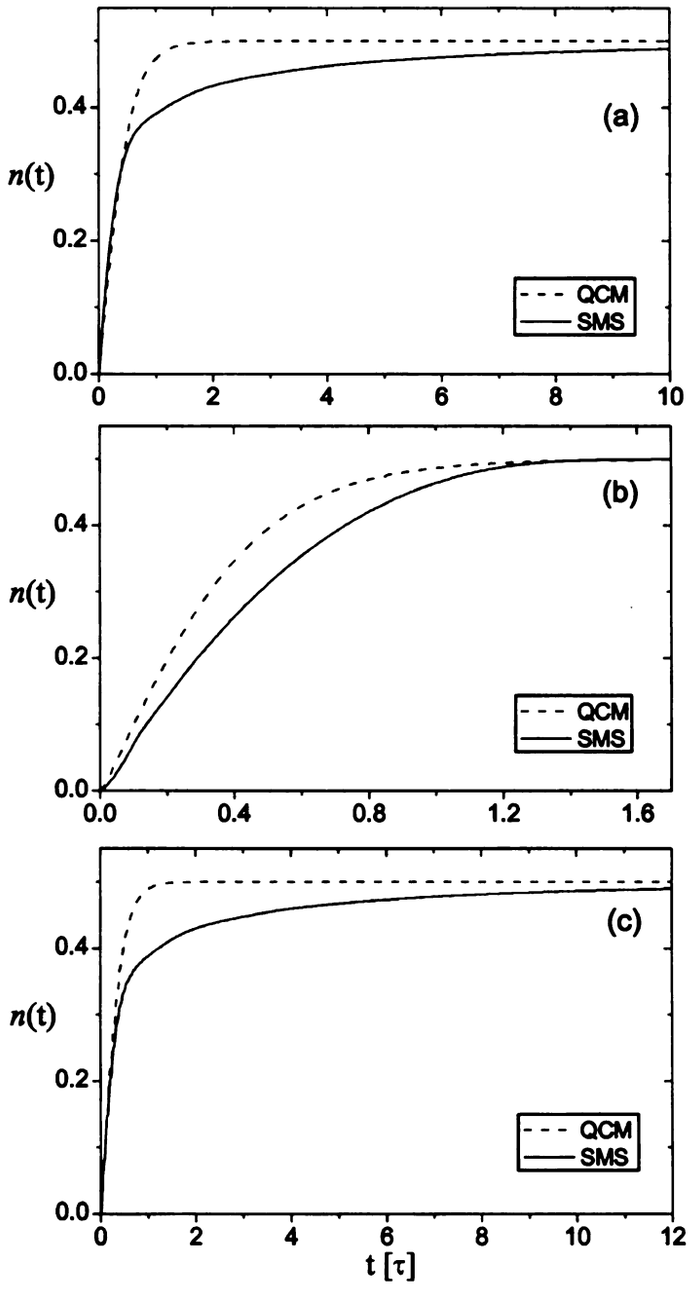

Figure 4.9: The same as figure 4.8 but with $\nu = 1$. For (a), (b) and (c), t is rescaled with $\tau = 8.96\Gamma_S^{-1}, 436.8\Gamma_S^{-1}$ and $1800\Gamma_S^{-1}$, respectively.

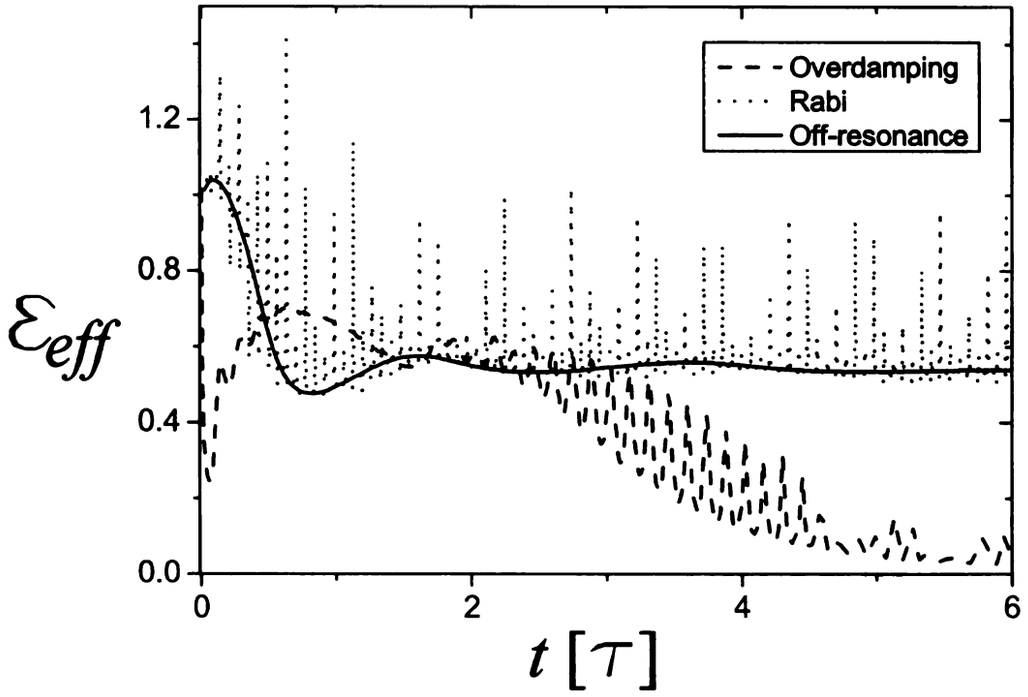

Figure 4.10: ξ_{eff} as a function of evolution time, which is rescaled with the transfer time τ for each dynamical regime. Parameters are given the same as in figure 4.5.

Unlike in the QCM model, the atomic dipole interaction, essentially a virtual photon exchange effect, is not included in the SMS model since it only accounts for 'real' photons. Thus the SMS model is valid only if the dipole interaction is negligible. In practice, this requires $k_L W \gg A$, as discussed in section 4.6.2. For $k_L W = 100$ and $A = 10$, we have seen in 4.3.1 that the phase shift due to dipole interaction stays small throughout the dynamics, thus validating the SMS model using these parameters.

In the SMS model, in both off-resonance and Rabi regimes, the laser depletion effect is negligible, allowing pump 2 to homogenously excite atoms across the condensate. Thus all atoms contemporarily experience ac-Stark shift or phase switching as in the QCM dynamics, with spatial homogeneity preserved. In the weak damping regime, however, the laser depletion effect is strong, and amplification of the signal wave is sequentially driven from front to back. Yet due to the elimination of ac-Stark

shift and that the phase of signal wave is preserved during MWA, the relative phase between pump 1 and the signal wave is homogeneously conserved at all time. Consequently, the generated idler beam constantly possesses the initial phase of $\theta_{12}(0)$, making an overdamped MWA a good candidate for state mapping.

To verify the above analysis, in figure 4.11 we plot the phase $\theta_{12}(\tilde{z},\tilde{t})$ at $\tilde{x},\tilde{y}=0$. In figure (a) for the off-resonance regime, $\theta_{12}(t)$ is shifted linearly in time in a 2π interval, as expected. Its spatial homogeneity is preserved through $t=\tau/2$, after which the rear $+\tilde{z}$ region grows out of phase with the front $-\tilde{z}$ region. While this indicates the emergence of phase inhomogeneity, the fact is that in the out-of-phase region, pump 1 is (nearly) depleted, so that its phase relative to the signal wave become meaningless. The spatial homogeneity is preserved in a sense that θ_{12} stays uniform across the region where both pump 1 and signal wave are macroscopically populated. In figure (b) for the overdamping regime, $\theta_{12}(t)$ is found to be at its initial value of zero through the dynamics in regions where pump 1 atoms are undepleted, thus preserving the spatial homogeneity. In figure (c) for the Rabi regime, θ_{12} is switched between 0 and π at the Rabi-frequency of pump 2, agreeing with the QCM result. Similarly to the off-resonance regime in figure (a), here the phase homogeneity is as well preserved.

4.4.4 Further discussions

In this part of the chapter, we have studied the MWA dynamics via the semi-classical full-mode theory, taking into account the laser depletion and spatial effects. In both off-resonance and Rabi regimes, the laser depletion is negligible. Because of the spatial effect, the signal wave is firstly amplified in the back along the beam propagation direction. In the two regimes, the population transfer is fast before half of pump 1 atoms are depleted, and agrees well with the QCM theory. Then, as the spatial modes evolve into mismatching distributions, the population transfer is sig-

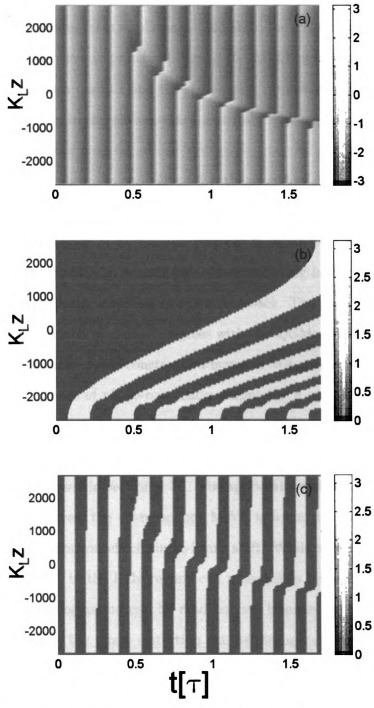

Figure 4.11: Figures (a)-(c) are the surface plots of $\theta_{12}(\tilde{z},\tilde{t})$ at $\tilde{x},\tilde{y}=0$ for dynamical regimes in figure 4.5 (a)-(c). Initially, $\theta_{12}(\tilde{z},0)=0$.

nificantly slowed down, becoming divergent from the QCM results. In all dynamical regimes, the phase of each matter wave is found to be practically homogeneous across the condensates. Asides from small mean-field shift due to atomic dipole interaction, the phase of signal wave is preserved during the MWA dynamics. In contrast, the relative phase between pump 1 and the signal wave respectively experiences ac-Stark shift and π-switching in the off-resonance and Rabi regimes, but is conserved in the overdamping regime.

Additionally, as shown in appendix 4.6.4, the atom loss dynamics similarly agrees with QCM until the half-depletion point, and then diverges. The ultimate atom loss fraction upon completion of population transfer is enhanced by a factor of $3 \sim 4$. In the overdamping region, however, due to a dominating laser depletion effect, the signal wave is sequentially amplified from front to back. The population transfer yield smooth dynamics, which moderately agrees with the QCM results all the time. The atom loss fraction, however, is constantly a factor of ≈ 4 greater than that via QCM.

Hence, for purpose of phase-coherently amplifying a matter wave, it is feasible to operate MWA in any dynamical regimes. For a given laser intensity, however, the amplification rate is always higher if using resonant driving, with which P_e is maximized, as discussed in section 4.3.1. For applications of state mapping between light and matter waves, the off-resonance MWA is found to be unsuitable, due to the strong phase distortion effect via ac-Stark shift. While as well undergoing phase distortion, the MWA in the Rabi regime can nonetheless be used for state mapping in that the phase information can be read out via interferometric methods. In the overdamping regime, the phase distortion can be strongly suppressed, also allowing state mapping.

In the resonant regime, due to the sudden slowdown of population transfer beyond the half-depletion point, for efficiency it is the optimal strategy is to stop the dynamics at the half-depletion time. In this domain, the SMS dynamics turns out to

agree well with the QCM predictions. Thus we can approximate the SMS dynamics by the analytical formulas derived in the QCM model. Using equation (4.13), the half-depletion time τ_h, for which $n(\tau_h) = \frac{1}{2}n(0) + \frac{1}{4}$, is given by

$$\tau_h = \frac{2}{\Gamma_s} \ln\left(\frac{3\nu^2 + 7\nu + 2}{\nu^2 + 3\nu}\right). \tag{4.42}$$

The atom loss fraction at τ_h for $\nu < A^2$ is then

$$\epsilon_{loss}(\tau_h) = \frac{\gamma}{\Gamma_s} \ln\left(1 + \frac{1}{2}\nu\right), \tag{4.43}$$

as from equation (4.112) in the appendix.

In the overdamping regime, both the dynamics of differential population fraction $n(t)$ and atom loss fraction $\varepsilon_{loss}(t)$ is more smooth through the dynamics, following the QCM dynamics. It is thus equally efficient to evolve the system until the depletion of pump 1. The transfer dynamics can then be approximated by equation (4.13). The final atom loss fraction is, however, about four times greater than that of QCM, given by

$$\epsilon_{loss}(\tau) = 4\frac{\gamma}{\Gamma_s} \ln(1 + \nu). \tag{4.44}$$

4.5 Conclusion

To conclude, focusing on a prototypical three-level Raman system, we have extended the study of matter-wave amplification to the resonant driving regime, in order to find the optimal scheme for applications of phase-coherently amplifying a matter-wave, as well as quantum state mapping between light and matter waves. We developed the quantum single-mode as well the semiclassical multi-mode theory. Comparatively, the former yields more intuitive and computationally accessible dynamics associated with clear physical interpretations, while the latter takes into

account the laser depletion and spatial effects and is thus more 'physical'.

Depending on driving laser, the system dynamics can be classified into off-resonance, overdamping and Rabi dynamical regimes. For population dynamics, the single-mode theory predicts correct behaviors in the overdamping regime, but is valid only through half depletion of pump 1 atoms in the off-resonance and Rabi regimes, after which the population transfer becomes inefficient. We find that for a given laser intensity, the largest amplification rate is obtained using resonant driving, whereas the ultimate maximum rate is achieved in the Rabi regime. On the other hand, the atom loss fraction upon completing population transfer is a universal quality independent of dynamical regimes. In all dynamical regimes, the phase of each matter wave is effectively homogeneous across the condensates. The relative phase between pump 1 and the signal wave respectively experiences ac-Stark shift and π-switching in the off-resonance and Rabi regimes, but is preserved in the overdamping regime.

In short, it is the optimal strategy to use resonant driving, instead of the commonly used off-resonance one, to perform MWA for the purposes of amplifying a matter wave and/or mapping quantum states between light and matter waves. If in the Rabi regime, it is most efficient to stop the dynamics once half of pump 1 atoms are transferred to the signal wave.

4.6 Derivations and further discussions

4.6.1 Master-equation formalism

In this section, we develop the master-equation formalism for the Λ-MWA system. Let $\hat{\Psi}_j(\mathbf{r})$ $(j = 1, 2, 3)$ be the field annihilate operator for level $|j\rangle$, the standard master equation for the Raman MWA system depicted in figure 4.1 (a) reads [59] (A detailed

derivation of this kind of master equation is given in the appendix of chapter II)

$$\begin{aligned}\dot{\rho}(t) &= -i[\hat{H}_0, \rho(t)] - \int d^3r d^3r' \times \\ &\sum_{j=1,2} \Big[L_j(\mathbf{r}-\mathbf{r}') \hat{\Psi}_3^\dagger(\mathbf{r}) \hat{\Psi}_j^\dagger(\mathbf{r}') \hat{\Psi}_j(\mathbf{r}) \hat{\Psi}_3(\mathbf{r}') \rho(t) \\ &\quad - L_j^*(\mathbf{r}-\mathbf{r}') \hat{\Psi}_j^\dagger(\mathbf{r}) \hat{\Psi}_3(\mathbf{r}) \rho(t) \hat{\Psi}_3^\dagger(\mathbf{r}') \hat{\Psi}_j(\mathbf{r}') + H.c. \Big] .\end{aligned} \tag{4.45}$$

Here, the one-body Hamiltonian $\hat{H}_0$ is given by

$$\begin{aligned}\hat{H}_0 &= \int d^3r (\Delta - i\frac{\gamma}{2}) \hat{\Psi}_3^\dagger(\mathbf{r}) \hat{\Psi}_3(\mathbf{r}) + \\ &\quad + \int d^3r \frac{\Omega(\mathbf{r})}{2} \hat{\Psi}_3^\dagger(\mathbf{r}) \hat{\Psi}_1(\mathbf{r}) + H.C,\end{aligned} \tag{4.46}$$

with Δ the detuning of pump 2 from resonance and Ω the Rabi frequency. γ is the spontaneous relaxation rate of $|3\rangle$ level. The nonlinear two-body cooperative coefficient is given by [123]

$$\begin{aligned}L_j(\mathbf{r}-\mathbf{r}') &= \frac{d_j^2 c}{2(2\pi)^3 \epsilon_0} \int d^3\mathbf{k}\; k(1 - |\hat{d}_j \cdot \hat{k}|^2) \\ &\times e^{i\mathbf{k}\cdot(\mathbf{r}-\mathbf{r}')} \left[\pi\delta(ck - v_j + \Delta) + i\frac{\mathcal{P}}{ck - v_j + \Delta} \right] .\end{aligned} \tag{4.47}$$

for $j = 1, 2$. Here, $\hbar v_j$ is the level-spacing between $|3\rangle$ and $|j\rangle$, while d_j and $\hat{d}_j$ are amplitude and unit vector of dipole moment for corresponding transitions. The symbol $\mathcal{P}$ stands for taking principle value when performing integration. This integral can be carried out analytically, giving

$$L_j(\mathbf{r}-\mathbf{r}') = \frac{3\Gamma_j}{4} e^{-i\varsigma_j} \left[\sin^2\theta \frac{i}{\varsigma_j} + (1 - 3\cos^2\theta) \left(\frac{1}{\varsigma_j^2} - \frac{i}{\varsigma_j^3} \right) \right] , \tag{4.48}$$

with $\varsigma_j = (v_j - \Delta)|\mathbf{r} - \mathbf{r}'|/c$, and θ being the angle between $\hat{d}_j$ and $\mathbf{r} - \mathbf{r}'$. $\Gamma_j = (v_j - \Delta)^3 d_j^2/(3\pi\epsilon_0\hbar c^3)$ is the spontaneous decay rate from the Δ-detuned $|3\rangle$ to ground $|j\rangle$ level.

In the master equation (4.45), the real part of $L_j(\mathbf{r} - \mathbf{r}')$, related to the optical depth of collective emission, characterizes the population transfer between level $|3\rangle$ and $|j\rangle$. The imaginary part contributes an energy shift due to (virtual) photon exchange between atoms, the laser-induced dipole-dipole interaction. In the limit $|\mathbf{r} - \mathbf{r}'| \to 0$ we find

$$L(0) = \frac{\Gamma}{2} + i\delta, \tag{4.49}$$

where the imaginary part, δ, is an infinite quantity, reflecting the fact that the standard two-level atom-field interaction model is not properly renomalized. Physically, this term is a Lamb-type shift in the energy of the excited-state due to interaction with the vacuum modes of the EM field. In our system we can always choose a rotating frame to absorb this shift, so that we can take $\delta = 0$ without loss of generality.

4.6.2 Evaluating cooperative parameter

In the strong interaction regime, the spatial profile of the condensate is well approximated by the Thomas-Fermi distribution, as [6]

$$|\Phi_{TF}(\mathbf{r})|^2 = \frac{m}{4\pi\hbar^2 a}\left(\mu - \frac{m}{2}\left(\omega_\perp^2\rho^2 + \omega_z^2 z^2\right)\right) \tag{4.50}$$

with a is the s-wave scattering length, m is atomic mass, and

$$\mu = \left(\frac{15\sqrt{m}\omega_\perp^2\omega_z\hbar^2 a}{4\sqrt{2}}\right)^{2/5} \tag{4.51}$$

is the chemical potential determined by wavefunction normalization. Here, we have assumed the external potential to be an azimuthal-symmetry harmonic trap, with $\omega_\perp$

and ω_z the transverse and longitude trapping frequency. Such a density distribution corresponds a RMS width of

$$W = \frac{1}{\sqrt{7}} \left(\frac{15a\omega_z \hbar^2}{m^2 \omega_\perp^3} \right)^{1/5}, \tag{4.52}$$

and length of

$$L = \frac{1}{\sqrt{7}} \left(\frac{15a\omega_\perp^2 \hbar^2}{m^2 \omega_z^4} \right)^{1/5}. \tag{4.53}$$

With such defined W and L, the Thomas-Fermi distribution (4.50) can then be simplified to

$$|\Phi_{TF}(\mathbf{r})|^2 = \frac{15}{56\sqrt{7}\pi W^2 L} \left[1 - \frac{1}{7} \left(\frac{\rho^2}{W^2} + \frac{z^2}{L^2} \right) \right]. \tag{4.54}$$

Depending on W smaller or greater than L, the condensate is in a 'cigar' or 'disk' shape. Inserting this profile back to (4.9), the collective parameter f_j can be numerically evaluated. The evaluation is nonetheless difficulty, since it involves a six-dimension integral with poles. In the following, we show a method to reduce the dimension of this integral from six to three, providing numerical accessibility.

To proceed, the collectivity parameter is given by

$$f = \int d^3r d^3r' L(\Delta\mathbf{r}) |\phi(\mathbf{r})|^2 |\phi(\mathbf{r}')|^2 e^{i\mathbf{k}_0 \cdot \Delta\mathbf{r}} \tag{4.55}$$

with $\Delta\mathbf{r} = \mathbf{r} - \mathbf{r}'$ and

$$L(\Delta\mathbf{r}) = \frac{3\Gamma}{2} e^{-i\varsigma} \left[\sin^2\theta \frac{i}{\varsigma} + (1 - 3\cos^2\theta) \left(\frac{1}{\varsigma^2} - \frac{i}{\varsigma^3} \right) \right] \tag{4.56}$$

where $\varsigma = k_L |\Delta\mathbf{r}|$, θ is the angle between Δ the dipole moment and $\Delta\mathbf{r}$. Defining dimension-less coordinates

$$x_c = \frac{x + x'}{2\sqrt{7}W}, \quad y_c = \frac{y + y'}{2\sqrt{7}W} \quad z_c = \frac{z + z'}{2\sqrt{7}L}$$

$$x_r = \frac{x - x'}{\sqrt{7}W}, \quad y_r = \frac{y - y'}{\sqrt{7}W} \quad z_r = \frac{z - z'}{\sqrt{7}L} \tag{4.57}$$

we have

$$\begin{aligned} f &= \frac{225}{64\pi^2} \int d^3r_c d^3r_r L(x_r, y_r, z_r) \\ &\left[1 - \left(r_c^2 + \frac{r_r^2}{4} + \mathbf{r}_c \cdot \mathbf{r}_r\right)\right]\left[1 - \left(r_c^2 + \frac{r_r^2}{4} - \mathbf{r}_c \cdot \mathbf{r}_r\right)\right] \end{aligned} \tag{4.58}$$

with

$$L(x_r, y_r, z_r) = \frac{3\Gamma}{2} e^{-i\varsigma}\left[\sin^2\theta \frac{i}{\varsigma} + (1 - 3\cos^2\theta)\left(\frac{1}{\varsigma^2} - \frac{i}{\varsigma^3}\right)\right]. \tag{4.59}$$

Here, $\varsigma = k_L\sqrt{7W^2\rho_r^2 + 7L^2 z_r^2}$ and $\cos^2\theta = \frac{y_r^2}{\rho_r^2 + z_r^2}$, with $\rho_r = \sqrt{x_r^2 + y_r^2}$. We calculate for $\mathbf{k}_0 = k_L\hat{z}$. First, we do the d^3r_c integral, where we let $\mathbf{r}_r = r_r\hat{z}$.

$$\begin{aligned} f &= \frac{225}{64\pi^2} \int d^3r_r L(x_r, y_r, z_r) e^{ik_L\sqrt{7}Lz_r} 2\pi \int_0^{\sqrt{1-r_r^2/4}} dr_c r_c^2 \\ &\times \int_{-\text{Min}\{(1-r_c^2-r_r^2/4)/r_c r_r, 1\}}^{\text{Min}\{(1-r_c^2-r_r^2/4)/r_c r_r, 1\}} d\cos\theta \left[\left(1 - \left(r_c^2 + \frac{r_r^2}{4}\right)\right)^2 - r_c^2 r_r^2 \cos^2\theta\right] \\ &= \frac{225}{64\pi^2} \int d^3r_r L(x_r, y_r, z_r) e^{ik_L\sqrt{7}Lz_r} 2\pi \left\{\int_0^{1-r_r/2} dr_c\, r_c^2 \right. \\ &\times \int_{-1}^{1} d\mu \left[\left(1 - \left(r_c^2 + \frac{r_r^2}{4}\right)\right)^2 - r_c^2 r_r^2 \mu^2\right] + \int_{1-r_r/2}^{\sqrt{1-r_r^2/4}} dr_c \\ &\left. r_c^2 \int_{-(1-r_c^2-r_r^2/4)/r_c r_r}^{(1-r_c^2-r_r^2/4)/r_c r_r} d\mu \left[\left(1 - \left(r_c^2 + \frac{r_r^2}{4}\right)\right)^2 - r_c^2 r_r^2 \mu^2\right]\right\} \\ &= \frac{225}{64\pi^2} \int d^3r_r L(x_r, y_r, z_r) e^{ik_L\sqrt{7}Lz_r} \\ &\times 2\pi(-2 + r_r)^4 \frac{32 + r_r(64 + 3r_r(8 + r_r))}{3360} \\ &= \frac{15}{7168\pi} \int d^3r_r L(x_r, y_r, z_r) e^{ik_L\sqrt{7}Lz_r} (-2 + r_r)^4 \left[32 + r_r(64 + 3r_r(8 + r_r))\right] \end{aligned}$$

Note here $e^{ik_L\sqrt{7}Lz_r}$ can be replaced by $\cos(k_L\sqrt{7}Lz_r)$, due to the symmetry on z_r. This integral is hard to be solved, because it is oscillatory. To overcome this difficulty, we change the integrand to

$$\begin{aligned} f &= \frac{15}{7168\sqrt{7}^3\pi k_L^3 W^2 L}\int d^3r_0 L(x_0,y_0,z_0) \\ &\quad \times e^{iz_0}(-2+r_1)^4\left[32+r_1(64+3r_1(8+r_1)\right] \end{aligned} \tag{4.60}$$

where

$$\begin{aligned} r_1 &= \sqrt{\frac{x_0^2+y_0^2}{7(k_L W)^2}+\frac{z_0^2}{7(k_L L)^2}} \\ &= \sqrt{\frac{r_0^2\sin^2\theta}{7(k_L W)^2}+\frac{r_0^2\cos^2\theta}{7(k_L L)^2}} \\ &= \frac{r_0}{\sqrt{7}k_L W}\sqrt{1-(1-1/A^2)\cos^2\theta}, \end{aligned} \tag{4.61}$$

The boundary condition of $r_1 \le 2$ is then $\cos^2\theta \ge (1-28k_L^2W^2/r_0^2)/(1-1/A^2) \equiv \mu^2$, valid for the aspect ratio $A > 1$. The two-body nonlinearity is scaled to give $L(0) = 1 + i\delta$

$$L(r_0,\theta,\phi) = \frac{3}{2}e^{-ir_0}\left[(1-\sin^2\theta\sin^2\phi)\frac{i}{r_0}+(1-3\sin^2\theta\sin^2\phi)\left(\frac{1}{r_0^2}-\frac{i}{r_0^3}\right)\right] \tag{4.62}$$

where $r_0 = \sqrt{x_0^2+y_0^2+z_0^2}$. The integral is then

$$\begin{aligned} f &= \frac{15}{7168\sqrt{7}^3\pi k_L^3 W^2 L}\int_0^{2\sqrt{7}k_L WA} dr_0\, r_0^2\left\{\int_{-1}^{-\mu} d\cos\theta+\int_{\mu}^{1} d\cos\theta\right\} \\ &\quad \times e^{ir_0\cos\theta}(-2+r_1)^4\left[32+r_1(64+3r_1(8+r_1)\right]\int_0^{2\pi} d\phi L(r_0,\theta,\phi) \qquad (4.63) \\ &= \frac{15}{7168\sqrt{7}^3\pi k_L^3 W^2 L}\int_0^{2\sqrt{7}k_L WA} dr_0\, r_0^2\, 2\int_{-1}^{-\mu} d\cos\theta\cos(r_0\cos\theta) \end{aligned}$$

$$\times(-2+r_1)^4\left[32+r_1(64+3r_1(8+r_1)\right]\int_0^{2\pi}d\phi L(r_0,\theta,\phi) \tag{4.64}$$

where $\mu=\sqrt{(1-28k_L^2W^2/r_0^2)/(1-1/A^2)}$ or 0 if $28k_L^2W^2/r_0^2>1$. In this way, we have successfully reduced the six-dimension integral to only 3, providing the feasibility to be numerically solved by mathematica codes.

For an analytical expression of f_j, we approximate the Thomas-Fermi profile (4.54) by a Gaussian distribution of

$$|\Phi_{GS}(\mathbf{r})|^2=\frac{1}{(2\pi)^{3/2}W^2L}\exp\left(-\frac{\rho^2}{2W^2}-\frac{z^2}{2L^2}\right), \tag{4.65}$$

which yields to the same RMS width and length with (4.54). Using formula (4.47) for $L_j(\mathbf{r}-\mathbf{r}')$, the collective parameter f_j is then explicitly given by

$$f_j = \frac{3}{8\pi^2k_L^3}\int d^3\mathbf{k}\,k(1-|\hat{d}_j\cdot\hat{k}|^2)\chi_j(\mathbf{k})\left[\pi\delta(k-k_L)+i\frac{\mathcal{P}}{k-k_L}\right], \tag{4.66}$$

with

$$\chi_j(\mathbf{k})=\int d^3rd^3r'|\phi(\mathbf{r})\phi(\mathbf{r}')|^2e^{-i(\mathbf{k}-\mathbf{k}_L)\cdot(\mathbf{r}-\mathbf{r}')}. \tag{4.67}$$

Here we have assumed $v_{1,2}-\Delta=ck_L$, i.e., the $|1\rangle$ and $|2\rangle$ level are degenerate. For $\hat{d}_1=\hat{d}_2$, we then have $\chi_1(\mathbf{k})=\chi_2(\mathbf{k})\equiv\chi(\mathbf{k})$, and therefore $f_1=f_2\equiv f$. Using straightforward center-of-mass and relative coordinate transformation, $\chi_j(\mathbf{k})$ can be analytically evaluated to give

$$\chi(\mathbf{k})=\exp\left(-k^2\sin^2\theta W^2-(k\cos\theta-k_L)^2L^2\right), \tag{4.68}$$

for $\mathbf{k}_L=k_L\hat{z}$. Inserting this back to (4.66), it is clear that f is dominantly contributed by integration in the regime near $\theta=0$, due to the exponentially decrease of $\chi_j(\mathbf{k})$ in θ^2.

To proceed calculating this integral, we introduce the following dimensionless parameters, $w = k_L W$, $\ell = k_L L$. From equation (4.66), for $\hat{d}_j = \frac{1}{\sqrt{2}}(\hat{x} \pm i\hat{y})$, the integrand is azimuth-symmetric, so that

$$f = \frac{3}{4\pi k_L^3} \int_{-\infty}^{\infty} dk \, d\cos\theta \, k^3 \frac{1+\cos^2\theta}{2} \chi_j(\mathbf{k}) \left[\pi\delta(k-k_L) + i\frac{\mathcal{P}}{k-k_L} \right], \quad (4.69)$$

Introducing a small-valued parameter $\nu = 1 - \cos\theta$, the above integral is rewritten in the form of

$$f = \frac{3}{4\pi} \int_{-\infty}^{\infty} dk \int_0^2 d\nu \, k^3 (1 - \nu + \frac{\nu^2}{2}) \exp[-w^2 k^2 (2\nu - \nu^2) - \ell^2 (k - 1 - k\nu)^2] \times \left[\pi\delta(k-1) + i\frac{\mathcal{P}}{k-1} \right], \quad (4.70)$$

where we have substituted $k \to k/k_L$. It is noticed that for practical parameters of $w, \ell \gg 1$, this integral is no-vanishing only at $\nu \ll 1$. To calculate the real part f_R, using $2\nu \gg \nu^2$ and $1 - \nu \approx 1$, and performing the $\delta(k-1)$ integral give us

$$f_R \approx \frac{3}{4} \int_0^2 \exp(-2w^2\nu - \ell^2\nu^2) d\nu = \frac{3\sqrt{\pi}}{8\ell} \exp(w^4/\ell^2) erfc(\frac{w^2}{\ell}). \quad (4.71)$$

It turns out that this function can be well approximated by a much more evident form of

$$f_R = \frac{3\sqrt{\pi}}{8(\ell^{4/3} + (\sqrt{\pi}w^2)^{4/3})^{3/4}}. \quad (4.72)$$

To evaluate the imaginary principle-value part, we introduce $x = k - 1$, so that the corresponding integral becomes

$$f_I = \frac{3}{4\pi} \int_{-\infty}^{\infty} dx \int_0^2 d\nu \, \frac{(1+x)^3}{x} (1 - \nu + \frac{\nu^2}{2}) \exp[-w^2 (x+1)^2 (2\nu - \nu^2) - \ell^2 (x - \nu - x\nu)^2], \quad (4.73)$$

To the leading order in ν and x, the integral is simply

$$f_I = \frac{3}{4\pi}\int_{-\infty}^{\infty} dx \int_0^2 d\nu \,(\frac{1}{x}+3)\exp[-2w^2\nu - \ell^2(x-\nu)^2], \tag{4.74}$$

$$\tag{4.75}$$

The expression for imaginary part is then obtained in the limit of large and small Fresnel number $\mathcal{F}$ by

$$f_I \approx \begin{cases} \frac{3}{8\sqrt{\pi}\ell}(2\ln(\ell/w^2) - \gamma_e, & \mathcal{F} \gg 1; \\ \frac{3(\ell^2+w^2)}{8\sqrt{\pi}w^4\ell}, & \mathcal{F} \ll 1. \end{cases} \tag{4.76}$$

$$\tag{4.77}$$

Here $\gamma_e = 0.577216$ is Euler's constant, and the Fresnel number

$$\mathcal{F} = \frac{k_L W^2}{2\pi L} \tag{4.78}$$

is a measure of the number of superradiant endfire modes within the end-fire angle $\theta_s = \frac{W}{L}$. When $\mathcal{F} \gg 1$, there are many competing end-fire modes, while for $\mathcal{F} \leq 1$, there are just two end-fire modes, one for each direction along the z-axis.

To show the validity of these formulas, in figure 4.12, we compare (4.72) and (4.76) to the exact results by numerically evaluating f for the Thomas-Fermi profiles (4.54). For all range of width W and aspect ratio $A = L/W$, good agreements are found for the real part of f. For the imaginary part, however, formula (4.76) is valid only for $W \gtrsim 2\lambda_L$, especially for large aspect ratio A. In practice, this parameter region nonetheless matches that of typically prepared condensates in undergoing MWA experiments [102, 101, 108, 112].

Finally, for typical MWA experiments performed with 'cigar'-shape condensates, $k_L W \gg A$ [108], so that $f_I/f_R \approx A/(k_L W) \ll 1$. This indicates that mean-

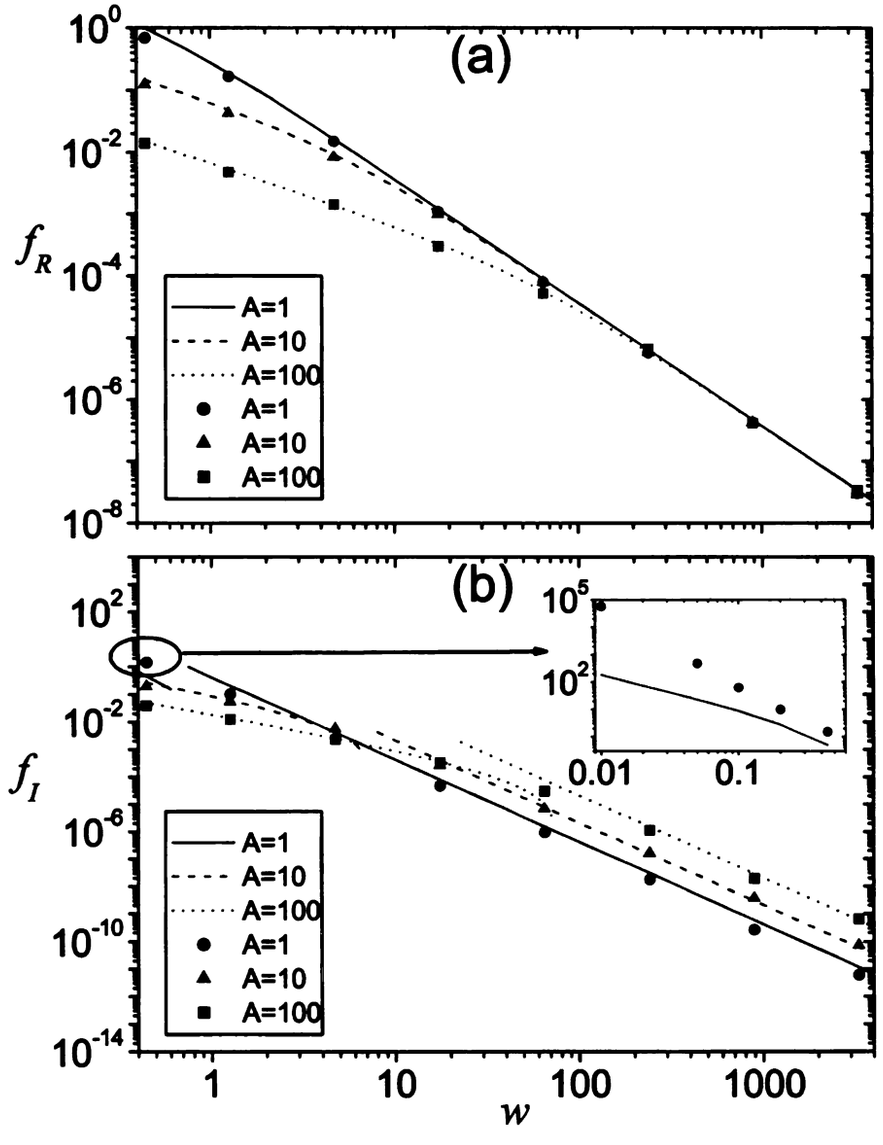

Figure 4.12: The cooperative parameter f for Thomas-Fermi condensates, where figure (a) and (b) show the real and imaginary parts of f_R and f_I. In both figures, discrete points are numerical results for Thomas-Fermi profile, while lines are plotted for formula (4.72) and (4.76), respectively.

field dephasing due to dipole-dipole interaction is negligible compared to population transfer, thus allowing amplifying the signal wave without introducing significant phase distortion. Henceforth, all analysis and discussions are based on $f_R \gg f_I$. We note asides from this laser-induced dipole interaction, other dephasing channels, such as s-wave collision, can also be safely neglected due to the short time scale ($\sim$ ns) of the MWA process under considerations.

4.6.3 Derivation of Maxwell-Schrödinger equation

Let $\Psi_j(\mathbf{r})$ (j=1,2,3) be the Schrödinger field of state $|j\rangle$, and $E_L^{(+)}$ and $E_S^{(+)}$ be the positive-frequency optical fields of the laser pump 2 and scattered idler field, the generic Maxwell-Schrödinger equation reads [257]

$$
\begin{aligned}
i\hbar\frac{\partial}{\partial t}\Psi_1(\mathbf{r}) &= \left[-\frac{\hbar^2}{2m}\nabla^2 + V_{trap}(\mathbf{r})\right]\Psi_1(\mathbf{r},t) - \mathbf{d}_1\cdot\mathbf{E}_L^{(-)}\Psi_3(\mathbf{r},t), \quad (4.79)\\
i\hbar\frac{\partial}{\partial t}\Psi_2(\mathbf{r},t) &= \left[-\frac{\hbar^2}{2m}\nabla^2 + V'_{trap}(\mathbf{r})\right]\Psi_2(\mathbf{r},t) - \mathbf{d}_2\cdot\mathbf{E}_S^{(-)}\Psi_3(\mathbf{r},t), \quad (4.80)\\
i\hbar\frac{\partial}{\partial t}\Psi_3(\mathbf{r},t) &= \left[-\frac{\hbar^2}{2m}\nabla^2 + V''_{trap}(\mathbf{r}) + \hbar\left(\omega_3 - i\frac{\chi_s\gamma}{2}\right)\right]\Psi_3(\mathbf{r},t)\\
&\quad - \left[\mathbf{d}_1^*\cdot\mathbf{E}_L^{(+)}\Psi_1(\mathbf{r},t) + \mathbf{d}_2^*\cdot\mathbf{E}_S^{(+)}\Psi_2(\mathbf{r},t)\right], \quad (4.81)\\
\frac{\partial^2}{\partial t^2}\mathbf{E}_{L,S}^{(\pm)} &= c^2\nabla^2\mathbf{E}_{L,S}^{(\pm)} - \frac{1}{\epsilon_0}\frac{\partial^2}{\partial t^2}\mathbf{P}_{1,2}^{(\pm)}. \quad (4.82)
\end{aligned}
$$

Here, $E_{L,S}^{(-)} = E_{L,S}^{(+)*}$ are the negative-frequency electric fields, $\hbar\omega_3$ is bare energy of level $|3\rangle$, and we have assumed $|1\rangle$ and $|2\rangle$ to be degenerate. The non-Hermitian term of $-i\hbar\chi_s\gamma$, with χ_s the time-dependent superradiance enhancement factor given in Eq. (4.106) in appendix, describes the atom loss from the matter-waves under consideration via spontaneous and superradiant decays of the $|3\rangle$ level. The trapping potentials for $|1\rangle$, $|2\rangle$ and $|3\rangle$ states are V_{trap}, V'_{trap} and V''_{trap}, respectively. $\mathbf{d}_{1,2} = \frac{1}{\sqrt{2}}(\hat{\mathrm{x}} - i\hat{\mathrm{y}})d_{1,2}$ are the dipole moments for the $|1\rangle \leftrightarrow |3\rangle$ and $|2\rangle \leftrightarrow |3\rangle$ transitions.

$\mathbf{P}_{1,2}^{(\pm)}$ are the macroscopic polarizations of the atomic medium, defined as

$$\mathbf{P}_{1,2}^{(+)}(\mathbf{r}) = \frac{1}{\sqrt{2}}(\hat{\mathrm{x}} - i\hat{\mathrm{y}})d_{1,2}\Psi_{1,2}^{*}(\mathbf{r})\Psi_3(\mathbf{r}). \tag{4.83}$$

As seen in the single-mode model, in present dynamical regimes of interests, the MWA is processed within a time scale of $1 \sim 10^3$ns, much shorter than any time scales related to atomic motions. Thus we can neglect translational degrees of freedom, leaving only the light-matter coupling terms in equation (4.79)-(4.82). For $\hat{\mathbf{z}}$ being the common propagation direction of pump 2 and idler beams, we introduce the following slowly varying envelope functions,

$$\mathbf{E}_{L,S}^{(+)}(\mathbf{r},t) = \frac{1}{\sqrt{2}}(\hat{\mathrm{x}} - i\hat{\mathrm{y}})E_{L,S}^{(+)}(\mathbf{r},t)e^{i(k_L z - \omega_L t)}, \tag{4.84}$$

with $\omega_L = ck_L$ laser frequency. The normalized slowly-varying Schrödinger fields are introduced in a similar manner, where

$$\begin{aligned}\Psi_{1,2}(\mathbf{r},t) &= \sqrt{N}\psi_{1,2}(\mathbf{r},t)\\ \Psi_3(\mathbf{r},t) &= \sqrt{N}\psi_3(\mathbf{r},t)e^{i(k_L z - \omega_L t)}\end{aligned}$$

with N the total atom number.

In the rotation frame of laser frequency ω_L, the Maxwell-Schrödinger equation (4.79)-(4.82) is then rewritten as

$$\frac{\partial}{\partial t}\psi_1(\mathbf{r},t) = \frac{id_1}{\hbar}E_L^{(+)*}(\mathbf{r},t)\psi_3(\mathbf{r},t), \tag{4.85}$$

$$\frac{\partial}{\partial t}\psi_2(\mathbf{r},t) = \frac{id_2}{\hbar}E_S^{(+)*}(\mathbf{r},t)\psi_3(\mathbf{r},t), \tag{4.86}$$

$$\frac{\partial}{\partial t}\psi_3(\mathbf{r},t) = -\left(i\Delta + \frac{\chi_s\gamma}{2}\right)\psi_3(\mathbf{r},t) + \frac{id_1^*}{\hbar}E_L^{(+)}(\mathbf{r},t)\psi_1(\mathbf{r},t) + \frac{id_2^*}{\hbar}E_S^{(+)}(\mathbf{r},t)\psi_2(\mathbf{r},t), \tag{4.87}$$

$$\frac{\partial}{\partial t}E_L^{(+)}(\mathbf{r},t) = -c\frac{\partial E_L^{(+)}(\mathbf{r},t)}{\partial z} + i\frac{d_1\omega_L N}{2\epsilon_0}\psi_1^*(\mathbf{r},t)\psi_3(\mathbf{r},t), \tag{4.88}$$

$$\frac{\partial}{\partial t}E_S^{(+)}(\mathbf{r},t) = -c\frac{\partial E_S^{(+)}(\mathbf{r},t)}{\partial z} + i\frac{d_2\omega_L N}{2\epsilon_0}\psi_2^*(\mathbf{r},t)\psi_3(\mathbf{r},t), \tag{4.89}$$

with $\Delta = \omega_3 - \Omega_L$. In obtained these equations, we have applied the standard slowly-varying envelope approximation, where

$$\begin{aligned}
\left|\frac{\partial E_{L,S}^{(+)}(\mathbf{r},t)}{\partial t}\right| &\ll \omega_L \left|E_{L,S}^{(+)}(\mathbf{r},t)\right| \\
\left|\nabla E_{L,S}^{(+)}(\mathbf{r},t)\right| &\ll k_L \left|E_{L,S}^{(+)}(\mathbf{r},t)\right| \\
\left|\frac{\partial}{\partial t}\left(\psi_{1,2}^*\psi_3\right)\right| &\ll \omega_L \left|\psi_{1,2}^*\psi_3\right|.
\end{aligned}$$

Defining new variables $p = t + c^{-1}z$, $q = t - c^{-1}z$, we have $\frac{\partial}{\partial t} + c\frac{\partial}{\partial z} = 2\frac{\partial}{\partial p}$, reducing the equation of motion for light fields to

$$\frac{\partial E_L^{(+)}(\mathbf{r},t)}{\partial p} = i\frac{d_1\omega_L N}{4\epsilon_0}\psi_1^*(\mathbf{r},t)\psi_3(\mathbf{r},t), \tag{4.90}$$

$$\frac{\partial E_S^{(+)}(\mathbf{r},t)}{\partial p} = i\frac{d_2\omega_L N}{4\epsilon_0}\psi_2^*(\mathbf{r},t)\psi_3(\mathbf{r},t). \tag{4.91}$$

Using $t = \frac{1}{2}(p+q)$, and $z = \frac{c}{2}(p-q)$, we further rewrite

$$E_{L,S}^{(+)}(\mathbf{r},t) \equiv E_{L,S}^{(+)}\left(\vec{\rho}, \frac{c}{2}(p-q), \frac{1}{2}(p+q)\right), \tag{4.92}$$

and

$$\psi_j^*(\mathbf{r},t)\psi_3(\mathbf{r},t) = \sigma_{j3}\left(\vec{\rho}, \frac{c}{2}(p-q), \frac{1}{2}(p+q)\right), \tag{4.93}$$

for $j = 1, 2$. In these new forms, equation (4.90) and (4.91) converted into integration forms of

$$E_L^{(+)}\left(\vec{\rho}, \frac{c}{2}(p-q), \frac{1}{2}(p+q)\right) = \tag{4.94}$$

$$
\begin{aligned}
& i\frac{d_1\omega_L N}{4\epsilon_0}\int_{-\infty}^{p}\sigma_{13}\left(\vec{\rho},\frac{c}{2}(p'-q),\frac{1}{2}(p'+q)\right)dp' \\
E_S^{(+)}&\left(\vec{\rho},\frac{c}{2}(p-q),\frac{1}{2}(p+q)\right)=E_L(-\infty) \\
& +i\frac{d_2\omega_L N}{4\epsilon_0}\int_{-\infty}^{p}\sigma_{23}\left(\vec{\rho},\frac{c}{2}(p'-q),\frac{1}{2}(p'+q)\right)dp'.
\end{aligned}
\tag{4.95}
$$

Here $E_L(-\infty)$ is the applied electric field of pump 2 outside the medium. Defining $z'=\frac{c}{2}(p'-q)$, and recognizing $\frac{1}{2}(p+q)=t$, $\frac{c}{2}(p-q)=z$, the above equations are simplified to

$$
E_L^{(+)}(\vec{\rho},z,t))=i\frac{d_1\omega_L N}{2c\epsilon_0}\int_{-\infty}^{z}\sigma_{13}\left(\vec{\rho},z',t-\frac{z-z'}{c}\right)dz', \tag{4.96}
$$

$$
E_S^{(+)}(\vec{\rho},z,t)=E_L(-\infty)+i\frac{d_2\omega_L N}{2c\epsilon_0}\int_{-\infty}^{z}\sigma_{23}\left(\vec{\rho},z',t-\frac{z-z'}{c}\right)dz'. \tag{4.97}
$$

These expressions have a clear physical interpretation: a $\hat{z}$-propagating electric field at position $(\vec{\rho},z)$ and time t is determined by the summation of dipole moments at an anterior position $z'\leq z$ and a prior time $t-\frac{z-z'}{c}$. The retardation in time of $\frac{z-z'}{c}$ is the time it takes for the light to travel from z' to z. In practice, the typical condensate sizes are of sub-millimeters. Thus the retardation within condensates is $\lesssim 10^{-12}$s, which is much shorter than atomic dynamics time scales of $\sim 10^{-9}$s, and can thus be neglected. Physically, neglecting retardation corresponds to Markovian approximation, in which electric fields adiabatically follow atomic dynamics [123]. Converting back to differential forms, we have

$$
\frac{\partial E_L^{(+)}(\mathbf{r},t)}{\partial z} = i\frac{d_1\omega_L N}{2c\epsilon_0}\psi_1^*(\mathbf{r},t)\psi_3(\mathbf{r},t), \tag{4.98}
$$

$$
\frac{\partial E_S^{(+)}(\mathbf{r},t)}{\partial z} = i\frac{d_2\omega_L N}{2c\epsilon_0}\psi_2^*(\mathbf{r},t)\psi_3(\mathbf{r},t). \tag{4.99}
$$

Compared to the original equation (4.88) and (4.89), here time partial-derivative terms are dropped. The resulting equation directly leads to equation (4.32)-(4.33).

Finally, it is noticed that the dynamics is uncoupled along $\hat{\mathbf{x}}$ and $\hat{\mathbf{y}}$ directions, a consequence from that light beams are assumed to propagate along the $\hat{\mathbf{z}}$ direction. This enables us to separately solve for the dynamics at different locations in the $x-y$ plane, thus greatly reducing computational complexity.

4.6.4 Atom loss: QCM and SMS theory

Atom loss via QCM model

As previously discussed, atom loss in this scheme is due to $|3\rangle$ coupling to other quasi modes, a process initialized by spontaneous emission, and potentially enhanced by the superradiance effect. To study the superradiance enhancement effect on atom loss, we consider a many-mode system where $|3\rangle$ is simultaneously coupled to multiple quasi modes besides that of c_1 and c_2. Let $N_{j,\mathbf{k}_s}$ be the atom number in the side mode of $|j,\mathbf{k}_s\rangle$ (j is the electronic level and $\hbar(\mathbf{k}_L-\mathbf{k}_s)$ is momentum), the rate equation is approximately

$$\begin{aligned}
\frac{d}{dt}N_1 &= -\Gamma P_e N_1 f_R N_2 - P_e N_1 \sum_{j,\mathbf{k}_s} \Gamma_j f_{j,\mathbf{k}_s} N_{j,\mathbf{k}_s} - \gamma P_e N_1, \\
\frac{d}{dt}N_2 &= \Gamma P_e N_1 f_R (N_2+1), \\
\frac{d}{dt}N_{j,\mathbf{k}_s} &= \Gamma_j P_e N_1 f_{j,\mathbf{k}_s}(N_{j,\mathbf{k}_s}+1).
\end{aligned} \tag{4.100}$$

Here Γ_j is the spontaneous emission emission rate from the excited $|3\rangle$ to the j-th level, satisfying $\sum_j \Gamma_j = \gamma$. $f_{j,\mathbf{k}_s}$ is the collectivity parameter for the $|j,\mathbf{k}_s\rangle$ mode, which for condensates of Thomas-Fermi profile (4.54) is

$$f_{j,\mathbf{k}_s} \approx \frac{3(1-|\hat{k}_s\cdot\hat{d}_j|^2)}{8k_L^2 W\sqrt{W^2\cos^2\theta_s + L^2\sin^2\theta_s}}. \tag{4.101}$$

Here θ_s is angle between $\mathbf{k}_s$ and $\hat{z}$, $\hat{d}_j$ is the unit vector along the dipole direction for the corresponding transition. Note here for each electronic level, $\sum_{\mathbf{k}_s} f_{j,\mathbf{k}_s} = 1$.

As θ_s increases from 0 to $\pi/2$, $f_{j,\mathbf{k}_s}$ sharply decreases from f_R to $\frac{1}{2A} f_R$ for $\sigma^{\pm}$-polarized or 0 for π-polarized dipole moment. For an analytical solution of equation (4.100), we approximate $f_{j,\mathbf{k}_s}$ with a step function

$$f_{j,\mathbf{k}_s} = \begin{cases} f_R, & \theta_s \leq \theta_e; \\ \frac{1}{A} f_R, & \theta_s > \theta_e. \end{cases} \tag{4.102}$$

Here $\theta_e = \frac{W}{L}$ is the superradiance-emission angle. Due to $A \gg 1$, $f_{j,\mathbf{k}_s}$ is much smaller when $\theta_s > \theta_e$. Thus, the quasi modes can be classified to end-fire (EF) and non-end-fire (NEF) modes, corresponding to yielding a θ_s less or greater than θ_e. Due to a much smaller collective parameter, the population in each NEF mode stays well below one during the dynamics, as a consequence of mode competition with EF ones. To verify this, we iteratively solve equation (4.100) assuming small atom loss fraction. To leading order, we find upon depletion of pump 1 that

$$N_{j,\mathbf{k}_s}(\infty) = (1+\nu)^{\mu(j,\mathbf{k}_s)} - 1. \tag{4.103}$$

Here $\mu(j,\mathbf{k}_s) = \frac{\Gamma_j f_{j,\mathbf{k}_s}}{\Gamma_2 f_R}$, and $\nu = \frac{N_1(0)}{N_2(0)}$ is the initial ratio for populations in pump 1 and the signal wave. For $\Gamma_j = \Gamma$ $(j = 1, 2, 3\cdots)$, the occupation numbers in EF and NEF modes are respectively ν and $\frac{1}{A}\ln(1+\nu)$. For typical parameters of $A, \nu = 10 \sim 100$, while EF modes are mesoscopically populated, the NEF mode remains nearly empty, with a occupation significantly less than one. Therefore, superradiance emission occurs only for the EF modes, and decaying into NEF modes is effectively a spontaneous process. This iterative approach has been validated by verifying $\sum_{j,\mathbf{k}_s} N_{j,\mathbf{k}_s}(\infty) \ll N$ for self-consistence.

Following the above arguments, we simplify the equation (4.100) to

$$\frac{d}{dt}N_1 = -P_e\Gamma f_R N_1\left(N_2 + M_{EF}\sum_j N_{j,0}\right) - \gamma P_e N_1,$$
$$\frac{d}{dt}N_2 = P_e\Gamma f_R N_1(N_2+1),$$
$$\frac{d}{dt}N_{j,0} = P_e\Gamma f_R N_1(N_{j,0}+1).$$

Here we have used $\Gamma_j = \Gamma$, and replaced $\sum_{\mathbf{k}_s}$ with the number of EF mode M_{EF}, given by

$$M_{EF} = \frac{2k_L^2 W^2}{A^2}. \tag{4.104}$$

These equations can be iteratively solved, where for $\Gamma_s \gg \gamma$,

$$N_{j,0} \approx \nu\left(1 - \frac{1+\nu}{\nu + \exp(P_e\Gamma_s t)}\right). \tag{4.105}$$

Defining a superradiance enhancement factor

$$\chi_s(t) = 1 + \frac{3\nu}{4A^2}\left(1 - \frac{1+\nu}{\nu+\exp(P_e\Gamma_s t)}\right) \tag{4.106}$$

the equation of motion for N_1, N_2 can be rewritten in a compact form of

$$\frac{d}{dt}N_1 = -\Gamma P_e f_R N_1 N_2 - \chi_s\gamma P_e N_1, \tag{4.107}$$
$$\frac{d}{dt}N_2 = \Gamma P_e N_1 f_R(N_2+1). \tag{4.108}$$

At $t = 0$, $\chi_s = 1$, so that there is no superradiance enhancement effect, as the EF modes are initially vacuum. Then, as the EF modes are gradually populated, χ_s increases monochromatically, and eventually saturates to an asymptotical value of $1 + \frac{3\nu}{4A^2}$. For negligible superradiance enhancement on atom loss, it then requires

$\nu \ll A^2$, so that $\chi_s \approx 1$. For the parameters $A = 10, \nu = 9$ as in section 4.3.1, $\chi_s \leq 1.07$, indicating only weak enhancement effect.

To quantify the atom loss, we define the atom loss fraction, as $\varepsilon_{loss}(t) = 1 - \frac{1}{N}(N_1+N_2+N_3)$. An analytical formula for ε_{loss} is obtained by solving the dynamics making use of equation (4.13), which for $\nu < A^2$ is approximately

$$\varepsilon_{loss}(t) \approx \sqrt{\chi_s}\gamma \left(P_e t - \frac{\ln(\nu + e^{P_e \Gamma_s t}) - \ln(1+\nu)}{\Gamma_s} \right). \tag{4.109}$$

As shown in figure 4.13, this formula agrees well with the exact numerical results in all dynamical regimes. Upon completion of population transfer, the total loss fraction is

$$\varepsilon_{loss}(\infty) = (1 + \frac{3\nu}{8A^2}) \frac{\gamma \ln(1+\nu)}{\Gamma_s}. \tag{4.110}$$

This result is independent of P_e, and is thus a universal property for different dynamical regimes. The universality origins in that the loss fraction is essentially determined by the branch ratio of MWA and atom loss, which is independent of pump 2. Physically, while the instant atom loss rate is proportional to occupation fraction P_e in the excited state, the transfer time is proportional to the inverse of P_e. The final loss fraction, obtained by integrating loss rate over transfer time, is then independent of P_e, or pump 2. For parameters used in section 4.3.1, it gives $\varepsilon_{loss}(\infty) = 0.045$, compared to the numerical result of 0.043, as seen in figure 4.13.

Under short evolving time of $t \ll \tau$, the loss fraction $\varepsilon_{loss} \approx \frac{\nu}{1+\nu}\sqrt{\chi_s} P_e \gamma t$, while the gain factor $G_q \approx 1 + \frac{\nu}{1+\nu} P_e \Gamma_s t$. Thus atom loss per decibel gain η is then

$$\eta = \frac{\varepsilon_{loss}}{\ln G} = \frac{\sqrt{\chi_s}\gamma}{\Gamma_s}, \tag{4.111}$$

For $\nu < A^2$, $\sqrt{\chi_s} \approx 1$, so that $\eta \approx \gamma/\Gamma_s$, which is proportional to the inverse of optical depth. A plot of η as a function of time for $\nu = 9, 99$ and 999, corresponding

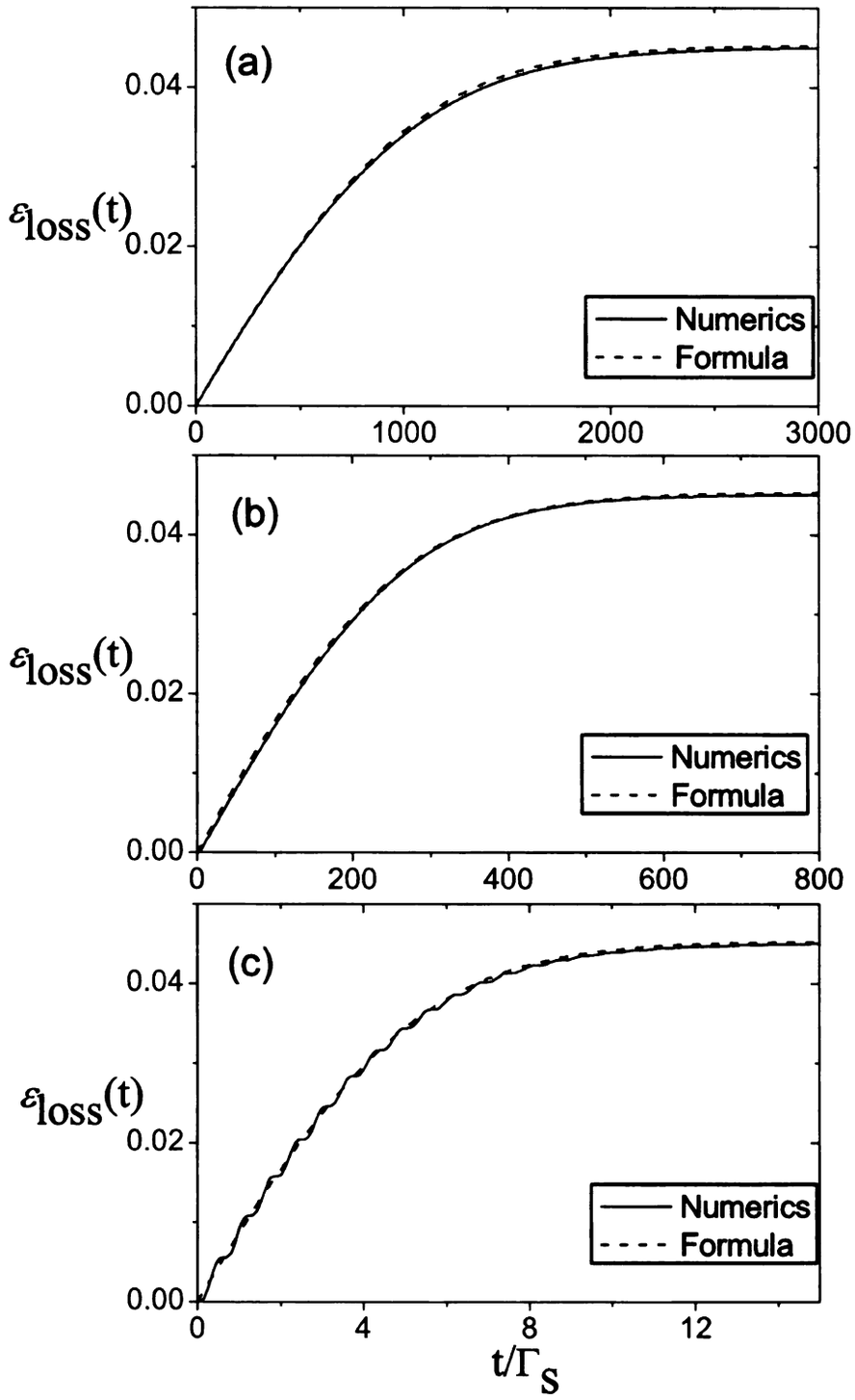

Figure 4.13: The evolution of atom loss fraction ϵ_{loss}, where figures (a), (b) and (c) show off-resonance, overdamping and Rabi regimes, respectively. In all figures, solid lines are numerical results, while dashed lines represent the analytical formula (4.109). Parameters for each dynamical regime are the same with figure 4.2.

to $n_2(0) = 0.1, 0.01$ and 0.001, is shown in figure 4.14. For $t < 0.25\tau$, η is shown to lie closely with γ/Γ_s, regardless of ν. As evolving, η only slightly grows for $\nu = 9$ and 99, but sharply increases to about twice larger than γ/Γ_s for $\nu = 999$. Upon population converting when $t = \tau$, respectively for $\nu = 9, 99$ and 999, η reaches $0.0194, 0.0205$ and 0.040, and then eventually saturates to $0.020, 0.022$ and 0.040. Thus to a good approximation, η is given by γ/Γ_s throughout the dynamics for both $\nu = 9$ and 99. The loss fraction can then be fairly estimated by

$$\varepsilon_{loss}(t) = \frac{\gamma}{\Gamma_s} \ln G_q(t), \tag{4.112}$$

valid for $\nu < A^2$. Notice that at $t = \infty$, $G_q \approx 1 + \nu$, $\varepsilon_{loss}(\infty) = (\gamma/\Gamma_s)\ln(1+\nu)$, thus recovering formula (4.110). For $\nu = 999$, η is much greater, because in this case, $\nu > A^2$ so that χ_s is no longer a small quantity.

Atom loss via SMS model

We now study the laser depletion and spatial effects on atom loss. In figure 4.15, we plot the dynamics of atom loss fraction ϵ_{loss} for the three dynamical regimes in figure 4.8 (a)-(c). In figure (a) for the off-resonance regime, ε_{loss} closely follows the QCM curve through $t \approx \tau/2$, the half-depletion time of pump 1. Then, instead of saturating to 0.451 at $t = \tau$ as in the QCM model, it continues to grow and eventually approaches an asymptotical value of 0.145. A qualitatively similar behavior is shown for the Rabi regime in figure (b), but on a much shorter time scale. The agreements of SMS and QCM in the two regimes before half-depletion time is because the mean occupation of the excited level n_3, and thus the loss rate, is the same in the two models, since the laser depletion is negligible. For $t > \tau$, the majority of atoms are transferred to the signal mode in the QCM model. Whereas in the SMS model, due to a reduced effective optical thickness, the population transfer is greatly slowed

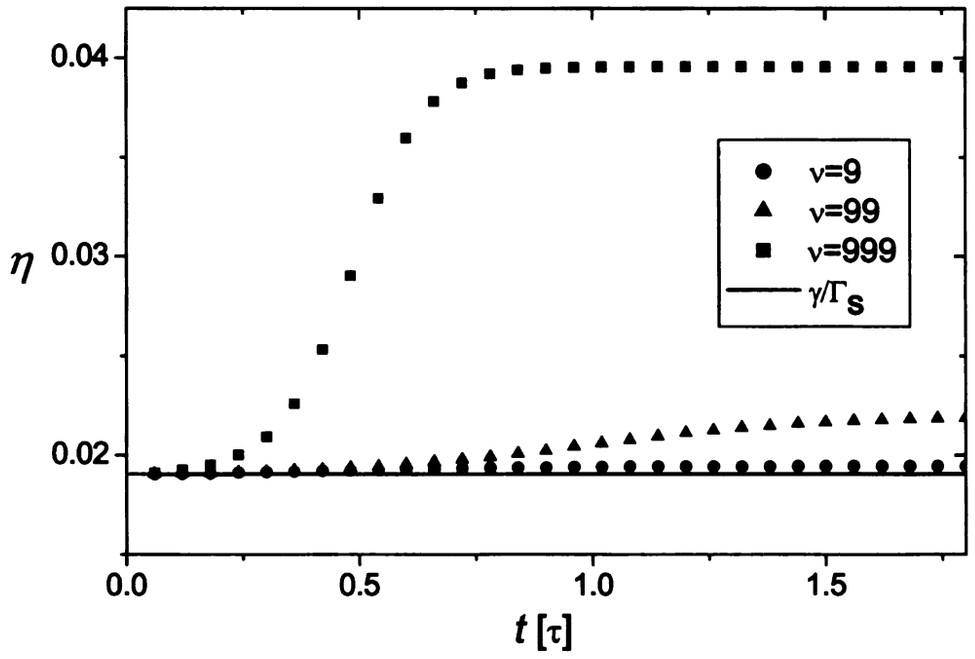

Figure 4.14: The loss fraction per decibel gain η as a function of rescaled time for $\nu = 9, 99$ and 999. Here, $N = 3 \times 10^6$ is fixed, $A = 10$, and all other relevant parameters are given the same as in section 4.3.1.

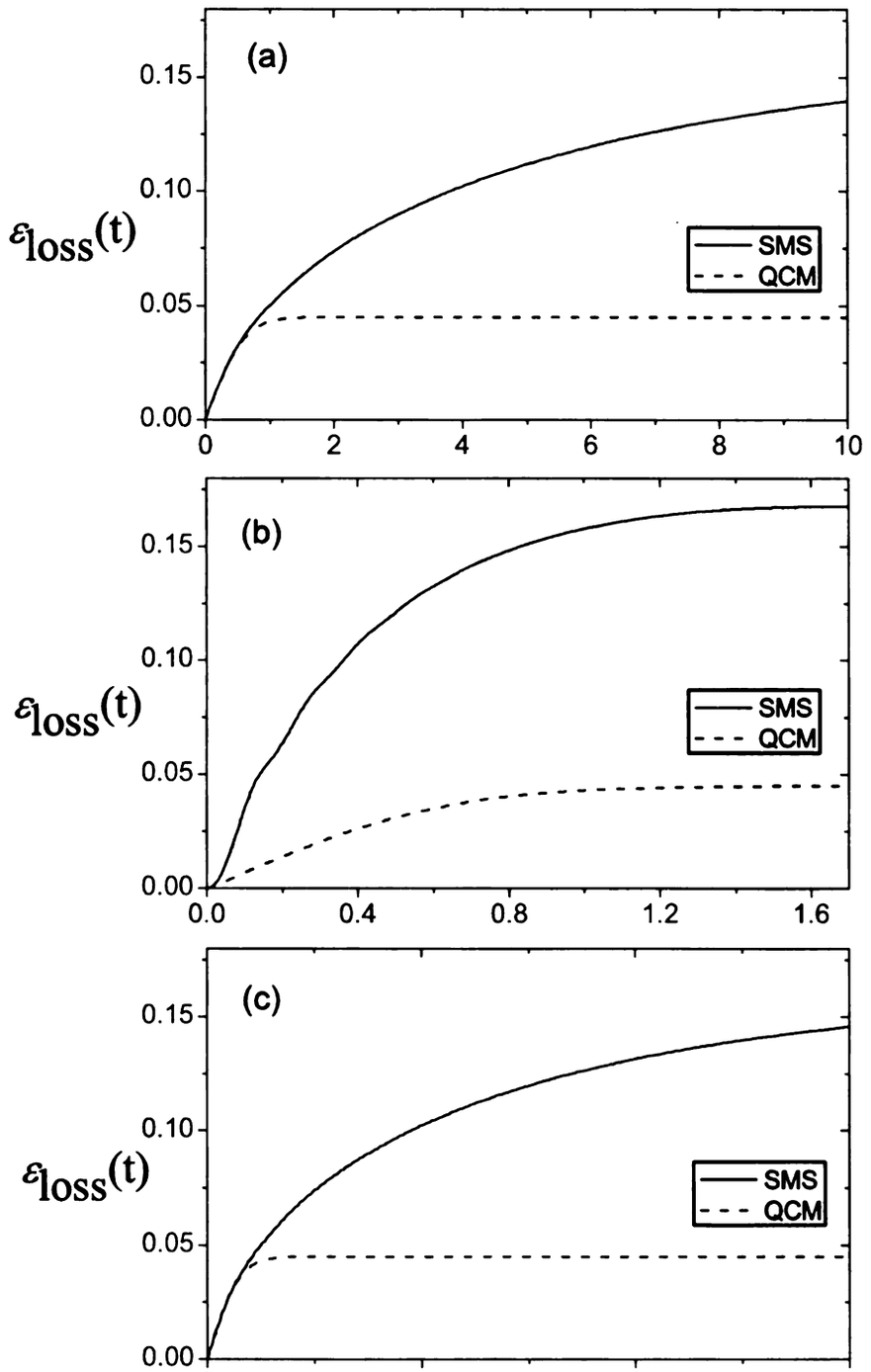

Figure 4.15: The atom loss fraction $\epsilon_{loss}(\tau)$ as a function of rescaled time, where (a), (b) and (c) are for the off-resonance, overdamping and Rabi regimes. In all figures, solid and dashed lines are the numerical results via SMS and QCM, respectively. Parameters for each regime are the same as given in corresponding figures 4.5.

down, leaving roughly half atoms in pump mode at the time of $t = \tau$. The atom loss thus continues through the depletion of pump 1, which occurs at a much later time. In contrast, in the overdamping regime, the loss dynamics in SMS model is about four times larger than that the QCM result, throughout the dynamics. The ultimate loss fraction is 17%. The boost of ε_{loss} in SMS dynamics is attributed to a larger occupation in the excited level, due to a reduced optical thickness and thus a weaker Zeno suppression effect. As discussed in section 4.6.4, the ultimate atom loss fraction is inversely proportional to the optical thickness. In all regimes, the spatial effect reduces the optical thickness by about a half, so that the atom loss is expected to be doubled. This is compared to an enhancement factor of $3 \sim 4$ from the numeric results shown in figure 4.15. For $\nu = 1$, very similar divergent behavior is observed, as seen in figure 4.16. Again, this reflects that the spatial effects depends little on the population distribution between pump and the signal wave.

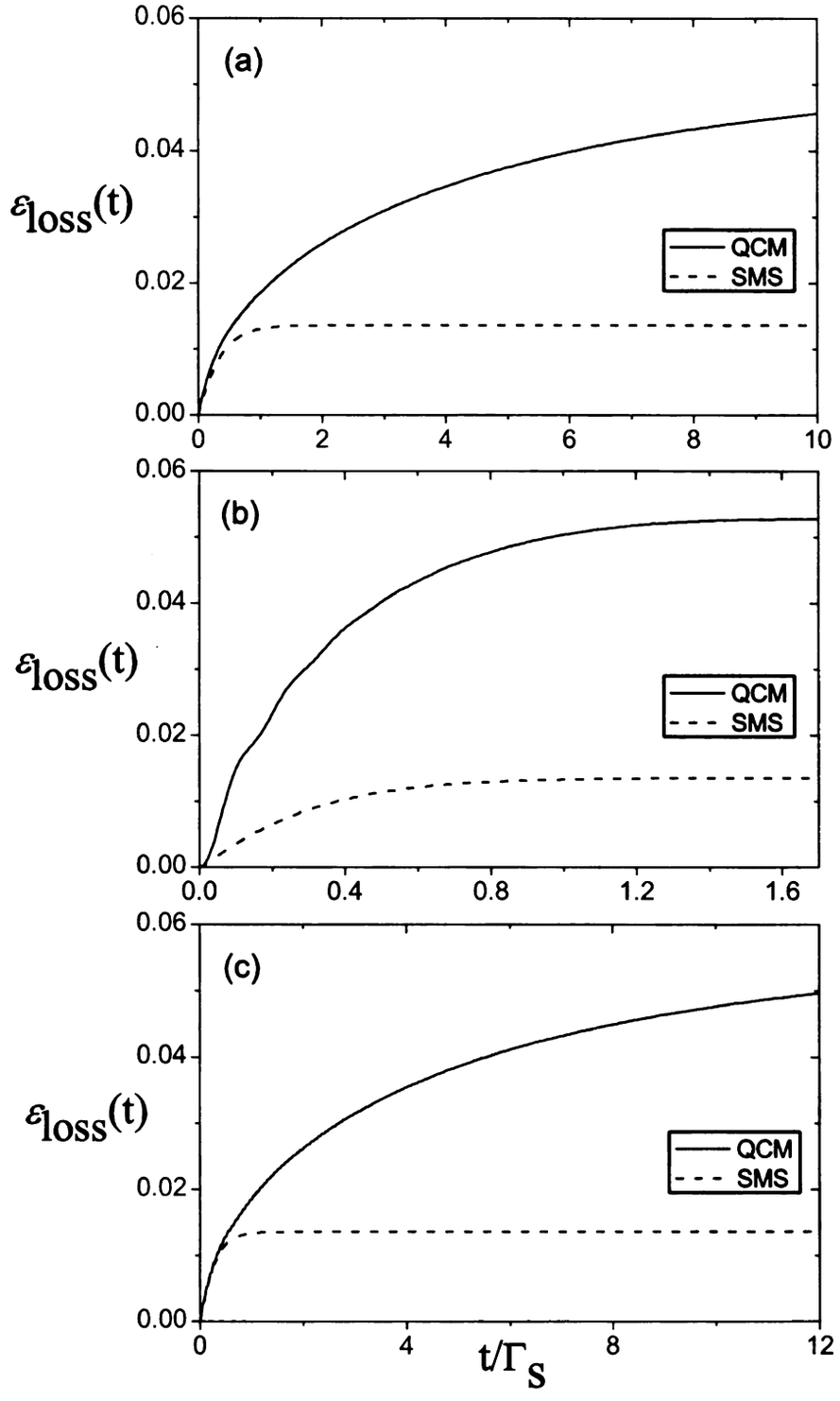

Figure 4.16: The same as figure 4.15, but with $\nu = 1$.

Chapter 5

On-demand generation of entanglement of atomic qubits via optical interferometry

In an effort to realize practical quantum information processing (QIP), in this chapter, we examine the feasibility to create entanglement between distant single-atom qubits via a common photonic channel in an optical interferometer. As well understood, when a coherent state is used as the input of a Mach-Zehnder interferometer, a high-finesse optical cavity is required to overcome sensitivity to spontaneous emission. However, we find that a number-squeezed light field in a twin-Fock (TF) state can in principle create useful entanglement without cavity-enhancement. Both approaches require single photon counting detectors, and best results are obtained by combining cavity-feedback with twin-Fock inputs. Such an approach may allow a fidelity of .99 using a two-photon input and currently available mirror and detector technology. If using maximally entangled NOON state ($\frac{1}{\sqrt{2}}(|N,0\rangle + |0,N\rangle)$) and nonlinear beamsplitter, similar performance can be achieved without the need to count single photons. The problem is, however, the NOON state is subject to fast

decoherence. To overcome this difficulty, we propose to use less-extreme schrödinger state, which can provide similar performance yet is more robust against decoherence. The presently proposed approaches are scalable, and can be conveniently extended to generate multi-site entanglement and entanglement swapping, both of which are necessities in quantum networks. The major results of this chapter have been published in "On-demand generation of entanglement of atomic qubits via optical interferometry", by Y. P. Huang and M. G. Moore in Phys. Rev. A. **77**, 032349 (2008).

This chapter is organized as follows. In section 5.1, we briefly review the existing implementations of quantum information processing employing isolated atomic qubits, and then give an overview on our work. In Sec. 5.2, we present a basic model of the interferometrical generation of entanglement between two atomic qubits. In section 5.3.1, we study the MZ-interferometrical approach using the TF input light field. Then in Sec.5.3.2, we investigate an alternative approach employing NOON states and nonlinear beamsplitters. In Sec. 5.4, as examples, we briefly show how the present scheme can be applied to realize deterministic teleportation, multi-site entanglement, and entanglement swapping. This is followed by a short discussion and conclusion in Sec. 5.5

5.1 Introduction

Future quantum information processing, if can ever reach practical level, will rely on deterministic computational gates and communication protocols that operate at high fidelities [136, 149, 175]. As quantum entanglement lies in the heart of QIP, this necessarily requires realtime generation of entanglement amongst arbitrary qubits performed at near-unit success probability and fidelity. For atom-type qubits, this entanglement can be generated either via a photonic channel, utilizing entangled photon-pairs [175, 181] or cavity-decay photons [182, 183, 184, 185], or an atomic

channel as in recent trapped-ion experiments [186, 187]. For high-speed quantum computation and/or long-distance communication, a photonic quantum channel is clearly ideal, as photons are robust carriers of quantum information that travel at the speed of light. Since isolated trapped-atomic qubits have long coherence times and are easily manipulated with electromagnetic fields, it is of general interest to consider the problem of creating entanglement between two isolated atomic qubits via their mutual interaction with a single photonic channel. The primary obstacle to such a protocol lies in the problem of eliminating spontaneous emission while obtaining a sufficiently strong atom-photon interaction. Recent attempts to overcome this difficulty have primarily relied on the use of collective-state qubits in atomic ensembles to enhance the dipole moment of the qubit [150, 259, 260]. This enhancement effect has allowed Duan, Cirac, Zoller and Polzik to implement a quantum teleportation scheme between two atomic samples, where a coherent beam is passed successively through and the entanglement is generated by measuring its final Faraday-rotation angle [150]. Very recently, a probabilistic scheme to entangle two distant quantum dots using cavity enhancement has been proposed using bright coherent light via homodyne detection and post-selection [261].

In this chapter, we investigate an approach in which *single*-atom qubits are deterministically entangled by use of an optical interferometer, thus avoiding collisional decoherence mechanisms inherent in atomic ensembles. It is well-known that the back-action of a single atom onto a focused laser pulse is very weak, so that generating useful atom-photon entanglement in this manner will generally fail due to spontaneous emission [262]. Our goal, however, is to overcome this difficulty by using the extreme sensitivity of sub-shot-noise interferometers [157, 158, 119, 159, 160, 24, 25, 26, 27] to detect the weak phase imprinted on the forward scattered light in the regime where spontaneous emission is negligible. In addition, we also consider the more generic approach of using high-finesse optical resonators [155, 156] to enhance the atom-photon

interaction.

Our interferometry apparatus follows the Faraday-rotation scheme of Duan, Cirac, Zoller, and Polzik [150], with the collective atomic ensembles replaced by single trapped atoms, and with the coherent light replaced by a highly non-classical many-photon state. As we will show, an interferometer employing coherent light input is limited to shot-noise sensitivity, and will thus not work when the ensembles are replaced by single atoms without the introduction of extremely high-finesse optical resonators. If the coherent state input is replaced with a twin-Fock (TF) input state, however, we find that a cavity is in principle no longer required. Cavity feedback may still provide additional improvement in performance. For example, $f = .99$ can be achieved if we use the TF state with 4×10^4 photons and no cavity, or only two photons and cavities with $M = 2 \times 10^4$. The later requires a single photon-on-demand [263] injected into each interferometer input, with an accurate measurement of the two-photon output state, which appears within the realm of experimental feasibility. Both MZ-interferometer-based approaches require detectors with single-photon resolution [264]. This requirement, however, can be overcome by employing a non-MZ interferometer based on NOON states and nonlinear beamsplitters. Such an interferometer yields a sensitivity close to the TF state in detecting phase imbalance, and thus can achieve similar performance without counting single photons. While the TF and NOON states have recently been shown as unable to measure any phase below shot-noise in a single measurement due to large quantum fluctuations [244, 250, 119], our present work shows that single-measurements with these states can still be highly useful as 'quantum switches' with Heisenberg-limited sensitivity.

Our proposed interferometry approach to entangle atomic-qubits can be performed on-demand and is scalable. We envision generalizing such a device to a complete set of quantum information processing protocols whereby stationary single-atom qubits are held in isolated traps, with arbitrary single-atom and multi-atom operations

achieved via sequences of light pulses guided amongst the atoms and into detectors by fast optical switching. The goal of this chapter is to perform a theoretical analysis of interferometrical generation of entanglement between two arbitrary qubits, and to determine the fundamental limitations imposed by quantum mechanics.

5.2 The model

In our scheme, a single pulse of light is passed through an optical interferometer, with the different 'arms' of the interferometer corresponding to different photon polarization states. The beam passes through two atomic qubits, i.e. trapped ions, neutral atoms and/or quantum dots, such that each polarization state interacts with a different internal atomic state. This can be achieved using an 'X'-type scheme, as described in [150], in which the Zeeman sublevels of an $F = 1/2$ ground state form the qubit, or in a Λ-type level scheme, with the $m = \pm 1$ states of an $F = 1$ ground state forming the qubits. In both cases, the 'arms' of the interferometer would correspond to orthogonal circular polarization states. The interferometer output is determined by a state-dependent phase-shift acquired via the atom-photon interaction. This requires a large detuning from the atomic resonance, as there is no phase acquired on resonance. Measurement of a phase imbalance at the interferometer output cannot determine which qubit contributed the phase-shift, resulting in entanglement between them.

We consider atomic qubits based on two degenerate hyperfine states, arbitrarily labeled as $|0\rangle$ and $|1\rangle$. For a general consideration, our goal is to entangle two uncorrelated qubits, labeled x and y, which are initially in states of $|\psi_x\rangle$, $|\psi_y\rangle$, where

$$|\psi_\mu\rangle = \chi_0^\mu |0\rangle_\mu + \chi_1^\mu |1\rangle_\mu, \tag{5.1}$$

and $\mu \in \{x, y\}$. The qubits are placed inside an optical interferometer with the setup

depicted in Fig. 5.1, where the states $|0\rangle_x$ and $|0\rangle_y$ interact with photons in the upper arm of the interferometer, while $|1\rangle_x$ and $|1\rangle_y$ interact with the lower. Such interaction is represented by the qubit-photon interaction propagator,

$$\hat{U}_\mu = \exp[-i\theta(\hat{a}_0^\dagger \hat{a}_0 \hat{c}_{\mu 0}^\dagger \hat{c}_{\mu 0} + \hat{a}_1^\dagger \hat{a}_1 \hat{c}_{\mu 1}^\dagger \hat{c}_{\mu 1})], \tag{5.2}$$

where $\hat{c}_{\mu m}$ is the annihilation operator for an atom at location $\mu \in \{x, y\}$ in internal state $m \in \{0, 1\}$. This interaction operator is valid in the far-off-resonance regime, where the electronically excited state can be adiabatically eliminated. The interaction is governed by the phase-shift

$$\theta = \frac{|d\mathcal{E}(\omega)|^2 \tau}{\hbar^2 \Delta}, \tag{5.3}$$

where τ is the atom-photon interaction time, Δ is the detuning between the laser and atomic resonance frequencies, d is the electric dipole moment and $\mathcal{E}(\omega) = \sqrt{\hbar\omega/(2\varepsilon_0 V)}$ is the 'electric field per photon' for laser frequency ω and mode-volume V. Introducing the spontaneous emission rate $\Gamma = d^2\omega^3/(3\pi\varepsilon_0\hbar c^3)$, taking the photon mode as having length L and width W (at the location of the atom), and taking the interaction time as $\tau = L/c$, we arrive at the single-atom phase-shift

$$\theta = \frac{3}{8\pi}\left[\frac{\lambda}{W}\right]^2 \frac{\Gamma}{\Delta}, \tag{5.4}$$

where λ is the laser wavelength. This is the phase-shift acquired by an off-resonant photon forward-scattered by a single atom, and is independent of the pulse length.

The interferometer output is then determined by the phase-shift acquired via the atom-photon interaction. Introducing the qubit-pair basis $|ij\rangle \equiv |i\rangle_x \otimes |j\rangle_y$ with $i, j = 0, 1$, the states $|01\rangle$ and $|10\rangle$ both correspond to a balanced interferometer with zero net phase-shift, and thus constitute a 'balanced' qubit-pair subspace. In contrast, the states $|00\rangle$ and $|11\rangle$ have equal and opposite non-zero phase-shifts, and thus

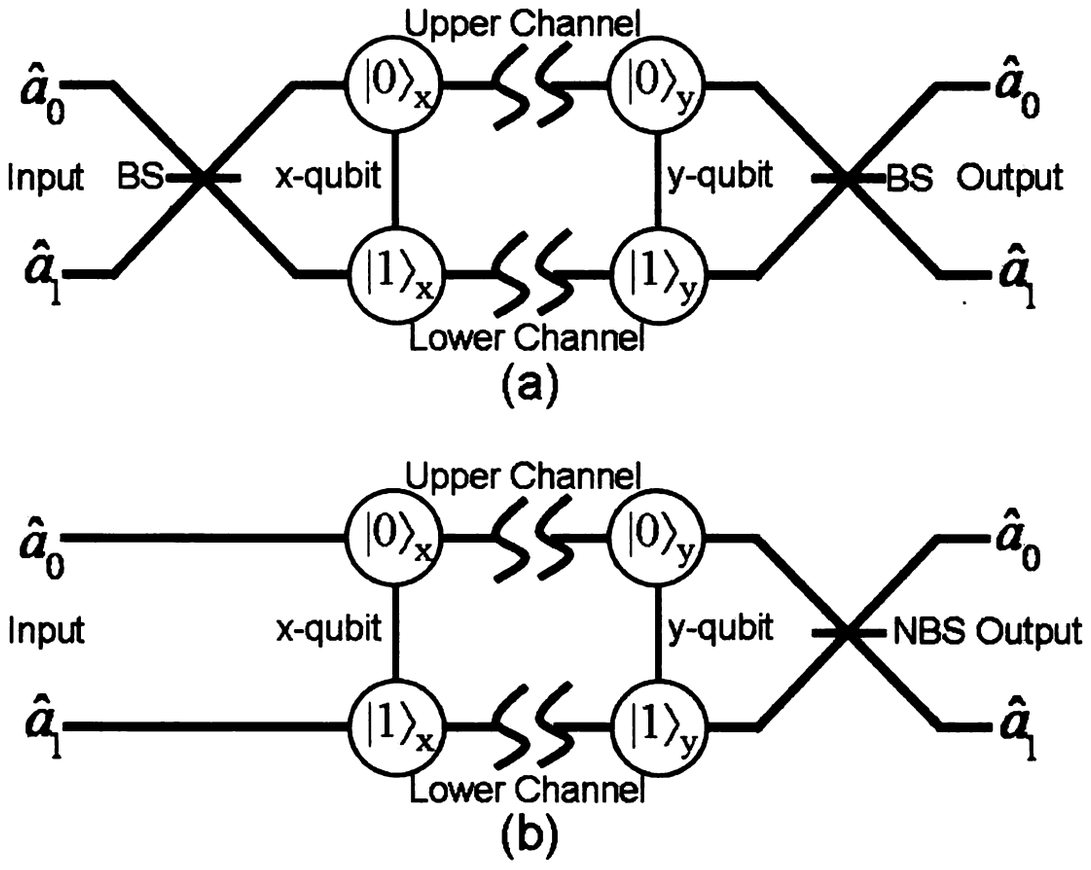

Figure 5.1: Schematic setup of entanglement generation with optical interferometers. Figure (a) shows the setup with the MZ interferometer which consists of two linear 50/50 beamsplitters (BS). Figure (b) shows the setup with the NOON-state interferometer consisted of only one nonlinear beamsplitter (NBS).

constitute an 'imbalanced' subspace. Measuring the photon number distribution at the interferometer output distinguishes between zero and nonzero magnitudes of the phase-shifts, and thus collapses the qubits onto the balanced or imbalanced subspaces, based on which entanglement between the two is established.

5.3 Implementations

In this section, we present two feasible implementations of the prescribed protocol. The first employs MZ-interferometry with highly-number squeezed TF states

as input. The second uses a NOON-state interferometer configured on nonclassical beamsplitters.

5.3.1 MZ interferometry with Twin-Fock input states

The basic set-up for entanglement generation using MZ interferometer is shown in Fig.5.1 (a). The MZ interferometer consists of two 50/50 linear beamsplitters. The input light field is bifurcated at the first beamsplitter, guided to interact sequently with the qubits, and then recombined at the second beamsplitter. Passage of photons through the MZ interferometer can be described by the propagator,

$$\hat{U} = \hat{U}_{BS}\hat{U}_y\hat{U}_x\hat{U}_{BS}, \tag{5.5}$$

where $\hat{U}_{BS}$ is the 50/50 beamsplitter propagator,

$$\hat{U}_{BS} = \exp[-i(\hat{a}_0^\dagger\hat{a}_1 + \hat{a}_1^\dagger\hat{a}_0)\pi/4]. \tag{5.6}$$

Without specifying the input light field, the initial states of the system can be written in a general form

$$|\Psi_i\rangle = \Phi(\hat{a}_0^\dagger, \hat{a}_1^\dagger)|0\rangle \otimes |\psi_x\rangle \otimes |\psi_y\rangle, \tag{5.7}$$

where $|0\rangle$ is electromagnetic vacuum state and $\Phi(\hat{a}_0^\dagger, \hat{a}_1^\dagger)$ defines the light field. The state of the system at the interferometer output is then given by

$$\begin{aligned} |\Psi_f\rangle &= \hat{U}|\Psi_i\rangle \\ &= \Phi(\hat{U}\hat{a}_0^\dagger\hat{U}^\dagger, \hat{U}\hat{a}_1^\dagger\hat{U}^\dagger)|0\rangle \otimes |\psi_x\rangle \otimes |\psi_y\rangle. \end{aligned} \tag{5.8}$$

Introducing dual-qubit spin operator

$$\sigma_z = \frac{1}{2} \sum_{\mu=x,y} (\hat{c}^\dagger_{\mu 0} \hat{c}_{\mu 0} - \hat{c}^\dagger_{\mu 1} \hat{c}_{\mu 1}), \tag{5.9}$$

we find that

$$\hat{U} \hat{a}^\dagger_0 \hat{U}^\dagger = i e^{i\theta} [\sin(\theta \sigma_z) \hat{a}^\dagger_0 + \cos(\theta \sigma_z) \hat{a}^\dagger_1], \tag{5.10}$$

$$\hat{U} \hat{a}^\dagger_1 \hat{U}^\dagger = i e^{i\theta} [\cos(\theta \sigma_z) \hat{a}^\dagger_0 - \sin(\theta \sigma_z) \hat{a}^\dagger_1]. \tag{5.11}$$

The final state can now be rewritten as

$$|\Psi_f\rangle = \sum_{i,j=0,1} \chi^x_i \chi^y_j |\Phi(\theta_{ij})\rangle \otimes |ij\rangle \tag{5.12}$$

where $|\Phi(\theta_{ij})\rangle$ is the output light field in the presence of qubits-dependent interferometer phase $\theta_{ij} = \theta \times (1 - i - j)$. It is now evident that the interferometer output is determined by the joint states of the qubits. The states $|01\rangle$ and $|10\rangle$ result in zero phase-shifts with $\theta_{01} = \theta_{10} = 0$, while $|00\rangle$ and $|11\rangle$ result in equal and opposite phases with $\theta_{00} = -\theta_{11} = \theta$. If the interferometer is incapable of distinguishing positive and negative phases, a measurement of the output light field will therefore collapse the qubits onto either balanced or imbalanced subspaces (resulting in zero or nonzero phase-shifts), and in this way generate entanglement between them.

In the framework of optical MZ interferometry, a first thought might be to use coherent input states, as they are most attainable in practice. As explained in details in appendix 5.6.1, however, this method is prohibited by fundamental physics laws, originated in the well-known fact that the atom-photon interaction in free space is dominated by the spontaneous emission. To overcome this difficulty would require to put the atomic qubits in optical resonators. In appendix 5.6.1, we found that a fidelity of .99 can be achieved using ring cavities which cycle photons for 6.6×10^5

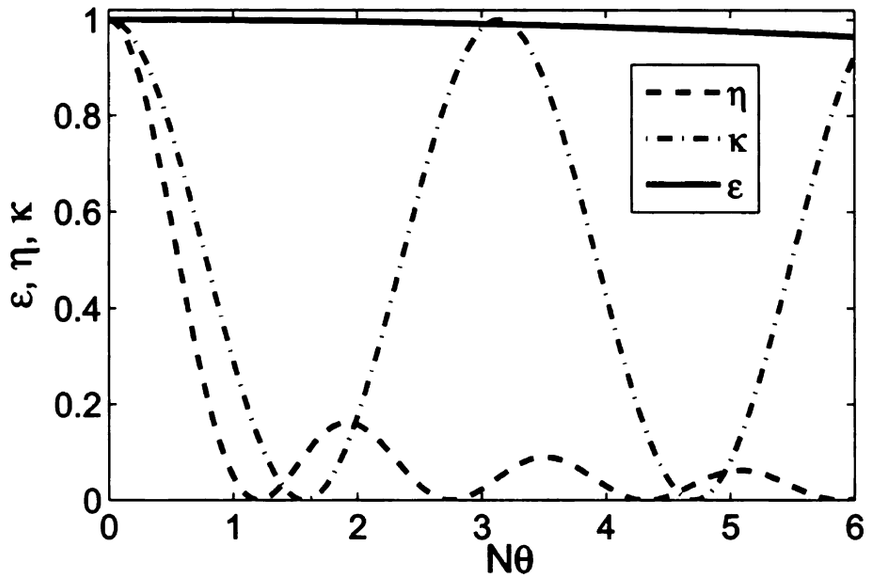

Figure 5.2: (color online) An example of intrinsic error due to interferometer sensitivity. Errors for MZ interferometer with coherent ε (solid), TF input η (dashed), and NOON-state interferometer κ (dashed-dotted) are plot as functions of $N\theta$ (with $N = 10^3$), respectively. Note while ε is dependent on $N\theta^2$, both η and κ are dependent on $N\theta$.

times, with about 4 photons needing to be measured accurately at one output.

To achieve a higher fidelity, and/or to eliminate the need for a high-finesse resonator, we now consider using sub-shot-noise interferometers to overcome the spontaneous emission to phase sensitivity. In this section, we investigate the fundamental limits when a twin-Fock (TF) photon input state is used to increase the phase sensitivity of the MZ interferometer. In this setup, the photon number-difference between the outputs must be measured. A result of zero number-difference constitutes a null result, projecting the qubits onto balanced subspace. Otherwise, the qubits are projected to the imbalanced subspace.

To formulate the process, the input state is given in the form of $|N, N\rangle$, with the dual-Fock basis defined as

$$|k, l\rangle = (\hat{a}_0^\dagger)^k (\hat{a}_1^\dagger)^l |0\rangle / \sqrt{k!\, l!}. \tag{5.13}$$

Following equation (5.12), the output state is given by

$$|\Psi_f\rangle = \sum_{ij} \chi_i^x \chi_j^y |ij\rangle \otimes \sum_{m=-N}^{N} \xi_m(\theta_{ij}) |N+m, N-m\rangle, \tag{5.14}$$

where

$$\xi_m(\theta_{ij}) = \sum_{l=\max\{0,-m\}}^{\min\{N,N-m\}} (-1)^{m+l} \begin{pmatrix} m+l \\ N \end{pmatrix} \begin{pmatrix} l \\ N \end{pmatrix} \times \frac{\sqrt{(N+m)!(N-m)!}}{N!} (\sin\theta_{ij})^{m+2l} (\cos\theta_{ij})^{2N-m-2l}.$$

The desired two-qubit entangled state is then created by measuring the photon number difference between the upper and lower outputs. It is seen from Eq. (5.14) that the probability of detecting a difference of $2m$ is given by

$$P(2m) = \Lambda \delta_{m,0} + (1-\Lambda)\xi_m^2(\theta), \tag{5.15}$$

where again $\Lambda = |\chi_0^x \chi_1^y|^2 + |\chi_1^x \chi_0^y|^2$. The probability to detect zero photon number difference (or a null result) is thus

$$P(0) = \Lambda(1-\eta) + \eta, \tag{5.16}$$

where $\eta = \xi_0^2(\theta)$ is the probability of a false null result. On detecting the null result, the qubit state will collapse onto

$$|\Psi_B\rangle = \frac{1}{\sqrt{\Lambda(1-\eta)+\eta}} \times \left[\chi_0^x \chi_1^y |01\rangle + \chi_1^x \chi_0^y |10\rangle + \sqrt{\eta}(\chi_0^x \chi_0^y |00\rangle + \chi_1^x \chi_1^y |11\rangle)\right], \tag{5.17}$$

with the corresponding fidelity

$$f_{null} = \frac{\Lambda}{\Lambda + (1-\Lambda)\eta}. \tag{5.18}$$

The remaining time, a photon number difference $m \neq 0$ is detected, with the qubits collapsed to

$$|\Psi_U\rangle = \chi_0^x \chi_0^y |00\rangle + (-1)^m \chi_1^x \chi_1^y |11\rangle. \tag{5.19}$$

Here, similar to the coherent state, the exact photon number difference must be measured in order to successfully disentangle the qubits. The overall fidelity in this entanglement generation is then

$$\begin{aligned} f_{avg} &= 1 - (1-\Lambda)\epsilon \\ &\geq 1 - \epsilon. \end{aligned} \tag{5.20}$$

The TF input yields a intrinsic error due to interferometer sensitivity given by η. In contrast, for the coherent input, the intrinsic error is $\varepsilon = e^{-N\theta^2}$, as derived in appendix 5.6.1. A comparison plot of η and ε is shown in Fig. 5.2, where it is seen that η decreases with N much faster than ε. In fact, for $N\theta < 1$, $\eta \approx e^{-N^2\theta^2}$, which is characteristic of a Heisenberg-limited phase sensitivity. This means that significantly fewer photons are required to obtain equal fidelity, with a corresponding reduction in spontaneous emission. In Fig. 5.2, we see that the false-null probability η is exactly zero for a periodic set of values of $N\theta$. The first such zero occurs at $N\theta = 1.196 \equiv x_1$. Thus if one can precisely control $N\theta$, *it is possible to achieve teleportation without intrinsic error due to false-null results.* In this case, the success of teleportation is governed only by spontaneous emission probability $P_{sp} = 2N\theta\Gamma/\Delta = 2x_1\Gamma/\Delta$. The

condition $N\theta = x_1$, together with (5.4), means that $\Gamma/\Delta = (8x_1/N)\,(W/\lambda)^2$, so that

$$P_{sp} = \frac{16x_1^2}{N}\left(\frac{W}{\lambda}\right)^2. \tag{5.21}$$

For the case of a tightly focussed beam, we can take $W/\lambda \approx 3$ this gives $P_{sp} = 206/N$. The theoretical limit to fidelity therefore scales as $\sim 1 - 200/N$, thus a fidelity of $f = .99$ would require $N = 2 \times 10^4$ (or a total of 4×10^4 photons), while a fidelity of $f = .999$ could be achieved with $N = 2 \times 10^5$. An extremely high fidelity of $f = .999999$ would therefore require $N = 2\times 10^8$. The addition of a Q-switched cavity with M cycles replaces N with the effective photon number MN, resulting in the spontaneous emission probability results in $P_{sp} = 206/(NM)$, which for $M = 2\times 10^4$, would reduce the photon numbers to $N = 1$ for $f = .99$, $N = 10$ for $f = .999$, and $N = 10^4$ for $f = .999999$.

The exactly elimination of false-null-induced reduction in fidelity requires the precise control of single-particle phase shift θ, as well as the particle number N. Imprecise controls of either will lead to $\eta \neq 0$, and thus a reduction in overall fidelity. To estimate this effect, we let $N\theta = x_1 + \delta$, with δ resulted from the displacement of θ and/or N. Expanding $\eta(x_1 + \delta)$ near $\eta(x_1) = 0$ gives

$$\eta(x_1 + \delta) \approx 1.3\ \delta^2, \tag{5.22}$$

For a fidelity of $f = 1 - 200/N$ (with $\eta = 200/N$), it requires $\delta < 12.4/\sqrt{N}$. This then requires $\theta_1 - 9.5\ \theta_1^{1.5} < \theta < \theta_1 + 9.5\ \theta_1^{1.5}$, where $\theta_1 = x_1/N$ is the desired per-atom phase shift. This allows a relatively flexible control of θ.

Lastly, we note that for the TF input and the present parameter choice of $N\theta = x_1$, a single photon loss will immediately reduce the fidelity, with a worst-case result of $f = 0.73$ and thus disrupt the on-demand entanglement generation scheme. This is because a lost photon will lead to a rapid degradation of the interferometer sensitivity.

To see this, for the TF input state, one photon lost from the q-th path during qubit-to-qubit propagation will result in the final state

$$|\Psi'_f\rangle = \sqrt{\frac{1}{N}}\hat{U}_{BS}\hat{U}_y\hat{a}_q\hat{U}_x\hat{U}_{BS}|\Psi_i\rangle, \tag{5.23}$$

Use the identity

$$\hat{U}_{BS}\hat{U}_y\hat{a}_q\hat{U}_y^\dagger\hat{U}_{BS}^\dagger = e^{i\theta\hat{c}_{yq}^\dagger\hat{c}_{yq}}(\hat{a}_q - i\hat{a}_{1-q})/\sqrt{2}, \tag{5.24}$$

The identity

$$\hat{U}_{BS}\hat{U}_y\hat{a}_q\hat{U}_y^\dagger\hat{U}_{BS}^\dagger = e^{i\theta\hat{c}_{yq}^\dagger\hat{c}_{yq}}(\hat{a}_q - i\hat{a}_{1-q})/\sqrt{2}, \tag{5.25}$$

leads to

$$\begin{aligned}
|\Psi'_f\rangle &= \sqrt{\frac{1}{2N}}\left[e^{i\theta\hat{c}_{yq}^\dagger\hat{c}_{yq}}(\hat{a}_q - i\hat{a}_{1-q})\right]\hat{U}|\Psi_i\rangle, \qquad (5.26)\\
&= \sqrt{\frac{1}{2N}}\sum_{ij}\chi_i^x\chi_j^y\hat{P}_q|ij\rangle \otimes \sum_{m=-N}^{N}\xi_m(\theta_{ij}) \times \\
&\quad [(-i)^q\sqrt{N+m}|N+m-1, N-m\rangle + \\
&\quad (-i)^{1-q}\sqrt{N-m}|N+m, N-m-1\rangle],
\end{aligned}$$

with the projector $\hat{P}_q$ defined as

$$\begin{aligned}
\hat{P}_q &= e^{i\theta\hat{c}_{yq}^\dagger\hat{c}_{yq}} \\
&= e^{i\theta}|q\rangle_y\langle q| + |1-q\rangle_y\langle 1-q|. \qquad (5.27)
\end{aligned}$$

A lost photon will therefore result in odd number differences of photons measured in the two output ports. Since without photon loss, a TF state will always result in

even number differences, it is in this way possible to determine the loss of a single photon (while without knowing which path it is lost from). Seemingly, this makes it possible to detect the phase imbalance if we accordingly redefine a null result as the measured photon number difference being 1. The false-null rate as given by

$$\eta^{loss} = |\xi_0(\theta) + i\xi_1(\theta)\sqrt{1+1/N}|^2, \tag{5.28}$$

is, however, no long a small quantity. A comparison of η^{loss} and η is plotted in Fig. 5.3, where it is shown η^{loss} behaves as the envelope of η without the zero-value points. In particular, with the present choice of $N\theta = x_1$, it is found $\eta^{loss} \approx 0.27$, in contrast to the corresponding rate $\eta = 0$ without the loss. Depending on the qubits' states, a photon loss will thus immediately degrade the fidelity to $f \geq 0.73$.

On the other hand, η^{loss} is yet much smaller than the corresponding false-null rate ε for the coherent state. Hence, if we presume one photon will be lost and set the value of $N\theta$ accordingly, we may still generate entanglement without the cavity enhancement. In fact, as shown in Fig. 5.3, a least-square fit finds

$$\eta^{loss} = \frac{0.33}{N\theta}. \tag{5.29}$$

Letting $\eta^{loss} = P_{sp}$ and using equation (5.4) gives

$$P_{sp} = \frac{2.6}{N^{1/3}}, \tag{5.30}$$

for $W/\lambda = 3$. The limit to fidelity thus scales as $1 - 2.6/N^{1/3}$, and a fidelity of $f = .99$ will require $N = 1.8 \times 10^7$, compared to $N = 2 \times 10^4$ without photon loss. Entanglement can in this sense still be generated without the need of cavities, while the single-photon loss can be compensated by using more photons. Lastly, we note that $f \sim 1 - 2.6/N^{1/3}$ is also the lower limit on the fidelity achievable when the

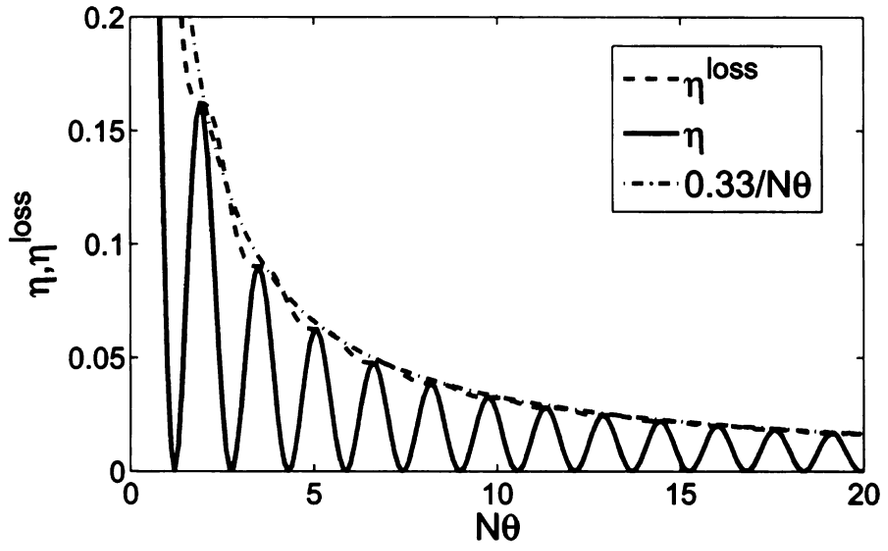

Figure 5.3: Comparison of η^{loss} and η. Note that both depend only on the product $N\theta$.

phase shift can not be tuned such that $\eta(N\theta) = 0$. This is simply because η^{loss} is the envelop of η, and for any N and θ, $\eta \leq \eta^{loss}$.

To sum up, in this section we have shown that for a MZ interferometer with the TF input, atom-atom entanglement can be generated with much higher fidelity, and the need for high-finesse optical resonators can in principle be eliminated. Particularly, we found a fidelity of .99 is quantum-mechanically allowed with 20,000 photons, or more intriguingly with only 2 photons, provided ring cavities which cycle photons 2×10^4 times are additionally incorporated. The 2-photon TF state could be generated with a pair of single-photon-on-demand sources (one for each input) and a precise photon detector to measure the two-photon output state, technologies that are rapidly advancing at present. Finally, we have shown the present scheme is relatively insensitive to deviations in the per-atom phase shift, yet is highly sensitive to loss of a single photon. This is somewhat mitigated by the fact that for the 2-photon state, the loss of a photon could be readily detected, so that success is heralded by the detection of both photons.

5.3.2 NOON-state interferometry with nonlinear beamsplitters

In above sections, we have discussed generating entanglement between atomic qubits using an optical MZ interferometer with TF input states and linear beamsplitters. While both are shown to be able to achieve a close-to-unit fidelity in the presence of intrinsic quantum errors, they require precise measurement of output light field at the single-photon level. In this section, we show this requirement can be overcome by using a non-MZ interferometer based on NOON states and nonlinear beamsplitters [242].

A NOON state is a Shrödinger cat state that corresponds to an equally-weighted superposition of all-upper-channel and all-lower-channel states [24, 265, 266, 267, 180]

$$|\text{NOON}\rangle = \frac{1}{\sqrt{2}}(|N,0\rangle + e^{i\phi}|0,N\rangle), \tag{5.31}$$

where ϕ is the relative phase which we take for zero for simplicity. The nonlinear beamsplitter can either be a four-wave mixer [26] or a quantum circuit constructed from CNOT gates [136]. The action of such beamsplitters is presented by a projecting operator $\hat{U}_{NBS}$ of the general form

$$\hat{U}_{NBS} = \frac{1}{\sqrt{2}}\sum_{s}(e^{i\phi}|s,0\rangle + |0,s\rangle)\langle 0,s| + e^{i\varphi}(e^{i\phi}|s,0\rangle - |0,s\rangle)\langle 0,s|, \tag{5.32}$$

where for simplicity we let the relative phases $\phi = \varphi = 0$. Note for the four-wave mixer, this projector is valid only for even-number s. A realization of this nonlinear beamsplitter in nonlinear Kerr medium is presented in the appendix. Using this nonlinear beamsplitter, a NOON state can be generated from a single Fock state $|N,0\rangle$, i.e., by injecting N photons in its upper input channel.

The set-up of the NOON-state interferometer differs from a MZ interferometer in

that now the first beamsplitter is dropped (or more precisely, it is formally replaced by the assumption of a NOON input state) while the second one is replaced by the nonlinear beamsplitter, as shown in Fig.5.1 (b). For measurement, a photo detector is placed in the lower (or equivalently, the upper) output port to detect the presence of outcoming photons, while without counting them. Because the output light field consists of $|N,0\rangle$ and $|0,N\rangle$ states, corresponding to all photons coming out from upper or lower port, a photon detector with a resolution of $< N/2$ would be sufficient to distinguish them. This exhibits an essentially improvement from the previous MZ interferometry schemes, where the detector resolution must be less than one. A null result, meaning no photon is detected at the lower channel, will collapse the qubits onto

$$\chi_0^x\chi_1^y|01\rangle + \chi_1^x\chi_0^y|10\rangle + |\kappa\rangle, \tag{5.33}$$

with $|\kappa\rangle$ the intrinsic state error due to a false-null result. In contrast, if the detector has detected a photon, the qubits will collapse into the imbalanced subspace

$$\chi_0^x\chi_0^y|00\rangle + \chi_1^x\chi_1^y|11\rangle. \tag{5.34}$$

Here, we emphasize that this state is independent on the exact number difference n between the upper and lower outputs. This is essentially different from the corresponding ones in (5.71) with the coherent state and in (5.19) with the TF state, both of which are dependent on n.

To derive these results, we follow the previous approach and find the final state of system as

$$\begin{aligned}|\Psi_f\rangle &= \hat{U}_{NBS}\hat{U}_y\hat{U}_x\left[\frac{1}{\sqrt{2}}(|N,0\rangle + |0,N\rangle)\otimes|\psi_x\rangle\otimes|\psi_y\rangle\right] \\ &= \sum_{i,j=0,1}\chi_i^x\chi_j^y|ij\rangle\otimes[\cos N\theta_{ij}|N,0\rangle - i\sin N\theta_{ij}]0,N\rangle],\end{aligned}$$

where we have dropped an irrelevant global-phase term in the last step. The probability of a null result is thus

$$P_{null} = \Lambda(1-\kappa) + \kappa, \tag{5.35}$$

with $\kappa = \cos^2 N\theta$ is the intrinsic error rate. On detecting this null result, the qubits will collapse onto

$$|\Psi_B\rangle = \frac{1}{\sqrt{\Lambda(1-\kappa)+\kappa}} \left[\chi_0^x \chi_1^y |01\rangle + \chi_1^x \chi_0^y |10\rangle + \sqrt{\kappa}(\chi_0^x \chi_0^y |00\rangle + \chi_1^x \chi_1^y |11\rangle)\right] \tag{5.36}$$

where $\kappa = \cos^2 N\theta$ is the false null rate. The corresponding fidelity is then

$$f_{null} = \frac{\Lambda}{\Lambda + (1-\Lambda)\kappa}. \tag{5.37}$$

The remaining time, a not-null result is detected, projecting the qubits onto the imbalanced subspace,

$$|\Psi_U\rangle = \frac{1}{\sqrt{1-\Lambda}} \left(\chi_0^x \chi_0^y |00\rangle + \chi_1^x \chi_1^y |11\rangle\right). \tag{5.38}$$

The overall fidelity averaged over the null and not-null results is given by

$$f_{avg} = 1 - (1-\Lambda)\kappa. \tag{5.39}$$

The fidelity in this entanglement generation is thus similar to the MZ interferometry cases but with the intrinsic error rate given by κ. A comparison of $\varepsilon, \eta, \kappa$ is shown in Fig. 5.2, where it is shown that for $N\theta < 1$, κ is close to η, exhibiting a Heisenberg-limited phase sensitivity. Furthermore, κ is exactly zero at $N\theta = \pi/2$, compared to at 1.196 for η. This means the NOON-state interferometer can achieve similar performances with the TF state. The fidelity after taking into account the possibility of

spontaneous emission therefore scales as $f \approx 1 - 350/N$. A fidelity of $f = .99$ and $f = .999$ will then require $N = 3.5 \times 10^4$ and $N = 3.5 \times 10^5$ photons, respectively. Since there is no requirement on exactly counting output photons, N can in principle be made large, allowing an arbitrary close-to-unit fidelity, at least quantum mechanically. Finally, similar to TF state, in order to suppress false-null rate, for a fidelity of $\approx 1 - 350/N$, θ must be tuned within an interval of $(\theta_1 - 8.1\theta_1^{1.5}, \theta_1 + 8.1\theta_1^{1.5})$ with $\theta_1 = \pi/2N$.

The present entanglement generation using NOON states will be completely disrupted by a single-photon loss. This is due to the fact that a randomly lost photon will immediately collapse the NOON state to a statistical mixture of all-upper-channel and all-lower-channel states, whose reduced density is given by

$$\rho^{loss} = \frac{1}{2}(|N-1,0\rangle\langle N-1,0| + |N-1,0\rangle\langle N-1,0|). \tag{5.40}$$

This mixture state is apparently incapable of detecting phase imbalances. This problem, however, might be overcome by using a class of less-extreme cat-like states [268, 249]. Such states correspond to a symmetric superposition of two well-separated wavepackets in number-difference space. In the case of small photon losses, instead of being completely destroyed, they will decay into a mixture of smaller-sized cat-like states, which are still suitable for the purpose of detecting phase imbalance. Hence, asides from a reduction in fidelity due to phase randomization, faithful entanglement might be generated despite of photon loss. This study is presented in appendix 5.6.3.

Finally, we note that the present NOON-state interferometer relies on highly nonclassical light source with definite photon number. This requirement is, however, not a necessity. For example, our scheme can be directly extended to use more 'classical' cat input states that correspond to the superposition of coherent states,

$$|\alpha\rangle_0 \otimes |0\rangle_1 + |0\rangle_0 \otimes |\alpha\rangle_1. \tag{5.41}$$

Such a state can be rewritten as,

$$\sum_m f(m)(|m,0\rangle + |0,m\rangle). \tag{5.42}$$

where $f(m)$ is the coefficient of the coherent state and can be approximated by

$$f(m) = \frac{1}{\sqrt{\mathcal{N}}} e^{-(m-N)^2/4N}. \tag{5.43}$$

where $\mathcal{N}$ is the normalization factor. A state yielding this distribution but containing only even ms has been proposed to generate probabilistically with a success probability of half, where a single coherent light and a four-wave mixer are employed [26]. With this input, the final state of the system becomes

$$|\Psi_f\rangle = \sum_{i,j=0,1} \chi_i^x \chi_j^y |ij\rangle \otimes \sum_m f(m)[\cos m\theta_{ij}|m,0\rangle - i \sin m\theta_{ij}]0,m\rangle]. \tag{5.44}$$

By choosing $N\theta = \pi/2$, similar to the single NOON state, upon detecting photons from the lower port, the qubit will collapse to imbalanced subspace (5.38). Otherwise, if no photon is detected from the lower port, the qubits will collapse to the state (5.36) but with the false null rate given by

$$\begin{aligned} \kappa' &= \frac{1}{2\mathcal{N}} \sum_m e^{-(m-N)^2/2N}(1 + \cos m\theta) \\ &= \frac{1}{2}(1 - e^{-\theta^2 N/2}) \end{aligned} \tag{5.45}$$

Since $N\theta = \pi/2$, we have $\kappa' \approx \pi^2/16N$, which is negligible compare to the fidelity reduction ($\approx 350/N$) due to the probability of spontaneous emission.

To conclude, in this section, we have shown that a NOON-state interferometer can achieve similar performance with the TF state, yet without the requirement for precisely measuring the output light field. While this scheme is not tolerant of a

single photon loss, this problem might be overcome by using a class of less extreme cat states. Also, besides using a single NOON input state with definite photon number, we showed the present scheme can also use a class of states with indefinite photons that correspond to the superposition of NOON states.

5.4 Examples of applications

The present interferometrical method of generating entanglement can serve as a basic protocol in the quantum information processing, based on which quantum computation and communication can be realized with the aid of local qubit operations. As an example, here we first show how it can be used to teleport an arbitrary quantum state from one qubit to another. We assume the x-qubit is the source qubit carrying an unknown teleporting quantum state, and y-qubit is target qubit which the state is transported to. The x-qubit is initially in the state

$$|\psi_x\rangle = \chi_0^x|0\rangle_x + \chi_1^x|1\rangle_x, \tag{5.46}$$

while the y-qubit is initially prepared as

$$|\psi_y\rangle = \frac{1}{\sqrt{2}}(|0\rangle_y + |1\rangle_y). \tag{5.47}$$

We first collapse the two qubits into entangled qubit-pair interferometrically using our method. Once the qubit-pair is generated, completing the teleportation requires that the qubits be disentangled. This can be accomplished in the following manner. Conditional upon a null result, a π-pulse is applied to the source qubit, flipping $|0\rangle_x \leftrightarrow |1\rangle_x$. When using a MZ interferometer with the coherent or TF state, in the case of an odd measured n, an additional relative π phase must be applied to the

state $|1\rangle_x$ (or $|1\rangle_y$). After these steps, the qubits' state becomes

$$\chi_0^x|00\rangle + \chi_1^x|11\rangle. \tag{5.48}$$

A $\pi/2$-pulse is then applied to the source (or the target) qubit, transforming the state into

$$[\chi_0^x|00\rangle - i\chi_0^x|10\rangle - i\chi_1^x|01\rangle + \chi_1^x|11\rangle]/\sqrt{2}. \tag{5.49}$$

This is followed by a state measurement of x-qubit. If it is measured $|0\rangle_x$, the y-qubit will collapse to

$$\chi_0^x|0\rangle_y - i\chi_1^x|1\rangle_y, \tag{5.50}$$

after which a $\pi/2$ phase is imprinted onto $|1\rangle_y$. Otherwise, it is measured in $|1\rangle_x$, and a $\pi/2$ phase is imprinted onto $|0\rangle_y$. After these conditional operations, the y-qubit will end up in the desired state

$$\chi_0^x|0\rangle_y + \chi_1^x|1\rangle_y, \tag{5.51}$$

which accomplishes the teleportation.

Besides the state teleportation between two qubits, our scheme can be easily generalized to generate many-qubit entanglement [269] as well as realize entanglement swapping [270, 151]. For example, the three-particle Greenberger-Horne-Zeilinger (GHZ) state,

$$(|000\rangle_{xyz} + |111\rangle_{xyz})/\sqrt{2}, \tag{5.52}$$

can be created by first preparing each qubit in the state

$$|\psi_\mu\rangle = \frac{1}{\sqrt{2}}(|0\rangle_i + |1\rangle_i), \tag{5.53}$$

with $i = x, y, z$. Then the two-qubit protocol is used to collapse x and y into the

state

$$(|00\rangle_{xy} + |11\rangle_{xy})/\sqrt{2} \otimes (|0\rangle_z + |1\rangle_z)/\rangle/\sqrt{2}. \tag{5.54}$$

If the same two-qubit procedure is applied to B and C, the GHZ state is obtained. This simple scheme can be extended in a straightforward manner to producing an N-particle Shrödinger cat state.

To realize entanglement swapping, we take an initially entangled qubit-pair,

$$\frac{1}{\sqrt{|c_{00}|^2 + |c_{11}|^2}}(c_{00}|00\rangle_{xy} + c_{11}|11\rangle_{xy}), \tag{5.55}$$

and an uncorrelated third qubit

$$|\psi_z\rangle = \frac{1}{\sqrt{2}}(|0\rangle_z + |1\rangle_z) \tag{5.56}$$

and apply our protocol to qubits y and z to create a GHZ-like state. Then, by disentangling y in the same manner as described for the source qubit in teleportation, we arrive at the desired swapped state

$$\frac{1}{\sqrt{|c_{00}|^2 + |c_{11}|^2}}(c_{00}|00\rangle_{xz} + c_{11}|11\rangle_{xz}). \tag{5.57}$$

5.5 Conclusion

In conclusion, we have used the formalism of the optical interferometer to treat the problem of creating entanglement among two single-atom qubits via a common photonic channel. We have compared the results from a MZ-interferometer with a coherent input state and high-finesse cavity enhancement, with TF input and those from a non-MZ interferometer based on the NOON state and nonlinear beamsplitter. Our

results suggest that high-fidelity entanglement can in principle be generated via any of the interferometrical approaches. Experimentally feasible schemes under current techniques are found by combining Heisenberg-limited interferometer with photon resonators. In particular, we find that a two-photon input state has a fundamental upper-limit to fidelity of .99, and provides the advantage that failure due to photon losses could be readily detected. Our interferometrical approaches of generating entanglement is operated with close-to-unity success probabilities and are scalable, and thus can serve as a universal protocol in quantum information processing, based on which quantum computation and communication can be realized with the aid of single-qubit operations.

5.6 Further discussions

5.6.1 MZ-interferometry with coherent input states

In this section, we examine the MZ-interferometric generation of entanglement employing coherent input states. We consider the upper channel (with operator $\hat{a}_0^\dagger$) initially in a coherent state, while the lower channel $\hat{a}_1^\dagger$ is in the vacuum state. A detector is used to count the photons coming from the upper output channel, while output in the lower channel is unmeasured. A null result, meaning zero photons detected, results in the qubits collapsing onto the balanced subspace,

$$\chi_0^x \chi_1^y |01\rangle + \chi_1^x \chi_0^y |10\rangle + |\varepsilon\rangle, \tag{5.58}$$

where $|\varepsilon\rangle$ is the intrinsic state error due to the possibility of a false null result. This error, which adds imbalanced states to the desired balanced subspace, sets the upper limit of the obtainable teleportation fidelity. If $n \neq 0$ photons are detected, the qubits

will collapse onto imbalanced subspace

$$\chi_0^x \chi_0^y |00\rangle + \chi_1^x \chi_1^y (-1)^n |11\rangle, \tag{5.59}$$

without intrinsic error. We note that the possibility of a dark count *will* introduce an analogous error, but this error rate is governed by technical aspects of the photodetector, and is presumably not an intrinsic quantum error.

To derive these results for coherent input state, the initial state of the complete system is given by equation (5.7), with

$$\Phi_i(\hat{a}_0^\dagger, \hat{a}_1^\dagger) = e^{-\alpha \hat{a}_0^\dagger + \alpha^* \hat{a}_0} \tag{5.60}$$

Following equation (5.12), the state of the system at the interferometer output is obtained as

$$|\Psi_f\rangle = \sum_{i,j=0,1} \chi_i^x \chi_j^y |ij\rangle \otimes |\bar{\alpha} \sin\theta_{ij}\rangle_0 \otimes |\bar{\alpha} \cos\theta_{ij}\rangle_1 \tag{5.61}$$

where $\bar{\alpha} = -i\alpha e^{i\theta}$ and the states $|\alpha\rangle_{0,1}$ indicate optical coherent states for the upper and lower interferometer outputs, respectively. Expanding the upper channel onto photon number-eigenstates and making the small-angle approximation gives

$$|\Psi_f\rangle = \sum_{n=0}^{\infty} |n\rangle_0 \otimes |\bar{\alpha}\rangle_1 \otimes |\phi_n\rangle_{xy}, \tag{5.62}$$

where $|n\rangle_0$ indicates a state with n photons in the upper output, and

$$|\phi_0\rangle_{xy} = \chi_0^x \chi_1^y |01\rangle + \chi_1^x \chi_0^y |10\rangle + |\varepsilon\rangle \tag{5.63}$$

$$|\phi_{n\neq 0}\rangle_{xy} = f_n \left[\chi_0^x \chi_0^y |00\rangle + (-1)^n \chi_1^x \chi_1^y |11\rangle\right], \tag{5.64}$$

where

$$|\varepsilon\rangle = e^{-|\alpha|^2\theta^2/2}(\chi_0^x\chi_0^y|00\rangle + \chi_1^x\chi_1^y|11\rangle) \tag{5.65}$$

and

$$f_n = \frac{\bar{\alpha}^n}{\sqrt{n!}}e^{-|\alpha|^2\theta^2/2}. \tag{5.66}$$

The photon number in the upper channel is then measured with single-photon resolution, while the output from the lower channel is left unmeasured. From equation (5.62), the probability of detecting n photons $P(n)$ is given by

$$P(n) = \Lambda\delta_{n,0} + (1-\Lambda)e^{-N\theta^2}\frac{N\theta^2)^n}{n!} \tag{5.67}$$

where $\Lambda = |\chi_0^x\chi_1^y|^2 + |\chi_1^x\chi_0^y|^2$ is the weight of balanced-space states in the initial qubits' state. The probability of detecting zero photons is thus

$$P(0) = \Lambda(1-\varepsilon) + \varepsilon, \tag{5.68}$$

where $\varepsilon = e^{-N\theta^2}$ indicates the probability of a false null result. On detecting the null result, the qubits' state will collapse onto

$$|\Psi_B\rangle = \frac{1}{\sqrt{\Lambda(1-\varepsilon)+\varepsilon}}\left[\chi_0^x\chi_1^y|01\rangle + \chi_1^x\chi_0^y|10\rangle + \sqrt{\varepsilon}(\chi_0^x\chi_0^y|00\rangle + \chi_1^x\chi_1^y|11\rangle)\right]. \tag{5.69}$$

The fidelity upon this null result f_{nul}, which measures the weight of balanced states in $|\Psi_B\rangle$, is thus

$$f_{nul} = \frac{\Lambda}{\Lambda + (1-\Lambda)\varepsilon}, \tag{5.70}$$

which is non-unity due to the non-zero probability of a false null result. The condition for faithful teleportation is then $\varepsilon \ll 1$, or $N\theta^2 \gg 1$, characteristic of a standard-

quantum-limit interferometer.

The remaining time, a photon-number $n \neq 0$ is detected, with the qubit-state collapsing onto the imbalanced space with unit fidelity,

$$|\Psi_U\rangle = \frac{1}{\sqrt{1-\Lambda}} \left(\chi_0^x \chi_0^y |00\rangle + (-1)^n \chi_1^x \chi_1^y |11\rangle\right). \tag{5.71}$$

The $(-1)^n$ term comes from the phase difference between number-states for the coherent states $|\alpha\rangle$ and $|-\alpha\rangle$, i.e. while measuring photon number can not distinguish the states $|00\rangle$ and $|11\rangle$, it can introduce relative phase between them. If the photon number is definitely non-zero, yet not measured exactly, then tracing over the photon number creates a statistical mixture of $|00\rangle$ and $|11\rangle$. In this case, the protocol would create an entangled state with non-unity success probability Λ, but success would be heralded by the verification of zero photons in the upper output. Most likely, the initial state $\chi_m^\mu = 1/\sqrt{2}$ would be prepared so that $\Lambda = 50\%$. For entanglement on-demand, however, it is necessary to determine the photon number exactly. This difficulty is somewhat mitigated by the fact that the average photon number is $\bar{n}_0 = -\ln \varepsilon$, i.e. only 5 photons must be counted for $\varepsilon = .01$ and 7 for $\varepsilon = 0.001$.

Leaving the lower output unmeasured means that computing the output state requires tracing over the lower mode. In the proceeding derivation we have taken this trace to be unity. In reality, it is less than unity due to the non-orthogonality of the balanced and imbalanced lower output states, governed by the overlap

$$\begin{aligned} |{}_1\langle \bar{\alpha} \cos\theta_{ii} | \bar{\alpha} \cos\theta_{ij} \rangle_1|^2 &\approx 1 - (1-\delta_{ij})\theta^4 N/8 \\ &= 1 - O(1/N). \end{aligned} \tag{5.72}$$

Here, $N = |\alpha|^2$ is the mean input photon number and the last equality is because our scheme requires $N\theta^2 \gg 1$. The resulting error is then $\sim 1/N$, which can be neglected for large N. This result validates the small-angle approximation made for the final

state as in (5.62), where the lower-channel light field is assumed θ-independent and factorized from the remaining system.

The overall fidelity due to state error in this interferometrical entanglement generation is obtained by averaging over the null- and not-null- results, giving

$$\begin{aligned} f_{avg} &= P(0) \times f_{nul} + \sum P(n \neq 0) \times 1 \\ &= 1 - (1 - \Lambda)\varepsilon \end{aligned} \tag{5.73}$$

Since $\Lambda \geq 0$, it is always $f_{avg} \geq 1 - \varepsilon$, regardless of the quantum states of the two qubits.

Aside from the technical challenge of single-photon counting, the fundamental quantum-mechanical barrier to successful teleportation lies in finding a balance between phase-shift detection and spontaneous-emission avoidance, as a single spontaneously scattered photon can destroy the coherence of a qubit. The spontaneous emission probability for a single qubit is $\theta N\Gamma/\Delta$, which becomes negligible when $\theta N\Gamma/\Delta \ll 1$. This condition must be satisfied without violating the shot-noise-sensitivity condition $N\theta^2 \gg 1$. From equation (5.4) it follows that compatibility requires $16(W/\lambda)^2 \ll 1$, which clearly violates the standard optical diffraction limit. That such a scheme can therefore not work is in agreement with common understanding [262].

To overcome the effects of spontaneous emission, we can place the two qubits in seperate high-finesse optical cavities, with mechanical Q-switching employed to restrict the photon to M passes through each qubit. This will increase the phase-shift θ and the spontaneous emission probability P_{sp} by a factor of M. This relaxes the compatibility condition to $8(W/\lambda)^2 \ll M$, which can be satisfied without sub-wavelength focussing.

The failure probabilities due to interferometry sensitivity and spontaneous emis-

sion are then $\varepsilon = e^{-NM\theta^2}$ and

$$P_{SP} = 2NM\theta\Gamma/\Delta, \tag{5.74}$$

respectively. Setting $P_{sp} = \varepsilon = .01$, corresponding to a fidelity of .99, and taking $W/\lambda = 3$ gives

$$\begin{aligned} M &= -144 \log \varepsilon/\varepsilon \\ &= 6.6 \times 10^5, \end{aligned} \tag{5.75}$$

which is large but not necessarily outside the range of current experimental techniques. For these parameters, the mean number of photons in the upper output is $\bar{n}_0 = 4$, and the input photon number is restricted only by the condition $N(\Gamma/\Delta)^2 = 144\,\varepsilon/M = 4.4 \times 10^{-6}$, together with the off-resonant condition $\Delta \gg \Gamma$.

A main difficulty in long-distance quantum communication is photon loss during qubit-to-qubit transmission, where the loss probability increase exponentially with the transport distance. In schemes based on cavity-QED [182, 183, 184, 185], atomic qubits' states are encoded in the internal (polarization) states of photons, and thus a lost photon will immediately reveal the atomic states and destroy the qubits via decoherence. In contrast, during an interferometrical communication, the qubits' state information is encoded in a form of relative phase-shifts of photons propagating in the upper and lower arms. Such a shift is not a measurable quantity until the two channels are recombined at a second beamsplitter. Thus the lost photon cannot reveal the state of the qubit, and one might suspect that the qubit coherence would be preserved. On the other hand, due to the photon-atom interaction, a lost photons will introduce a small relative phase-shift to the qubits. The magnitude of the relative phase is θ, but the sign depends on which interferometer 'arm' lost the photon. Tracing over which arm thus results in effective decoherence and thus a reduction in

the fidelity of entanglement.

To see this, we first consider one photon lost during propagating between the first and the second qubits. This will alter the final state into

$$|\Psi'_f\rangle = \sqrt{\frac{2}{N}}\hat{U}_{BS}\hat{U}_y\hat{a}_q\hat{U}_x\hat{U}_{BS}|\Psi_i\rangle, \tag{5.76}$$

with $q = 0, 1$ corresponding to the loss in upper and lower arms, respectively. The identity (5.25) enables us to write,

$$\begin{aligned} |\Psi'_f\rangle &= \sqrt{\frac{1}{N}}e^{i\theta\hat{c}^\dagger_{yq}\hat{c}_{yq}}(\hat{a}_q - i\hat{a}_{1-q})\hat{U}|\Psi_i\rangle & (5.77)\\ &= (-i)^q e^{i\theta\hat{c}^\dagger_{yq}\hat{c}_{yq}}|\Psi_f\rangle, & (5.78)\end{aligned}$$

where in the last step we have used the fact that for the present input state (5.60), $\hat{a}_q|\Psi_i\rangle = \alpha\delta_{q,0}|\Psi_i\rangle$. It is now clear that the net effect of one lost photon is equivalent to introducing a relative phase $\pm\theta$ to the qubit, where $\theta \ll 1$. In the case of random photon losses, such phase disturbances will lead to the unknown drift of the qubit's state and thus a reduction in the overall fidelity of the entanglement generation. To estimate this fidelity reduction, we introduce the lost photon number distribution $f(k)$. Because each photon is lost independently, $f(k)$ will exhibit a Poisson distribution, where for a mean loss number $\bar{k}$, the variance is $\sqrt{\bar{k}}$. For simplicity, we approximate $f(k)$ with a gaussian,

$$f(k) = \frac{e^{-(k-\bar{k})/2\bar{k}}}{\sqrt{2\bar{k}\pi}}. \tag{5.79}$$

The system's density ρ^{loss} after the loss is then a mixture of

$$\rho^{loss} = \sum_{k,k'}(-i)^{k'}f(k)f(k')(\hat{P}_0)^k(\hat{P}_1)^{k'}|\Psi_f\rangle\langle\Psi_f|(\hat{P}_1^\dagger)^{k'}(\hat{P}_0^\dagger)^k, \tag{5.80}$$

where $\hat{P}_q$ is the y-qubit projector defined in (5.27). Defining the reduced fidelity due to the photon loss,

$$f_{loss} = tr\{\rho\rho^{loss}\}, \tag{5.81}$$

it is found

$$\bar{k} = \frac{N\ln(2f_{loss}-1)}{\ln\epsilon}. \tag{5.82}$$

Taking $f_{loss} = 1-\epsilon = .99$ gives $\bar{k} = .004N$, meaning about one photon can be lost in every 250 photons.

5.6.2 An implementation of nonlinear beamsplitter

In this appendix, we supply a realization of the nonlinear beamsplitter for NOON interferometry in section 5.3.2. This approach, first proposed in ref. [26], is implemented with a Kerr-medium-type Hamiltonian,

$$H = \frac{\Omega}{4}(\hat{a}^\dagger\hat{b} + \hat{a}\hat{b}^\dagger)^2, \tag{5.83}$$

achievable in χ^3 nonlinear mediums. For convenience, we introduce the following spin (Schwinger) operators,

$$\begin{aligned} J_x &= \frac{1}{2}(\hat{a}^\dagger\hat{b} + \hat{a}\hat{b}^\dagger) \\ J_y &= \frac{1}{2i}(\hat{a}^\dagger\hat{b} - \hat{a}\hat{b}^\dagger) \\ J_z &= \frac{1}{2}(\hat{a}^\dagger\hat{a} - \hat{b}^\dagger\hat{b}), \end{aligned} \tag{5.84}$$

with which the Hamiltonian (5.83) is simply $H = \Omega J_x^2$. The goal is to investigate the time evolution of the quantum state $|\Psi\rangle(t)$ under this Hamiltonian, given by

$$|\Psi\rangle(t) = e^{-i\Omega J_x^2 t}|\Psi\rangle(t=0). \tag{5.85}$$

For an analytic solution, it is observed that

$$e^{i\frac{\pi}{2}J_y}J_x e^{-i\frac{\pi}{2}J_y} = J_z. \tag{5.86}$$

Hence,

$$|\Psi\rangle(t) = e^{-i\frac{\pi}{2}J_y}e^{-i\Omega J_z^2 t}e^{i\frac{\pi}{2}J_y}|\Psi\rangle(t=0). \tag{5.87}$$

Furthermore, it is found that

$$\begin{aligned}
e^{-i\frac{\pi}{2}J_y}\hat{a}^\dagger e^{i\frac{\pi}{2}J_y} &= \frac{1}{\sqrt{2}}(\hat{a}^\dagger + \hat{b}^\dagger) \\
e^{-i\frac{\pi}{2}J_y}\hat{b}^\dagger e^{i\frac{\pi}{2}J_y} &= \frac{1}{\sqrt{2}}(\hat{b}^\dagger - \hat{a}^\dagger) \\
e^{i\frac{\pi}{2}J_y}\hat{a}^\dagger e^{-i\frac{\pi}{2}J_y} &= \frac{1}{\sqrt{2}}(\hat{a}^\dagger - \hat{b}^\dagger) \\
e^{i\frac{\pi}{2}J_y}\hat{b}^\dagger e^{-i\frac{\pi}{2}J_y} &= \frac{1}{\sqrt{2}}(\hat{b}^\dagger + \hat{a}^\dagger) \\
e^{-i\pi J_x}\hat{a}^\dagger e^{-i\pi J_y} &= i\hat{b}^\dagger \\
e^{-i\pi J_x}\hat{b}^\dagger e^{-i\pi J_y} &= i\hat{a}^\dagger
\end{aligned} \tag{5.88}$$

Consider an initial state of $|\Psi\rangle(0) = |N/2\rangle$, we have

$$\begin{aligned}
|\Psi\rangle(t) &= e^{-i\frac{\pi}{2}J_y}e^{-i\Omega J_z^2 t}e^{i\frac{\pi}{2}J_y}|N/2\rangle \\
&= e^{-i\frac{\pi}{2}J_y}\sum_m e^{-i\Omega m^2 t}c_m|m\rangle
\end{aligned} \tag{5.89}$$

where $c_m = \langle m|e^{i\frac{\pi}{2}J_y}|N/2\rangle$. It is noticed in the above equation that if N is odd, m must be half integers, with $m = k + 1/2$, with k an integer. Choosing $\Omega t = \pi$, we have

$$e^{-i\Omega m^2 t} = e^{-i\pi(k+1/2)^2} = e^{-i\pi/4}. \tag{5.90}$$

Hence, the net action is to imprint a global $-\pi/4$ phase shift, with the final state given by

$$|\Psi_f\rangle = e^{-i\pi/4}|N/2\rangle \tag{5.91}$$

Similar behavior is found for the case of $|\Psi\rangle(0) = |-N/2\rangle$. If N is even, then $m = k$, with k an integer, so that

$$e^{-i\Omega m^2 t} = e^{-i\pi k^2} = (-1)^m = e^{-i\pi J_z} \tag{5.92}$$

As a result,

$$\begin{aligned} |\Psi_f\rangle &= e^{-i\frac{\pi}{2}J_y}\sum_m (-1)^m c_m|m\rangle \\ &= e^{-i\frac{\pi}{2}J_y}\sum_m |m\rangle\langle m|e^{-i\pi J_z}e^{i\frac{\pi}{2}J_y}|N/2\rangle \\ &= e^{-i\frac{\pi}{2}J_y}e^{-i\pi J_z}e^{i\frac{\pi}{2}J_y}|N/2\rangle. \end{aligned} \tag{5.93}$$

Using the fact $e^{-i\frac{\pi}{2}J_y}e^{-i\pi J_z}e^{i\frac{\pi}{2}J_y} = e^{-i\pi J_x}$, it is then obtained that

$$|\Psi_f\rangle = e^{-i\pi J_x}|N/2\rangle = i^N|-N/2\rangle. \tag{5.94}$$

A similar result is found for $|\Psi\rangle(0) = |-N/2\rangle$. Thus in summary, the action of this beamsplitter is simply

$$|\pm N/2\rangle \Rightarrow \begin{cases} e^{-i\pi/4}|\pm N/2\rangle, & \text{N odd;} \\ i^N|\mp N/2\rangle, & \text{N even.} \end{cases} \tag{5.95}$$

These results are trivial.

However, if we choose $\Omega t = \pi/2$, for N being even, we have

$$e^{-i\pi\frac{m^2}{2}} = \frac{e^{-i\pi/4} + (-1)^m e^{i\pi/4}}{\sqrt{2}}. \tag{5.96}$$

This immediately leads to the result of

$$\begin{aligned} |\pm N/2\rangle &\Rightarrow \frac{1}{\sqrt{2}}[e^{-i\pi/4}|\pm N/2\rangle + e^{i\pi/4} i^N |\mp N/2\rangle \\ &= \frac{1}{\sqrt{2}} e^{-i\pi/4}[|\pm N/2\rangle + i^{N+1}|\mp N/2\rangle, \end{aligned} \tag{5.97}$$

thus implementing the desired action (5.32).

5.6.3 NOON-interferometry with less-extreme cat states

As an example, we consider the following less-extreme cat state,

$$|\tilde{N}\rangle = \frac{1}{\sqrt{2}}\left[|N-\tilde{N},\tilde{N}\rangle + |\tilde{N},N-\tilde{N}\rangle\right], \tag{5.98}$$

with $0 < \tilde{N} \ll N/2$. For this state, a photon loss during transportation between the first and second qubits alternates the system's input state to

$$\begin{aligned} |\Psi_{loss}\rangle &= \sqrt{\frac{2}{N}}\hat{a}_j \hat{U}_x \left[|\tilde{N}\rangle \otimes |\psi_x\rangle \otimes |\psi_y\rangle\right] \\ &= \sqrt{\frac{2}{N}}\hat{U}_x \left[\hat{a}_j|\tilde{N}\rangle \otimes \hat{P}_j|\psi_x\rangle \otimes |\psi_y\rangle\right] \end{aligned} \tag{5.99}$$

with $j = 0, 1$ corresponding to the loss occurring in the upper and lower channel, respectively. The x-qubit projector $\hat{P}_j$ is defined in a similar manner as in (5.27), with the qubit y replaced by x. From the equation, the net effect of a single photon-loss on the atomic qubits is to introduce a phase shift to the x-qubit. Due to the random nature of photon loss, such a phase disturbance will lead to the unknown drift of the qubit's state and thus a reduction in the overall fidelity of the entanglement

generation, as is the case for the TF-interferometer approach. The effect on the probing light beam is that the quantum state after a single loss is alternated to

$$\rho_{photon} = |\Psi_{\ell 0}\rangle\langle\Psi_{\ell 0}| + |\Psi_{\ell 1}\rangle\langle\Psi_{\ell 1}| \tag{5.100}$$

with

$$|\Psi_{\ell 0}\rangle = |N - \tilde{N} - 1, \tilde{N}\rangle + |\tilde{N} - 1, N - \tilde{N}\rangle, \tag{5.101}$$

$$|\Psi_{\ell 1}\rangle = |N - \tilde{N}, \tilde{N} - 1\rangle + |\tilde{N}, N - \tilde{N} - 1\rangle. \tag{5.102}$$

Such a light beam is still cat-like in sense that it is the uncertainty in number difference between the two modes is of the order of total particle number. Compared to the extreme cat state, it yields a slightly reduced phase-measurement sensitivity. Therefore, although at a reduced fidelity, the entanglement before the qubit x and y can be established in presence of photon loss, due to the same reason for the MZ-interferometer approach.

Finally, the final state in the presence of multiple-photon loss is given by a mixture of

$$\rho' = \sum_{k,k'} f(k) f(k') |\Psi'_f(k,k')\rangle\langle\Psi'_f(k,k')| \tag{5.103}$$

where $f(k)$ is the loss statistical given by (5.79). The resulting state $|\Psi'_f(k,k')\rangle$, corresponding to k photons lost in upper and k' in lower, is given by

$$|\Psi'_f(k,k')\rangle = \frac{1}{\mathcal{N}} \hat{U}_{NBS} \hat{U}_y \hat{U}_x \left[\hat{a}_0^k \hat{a}_1^{k'} |\tilde{N}\rangle \otimes \hat{P}_0^k \hat{P}_1^{k'} |\psi_x\rangle \otimes |\psi_y\rangle \right], \tag{5.104}$$

with $\frac{1}{\mathcal{N}}$ the normalization factor. To maintain the cat-like nature, the number of lost photons must be much smaller than $\tilde{N}$. Finally, we note that in presence of photon loss, the particular kind of nonlinear beamsplitter presented in section 5.6.2 is no long

applicable, since it relies on even total number of photons in the beam.

Chapter 6

Interaction- and measurement-free Quantum Zeno gates on-demand for single-atom and single-photon qubits

In this chapter, we investigate a quantum-zeno approach to implement quantum information processing using single-atom and single-photon qubits. By extending the concept of 'interaction-free imaging' to the single atom level, we show that on-demand interaction- and measurement-free quantum logic gates can be realized for both single-atom and single-photon qubits. The interaction-free feature suppresses the possibility of qubit decoherence via atomic spontaneous decay, while the elimination of measurements can significantly reduce errors arising from detector inefficiency. We present a general theory of universal quantum Zeno gates, and discuss physical implementations for quantum information processing with single atoms and photons. In addition, we propose a loss-tolerant protocol for long-distance quantum communication using quantum Zeno gates incorporated into a Mach-Zehnder interferometer.

The efficiency of our Zeno gates is limited primarily by the imprecise control of atom-photon scattering and the finite number of feedback cycles N due to the limited finesse of the optical ring-cavity. We find the success probability scales as $1-O(\frac{1}{N})$, and for realistic parameters could be as high as 98.4%. Successful generation of atom-atom entanglement can be heralded by detection of the ancillary photon, upon which the fidelity scales as $1-O(\frac{1}{N^2})$, with an achievable fidelity of 99.994%, which comes at the cost of reducing the success probability by the detector efficiency. The major results of this part of work have been published in "Interaction- and measurement-free quantum Zeno gates for universal computation with single-atom and single-photon qubits ", by Y. P. Huang and M. G. Moore in Phys. Rev. A. **77**, 062332 (2008).

In collaborate with C. Piermarocchi's ground also in the Physics and Astronomy department of Michigan State University, we further propose a scheme for a two-qubit conditional quantum Zeno phase gate for semiconductor quantum dots. The proposed system consists of two charged dots and one ancillary neutral dot driven by a laser pulse tuned to the exciton resonance. The primary decoherence mechanism is phonon-assisted exciton relaxation, which can be viewed as continuous monitoring by the environment. Because of the Zeno effect, a strong possibility of emission is sufficient to strongly modify the coherent dynamics, with negligible probability of actual emission. We solve analytically the master equation and simulate the dynamics of the system using a realistic set of parameters. In contrast to standard schemes, larger phonon relaxation rates increase the fidelity of the operations. This work has been published in "Two-Qubit Conditional Phase Gate in Laser-Excited Semiconductor Quantum Dots Using the Quantum Zeno Effect", by K. J. Xu, Y. P. Huang, M. G. Moore, and C. Piermarocchi, in Phys. Rev. Lett. **103**, 037401 (2009).

The organization of this chapter is as follows. In section 6.1, we give an introduction on the background of quantum zeno effect and its applications in various fields, as well as presenting an overview of this chapter's main results. In section

6.2, we describe the general theory of quantum Zeno gates. In section 6.3, we propose the physical implementations of the Zeno gate for single atom and photons. Specifically, we present two elementary Zeno gates built on the dissipative interaction between photons and atoms in section 6.3.1. Then, in section 6.3.2, we build Zeno CNOT gates for single atom and photon qubits. We then analyze the realistic success probability and the fidelity upon heralded success of the present quantum Zeno gates in section 6.4. Then, we briefly describe the two-qubit Zeno phase gate for quantum dots in section 6.5. This is followed by conclusions in section 6.6. As extensions of our work, in the appendix, we additionally construct atom-to-photon and photon-to-atom state transfer gates, as well as provide two long-distance quantum communication protocols, one of which is tolerant of photon loss.

6.1 Introduction and Overview

In implementing quantum information processing using hybrid single-particle qubits, i.e., single atoms and photons, perhaps the biggest challenge is to phase-coherently mix them without incurring decoherence. If achieved, this could lead to two-qubit operations between remote atomic qubits via a photonic channel, thus eliminating the restriction to nearest-neighbor interactions when processing an array of atomic qubits. As presented in chapter 5, a feasible scheme for such entanglement-generation would involve passing a far-detuned light pulse over both atomic qubits, whose polarization interacts only with one of the qubit internal states. Detection of a certain phase-shift in the light pulse relative to an idler pulse could indicate that one of the qubits was in the interacting state, but not which one, thus collapsing the two-qubit state into an entangled state [150, 40]. While a light pulse containing many photons can have a strong effect on a single atom, the back-effect of the atom on the light-field is very small. The primary difficulty in creating entanglement between

two atomic qubits via a common photonic channel thus lies in the need to employ a sufficiently large number of photons to detect the small phase distortion generated by a single atom, while avoiding the loss of information due to atomic spontaneous decay and/or imperfect optics. This problem is typically addressed by using high-finesse optical cavities to enhance the coupling while reducing the spontaneous decay [271, 272], and/or replacing single atom qubits with collective ensemble qubits[150, 259, 260]. With atomic ensemble qubits, however, the coherence time will be limited by information-destroying short-range interactions (collisions). In order to avoid this limitation, one can use single isolated trapped atoms, which then requires a high-Finesse optical resonator in the strong-coupling regime, and/or the use of highly non-classical light pulses [40].

In cavity QED approaches, one usually seeks to suppress spontaneous emission by significantly decreasing the density of states of the electromagnetic vacuum, so that a coherent atom-photon interaction becomes possible over some timescale. Despite the widely-held belief that decoherence must always be avoided in quantum information processing, it has been known for some time that decoherence can instead be harnessed to implement high-efficiency coherent quantum logic gates for single photons and atoms [273]. These gates rely on the fact that strong coupling to the environment is equivalent to continuous measurement, and can therefore inhibit coherent quantum dynamics, in analogy with the quantum Zeno effect [274, 275, 276, 277, 278, 279]. To best understand how such an effect can lead to coherent entanglement generation, consider a set of experiments where the Zeno effect was used to allow a single photon to image an absorbing object without being absorbed, knows as high-efficiency interaction-free measurement (IFM), or alternatively as 'quantum interrogation', [280, 281, 282, 283, 284, 285, 286]. Replacing the classical absorber with an atomic qubit, prepared in a superposition of absorbing and transparent states, can coherently change the quantum state of the probe photon conditioned on the state of the

atomic qubit. This leads to atom-photon entanglement, generated via a mechanism in which the atom and photon arguably never interact directly, so that spontaneous emission (decoherence) is avoided even for a resonant photon. In such a system it is simply the possibility of a strong dissipative interaction which drives the Zeno effect and creates entanglement, without dissipation actually occurring. The Zeno effect forces the system to remain in a decoherence free subspace (DFS) [162, 163, 164], and thus greatly suppresses the possibility of decoherence via spontaneous decay.

Several schemes for quantum entanglement manipulation and/or gate operation via IFM have been recently proposed [194, 195, 196, 197, 198]. Utilizing the dissipative photon-atom interaction, Gilchrist *et al* propose implementing conditional, post-selection protocols to generate Bell-, W- and GHZ-type states for single atoms with a maximum success probability of 1/4 [194]. They also provided an approach to generate n-photon superposition state with n IFM devices aided by an ancillary atom, where the final atomic state is measured and a logical operation is performed conditioned on the measurement outcome. In a closely related work, Azuma proposed to generate Bell states of an electron-positron pair, where pair annihilation supplies the equivalent dissipative interaction to drive the Zeno effect [195]. Also demonstrated for such a system are a Bell-measurement circuit and a Controlled-Not (CNOT) gate, with a maximum success probability of 3/4 and 9/16. By chaining multiple IFM devices, Azuma was able to further push the success probability of the Bell-measurement circuit and consequently the CNOT gate to be near unity [196]. This CNOT gate requires four ancillary entangled qubits, two Bell-measurements, together with four classical measurements and multiple measurement-conditioned operations. This is arguably too complex a construction relative to the simplicity of the task. In a non-IFM-based yet related approach, Franson *et al* proposed using the quantum Zeno effect to inhibit more than one photon occupying the same optical fiber mode, and thus implement the $\sqrt{SWAP}$ gate between two photonic modes, leading

to subsequent improvements in quantum computing with single photons [197]. Also very interestingly, using 'chained' quantum Zeno effect, Hosten *et al* demonstrated the *counterfactual* quantum computation, where the potential outcome of a quantum computation can be inferred without actually running the computer [198]. In a non-IFM-based yet related approach, Franson *et al* proposed using the quantum Zeno effect to inhibit more than one photon occupying the same optical fiber mode, and thus implement the $\sqrt{SWAP}$ gate between two photonic modes, leading to subsequent improvements in quantum computing with single photons [197]. Also very interestingly, using 'chained' quantum Zeno effect, Hosten *et al* demonstrated the *counterfactual* quantum computation, where the outcome of a quantum computation can be inferred without actually running the computer [198].

In this chapter, we consider three important changes to the standard IFM gate which allow us to design an extremely simple and elegant set of quantum logic gates towards quantum information processing. First, in contrast to simply flipping the internal state of the probe qubit, we allow arbitrary state rotation of the probe qubit. Second, in addition to the usual IFM gate with photon as the probe and atom as the object, we construct a complementary gate where the role of atoms and photons are exchanged. Third, we consider the placing multiple qubits in a single IFM circuit. With these changes, we are able to construct interaction- and measurement-free quantum logic gates in a straight forward manner.

We begin by presenting a generalized theory of the operating principle, and then consider physical implementations of such Zeno gates. Specifically, we design atom-photon, atom-atom and photon-photon CNOT gates, as well as atom-to-photon and photon-to-atom state transfer circuits. We also consider a long-distance quantum communication protocol which is tolerant to photon transmission losses. All of our quantum Zeno gates are high-efficiency in the sense that they deviate from unit success probability by a factor $\sim \frac{1}{N}$ and from unit fidelity upon heralded success by

only $\sim \frac{1}{N^2}$. Here N is the (effective) measurement number, limited only by technical considerations. One interesting feature of our design is that the IFM probe qubit acts only as an ancillary qubit, which is disentangled from the logical qubits at the end of the gate operation, so that no measurement of this qubit is required. The elimination of this measurement greatly boosts the success probability by removing errors due to detector inefficiency, as opposed to several previous schemes [182, 136, 168, 287, 288, 289, 170, 185, 290, 174]. On the other hand, detection of the ancillary qubit in the output channel would 'herald' successful gate operation, thus improving the fidelity of state creation by an additional factor $1/N$. In this way one can trade-off success probability for fidelity, where success probability is decreased only by the detector inefficiency. As is typical in cavity QED applications, the trade-off for high-fidelity is gate speed, as increasing N necessarily slows down the gate operation.

6.2 Quantum Zeno Gate: General theory

The quantum Zeno effect occurs when a rapid sequence of strong measurements is performed on a slowly evolving quantum system, with the result that the system is 'frozen' in its initial state, i.e. the quantum watched-pot boils more slowly than the unwatched pot. In the standard quantum Zeno effect, a two-level system (with states denoted $|0\rangle$ and $|1\rangle$) is rotated by a sequence of M rotations, each of angle θ/M. In the absence of measurements, this results in a net rotation of θ, so that a system initially prepared in state $|\Psi_i\rangle = |0\rangle$ is transformed to the superposition state $|\Psi_f\rangle = \cos\theta|0\rangle + \sin\theta|1\rangle$. The Zeno effect occurs when the system is measured in the $\{|0\rangle, |1\rangle\}$ basis after each θ/M rotation. It is readily found that the probability to find the particle in state $|0\rangle$ after M cycles is [274, 275, 276, 277]

$$P_0 = [1 - \sin^2(\theta/M)]^M$$

$$\approx 1 - \frac{\theta^2}{M} \quad . \tag{6.1}$$

This probability approaches unity in the limit $M \rightarrow \infty$, so that the system remains 'frozen' in the initial state.

An analogous effect occurs in the case of a two-level system evolving under continuous coherent evolution and dissipation, as illustrated in Figure 6.1. The coherent evolution is governed by the Hamiltonian

$$\hat{H}_\Omega = \frac{\hbar\Omega}{2}\sigma_y, \tag{6.2}$$

where σ_y is a Pauli spin matrix in the y direction. In the absence of dissipation, a system prepared initially in the state $|\Psi(0)\rangle = |0\rangle$ evolves after time t into the superposition state

$$|\Psi(t)\rangle = \cos(\Omega t/2)|0\rangle + \sin(\Omega t/2)|1\rangle. \tag{6.3}$$

In a quantum Zeno system, however, spontaneous emission is introduced, coupling the system to a reservoir. Standard quantum treatment of such systems is via a master equation for the system density matrix. In the current model, the scattered state after a spontaneous decay corresponds to the photon escaping from the system. Due to irreversibility, this state is dynamically decoupled from the rest of system during the subsequent evolution of the system. This allows us to map the master equation onto a pure-state representation, in which the system state is represented by a pure state in the unscattered subspace. The master equation dynamics can be then be exactly reproduced if this pure state evolves under an effective non-Hermitian Hamiltonian. Because of the non-Hermitian property, the state in this representation will no longer be normalized to unity as time evolves. This loss of normalization corresponds to the probability that the system has decayed. After a successful Zeno-gate operation, however, the system decay was prohibited by the Zeno effect. The quantum state of

system is then the evolved pure state, which must be re-normalized to unity.

For system depicted in Fig. 6.1, the state $|1\rangle$ decays at rate Γ to a third state $|g\rangle$. The effective non-Hermitian Hamiltonian in the pure-state representation of $\{|0\rangle, |1\rangle\}$ is then,

$$\hat{H}_{eff} = \hat{H}_{\Omega} - i\frac{\hbar\Gamma}{2}|1\rangle\langle 1|. \tag{6.4}$$

Derivation of this effective Hamiltonian, as well as further explanations of pure-state representation, is given in appendix 6.7.1. The reduction in normalization, $P(t) = \langle\Psi(t)|\Psi(t)\rangle$, corresponds to the probability that the system has decayed to state $|g\rangle$.

This evolution can be solved analytically, and in the regime $\Gamma \gg \Omega$, we find that the probability for the system to be found in the initial state $|0\rangle$ is given by $P_0(t) = e^{-\Omega^2 t/\Gamma}$. In the relevant case $\Omega t \sim 1$ and $\Gamma t \gg 1$, this becomes

$$P_0(t) \approx 1 - \frac{(\Omega t/2)^2}{\Gamma t/4}, \tag{6.5}$$

which approaches unity as Γt is increased with Ωt held fixed, in which limit the system is again 'frozen' in the initial state. The discrete and continuous systems can be mapped onto one another if we equate $\theta \leftrightarrow \Omega t/2$ and $M \leftrightarrow M_{eff} = \Gamma t/4 = \theta\Gamma/2\Omega$. The equivalence between the two systems can be understood by interpreting the spontaneous emission in the continuous case as a source of effective 'measurements' by the reservoir. The measurements are implemented because the presence or absence of spontaneous emitted photons will immediately reveal the state information and collapse the system into either $|1\rangle$ or $|0\rangle$. For a decay rate Γ, a single effective measurement duration is $4\Gamma^{-1}$. The effective number of measurements M_{eff} during a interval t is therefore $t/4\Gamma^{-1} = \Gamma t/4$. Equations (5) and (1) are in this sense exactly equivalent. We note a large M_{eff} corresponds to a large ratio of Γ/Ω, and hence a stronger dissipation is favorable for the continuous system. This is exactly opposed to the conventional approach, where dissipation must be negligible during a quantum

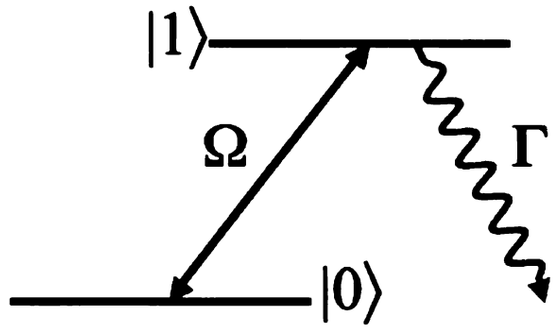

Figure 6.1: Level scheme for a two-state system with coherent coupling at Rabi frequency Ω and upper-state decay at rate Γ.

gate operation.

Using these results for the quantum Zeno effects, we now describe the general theory of quantum Zeno gates. Our model applies to both the discrete and continuous Zeno effects, as they can be exactly mapped onto each other. We will therefore treat only the continuous Zeno effect, with the understanding that analogous results for the discrete Zeno effect can be obtained by substituting M for M_{eff}. We show the generalized two-qubit logic gates can be realized via a single IFM in a direct or indirect manner. For the direct gate, one qubit acts as a 'probe', probing the quantum state of the 'object' qubit repeatedly or continuously, while the object qubit coherently driven on a timescale slow compared to the measurement time. The coherent evolution of the probe qubit will be allowed or prohibited depending on the state of the object qubit and thus create entanglement to implement the gate operation. This gate, however, requires the two qubits start inside the DFS, as states outside the DFS will immediately decay, resulting in loss of quantum information. Such direct gates are therefore incapable of implementing Unitary operations, which must be defined for all possible input states. We have found that with the addition of an ancillary qubit, Unitary quantum phase gates can be realized, even without the need to measure the final state of ancillary qubit. In these gates, the ancillary qubit acts as the probe measuring the joint quantum state of the two logical qubits, during which the three

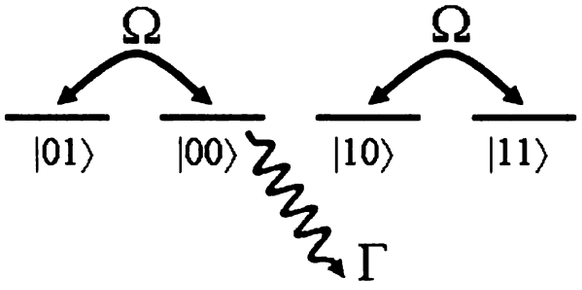

Figure 6.2: Scheme for the direct two-qubit quantum Zeno gate via a single IFM. Each state is of the form $|q_1 q_2\rangle$, where q_1 and q_2 are the probe and object qubits. The coherent Rabi oscillation is applied to the probe qubit as indicated by the blue arrows, while the green arrow indicates spontaneous decay.

qubits remain in a DFS.

For the direct logic gate, only two qubits are involved. As shown in figure 6.2, only the $|00\rangle$ state decays, so that the $|01\rangle$, $|10\rangle$ and $|11\rangle$ states form a DFS, where the two-qubit states are in the form $|q_1 q_2\rangle$, with q_1 and q_2 the probe and object qubits, respectively. Achieving this state selective decoherence is the primary design challenge in physical implementation of such gates. We will see, however, that the DFS states correspond to states where there is no interaction between each other, i.e. their wavefunction overlap is zero.

As the two logical qubits are required to be initially in the DFS, their initial state is

$$|\Psi_i\rangle = c_{01}|01\rangle + c_{10}|10\rangle + c_{11}|11\rangle, \tag{6.6}$$

The coefficients c_{ij}, with $i, j = 0, 1$, are arbitrary and normalized to one. The goal is to transform this state to the final state

$$\begin{aligned} |\Psi_f\rangle &= c_{01}|01\rangle + (c_{10}\cos\theta - c_{11}\sin\theta)|10\rangle \\ &+ (c_{10}\sin\theta + c_{11}\cos\theta)|11\rangle, \end{aligned} \tag{6.7}$$

with θ arbitrarily adjustable. Applying a slow σ_y pulse to the probe qubit rotates its state according to Hamiltonian (6.2). The attempt to rotate the probe qubit will therefore take the system out of the DFS if the object qubit is in the states $|0\rangle$, in which case the quantum Zeno effect will 'freeze' the system in its initial state and prevent the rotation of the probe qubit. Only if the object qubit is in the $|1\rangle$ state will the ancillary qubit undergo rotation and change its state. The final state of the system will then be (6.7) with $\theta = \Omega t/2$, and thus the desired target state is obtained. The success probability in this gate operation is given by the standard Zeno formula

$$P_{success} = 1 - |c_{01}|^2 \frac{\theta^2}{M_{eff}}, \tag{6.8}$$

where the effective number of measurements is $M_{eff} = \theta\Gamma/2\Omega$.

We now describe a quantum-Zeno phase-gate based on a three-qubit system, where one qubit serves as an ancillary, and two-qubits are the logical qubits. The operation of a phase gate on a two-qubit state is to transform an initial state of

$$|\Psi_i\rangle = c_{00}|00\rangle + c_{01}|01\rangle + c_{10}|10\rangle + c_{11}|11\rangle \tag{6.9}$$

into the final state

$$|\Psi_f\rangle = c_{00}|00\rangle + c_{01}|01\rangle + c_{10}|10\rangle - c_{11}|11\rangle. \tag{6.10}$$

Our scheme consists of a pair of logical qubits in an arbitrary initial state, together with a third ancillary qubit prepared in the $|0\rangle$ state. The initial state of the system is therefore

$$|\Psi_{in}\rangle = c_{00}|000\rangle + c_{01}|010\rangle + c_{10}|100\rangle + c_{11}|110\rangle, \tag{6.11}$$

where the three-qubit states are in the form $|q_1 q_2 a\rangle$, where q_1 and q_2 are the logical qubit quantum numbers and a describes the ancillary qubit. A single-qubit 2π-pulse is

applied to the ancillary qubit, rotating its state from $|0\rangle$ through $|1\rangle$ and back to $-|0\rangle$, which imprints a π-phase shift on the state of the system in the absence of dissipation. The complete state space of the three-qubit system consists of eight states. As shown in Figure 6.3, the states $|000\rangle, |100\rangle, |010\rangle, |110\rangle$ and $|111\rangle$ form a DFS, while the states $|001\rangle, |101\rangle$ and $|011\rangle$ decay at rates $2\Gamma, \Gamma$ and Γ, respectively. The decay rate for state $|001\rangle$ is doubled because there exist two possible decay channels, i.e., of q_1, a and q_2, a. The attempt to rotate the ancillary qubit will therefore take the system out of the DFS if the logical qubits are in the states $|00\rangle, |01\rangle$, or $|10\rangle$, in which case the Zeno effect will prohibit the rotation. The ancillary qubit will thus undergo rotation only if the logical qubits are in the $|11\rangle$ state, after which the π-phase shift is imprinted. The final state of the system will thus be

$$|\Psi_{out}\rangle = (c_{00}|00\rangle + c_{01}|01\rangle + c_{10}|10\rangle - c_{11}|11\rangle) \otimes |0\rangle_a \tag{6.12}$$

with probability

$$P_{success} = 1 - (\frac{|c_{00}|^2}{2} + |c_{01}|^2 + |c_{10}|^2)\frac{\pi^2}{M_{eff}}. \tag{6.13}$$

Here $M_{eff} = \pi\Gamma/2\Omega$. The extra factor of $\frac{1}{2}$ for the $|00\rangle$ state is due to that the relevant decay rate is then 2Γ, resulting in doubled number of effective measurements. Upon successful operation, the phase-gate has been applied and the state of the ancillary qubit is not entangled with that of the logical qubits, so that no measurement of the ancillary qubit and/or conditional operations are required.

Lastly, we note for both the direct and indirect quantum Zeno gates, successful operation indicates that the system remained in the DFS throughout, so that entanglement has been achieved without any interaction between qubits. Merely the possibility of dissipative interaction and the constant monitoring of the system by its environment are sufficient to project the system into an entangled state. As fast gate

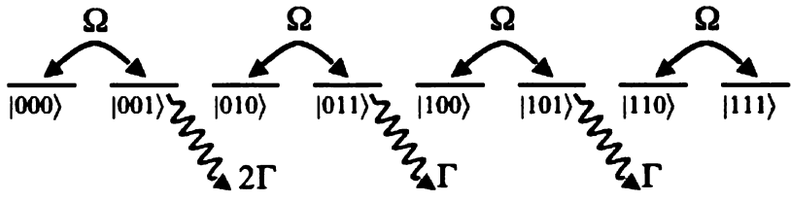

Figure 6.3: Scheme for a two-qubit phase gate with an ancillary qubit. Each state is of the form $|q_1 q_2 a\rangle$, where q_1 and q_2 are the logical qubits and a is the ancillary qubit. Note that the coherent Rabi coupling, indicated by the blue arrows, is applied to the ancillary qubit.

operation at high success probability is desired for scalable quantum computation, one should seek out a system with as large a decay rate Γ as possible, which is exactly the opposite regime one normally attempts to reach when quantum logic gates are based on ordinary coherent qubit-qubit interactions.

6.3 Implementations for single atomic and photonic qubits

Now we consider physical implementations of quantum-Zeno logic gates based on a single photon propagating in a high-finesse ring-cavity which interacts with a single atom. In the first part of this section, we propose two elementary interaction-free quantum gates. Then in the second part, we construct atom-atom, photon-photon and atom-photon CNOT gates from the elementary gates. Further quantum logical circuits, including atom-to-photon and photon-to-atom state transfer gates, as well long-distance quantum communication schemes, can be found in appendix 6.7.3 and 6.7.4, respectively.

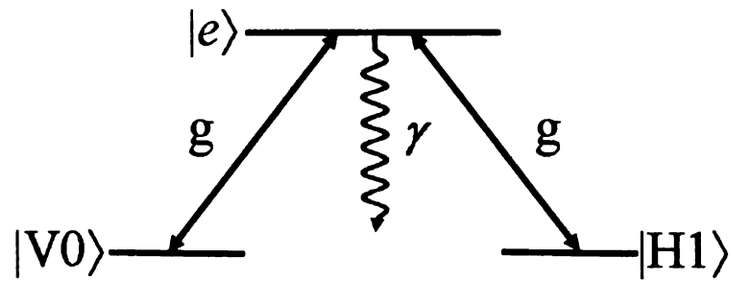

Figure 6.4: Level scheme for the elementary IFPG and IFRG gates. The states $|V0\rangle$ and $|H1\rangle$ are resonantly coupled to the excited state $|e\rangle$ with coupling strength g, while the state $|e\rangle$ spontaneously decays at rate γ.

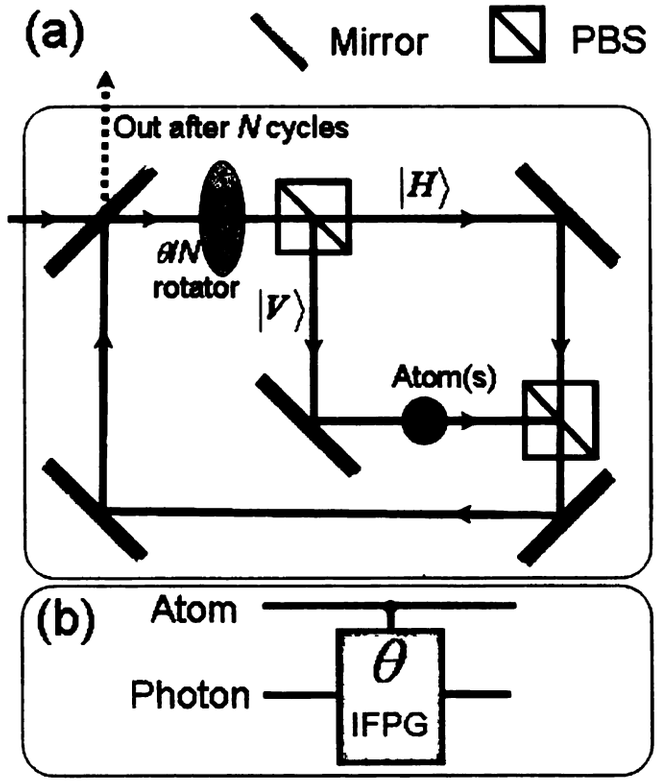

Figure 6.5: Figure (a): a schematic illustration of the physical implementation of IFPG; (b): its graphic representation.

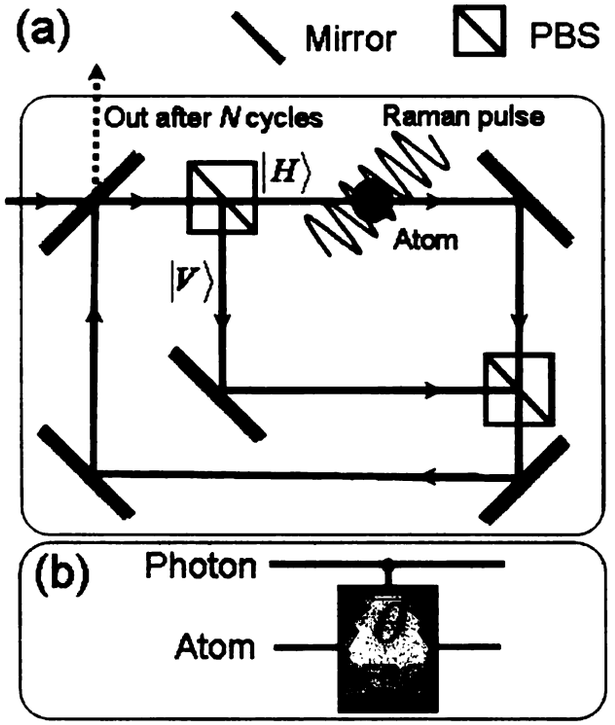

Figure 6.6: Figure (a): a schematic illustration of the physical implementation of IFRG; (b): its graphic representation.

6.3.1 Elementary atom-photon gates

The quantum logic circuits we propose are built from two elementary interaction-free quantum gates, which we term the Interaction Free Polarization Gate (IFPG) and the Interaction Free Raman Gate (IFRG). The IFPG is a generalization and refinement of previously proposed interaction-free gates [195, 194], and induces a rotation in the polarization of a photon conditioned on the state of a control atom. The IFRG reverses the role of atom and photon and induces a rotation of the atomic hyperfine state conditioned on the polarization of a control photon. The atom-photon interaction in these gates is based on a standard Λ-level scheme. The two atomic ground hyperfine states are labeled $|0\rangle$ and $|1\rangle$, and are coupled to an excited state $|e\rangle$ via absorption/emission of cavity photons with two orthogonal polarizations, labeled $|V\rangle$ and $|H\rangle$, respectively. We note that this choice of labels is purely symbolic, and in practice the two states will most likely be circular polarization states. The use of H and V is, however, in keeping with the early literature on interaction-free quantum interrogation [281, 285]. For the case of a single photon in the ring-cavity, the joint photon-atom states $|V0\rangle$ and $|H1\rangle$ couple strongly to $|e\rangle$ which then decays via spontaneous emission to a set of states having zero photons in the cavity, as shown in Figure 6.4. Due to selection rules, the joint-states $|H0\rangle$ and $|V1\rangle$ are not coupled to $|e\rangle$. Quantum back-reaction due to the non-emission of a photon therefore collapses the joint state onto the $\{|V1\rangle\,|H0\rangle\}$ subspace. For simplicity, we temporarily assume that the states $|H0\rangle$ and $|V1\rangle$ will immediately decay with unit probability.

The Interaction Free Polarization Gate is shown in figure 6.5 (a), with figure 6.5 (b) depicting a graphical representation of the gate. The circuit is modeled after the standard high-efficiency quantum interrogation circuit [285], which we have generalized to allow to an arbitrary polarization rotation angle θ, rather than the standard $\pi/2$ rotation. The gate consists of a high-finesse optical ring resonator, into which a single photon is injected and then released after N cycles. Each cycle consists of

passage through a θ/N polarization rotator followed by a pair of polarized beam-splitters (PBS), which spatially separate the H and V polarizations. The control atom is placed in the V arm. The input state must be of the form

$$|\Psi_{in}\rangle = c_{H0}|H0\rangle + c_{H1}|H1\rangle + c_{V1}|V1\rangle, \tag{6.14}$$

as the $|V0\rangle$ state leads to immediate loss of the photon via spontaneous emission. As only the V polarization interrogates the atom, it follows that the atomic state $|1\rangle$ is transparent to the photon. In this case, the effect of the atom is negligible, and the photon polarization rotates by the angle θ. If the atom is in state $|0\rangle$, however, the quantum Zeno effect will freeze the photon in the $|H\rangle$ state. Assuming successful operation, this leads to the output state

$$\begin{aligned} |\Psi_{out}\rangle &= c_{H0}|H0\rangle + (c_{H1}\cos\theta - c_{V1}\sin\theta)|H1\rangle \\ &+ (c_{H1}\sin\theta + c_{V1}\cos\theta)|V1\rangle, \end{aligned} \tag{6.15}$$

which shows that the photon polarization is rotated conditioned on the atom being in state $|1\rangle$.

The complementary Interaction Free Raman gate is depicted in figure 6.6 (a) and (b). It differs from the IFPG in that the atom is placed in the H arm, and the polarization rotator is replaced by a Raman pulse which couples the $|0\rangle$ and $|1\rangle$ atomic states via a $\hat{\sigma}_y$ rotation. The $\hat{\sigma}_y$ operation is timed so that the atomic state rotates by angle θ during the time it takes for the photon to travel N ring-cavity cycles. An arbitrary input state is of the form

$$|\Psi_{in}\rangle = c_{H0}|H0\rangle + c_{V0}|V0\rangle + c_{V1}|V1\rangle, \tag{6.16}$$

where the state $|H1\rangle$ is forbidden. If the photon is in $|H\rangle$, the quantum Zeno effect

freezes the atom in the $|0\rangle$ state; otherwise, the atomic spin rotates by θ. Upon successful operation, this results in the output state

$$\begin{aligned} |\Psi_{out}\rangle &= c_{H0}|H0\rangle + (c_{V0}\cos\theta - c_{V1}\sin\theta)|V0\rangle \\ &+ (c_{V0}\sin\theta + c_{V1}\cos\theta)|V1\rangle, \end{aligned} \tag{6.17}$$

which shows that the atomic state is rotated conditioned on the photon being in state $|V\rangle$.

6.3.2 Quantum Zeno CNOT gates

From these two elementary gates, we can construct the primary quantum logic gates necessary for universal quantum computation. The first gate we consider is the atom-atom Controlled-NOT gate, depicted schematically in figure 6.7 (a). In a CNOT gate, the state of the target qubit is flipped if the control qubit is in the logical $|1\rangle$ state, and is left unchanged otherwise. Our atom-atom CNOT uses a single IFPG with $\theta = \pi$, but with *two* atoms placed in the $|V\rangle$ arm. One atom serves as the control qubit and the other serves as the target. A single ancillary $|H\rangle$ photon is injected into the device to induce atom-atom entanglement via non-interaction with both atoms. The control atom differs from the target in that Hadamard transformations are applied to it before and after the interaction with the photon. For the IFPG with two atoms and one photon, the initial state is

$$|\Psi_{in}\rangle = |H\rangle \otimes (c_{00}|00\rangle + c_{01}|01\rangle + c_{10}|10\rangle + c_{11}|11\rangle). \tag{6.18}$$

If either atom is in the state $|0\rangle$, it will be sufficient to induce the quantum Zeno effect and freeze the photon in the $|H\rangle$ state. Thus only the $|11\rangle$ state is transparent to the photon, in which case the photon undergoes a π-rotation from $|H\rangle \rightarrow -|H\rangle$.

The output state of the two-atom π-IFPG is then

$$|\Psi_{out}\rangle = |H\rangle \otimes (c_{00}|00\rangle + c_{01}|01\rangle + c_{10}|10\rangle - c_{11}|11\rangle), \tag{6.19}$$

thus realizing a two-atom *phase-gate.* It is known that a phase-gate can be transformed into a CNOT gate via single-qubit operations, such as the Hadamard transform, defined as $|0\rangle \rightarrow (|0\rangle + |1\rangle)/\sqrt{2}$ and $|1\rangle \rightarrow (|0\rangle - |1\rangle)/\sqrt{2}$. Applying this transform to the state of the target atoms before and after the action of the π-IFPG gives the output state

$$|\Psi_{out}\rangle = |H\rangle \otimes (c_{00}|00\rangle + c_{01}|01\rangle + c_{11}|10\rangle + c_{10}|11\rangle), \tag{6.20}$$

corresponding to a CNOT operation on the two atoms. Due to our use of a π-polarization rotation, as opposed to the $\pi/2$ rotation of the standard IFM circuit, we find that at the output the photon is not entangled with the atoms. Because of this disentanglement, no detection of the photon and/or its polarization state is necessary. We note that during the N-cycles of the IFPG, the atoms and photon move through a highly entangled three-body state.

A photon-photon CNOT gate can be constructed similarly by injecting two photons into a π-IFRG containing a single ancillary atom. In this case, the control and target photons can be input as time-separated wave packets, or counter-propagate in the ring-cavity. This gate is depicted schematically in figure 6.7 (b). The analysis is the same as the atom-atom CNOT, with $H \leftrightarrow 0$ and $V \leftrightarrow 1$. After successful operation, the state of the atom is not entangled with the two-photon state, so that no atomic-state measurement is required for successful photon-photon gate operation.

A hybrid atom-photon CNOT, in which a stationary atomic qubit and a flying photonic qubit play the roles of control and target, can be constructed without the use of a third ancillary particle. In figure 6.8, we depict an atom-photon *phase gate.*

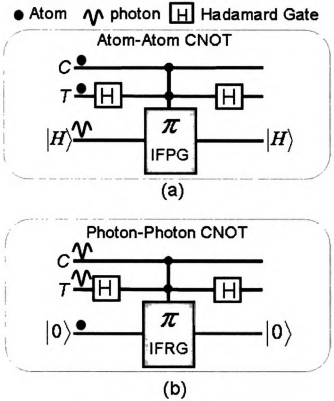

Figure 6.7: Graphical logic circuits for atom-atom (a) and photon-photon (b) CNOT gate. In both figures, we use 'C' for the control and 'T' for the target qubit.

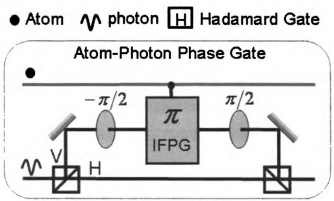

Figure 6.8: Graphical logic circuits for the atom-photon phase gate.

The input state for this gate is

$$|\Psi_{in}\rangle = c_{H0}|H0\rangle + c_{H1}|H1\rangle + c_{V0}|V0\rangle + c_{V1}|V1\rangle. \tag{6.21}$$

The first PBS sends the $|V\rangle$ polarization state along an upper arm, where a $-\pi/2$ rotator converts it to $|H\rangle$ polarization. The state of the system is then

$$|\Psi\rangle = c_{H0}|H0\rangle + c_{H1}|H1\rangle + c_{V0}|H'0\rangle + c_{V1}|H'1\rangle, \tag{6.22}$$

where the prime indicates the upper path. The π-IFPG then transforms the system to the state

$$|\Psi\rangle = c_{H0}|H0\rangle + c_{H1}|H1\rangle + c_{V0}|H'0\rangle - c_{V1}|H'0\rangle. \tag{6.23}$$

The subsequent $-\pi/2$ rotation on the upper arm and the PBS restores the $|H'\rangle$ state to $|V\rangle$, resulting in the desired phase-gate output state

$$|\Psi_{out}\rangle = c_{H0}|H0\rangle + c_{H1}|H1\rangle + c_{V0}|V0\rangle - c_{V1}|V1\rangle. \tag{6.24}$$

This state can then be converted into a CNOT gate by the addition of single-qubit Hadamard transformations onto the target qubit before and after the operation of the phase-gate. Thus either the atom or the photon can play the role of control qubit simply by applying the Hadamard sequence to the other particle.

Lastly, we note that Azuma [195, 196] recently proposed an alternative CNOT gate using essentially three IFM gates to prepare the required ancillary qubits, at least two more IFM gates for the required twice Bell measurements, as well as a considerable number of single-qubit measurements and measurement-conditioned operations. Thus we believe that our gates represent a significant advance, as they are accomplished within only a single IFM device and two logical Hadamard/Rotation operations, and most importantly, without any measurements or conditional operations.

6.4 Success Probability and Fidelity upon heralded success

In describing each of these quantum Zeno circuits we have assumed successful operation, and shown that the desired output could be achieved. In actuality, the descriptions we have provided are only exact in the limit $N \rightarrow \infty$, where N is the number of times the photon cycles through the ring-cavity. Three key factors determine the success probability. The first is finite N, restricted primarily by the reflectivity of the cavity mirrors and imperfections in whatever optical elements are included in the circuit. The second effect is imperfect absorption of the $|V0\rangle$ state, which we characterize by the parameter ϵ_0, so that the absorption probability for this state is $1-\epsilon_0$. Due to this imperfectness, the effective number of measurements for N feedback cycles is reduced to $(1-\epsilon_0)N$. The third factor is imperfect transparency of the $|V1\rangle$ state, characterized by the absorption probability ϵ_1. For an ideal system we would have $\epsilon_0 = \epsilon_1 = 0$, indicating that the selection rules of Figure 6.4 are precisely obeyed. In practice we expect finite selection-rule errors due to the combined effects of tight-focussing of the photon, which warps the photon polarization vector; and tight trapping of the atom, which may warp the atomic hyperfine spin vector. We use the term 'warp' to indicate an undesired spatial dependence. A rigorous calculation of these errors will be investigated in future work. At present we only calculate the effects of non-zero ϵ_0 and ϵ_1 and determine the acceptable upper-limits on these two parameters.

As having been shown in section II, a quantum Zeno system, while being an open system, can nonetheless be described in the pure-state representation, governed by a non-Hermitian Hamiltonian. For the single-atom IFPG, the quantum state of system can be represented by a pure state in the $\{|H0\rangle, |H1\rangle, |V0\rangle, |V1\rangle\}$ subspace. The final state can be derived from the initial-state via a non-Unitary propagator

$|\Psi_{out}\rangle = \hat{V}(\theta, N, \epsilon_0, \epsilon_1)|\Psi_{in}\rangle$, and the decay probability determined by $P_{decay} = 1 - \langle\Psi_{out}|\Psi_{out}\rangle$. The exact form of the propagator $\hat{V}(\theta, N, \epsilon_0, \epsilon_1)$ is derived in the appendix 6.7.2. The overall success probability, which is the probability for the system to be found in the target state at the output, is given by $P_{success} = |\langle\Psi_{target}|\Psi_{out}\rangle|^2$. Note since $|\Psi_{out}\rangle$ is now not normalized to unity, $P_{success}$ has implicitly taken into account the decay possibility.

If we consider the π-IFPG with an input state of the form (6.14) we find that the decay probability is given by

$$P_{decay} = |c_{H0}|^2\lambda_0 + \left(|c_{H1}|^2 + |c_{V1}|^2\right)\lambda_1 \tag{6.25}$$

where

$$\lambda_0 = \frac{\pi^2}{N}\frac{1+\sqrt{\epsilon_0}}{1-\sqrt{\epsilon_0}} - \frac{\pi^2}{N^2}\epsilon_0, \tag{6.26}$$

and

$$\lambda_1 = 1 - e^{-\epsilon_1 N/2} - \left(\frac{N\epsilon_1}{10}\right)^4. \tag{6.27}$$

The quantum gate can be considered 'efficient' if the failure probability scales as $P_{decay} \sim \frac{1}{N}$, which therefore requires $1-\sqrt{\epsilon_0} \sim 1$ and $\epsilon_1 \sim \frac{1}{N^2}$. The overall success probability is given to leading order by

$$\begin{aligned} P_{success} &= 1 - P_{decay} + O[\frac{1}{N^2}] \\ &= 1 - O[\frac{1}{N}], \end{aligned} \tag{6.28}$$

characteristic of high-efficiency quantum interrogation. We note that the IFRG operates on the same principles, and thus exhibits the same $1/N$ scaling behavior.

The condition $1-\sqrt{\epsilon_0} \sim 1$ indicates that ϵ_0 need not be negligible, but rather only not too close to one. This requirement is not very stringent, as previously described by Azuma [195]. We note, however, that previous athors have not considered imperfect

transparency of the $|V1\rangle$, described by ϵ_1. We see that this is actually the critical parameter upon which successful operation is sensitively dependent. For an N of 10^3, equation (6.27) implies that the absorption probability be $\sim 10^{-6}$ in order to maintain $1/N$ scaling. Clearly this will require very precise control over the atom-photon interaction. At present we do not know if it is possible to maintain both of these error parameters in their operational ranges simultaneously, although the weak constraint on ϵ_0 leads us to be optimistic. In future research we will address the interaction between tightly-trapped atoms and tightly-focussed photons in detail.

If we assume that absorption in the transparent state is negligible, the absorption of the absorbing state can be estimated using the standard cross-section of a two-level atom scattering resonant light, $\sigma = \lambda^2/2$. The absorption probability is thus determined by the ratio of σ to the focusing area A of the photon. Assuming a tightly focused light beam with transverse radius W, the absorption probability is thus

$$1 - \epsilon_0 = \frac{1}{2\pi}\left(\frac{\lambda}{W}\right)^2. \tag{6.29}$$

Taking the diffraction limit $W = \lambda$ gives

$$\lambda_0 \approx \frac{250}{N}. \tag{6.30}$$

This means for $N = 10^3$, the imperfection in absorbtion degrades the success probability from $\sim 99\%$ to $\sim 75\%$, while for $N = 10^4$ from 99.9% to 97.5%. On the other hand, to compensate for this small absorption probability would require an increase in the cycle parameter N by a factor of 25.

We can relate the maximum achievable cycling parameter N to the cavity finesse by taking into account the round-trip net transmission probability T. The probability to survive N cavity round-trips is R^N, where $R = 1 - T$. Thus the total loss probability due to imperfect optics is $P_{loss} = 1 - R^N = 1 - (1-T)^N \approx NT$. In order

to maintain the $250/N$ success rate imposed by realistic absorption probability, this requires $T \sim 250/N^2$, in analogy with the imperfect atomic transparency parameter ϵ_1. Presently, high-finesse super-mirrors [271, 272] can have $T < 10^{-6}$, which would correspond to $N \sim 1.5 \times 10^4$. An N of this size permit an overall success probability for the quantum Zeno gates of 98.4%, which would be competitive against potential competing methods. At present, achieving a net round-trip transmission probability of 10^{-6} for a single-photon pulse, while perhaps conceivable, would clearly require heroic experimental efforts.

Lastly, we note that for conventional schemes based on cavity QED, the system is operated in the strong coupling regime, where vacuum-Rabi oscillations dominate the dissipative atomic decay and cavity leakage [156, 271, 272]. This regime is characterized by a large single-atom cooperativity parameter, e.g., $C = g_c^2/\Gamma_c\kappa_c \gg 1$, where g_c, Γ_c and κ_c represent the atom-cavity coupling strength, the atomic spontaneous emission rate inside the cavity, and the cavity decay rate, respectively. Unlike the cavity-QED gates, the present Zeno gates are implemented in ring cavities. The coupling strength and spontaneous emission rate in these systems are given by their free-space values g and Γ. The lifetime of photons inside the ring cavity is $\tau \simeq L_c/cT$, where c is the speed of light and L_c is the coherent length of the photon. Physically, this is the total amount of time the photon interacts with the atom. Correspondingly, a 'cavity decay' rate is $\kappa = 1/\tau = cT/L_c$. The analogy of the cavity cooperativity C mapped onto the current ring-cavity system is thus

$$\begin{aligned} C_{ring} &= \frac{g^2}{\Gamma\kappa} \\ &= \frac{1}{2\pi}\left(\frac{\lambda}{W}\right)^2 \frac{1}{T}. \end{aligned} \tag{6.31}$$

For $T \ll 1$ and $W \approx \lambda$, we have $C_{ring} \gg 1$. The present Zeno-gate system in this sense also operates in the strong coupling regime. Seemingly, the Zeno and cavity-

QED gates would therefore require similar experimental conditions. This conclusion is, however, not necessarily true since the Zeno gates are operated in the regime of $g^2/\Gamma \ll g_c^2/\Gamma_c$ and $\kappa \ll \kappa_c$. The large effective cooperative parameter C_{ring} is merely due to the ratio of g^2/Γ to κ remaining large. Thus, while cavity-QED schemes demand $g_c \gg \Gamma_c$ and $g_c \gg \kappa_c$ being satisfied simultaneously, the Zeno-gate system only relies on $g \sim \Gamma$ and $T \ll 1$. Taking the coherence length of the laser pulse as c/Γ, the condition of $g \sim \Gamma$ would then require the single-photon pulse to be tightly focused down to $W \sim \lambda$, such that

$$\frac{g}{\Gamma} = \sqrt{\frac{1}{2\pi}}\frac{\lambda}{W} \sim 0.1. \tag{6.32}$$

It is worth noting that while in the strong coupling regime, the present scheme is still configured on free-space atom-photon interaction, in the sense that the photon is coupled to the continuum atomic states.

In above discussions, we have considered the reduction in success probability for IFPG and IFRG gates due to imprecise control of atom-photon scattering and/or optics imperfections. In practice, the resulting photon loss can be detected by the absence of the photon at the gate output. By adding a detector to the photon output channel, we find that the detection of a photon necessarily indicates that the device has operated successfully, as all failure mechanisms result in absorption or scattering of the photon out of the resonator mode. Conditioned on this heralded success, the fidelity of the gate operation, measuring the overlap of the target state and the final output state, will be given by

$$F_{herald} = \frac{P_{success}}{1 - P_{decay}}. \tag{6.33}$$

To leading order in $\frac{1}{N}$, F_{herald} is found

$$\begin{aligned} F_{herald} &= 1 - |c_{H0}|^2 \left(|c_{H1}|^2 + |c_{V1}|^2\right) \frac{(\lambda_0 - \lambda_1)^2}{4} \\ &= 1 - O[\frac{1}{N^2}], \end{aligned} \tag{6.34}$$

compared to $1 - O[\frac{1}{N}]$ for success probability. The small deviation from unity is due to a slight imbalance which occurs in the final normalization of the output state. The fidelity upon heralded success of the present quantum Zeno gates can thus be made extremely close to unity, e.g. for the 'realistic' $N = 1.5 \times 10^4$ the success probability is 98.4%, yet the corresponding fidelity is 99.994%.

6.5 Zeno phase gate for two quantum-dots

In this section, we extend the idea of the quantum Zeno gate to the system of quantum dots. We consider a system with three vertically grown QDs. The schematic view is shown in Fig.6.9, where QD1 is the central neutral dot, and QD2 and QD3 are the two lateral charged dots. Photon absorption creates exciton states in QD1, and trion states in QD2 and QD3. We assume that the ground trion energy in the two lateral dots is the same and is lower than the ground exciton energy in the central dot. QD1 is driven by the external laser field which can induce Rabi Oscillations between zero and one exciton. We assume that the driving laser field is σ_- polarized with energy resonant with the ground exciton transition on QD1. Due to the difference between the exciton and trion energy, QD2 and QD3 are off-resonance. The standard selection rules of semiconductor quantum dots apply, i.e. the σ_- laser creates an exciton with electron spin up($+\frac{1}{2}$) and a heavy hole spin down($-\frac{3}{2}$) in QD1 only. For the selection rules, notice that if the electron in QD2 is spin down, the exciton in QD1 can transfer to QD2 to form a trion. If the electron in QD2 is spin up, the

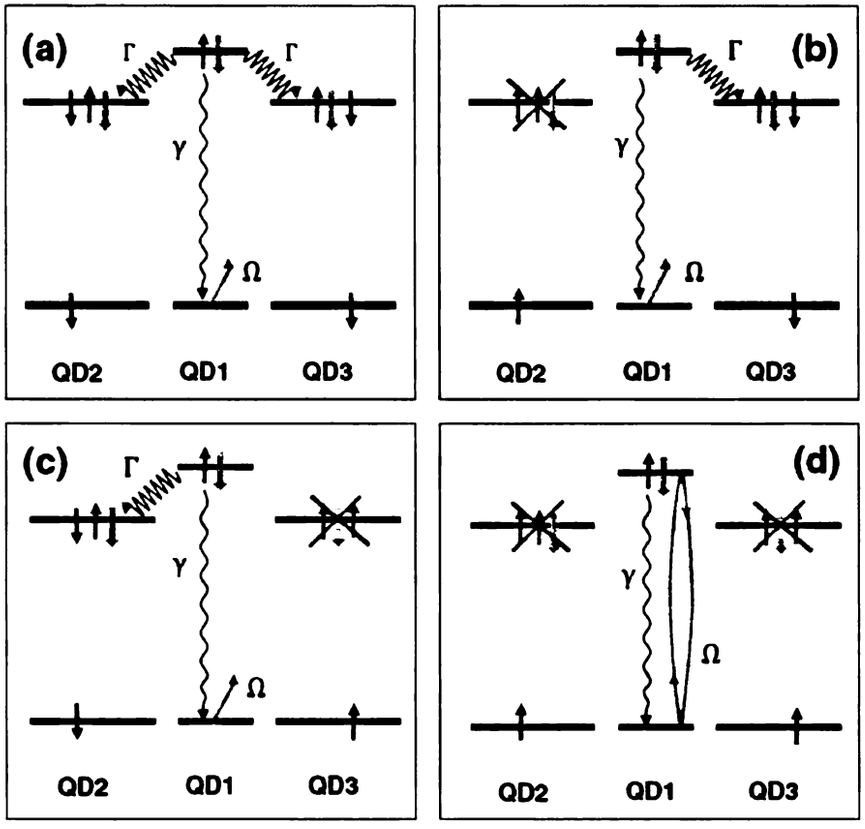

Figure 6.9: Scheme of the dynamics of the system under different initial states. The blue (gray) arrow represents the electron (hole) spins. The energy levels for QD1 are the empty dot (lower) and the first exciton level (upper). The energy levels in QD2 and QD3 are charged dot ground states (lower) and trion levels (upper). (a)-(c) If either electron in QD2 and QD3 is spin down, the exciton in QD1 can decay into the neighboring dots and be *detected* (detectors QD2 and/or QD3 switched *on*). Therefore the QZE prevents the Rabi Oscillation in QD1, no phase shift is present after a π pulse. (d) Only if both detectors are switched *off*, a π Rabi Oscillation can be performed in QD1.

exciton in QD1 cannot transfer to QD2 due to the Pauli exclusion principle. In any case, relaxation via phonon emission conserves the spin of the involved quasi-particles. The electrons in QD2 and QD3 (*detectors*) monitor the evolution of the exciton in the QD1. Our electron-detectors in QD2 and QD3 have a *quantum switch*. In fact, they can monitor the σ_- exciton by letting the system emit a phonon only if their spin is down. If the electron spin in the detectors QD2 or QD3 is up, the detector is *switched off*, since it will not be able to provide the information about the presence of the polarized exciton. If we consider a weak resonant 2π pulse with Rabi energy $\Omega \ll \Gamma$, where Γ is the phonon emission rate, then it is sufficient to have one detector *on* to induce the QZE and freeze the system. Only when both detectors are *off*, the 2π pulse will give an overall π phase to the wave-function of the system. In this scheme, a 2π exciton Rabi flopping provides then a conditional phase gate on the two spins. Note that the stronger the phonon dissipation, the better is for the gate. This is a different approach with respect to current schemes which tends always to fight dissipation.

6.6 Conclusion

In conclusion, we have presented a general theory of interaction- and measurement-free quantum Zeno gates and discussed their physical implementation via high-finesse optical resonators for systems of single-atom and single-photon qubits. We have constructed a useful set of logic circuits towards quantum information processing with only one or at most two IFM devices. Because of the interaction- and measurement-free features, as well as the lack of need for pre-existing entangled photon-pairs, our gates are able to overcome some of the major obstacles in processing information with single photons and atoms. This work is a significant extension and improvement of several previously studied IFM gates [194, 195, 196]. We have for

the first time 1) introduced the interaction-free raman gate, with which the photon-photon CNOT gate is accomplished using only a single IFM device; 2) constructed the atom-atom and hybrid atom-photon CNOT gate using circuits which are much simpler and easier to implement; 3) constructed direct, reversible atom-photon state transfer circuits; 4) solved the problem of photon loss during long-distance quantum communication via lossy channels with a photon-loss-tolerant protocol. Most importantly, compared to previously studied IFM gates, our gates do not require any measurements and are operated asymptotically on-demand. This elimination of measurement clearly distinguishes our Zeno logic gates from previous approaches [182, 136, 168, 287, 288, 289, 194, 195, 196, 170, 185, 290, 174]. We have also shown that the success probability and fidelity upon heralded success for our Zeno gates scale at $1 - O[\frac{1}{N}]$ and $1 - O[\frac{1}{N^2}]$ with N the (effective) number of measurements. Experimentally, N is limited by three major factors, the resonator finesse, the imperfect absorption of the absorbing state, and the imperfect transparency of transparent state. While the limits to controlling the imperfect absorbtion and transparency factors remain to be investigated, we have shown that with available mirror finesse factors and for realistic atom-photon scattering, a success probability of 98.4% or a fidelity of 99.994% upon heralded success may be attainable in the near future. To this end, we note that while the present Zeno gates are discussed in the context of single atomic and photonic qubits, they can also be implemented in other physical systems in a straightforward manner. A quantum dot system, for example, is an ideal alternative, due to its large dipole moment as well as the presence of ultra-fast phonon-assisted dissipation mechanisms. Indeed, we have extended the idea of quantum Zeno gates to the system of quantum dots, where in Ref. [291], we demonstrate an implementation of the quantum Zeno phase gate employing phonon dissipations.

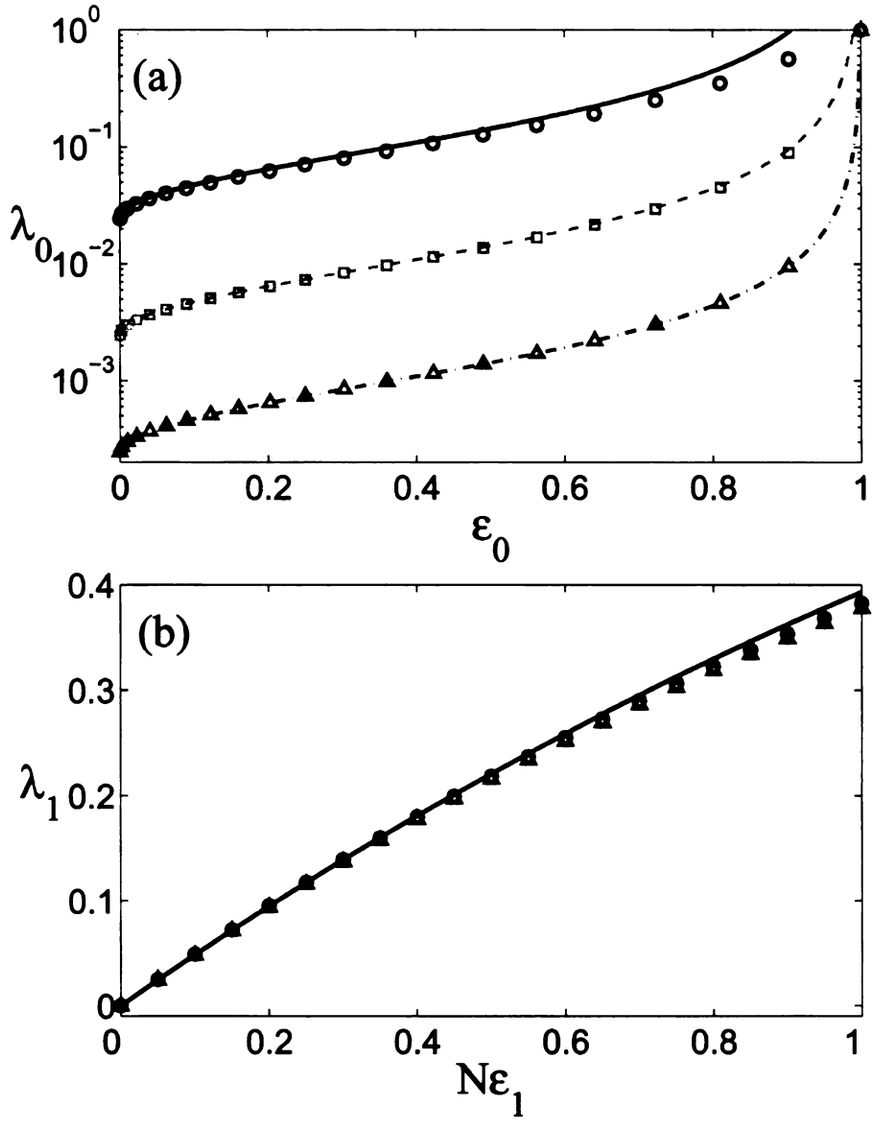

Figure 6.10: Decay parameters λ_0 and λ_1 versus the atom-photon scattering parameters ϵ_0 and ϵ_1. Figure (a) shows λ_0 versus ϵ_0 for $N = 10^2$ (solid line and circles), $N = 10^3$ (dashed line and squares), and $N = 10^4$ (dahsed-pointed line and triangles). All lines are the analytic approximations given in equation (6.26), while the points correspond to exact numerical calculations. In figure (b) we similarly plot λ_1 versus $N\epsilon_1$, where because the analytical approximation of λ_1 (6.27) depends only on the product $N\epsilon_1$, three lines for different Ns are overlapped. Both figures show excellent agreements between analytic approximations and numerical calculations.

6.7 Derivations and further discussions

6.7.1 Pure-State Representation

In this appendix, we will show that the dynamical evolution of quantum-Zeno systems, while involving dissipations into environment, can nonetheless be described in a pure-state representation with non-Hermitian Hamiltonians. Our analyses are based on the standard quantum treatment of an open system [59], where the dynamics is governed by a master equation for density matrix. We will take the system with the level scheme drawn in Fig. 6.1 for an example. Similar results can be obtained for other systems in a straightforward manner.

With $|g\rangle$ being the atomic state onto which the state $|1\rangle$ spontaneously decays, the master equation for this system is read as

$$\dot{\rho} = -\frac{i}{\hbar}[\hat{H}_{\Omega}, \rho] - \frac{\Gamma}{2}\left[|1\rangle\langle 1|\rho + \rho|1\rangle\langle 1| - 2|g\rangle\langle 1|\rho|1\rangle\langle g|\right]. \tag{6.35}$$

Here, ρ is the system's density matrix, Γ is the spontaneous emission rate. The Hamiltonian $\hat{H}_{\Omega}$, given by Eq (6.2), is the Rabi coupling between the states $|0\rangle$ and $|1\rangle$, which, however, does not act on $|g\rangle$. To solve this equation, we expand the density ρ onto the $\{|g\rangle\}$ and $\{|0\rangle, |1\rangle\}$ subspaces, and obtain

$$\rho = \rho_{gg} + \rho_{ss} + \rho_{gs} + \rho_{sg}, \tag{6.36}$$

with

$$\begin{aligned}
\rho_{gg} &= |g\rangle\langle g|\rho|g\rangle\langle g|; \\
\rho_{ss} &= \sum_{j,k=0,1} |j\rangle\langle j|\rho|k\rangle\langle k|; \\
\rho_{gs} &= \rho_{sg}^{\dagger} = \sum_{j=0,1} |g\rangle\langle g|\rho|j\rangle\langle j|;
\end{aligned}$$

(6.37)

The master equation (6.35) can now be separated into three equations

$$\dot{\rho}_{ss} = -\frac{i}{\hbar}[\hat{H}_{\Omega}, \rho_{ss}] - \frac{\Gamma}{2}\left[|1\rangle\langle 1|\rho_{ss} + \rho_{ss}|1\rangle\langle 1|\right], \tag{6.38}$$

$$\dot{\rho}_{gg} = \Gamma|g\rangle\langle 1|\rho_{ss}|1\rangle\langle g|, \tag{6.39}$$

$$\dot{\rho}_{gs} = \frac{i}{\hbar}\rho_{gs}\hat{H}_{\Omega} - \frac{\Gamma}{2}\rho_{gs}|1\rangle\langle 1|. \tag{6.40}$$

Clearly, equation (6.38), which governs the motion of ρ_{ss}, is uncoupled from the rest equations, meaning the states $|0\rangle, |1\rangle$ have formed a closed subspace. In this subspace, for any pure initial state $|\Psi(0)\rangle$, equation (6.38) has a pure-state solution, $\rho_{ss}(t) = |\Psi(t)\rangle\langle\Psi(t)|$, where

$$|\Psi(t)\rangle = e^{-i\hat{H}_{eff}t/\hbar}|\Psi(0)\rangle, \tag{6.41}$$

with $\hat{H}_{eff}$ defined in Eq (6.4). Since our Zeno logic gates are operated in the $\{|0\rangle, |1\rangle\}$ subspace, the state $|g\rangle$ becomes practically irrelevant, allowing us to describe the system in a pure state representation of $|0\rangle$ and $|1\rangle$ states. $\hat{H}_{eff}$ is then the effective Hamiltonian governing the pure-state dynamics in this subspace. The system decay is now governed by the non-Hermitian component of $\hat{H}_{eff}$, due to which the state $|\Psi(t)\rangle$ is no longer normalized to unity. Conservation of probability requires

$$Tr\{\rho_{gg}\} = 1 - Tr\{\rho_{ss}\}, \tag{6.42}$$

which shows that the reduction in in the normalization of $|\Psi(t)\rangle$ corresponds to the probability for the atom to have scattered into the state $|g\rangle$.

Finally, we note that if starting with an initial state in the $\{|0\rangle, |1\rangle\}$ subspace, the state $|g\rangle$ will always be uncoupled from the rest of system. This is because the

master equation (6.35) does not create any coherence between the two subspaces. This can be easily seen from Eq (6.40), where with zero initial values, the cross terms ρ_{gs}, ρ_{sg} will be identically zero at any later times.

6.7.2 Derivation of IFPG propagator

In this appendix we will derive the form of the propagator $\hat{V}(\theta, N, \epsilon_0, \epsilon_1)$ which describes the action of the elementary IFPG pictured in Fig. 6.4. In this system, only the $|V\rangle$ photon interacts with the atom, and the dissipative states exposed to spontaneous emission are $|V0\rangle$ and $|V1\rangle$. The standard master equation describing the dissipative evolution of the system during a single measurement cycle is then [59]

$$\begin{aligned}\dot{\rho} &= \sum_{i=0,1} \frac{\gamma_i}{2} \left[-|Vi\rangle\langle Vi|\rho - \rho|Vi\rangle\langle Vi| \right. \\ &\qquad \left. + 2|i\rangle'\langle Vi|\rho|Vi\rangle\langle i|' \right], \end{aligned} \tag{6.43}$$

where the state $|i\rangle'$ describes the scattered atomic qubit state with zero photons in the cavity. The rate constants γ_0 and γ_1 will need to be determined from detailed atom-photon scattering calculations. Following the previous appendix, this equation has a pure state solution in the $\{|H0\rangle, |H1\rangle, |V0\rangle, |V1\rangle\}$ subspace, from which we find that the initial state

$$|\Psi(0)\rangle = c_{H0}|H0\rangle + c_{H1}|H1\rangle + c_{V0}|V0\rangle + c_{V1}|V1\rangle \tag{6.44}$$

evolves into the final state

$$|\Psi(t)\rangle = c_{H0}|H0\rangle + c_{H1}|H1\rangle + c_{V0}e^{-\gamma_0 t/2}|V0\rangle + e^{-\gamma_1 t/2}|V1\rangle \tag{6.45}$$

The measurement stage of the IFPG corresponds to evolution under (6.43) for time t_m such that $e^{-\gamma_0 t_m} \equiv \epsilon_0$ and $e^{-\gamma_1 t_m} \equiv 1 - \epsilon_1$.

With $\hat{B}(\epsilon_0, \epsilon_1)$ as the propagator for the measurement stage and $\hat{R}(\theta, N)$ as the propagator for the rotation stage, the complete IFPG propagator is given by

$$\hat{V}(\theta, N, \epsilon_0, \epsilon_1) = \left[\hat{B}(\epsilon_0, \epsilon_1)\hat{R}(\theta, N)\right]^N. \tag{6.46}$$

In the basis $\{|H1\rangle, |V1\rangle, |H0\rangle, |V0\rangle\}$ the matrix forms of the propagators are

$$\hat{R}(\theta, N) = \begin{pmatrix} \cos\frac{\theta}{N} & \sin\frac{\theta}{N} & 0 & 0 \\ -\sin\frac{\theta}{N} & \cos\frac{\theta}{N} & 0 & 0 \\ 0 & 0 & \cos\frac{\theta}{N} & \sin\frac{\theta}{N} \\ 0 & 0 & -\sin\frac{\theta}{N} & \cos\frac{\theta}{N} \end{pmatrix} \tag{6.47}$$

and

$$\hat{B}(\epsilon_0, \epsilon_1) = \begin{pmatrix} 1 & 0 & 0 & 0 \\ 0 & \sqrt{1-\epsilon_1} & 0 & 0 \\ 0 & 0 & 1 & 0 \\ 0 & 0 & 0 & \sqrt{\epsilon_0} \end{pmatrix}. \tag{6.48}$$

We have found that to excellent approximation, the full propagator can be expressed as

$$\hat{V}(\theta, N, \epsilon_0, \epsilon_1) = \begin{pmatrix} -\xi_1 & \xi_2 & 0 & 0 \\ -\xi_2 & -\xi_1 & 0 & 0 \\ 0 & 0 & \eta_1 & \eta_2 \\ 0 & 0 & -\eta_3 & -\eta_4 \end{pmatrix} \tag{6.49}$$

where

$$\xi_1 = e^{-N\epsilon_1/4}, \tag{6.50}$$

$$\xi_2 = [N\epsilon_1/10]^2, \tag{6.51}$$

$$\eta_1 = \left[1 - \frac{\pi^2}{N}\frac{1+\sqrt{\epsilon_0}}{1-\sqrt{\epsilon_0}}\right]^{1/2}, \tag{6.52}$$

$$\eta_2 = \frac{\pi}{N}\left[\frac{1+\sqrt{\epsilon_0}}{1-\sqrt{\epsilon_0}}\right]^{1/2}, \tag{6.53}$$

$$\eta_3 = \pi\sqrt{\epsilon_0}/N, \tag{6.54}$$

$$\eta_4 = 10\sqrt{\epsilon_0}/N^2. \tag{6.55}$$

The validity of these approximations is illustrated in figure 6.10, where the decay parameters λ_0 and λ_1, given by Eqs (6.26) and (6.27), are plotted against the atom-photon scattering parameters ϵ_0 and ϵ_1. The excellent agreement confirms our conclusions regarding the sensitivity of the success probability and fidelity with respect to the scattering parameters ϵ_0 and ϵ_1.

6.7.3 Extension I: State transfer circuits

In this extension, we construct state-transfer circuits, which map the quantum state of an atom onto a photon and vice-versa. Unlike the CNOT gates, state-transfer circuits require two elementary interaction-free quantum-Zeno gates. The first serves to entangle the atom and photon, while the second is required for disentanglement. The atom-to-photon state-transfer circuit is depicted in Fig. 6.11 (a). It consists of a $\pi/2$ IFPG followed by a $-\pi/2$ IFRG. The photon is prepared in the $|H\rangle$ state, and the atom is initially in the unknown quantum state $c_0|0\rangle + c_1|1\rangle$. The goal of the circuit is then to transfer this unknown quantum state onto the state of the photon. With the input state taken as

$$|\Psi_{in}\rangle = |H\rangle \otimes (c_0|0\rangle + c_1|1\rangle) = c_0|H0\rangle + c_1|H1\rangle, \tag{6.56}$$

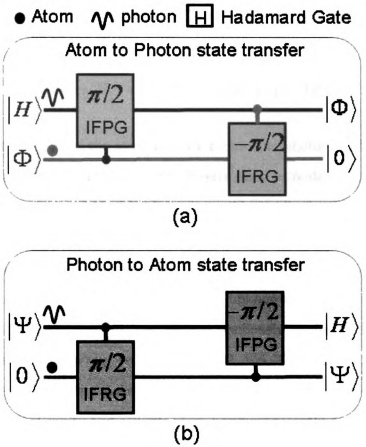

Figure 6.11: Graphical state-transfer circuits for atom-to-photon (a) and photon-to-atom(b), where $|\Phi\rangle$ and $|\Psi\rangle$ denote the arbitrary atomic and photonic states, respectively.

the action of the $\pi/2$ IFPG is to rotate the polarization of the photon by $\pi/2$ conditioned on the atom being in state $|1\rangle$, resulting in the state

$$|\Psi\rangle = c_0|H0\rangle + c_1|V1\rangle. \tag{6.57}$$

The $-\pi/2$ IFRG rotates the atomic state by $-\pi/2$ conditioned on the photon being in state $|V\rangle$, resulting in the output state

$$|\Psi_{out}\rangle = c_0|H0\rangle + c_1|V0\rangle = (c_0|H\rangle + c_1|V\rangle) \otimes |0\rangle. \tag{6.58}$$

Thus the quantum state of the atom is written onto the photon, and the atom and photon are successfully disentangled. The reverse photon-to-atom state transfer circuit is depicted in figure 6.11 (b). It operates identically to the atom-to-photon circuit, except the roles of atomic and photonic qubits are reversed. We emphasize here that the present state-transfer gates operate without the need to measure the final state of the particle initially possessing the unknown state. This is clearly different and significantly improved from several previously studied schemes, where a final (Bell) measurement is required [149, 175, 292, 136, 293, 186, 187, 294, 295]. We note that a measurement-free state-mapping scheme between a coherent light field in a high-finesse optical cavity and a single atom has been recently demonstrated [272].

6.7.4 Extension II: Long-distance quantum communication

This far, we have constructed the atom-atom phase (CNOT) gate using a single IFM device, where the two atomic qubits are required to be in a common optical resonator. This requirement restricts such a circuit to two qubits separated within one resonator length. For the purpose of quantum communications and/or gate operations between two distant atomic qubits, one alternative approach would be to indirectly entangle them via mutual non-interaction with a common ancillary photon.

As a first example, we deviate from the measurement-free feature and show that two uncorrelated qubits can be collapsed to the Bell $\Phi^{\pm}$ or $\Psi^{\pm}$ subspaces by using two atom-photon Zeno CNOT gates and measuring the final photon state. We note that for quantum communication via a lossy photonic channel, verifying the presence of the transported photon is somewhat helpful as it can detect the photon loss and thus improve the operation fidelity upon heralded success. In our scheme, the photon is initially in $|H\rangle$ state and the two atoms are in arbitrary states. The initial state of system is then written as

$$|\Psi_{in}\rangle = |H\rangle \otimes (c_{00}|00\rangle + c_{01}|01\rangle + c_{10}|10\rangle + c_{11}|11\rangle). \tag{6.59}$$

The photon non-interacts with the first atom via the atom-photon Zeno CNOT gate, where its polarization reverses ($|H\rangle \leftrightarrow |V\rangle$) only if the atomic qubit is in state $|1\rangle$. The system afterwards will be in

$$|\Psi'\rangle = |H\rangle \otimes (c_{00}|00\rangle + c_{01}|01\rangle) + |V\rangle \otimes (c_{10}|10\rangle + c_{11}|11\rangle). \tag{6.60}$$

After transmission, the photon then non-interacts with the second atom via a second identical Zeno CNOT gate, alternating the system into

$$\begin{aligned} |\Psi_{out}\rangle &= |H\rangle \otimes (c_{00}|00\rangle + c_{11}|11\rangle) \\ &+ |V\rangle \otimes (c_{10}|10\rangle + c_{01}|01\rangle). \end{aligned} \tag{6.61}$$

Accomplishing the quantum communication then requires measuring the photon on H/V basis. If it is measured in $|H\rangle$, the two atoms will be collapsed onto $c_{00}|00\rangle + c_{11}|11\rangle$ state, or the $\Phi^{\pm}$ subspace. Otherwise, they will be collapsed to $c_{01}|01\rangle + c_{10}|10\rangle$ state, or the $\Psi^{\pm}$ subspace. In either way, entanglement between the two is established, based on which long-distance logic gates can be realized with the addition

of single-qubit operations.

A main and common difficulty in quantum communication between distant qubits is photon loss during transmission, where the loss probability increases exponentially with the transport distance. In schemes based on cavity-QED [182, 183, 184, 185], the quantum states of atomic qubits are encoded in the internal (polarization) states of photons. A lost photon will therefore immediately collapse the atomic state(s) and destroy the qubit(s) via decoherence. This problem also exists in the above scheme, where the intermediate photon state is $|H\rangle$ or $|V\rangle$ depending on the first qubit being in $|0\rangle$ or $|1\rangle$, as shown in (6.60). One possible way to overcome this difficulty is to combine the atom-photon phase gate with interferometric phase measurements, as a photon lost inside an interferometer does not reveal the quantum state of the measured qubits [40]. In the following we neglect detector inefficiency and dark-count rates at present, to focus on the problem of transmission loss.

As an example, here we describe a photon-loss-tolerant protocol using π-IFPGs and a Mach-Zehnder (MZ) interferometer. The schematic setup is depicted in Fig. 6.12, where we introduce an ancillary qubit (a-qubit) to restore the quantum states of the two logical qubits in case of photon loss. In the scheme, a photon in $|H\rangle$ state is passed through a 50/50 beamsplitter and then guided through the π-IFPG gates where it non-interacts successively with the ancillary and x atom in the upper arm, or the y atom in the lower arm. The initial state of system is

$$|\Psi_{in}\rangle = |H\rangle \otimes |\Psi\rangle_a \otimes (c_{00}|00\rangle + c_{01}|01\rangle + c_{10}|10\rangle + c_{11}|11\rangle), \tag{6.62}$$

with the ancillary atom prepared in the state

$$|\Psi\rangle_a = \frac{1}{\sqrt{2}}(|0\rangle_a + |1\rangle_a). \tag{6.63}$$

After the photon passes through the first beamsplitter and non-interacts with ancillary

and the first logical qubit (x-qubit) via π-IFPG gates, the system will be in the state

$$|\Psi'\rangle = \frac{1}{2}[|H\rangle_u \otimes (|0\rangle_a - |1\rangle_a) \otimes \tag{6.64}$$
$$(c_{00}|00\rangle - c_{01}|01\rangle + c_{10}|10\rangle - c_{11}|11\rangle) + i|H\rangle_l \otimes$$
$$(|0\rangle_a + |1\rangle_a) \otimes (c_{00}|00\rangle + c_{01}|01\rangle + c_{10}|10\rangle + c_{11}|11\rangle)],$$

where $|H\rangle_{u,l}$ indicates the photon in the upper and lower interferometer arm. In absence of photon loss, the final state, obtained after the photon non-interacts with the second qubit (y-qubit) via another identical π-IFPG and then passes the second beamsplitter, is

$$|\Psi_{out}\rangle = (|H\rangle_u|0\rangle_a - i|H\rangle_l|1\rangle_a) \otimes (c_{01}|01\rangle - c_{10}|10\rangle)$$
$$-(|H\rangle_u|1\rangle_a - i|H\rangle_l|0\rangle_a) \otimes (c_{00}|00\rangle - c_{11}|11\rangle). \tag{6.65}$$

Measuring both the final states of the photon and the ancillary atom will thus project the two atoms onto either $c_{01}|01\rangle - c_{10}|10\rangle$ or $c_{00}|00\rangle - c_{11}|11\rangle$ states, which establishes the desired entanglement. Otherwise, if neither of the photon detectors is triggered, it is most likely that the photon is lost during transmission from either of the interferometer arms, but without knowing from which. Assuming equal loss possibilities for the two arms, the system will now be in a statistical mixture of

$$\rho^{loss} = \langle H|_u\Psi'\rangle\langle\Psi'|H\rangle_u + \langle H|_l\Psi'\rangle\langle\Psi'|H\rangle_l. \tag{6.66}$$

We then need to measure the ancillary atom on $|\pm\rangle_a = (|0\rangle_a \pm |1\rangle_a)/\sqrt{2}$ basis, and restore the quantum states of the qubits according to the measurement result. If it is measured in $|+\rangle$, the state of two atomic qubits is automatically restored, as seen

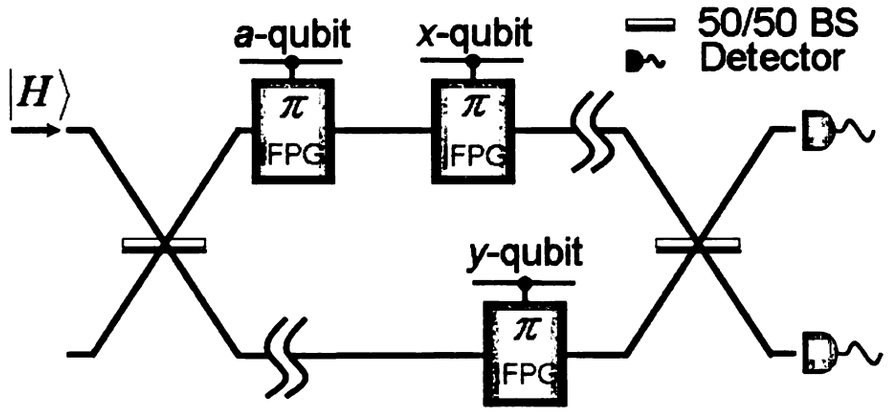

Figure 6.12: Schematic setup for long-distance entanglement generation with built-in error correction. A photon in $|H\rangle$ polarization state is passed through a MZ interferometer with three π-IFPGs, and is then measured by two detectors placed at the two interferometer outputs. The MZ interferometer consists of two 50/50 linear beamsplitters (BS) with a $\pi/2$ phase imprinted on the reflected photons. In figure, we label the ancillary and the two logical qubits as a-, x- and y-qubit, respectively.

in (6.64). Otherwise, if it is measured in $|-\rangle$, the atoms will be in state

$$c_{00}|00\rangle - c_{01}|01\rangle + c_{10}|10\rangle - c_{11}|11\rangle \tag{6.67}$$

and a relative π-phase applied on the first qubit immediately recovers the original quantum state of the two qubits. Upon recovery, the whole procedure can be repeated, until success.

Chapter 7

Summary and Outlook

In summary, in this dissertation we have studied the rich physics associated with linear and nonlinear mixing of light and matter waves, while emphasizing applications in quantum interferometry and information processing. A flow chart showing the structure of the dissertation is presented in Fig. 7.1. In the following, I will give a briefly summary on each project while listing the key innovations. I also discuss the future work that can lead to improvements of the present results.

- In chapter 2, we proposed a dynamical scheme to create and detect macroscopic Schrödinger-cat states in a double-well Bose-Einstein condensate (BEC) system. We for the first time proposed to use the technique of Feshbach resonance to suddenly change the inter-atom interaction from repulsive to attractive, thus dynamically generating the Schrödinger-cat state. In particular, we originally studied the decoherence properties of such cat states induced by the trapping lasers via the master-equation approach. Nonetheless, in the present work we have used the zero-temperature approximation, assuming all atoms are in the lowest-energy states. It remains as a future task to study the effect of finite temperature on the system dynamics, and particularly, to find out the susceptibility of our dynamical approach against possible collisional decoherence by

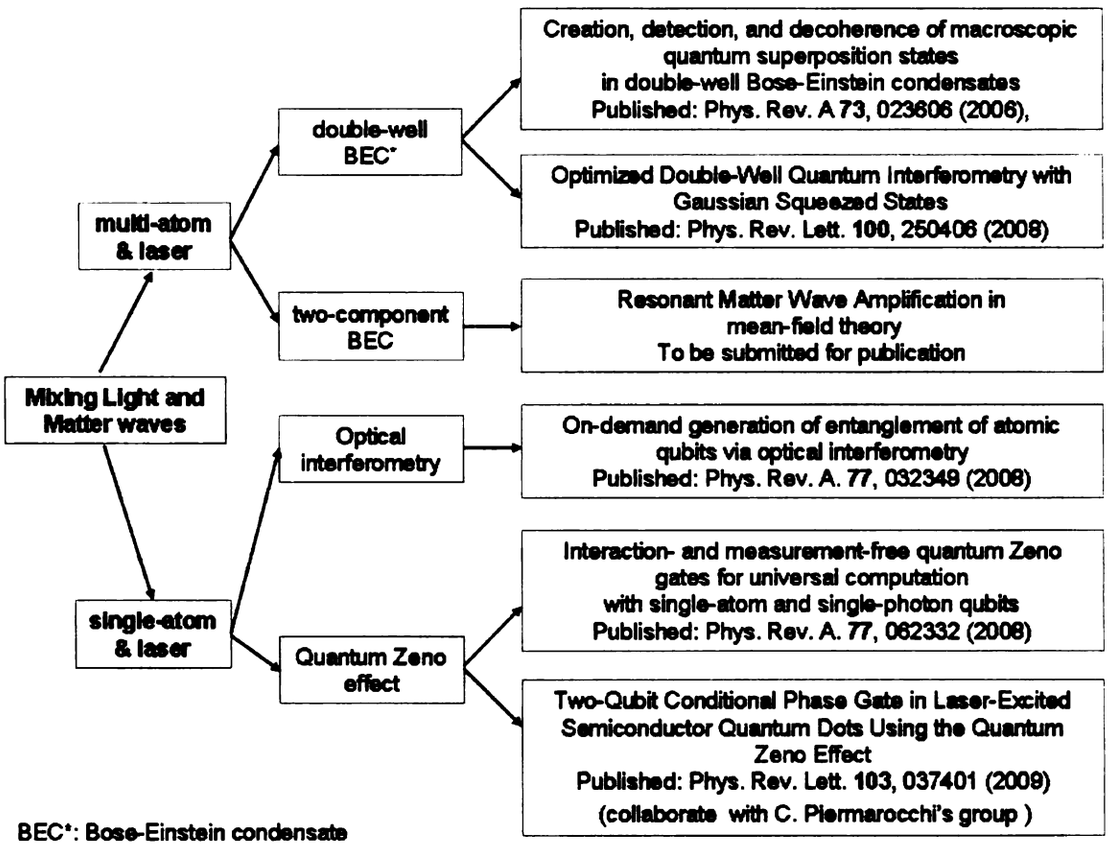

Figure 7.1: The flow chart of this dissertation.

thermal atoms. Further, we have assumed the localized left-well and right-well condensate modes to be constant throughout the dynamics. While this is a valid assumption as proven in recent experiments, it is more physical to employ adaptive time-variant mode functions.

- In chapter 3, we proposed to implement a Mach-Zehnder interferometer in a double-well BEC system for ultra-efficient phase measurements. The input state of the interferometer is the ground state of the system in presence of repulsive interaction, and is thus easy to produce. We for the first time systematically studied the optimal number-squeezing level of the input state for the best interferometer performance when measuring non-zero phases. The squeezing level is easily tuned by using the Feshbach resonance technique. Combined with adaptive measurement schemes, our apparatus can measure an arbitrarily unknown phase at a Heisenberg-scaling resolution within only a few measurements. This corresponds to an enormous improvement in the phase-measurement efficiency over the previous approaches, employing maximally number-squeezed or entangled input states. In this work, however, we have again used the zero-temperature and the time-invariant mode approximations, as in chapter 2. A future improvement can be to go beyond these approximations. Also, here we did not consider the possible collisional dephasing effect during the phase measurement process. It will be helpful to characterize this dephasing effect to determine the maximally allowed residual atom-atom interaction during the phase measurement, and possibly, to use this effect to further reduce the phase uncertainty.

- In chapter 4, we studied the matter-wave amplification (MWA) process in a two-component BEC system. Previous studies of this system were focused on the off-resonance dynamic regime, whereas here we extended the studies to the

resonant regime. We found that the atom loss fraction during the MWA process is a universal quantity independent of dynamical regimes. For a given laser intensity, a significantly faster amplification process can be achieved employing a resonant rather than off-resonance driving laser. Due to phase distortion by the ac-Stark shift, it turns out an off-resonance three-level system is unsuitable for state mapping between light and matter waves, while a resonant system is not subjected to this problem. We also identified the laser depletion and spatial effect by comparing the simulation results via quantum coupled-mode and semiclassical multi-mode theories. In the present multi-mode model, however, we only considered the light to propagate along the longitude axis of the condensates. While this is a valid approximation in the geometry limit of a large Fresnel-number $\mathcal{F}$, it is important to include the transversely-propagation light in the model when $\mathcal{F} \lesssim 1$, especially when such a geometry helps to reduce the atom loss fraction. Finally, in this work, the system dynamics is discussed in the context of mean field theory. To study the associated quantum fluctuation during the MWA process, a full quantum model is needed. This kind of work is important when a MWA system is used for coherent state-mapping between light and matter waves.

- In chapter 5, we proposed to create entanglement between single-atom qubits by putting them in a common optical interferometer. Previous approaches using single-atom qubits rely on using high-finesse cavities to enhance atom-photon interaction while suppressing spontaneous emission rates. We showed, however, that the requirement for cavities can be circumvented by employing ultra-sensitive interferometers operating at Heisenberg-scaling sensitivities. Specifically, we proposed to use a Mach-Zehnder interferometer with the maximally squeezed twin-Fock input state and the NOON-state interferometer with nonlinear beamsplitters. These new approaches can lead to scalable elements for

quantum information processing, with a close-to-unity success probability and fidelity. Yet, it remains as an experimental challenge to create highly squeezed optical beams in the twin-Fock state, although there have been some steady progresses. Towards this goal, we are now studying an optical four-wave mixing approach in thermal gases to create such beams of high brightness. Furthermore, in the NOON-state approach, the nonlinear beamsplitter is demonstrated in an atomic medium subjected to the Kerr-nonlinearity. It remains as the future task to carefully examine the performance of such a beamsplitter for various input states.

- In chapter 6, we used the quantum Zeno effect to construct a series of interaction- and measurement- free quantum logic gates. Applying to the system of single-atom and single-photon qubits, we have for the first time 1) introduced the interaction-free Raman gate, with which the photon-photon CNOT gate is accomplished using only a single interaction-free device; 2) constructed the atom-atom and hybrid atom-photon CNOT gate using circuits which are much simpler and easier to implement; 3) constructed direct, reversible atom-photon state transfer circuits. Besides, we have solved the problem of photon loss during long-distance quantum communication via lossy channels with a photon-loss-tolerant protocol. In collaboration with the C. Piermarocchi group, we further extended the two-qubit phase gate to the quantum-dot systems, where we for the first time proposed a feasible interaction-free quantum logic gate between two quantum-dot qubits. compared to previously studied quantum-Zeno gates, our gates do not require any measurements and are operated asymptotically on-demand. This elimination of measurement clearly distinguishes our Zeno logic gates from previous approaches. An important remaining task in the atom-photon project is to carefully characterize the property of single-atom and single-photon scattering in free space, as our scheme is sensitive to the

atom-photon scattering probabilities. In addition, to further improve the gate fidelity, a possible way is to replace the single-atom qubits with atomic-ensemble qubits, thus significantly increasing the photon absorption probability. This idea is, however, limited by the inherent collisional dephasing effect associated with the ensemble qubits. A meaningful work in future is to overcome this limitation, thereby greatly increasing the gate successful probability and fidelity. In the quantum-dot project, on the other hand, the qubit-system is embedded in a high-Q cavity to increase the lifetime of ancillary excitons. To obtain a better gate fidelity, one may seek to further extend the exciton's lifetime, for example, by optimizing the shape of the trapping cavity.

Bibliography

[1] C. Davisson and L. H. Germer. The scattering of electrons by a single crystal of nickel. *Nature*, 119:558, 1927.

[2] L. de Broglie. *Researches on the quantum theory.* PhD thesis, Paris, 1924.

[3] L. de Broglie. *Ann. Phys.*, 3:22, 1925.

[4] S. N. Bose. Plancks gesetz und lichtquantenhypothese. *Zeitschrift fr Physik*, 26:178, 1924.

[5] A. Einstein. Quantentheorie des einatomigen idealen gases. *Sitzungsberichte der Preussischen Akademie der Wissenschaften*, 1:3, 1925.

[6] L. P. Pitaevskii and S. Stringari. *Bose-Einstein condensation.* Clarendon Press, OXford, 2003.

[7] K. Huang. *Statistical Mechanics.* Wiley, New York, 1987.

[8] F. London. *Superfluids.* Wiley, New York, 1950.

[9] M. R. Andrews, C. G. Townsend, H.-J. Miesner, D. S. Durfee, D. M. Kurn, and W. Ketterle. Observation of interference between two bose condensates. *Science*, 275(5300):637–641, 1997.

[10] T. A. Fulton, P. L. Gammel, D. J. Bishop, L. N. Dunkleberger, and G. J. Dolan. Observation of combined josephson and charging effects in small tunnel junction circuits. *Phys. Rev. Lett.*, 63(12):1307–1310, Sep 1989.

[11] P. W. Anderson. *Rev. Mod. Phys.*, 38:298, 1966.

[12] H. Feshbach. *H. Feshbach.* Wiley, New York, Theoretical Nuclear Physics.

[13] S. J. J. M. F. Kokkelmans, J. N. Milstein, M. L. Chiofalo, R. Walser, and M. J. Holland. *Phys. Rev. A*, 65:053617, 2002.

[14] M. Greiner, C. A. Regal, and D. S. Jin. *Phys. Rev. Lett.*, 94:070403, 2005.

[15] Jelena Stajic, J. N. Milstein, Qijin Chen, M. L. Chiofalo, M. J. Holland, and K. Levin. *Phys. Rev. A*, 69:063610, 2004.

[16] O. Mandel M. Greiner, T. Esslinger, T. W. Häsch, and I. Bloch. *Nature (London)*, 415:39, 2002.

[17] T. Kinoshita, T. Wegner, and D. S. Weiss. *Science*, 305:1125, 2004.

[18] C. D. Fertig, K. M. O'Hara, J. H. Huckans, S. L. Rolston, W. D. Phillips, and J. V. Porto. *Phys. Rev. Lett.*, 94:120403, 2005.

[19] B. L. Tolra, K. M. O'Hara, J. H. Huckens, W. D. Phillips, S. L. Rolston, and J. V. Porto. *Phys. Rev. Lett.*, 92:190401, 2004.

[20] B. Paredes, A. Widera, V. Murg, O. Mandel, S. Föling, G. V. Shlyapnikov I. Cirac, T. W. Häsch, and I. Bloch. *Nature*, 429:277, 2004.

[21] T. L. Ho. *Phys. Rev. Lett.*, 87:060403, 2002.

[22] J. R. Abo-Shaeer, C. Raman, and W. Ketterle. *Phys. Rev. Lett.*, 88:070409, 2002.

[23] J. J. Bollinger, W. M. Itano, D. J. Wineland, and D. J. Heinzen. *Phys. Rev. A*, 54:R4649, 1996.

[24] J. J. Bollinger, Wayne M. Itano, D. J. Wineland, and D. J. Heinzen. *Phys. Rev. A*, 54:R4649, 1996.

[25] S. F. Huelga *et al.* *Phys. Rev. Lett.*, 79:3865, 1997.

[26] C. C. Gerry. *Phys. Rev. A*, 61:043811, 2000.

[27] W. J. Munro, K. Nemoto, G. J. Milburn, and S. L. Braunstein. *Phys. Rev. A*, 66:023819, 2002.

[28] B. Damski, J. Zakrzewski, L. Santos, P. Zoller, and M. Lewenstein. Atomic bose and anderson glasses in optical lattices. *Phys. Rev. Lett.*, 91(8):080403, Aug 2003.

[29] A. Sanpera, A. Kantian, L. Sanchez-Palencia, J. Zakrzewski, and M. Lewenstein. Atomic fermi-bose mixtures in inhomogeneous and random lattices: From fermi glass to quantum spin glass and quantum percolation. *Phys. Rev. Lett.*, 93(4):040401, Jul 2004.

[30] P. Bouyer and M. A. Kasevich. *Phys. Rev. A*, 56:R1083, 1997.

[31] Y. Shin, M. Saba, W. Ketterle T. A. Pasquini, D. E. Pritchard, and A. E. Leanhardt. *Phys. Rev. Lett.*, 92:050405, 2004.

[32] F. Dalfovo, S. Giogini, L. P. Pitaevskii, and S. Stringari. *Rev. Mod. Phys.*, 71: 463, 1999.

[33] M. A. Kasevich. *Science*, 298:1363, 2002.

[34] M. Antezza, L. P. Pitaevskii, and S. Stringari. *Phys. Rev. A*, 70:053619, 2004.

[35] G. Roati, E. de Mirandes, F. Ferlaino, H. Ott, G. Modugno, and M. Inguscio. *Phys. Rev. Lett.*, 92:230402, 2004.

[36] D. M. Harber J. M. Obrecht, J. M. McGuirk, and E. A. Cornell. *Phys. Rev. A*, 72:033610, 2005.

[37] T. Schumm, S. Hofferberth, L. M. Andersson, S. Wildermuth, S. Groth, I. Bar-Joseph, and J. Schmiedmayer. *Nature Physics*, 1:57, 2005.

[38] C.-S. Chuu, F. Schreck, T. P. Meyrath, J. L. Hanssen, G. N. Price, and M. G. Raizen. Direct observation of sub-poissonian number statistics in a degenerate bose gas. *Phys. Rev. Lett.*, 95(26):260403, Dec 2005.

[39] M. Shellekens, R. Hoppeler, A. Perrin, J.V. Gomes, D. Boiron, A. Aspect, and C.I. Westbrook. *Science*, 310:648, 2005.

[40] Y. P. Huang and M. G. Moore. Optimized double-well quantum interferometry with gaussian squeezed states. *Phys. Rev. Lett.*, 100(25):250406, 2008.

[41] M. H. Anderson, J. R. Ensher, M. R. Matthews, C. E. Wieman, and E. A. Cornell. *Science*, 269:198, 1995.

[42] K. B. Davis, M. O. Mewes, M. R. Andrews, N. J. van Druten, D. S. Durfee, D. M. Kurn, and W. Ketterle. Bose-einstein condensation in a gas of sodium atoms. *Phys. Rev. Lett.*, 75(22):3969–3973, Nov 1995.

[43] C. C. Bradley, C. A. Sackett, J. J. Tollett, and R. G. Hulet. Evidence of bose-einstein condensation in an atomic gas with attractive interactions. *Phys. Rev. Lett.*, 75(9):1687–1690, Aug 1995.

[44] C. C. Bradley, C. A. Sackett, and R. G. Hulet. Bose-einstein condensation of lithium: Observation of limited condensate number. *Phys. Rev. Lett.*, 78(6): 985–989, Feb 1997.

[45] Dale G. Fried, Thomas C. Killian, Lorenz Willmann, David Landhuis, Stephen C. Moss, Daniel Kleppner, and Thomas J. Greytak. Bose-einstein condensation of atomic hydrogen. *Phys. Rev. Lett.*, 81(18):3811–3814, Nov 1998.

[46] S. L. Cornish, N. R. Claussen, J. L. Roberts, E. A. Cornell, and C. E. Wieman. Stable $85rb$ bose-einstein condensates with widely tunable interactions. *Phys. Rev. Lett.*, 85(9):1795–1798, Aug 2000.

[47] G. Modugno, G. Ferrari, G. Roati, R. J. Brecha, A. Simoni, and M. Inguscio. Bose-einstein condensation of potassium atoms by sympathetic cooling. *Science*, 294(5545):1320–1322, 2001.

[48] A. Robert, O. Sirjean, A. Browaeys, J. Poupard, S. Nowak, D. Boiron, C. I. Westbrook, and A. Aspect. A bose-einstein condensate of metastable atoms. *Science*, 292(5516):461–464, 2001.

[49] F. Pereira Dos Santos, J. Léonard, Junmin Wang, C. J. Barrelet, F. Perales, E. Rasel, C. S. Unnikrishnan, M. Leduc, and C. Cohen-Tannoudji. Bose-einstein condensation of metastable helium. *Phys. Rev. Lett.*, 86(16):3459–3462, Apr 2001.

[50] Tino Weber, Jens Herbig, Michael Mark, Hanns-Christoph Nagerl, and Rudolf Grimm. Bose-einstein condensation of cesium. *Science*, 299(5604):232–235, 2003.

[51] Yosuke Takasu, Kenichi Maki, Kaduki Komori, Tetsushi Takano, Kazuhito Honda, Mitsutaka Kumakura, Tsutomu Yabuzaki, and Yoshiro Takahashi. Spin-singlet bose-einstein condensation of two-electron atoms. *Phys. Rev. Lett.*, 91(4):040404, Jul 2003.

[52] Axel Griesmaier, Jörg Werner, Sven Hensler, Jürgen Stuhler, and Tilman Pfau. Bose-einstein condensation of chromium. *Phys. Rev. Lett.*, 94(16):160401, Apr 2005.

[53] D. E. Pritchard, Helmerson K., and A. G. Martin. *Atomic Phyiscs II*, page 179. World Scientific, Singapore, 1989.

[54] K. Helmerson, A. Martin, and D. E. Pritchard. *J. Opt. Soc. Am. B*, 9:1988, 1992.

[55] C. N. Cohen-Tannoudji and W. D. Phillips. New mechanisms of laser cooling. *Phys. Today*, 43(10):33–40, 1990.

[56] Harald F. Hess. Evaporative cooling of magnetically trapped and compressed spin-polarized hydrogen. *Phys. Rev. B*, 34(5):3476–3479, Sep 1986.

[57] C. J. Myatt, E. A. Burt, R. W. Ghrist, E. A. Cornell, and C. E. Wieman. Production of two overlapping bose-einstein condensates by sympathetic cooling. *Phys. Rev. Lett.*, 78(4):586–589, Jan 1997.

[58] M.-O. Mewes, M. R. Andrews, D. M. Kurn, D. S. Durfee, C. G. Townsend, and W. Ketterle. Output coupler for bose-einstein condensed atoms. *Phys. Rev. Lett.*, 78(4):582–585, Jan 1997.

[59] Pierre Meystre. *Atom Optics*. Springer-Verlag, New York, 2001.

[60] József Fortágh and Claus Zimmermann. Magnetic microtraps for ultracold atoms. *Reviews of Modern Physics*, 79(1):235, 2007.

[61] J. D. Weinstein and K. G. Libbrecht. Microscopic magnetic traps for neutral atoms. *Phys. Rev. A*, 52(5):4004–4009, Nov 1995.

[62] H. Ott, J. Fortagh, G. Schlotterbeck, A. Grossmann, and C. Zimmermann. Bose-einstein condensation in a surface microtrap. *Phys. Rev. Lett.*, 87(23): 230401, Nov 2001.

[63] W. Hänsel, J. Reichel, P. Hommelhoff, and T. W. Hänsch. Trapped-atom interferometer in a magnetic microtrap. *Phys. Rev. A*, 64(6):063607, Nov 2001.

[64] A. Günther, S. Kraft, M. Kemmler, D. Koelle, R. Kleiner, C. Zimmermann, and J. Fortágh. Diffraction of a bose-einstein condensate from a magnetic lattice on a microchip. *Phys. Rev. Lett.*, 95(17):170405, Oct 2005.

[65] Y. Shin, C. Sanner, G.-B. Jo, T. A. Pasquini, M. Saba, W. Ketterle, D. E. Pritchard, M. Vengalattore, and M. Prentiss. Interference of bose-einstein condensates split with an atom chip. *Phys. Rev. A*, 72(2):021604, Aug 2005.

[66] G. J. Milburn, J. Corney, E. M. Wright, and D. F. Walls. Quantum dynamics of an atomic bose-einstein condensate in a double-well potential. *Phys. Rev. A*, 55(6):4318–4324, Jun 1997.

[67] A. Smerzi, S. Fantoni, S. Giovanazzi, and S. R. Shenoy. Quantum coherent atomic tunneling between two trapped bose-einstein condensates. *Phys. Rev. Lett.*, 79(25):4950–4953, Dec 1997.

[68] S. Raghavan, A. Smerzi, S. Fantoni, and S. R. Shenoy. Coherent oscillations between two weakly coupled bose-einstein condensates: Josephson effects, π oscillations, and macroscopic quantum self-trapping. *Phys. Rev. A*, 59(1):620–633, Jan 1999.

[69] A. J. Leggett. *Rev. Mod. Phys.*, 73:307, 2001.

[70] A. P. Hines, R. H. McKenzie, and G. J. Milburn. *Phys and Rev. A*, 67:013609, 2003.

[71] Michael Albiez, Rudolf Gati, Jonas Fölling, Stefan Hunsmann, Matteo Cristiani, and Markus K. Oberthaler. Direct observation of tunneling and nonlinear self-trapping in a single bosonic josephson junction. *Phys. Rev. Lett.*, 95(1): 010402, Jun 2005.

[72] A. Micheli, D. Jaksch, J. I. Cirac, and P. Zoller. *Phys. Rev. A*, 67:013607, 2003.

[73] A. Sørenson, L. M. Duan, J. I. Cirac, and P. Zoller. *Nature (London)*, 409:63, 2001.

[74] S. Raghavan, A. Smerzi, and V. M. Kenkre. *Phys. Rev. A*, 60:R1787, 1999.

[75] K. W. Mahmud, H. Perry, and W. P. Reinhardt. *J. Phys. B*, 36:L265, 2003.

[76] Matthew P. A. Fisher, Peter B. Weichman, G. Grinstein, and Daniel S. Fisher. Boson localization and the superfluid-insulator transition. *Phys. Rev. B*, 40(1): 546–570, Jul 1989.

[77] E. Schrödinger. *Naturwissenschaften*, 23:807, 1935.

[78] T. J. Osborne and M. A. Nielsen. *Phys. Rev. A*, 66:032110, 2002.

[79] M. C. Arnesen, S. Bose, and V. Vedral. *Phys. Rev. Lett.*, 87:017901, 2001.

[80] R. Gati, M. Albiez, J. Flling, B. Hemmerling, and M.K. Oberthaler. *Appl. Phys. B*, 82:207, 2006.

[81] C. Lee. *Phys. Rev. Lett.*, 97:150402, 2006.

[82] L. Pezzé, A. Smerzi, G. P. Berman, A. R. Bishop, and L. A. Collins. *Phys. Rev. A*, 74:033610, 2006.

[83] G. B. Jo *et al. Phys. Rev. Lett.*, 98:030407, 2007.

[84] H. Fizeau. *Ann. Phys. Chem.*, 3:457, 1853.

[85] L. Rayleigh. *Philos. Mag.*, 11:196, 1881.

[86] A. A. Michelson. *Am. J. Sci.*, 22:20, 1881.

[87] L. Marton. Electron interferometer. *Phys. Rev.*, 85(6):1057–1058, Mar 1952.

[88] H. Maier-Leibnitz and T. Springer. *Z. Phys.*, 167:368, 1962.

[89] G. Badurek, H. Rauch, and A. Zeilinger. *Physica B*, 151:R9, 1988.

[90] Douglas S. Robertson. Geophysical applications of very-long-baseline interferometry. *Rev. Mod. Phys.*, 63(4):899–918, Oct 1991.

[91] Ojars J. Sovers, John L. Fanselow, and Christopher S. Jacobs. Astrometry and geodesy with radio interferometry: experiments, models, results. *Rev. Mod. Phys.*, 70(4):1393–1454, Oct 1998.

[92] R. Colella, A. W. Overhauser, and S. A. Werner. Observation of gravitationally induced quantum interference. *Phys. Rev. Lett.*, 34(23):1472–1474, Jun 1975.

[93] Mark Kasevich and Steven Chu. Atomic interferometry using stimulated raman transitions. *Phys. Rev. Lett.*, 67(2):181–184, Jul 1991.

[94] Markus K. Oberthaler, Stefan Bernet, Ernst M. Rasel, Jörg Schmiedmayer, and Anton Zeilinger. Inertial sensing with classical atomic beams. *Phys. Rev. A*, 54 (4):3165–3176, Oct 1996.

[95] Karin Sangster, E. A. Hinds, Stephen M. Barnett, and Erling Riis. Measurement of the aharonov-casher phase in an atomic system. *Phys. Rev. Lett.*, 71(22): 3641–3644, Nov 1993.

[96] A. Görlitz, B. Schuh, and A. Weis. Measurement of the aharonov-casher phase of aligned rb atoms. *Phys. Rev. A*, 51(6):R4305–R4308, Jun 1995.

[97] S. A. Werner, J. L. Staudenmann, R. Colella, and A. W. Overhauser. *Neutron Interferometry*, page 209. Clarendon Press, OXford, 1979.

[98] A. Tonomura. *Electron Holography.* Springer-Verlag, New York, 1993.

[99] C. K. Law and N. P. Bigelow. Amplifying an atomic wave signal using a bose-einstein condensate. *Phys. Rev. A*, 58(6):4791–4795, Dec 1998.

[100] S. Inouye, A. P. Chikkatur, D. M. Stamper-Kurn, J. Stenger, D. E. Pritchard, and W. Ketterle. *Science*, 285:571, 1999.

[101] Mikio Kozuma, Yoichi Suzuki, Yoshio Torii, Toshiaki Sugiura, Takahiro Kuga, E. W. Hagley, and L. Deng. Phase-coherent amplification of matter waves. *Science*, 286(5448):2309–2312, 1999.

[102] S. Inouye, T. Pfau, S. Gupta, A. P. Chikkatur, A. Görlitz, D. E. Pritchard, and W. Ketterle. *Nature*, 402:641, 1999.

[103] M. G. Moore and P. Meystre. *Phys. Rev. Lett.*, 83:5202, 1999.

[104] Konstantin V. Krutitsky, Frank Burgbacher, and Jürgen Audretsch. Local-field approach to the interaction of an ultracold dense bose gas with a light field. *Phys. Rev. A*, 59(2):1517, Feb 1999.

[105] Özgür E. Müstecaplioğlu and L. You. Superradiant light scattering from trapped bose-einstein condensates. *Phys. Rev. A*, 62(6):063615, Nov 2000.

[106] S. Inouye, R. F. Löw, S. Gupta, T. Pfau, A. Görlitz, T. L. Gustavson, D. E. Pritchard, and W. Ketterle. Amplification of light and atoms in a bose-einstein condensate. *Phys. Rev. Lett.*, 85(20):4225, Nov 2000.

[107] E. D. Trifonov. *JETP*, 93(4):969, Oct 2001.

[108] Dominik Schneble, Yoshio Torii, Micah Boyd, Erik W. Streed, David E. Pritchard, and Wolfgang Ketterle. The onset of matter-wave amplification in a superradiant bose-einstein condensate. *Science*, 300(5618):475, 2003.

[109] N. Piovella, V. Beretta, G. R. M. Robb, and R. Bonifacio. Photon echo in the super-radiant light scattering from a bose-einstein condensate. *Phys. Rev. A*, 68(2):021801, Aug 2003.

[110] D. Schneble, K. C. Gretchen, W. S. Erik, B. Micah, D. E. Pritchard, and W. Ketterle. *Phys. Rev. A*, 69:041601(R), 2004.

[111] Y. Yoshikawa, T. Sugiura, Y. Torii, and T. Kuga. *Phys. Rev. A*, 69:041603(R), 2004.

[112] Dominik Schneble, Gretchen K. Campbell, Erik W. Streed, Micah Boyd, David E. Pritchard, and Wolfgang Ketterle. Raman amplification of matter waves. *Phys. Rev. A (Atomic, Molecular, and Optical Physics)*, 69(4):041601, 2004.

[113] Yu. A Avetisyan and E. D. Trifonov. Multimode model of superradiant scattering from bec of dilute gas. *Laser Phys. Lett.*, 7:373, 2004.

[114] Mary M. Cola and Nicola Piovella. Theory of collective raman scattering from a bose-einstein condensate. *Phys. Rev. A*, 70(4):045601, Oct 2004.

[115] E. D. Trifonov. *Laser Phys. Lett.*, 2(3):153, 2005.

[116] R. Bonifacio, N. Piovella, G. R. M. Robb, and M. M. Cola. *Opt. Commun*, 252: 381, 2005.

[117] A. Hilliard, F. Kaminski, R. le Targat, C. Olausson, E. S. Polzik, and J. H. Müller. Rayleigh superradiance and dynamic bragg gratings in an end-pumped bose-einstein condensate. *Phys. Rev. A (Atomic, Molecular, and Optical Physics)*, 78(5):051403, 2008.

[118] S. L. Rolston and W. D. Phillips. *Nature (London)*, 416:219, 2002.

[119] L. Pezzé and A. Smerzi. *Phys. Rev. A*, 73:011801(R), 2006.

[120] J. F. Sherson, H. Krauter, R. K. Olsson, B. Julsgaard, K. Hammerer, I. Cirac, and E. S. Polzik. Quantum teleportation between light and matter. *Nature*, 443:557–560, Dec 2006.

[121] Michael Fleischhauer, Atac Imamoglu, and Jonathan P. Marangos. Electromagnetically induced transparency: Optics in coherent media. *Reviews of Modern Physics*, 77(2):633, 2005.

[122] L.-M. Duan and C. Monroe. Robust probablistic quantum information processing with atoms photons and atomic ensembles. *Advances in atomic, molecular and optical physics*, 55:419, Dec 2008.

[123] W. Zhang and D. F. Walls. Quantum field theory of interaction of ultracold atoms with a light wave: Bragg scattering in nonlinear atom optics. *Phys. Rev. A*, 49:3799, 1994.

[124] Tun Wang and S. F. Yelin. Theory for raman superradiance in atomic gases. *Phys. Rev. A*, 72(4):043804, Oct 2005.

[125] H. Uys and P. Meystre. Superradiant raman scattering in an ultracold bose gas at finite temperature. *Phys. Rev. A*, 77(6):063614, 2008.

[126] E. D Trifonov and N. I Shamro. *Physical and Quantum Optics*, 96:258, 2004.

[127] O. Zobay and Georgios M. Nikolopoulos. Dynamics of matter-wave and optical fields in superradiant scattering from bose-einstein condensates. *Phys. Rev. A*, 72(4):041604, 2005.

[128] N. I Shamrov. *Journal of Applied Spectroscopy*, 73:68, 2006.

[129] O. Zobay and Georgios M. Nikolopoulos. Spatial effects in superradiant rayleigh scattering from bose-einstein condensates. *Phys. Rev. A*, 73(1):013620, 2006.

[130] O. Zobay and Georgios M. Nikolopoulos. Sequential superradiant scattering from atomic bose-einstein condensates. *Laser Physics*, 17:180, 2007.

[131] H. Uys and P. Meystre. Theory of coherent raman superradiance imaging of condensed bose gases. *Phys. Rev. A*, 75(3):033805, 2007.

[132] Yu. A Avetisyan and E. D. Trifonov. Maxwell-schrodinger equations for a dilute gas bose-einstein condensate coupled to an electromeganetic field. *Journal of Experimental and Theoretical Physics*, 106:426, 2008.

[133] Yu. A Avetisyan and E. D. Trifonov. Superradiant reflection and scattering of light from a bose-einstein condensate of a dilute gas. *Optics and Spectroscopy*, 105:557, 2008.

[134] Han Pu, Weiping Zhang, and Pierre Meystre. *Phys. Rev. Lett.*, 91:150407, 2003.

[135] L. E. Sadler, J. M. Higbie, S. R. Leslie, M. Vengalattore, and D. M. Stamper-Kurn. Coherence-enhanced imaging of a degenerate bose-einstein gas. *Phys. Rev. Lett.*, 98(11):110401, 2007.

[136] M. A. Nielsen and I. L. Chuang. *Quantum Computation and Quantum Information.* 2000.

[137] J. Audretsch, R. Blatt, M. Esfeld, C. Held, E. Joos, R. Löw, T. Pfau, G. Rempe, H. Weinfurter, and R. F. Werner. *Entangled World.* WILEY-VCH Verlag GmbH & Co. KGaA, 2006.

[138] R. P. Feynman. Sitmulating physics with computers. *Int. J. Theor. Phys.*, 21: 467, 1982.

[139] C. H. Bennett and G. Brassard. *Proc. IEEE. Int. Conf. Computer Systems and Signal Processing.* IEEE, New York, 1984.

[140] David Deutsch. The church-turing principle and the universal quantum computer. *Proceedings of the Royal Society of London A*, 400:97, 1985.

[141] David Deutsch and Richard Jozsa. Rapid solutions of problems by quantum computation. *Proceedings of the Royal Society of London A*, 439:553, 1992.

[142] Peter W. Shor. Algorithms for quantum computation: Discrete logarithms and factoring. *IEEE Symposium on Foundations of Computer Science*, page 124, 1994.

[143] Lieven M. K. Vandersypen, Matthias Steffen, Gregory Breyta, Costantino S. Yannoni, Mark H. Sherwood, and Isaac L. Chuang. Experimental realization of shor's quantum factoring algorithm using nuclear magnetic resonance. *Nature*, 414(6866):883–887, December 2001.

[144] L. K. Grover. A fast quantum mechanical algorithm for database search. *Proceedings, 28th Annual ACM Symposium on the Theory of Computing*, page 212, 1996.

[145] G. Vernam. *J. Am. Inst. Elect. Eng.*, 45:109, 1926.

[146] J. S. Bell. On the einstein podolsky rosen paradox. *Physics*, 1:195, 1964.

[147] Mark Fox. *Quantum Optics: an introduction.* Oxford University Press, 2006.

[148] Richard P. Feynman, Jr. Frank L. Vernon, and Robert W. Hellwarth. Geometrical representation of the schr[o-umlaut]dinger equation for solving maser problems. *Journal of Applied Physics*, 28(1):49–52, 1957.

[149] C. H. Bennett, G. Brassard, C. Crépeau, R. Jozsa, A. Peres, and W. K. Wootters. *Phys. Rev. Lett.*, 70:1895, 1993.

[150] L.-M. Duan, J. I. Cirac, P. Zoller, and E. S. Polzik. *Phys. Rev. Lett.*, 85:5643, 2000.

[151] L. M. Duan, M. D. Lukin, J. I. Cirac, and P. Zoller. long-distance quantum communication with atomic ensembles and linear optics. *Nature*, 414:413, 2001.

[152] Gustavo A. Narvaez, Gabriel Bester, Alberto Franceschetti, and Alex Zunger. Excitonic exchange effects on the radiative decay time of monoexcitons and biexcitons in quantum dots. *Physical Review B (Condensed Matter and Materials Physics)*, 74(20):205422, 2006.

[153] K. Hennessy, A. Badolato, M. Winger, D. Gerace, M. Atatüre, S. Gulde, S. Fält, E. L. Hu, and A. Imamoglu. Quantum nature of a strongly coupled single quantum dot-cavity system. *Nature*, 445:896, 2007.

[154] E. M. Purcell. *Phys. Rev.*, 69:681, 1946.

[155] C J. Hood, H. J. Kimble, and J.Ye. *Phys. Rev. A*, 64:033804(R), 2001.

[156] J. M. Raimond, M. Brune, and S. Haroche. *Rev. Mod. Phys.*, 73:565, 2001.

[157] B. Yurke, S. L. McCall, and J. R. Klauder. *Phys. Rev. A.*, 33:4033, 1986.

[158] M. J. Holland and K. Burnett. *Phys. Rev. Lett.*, 71:1355, 1993.

[159] A. Heidmann, R. J. Horowicz, S. Reynaud, E. Giacobino, C. Fabre, and G. Camy. *Phys. Rev. Lett.*, 59:2555, 1987.

[160] B. Lantz, P. Fritschel, H. Rong, E. Daw, and G. González. *J. Opt. Soc. Am. A*, 19:91, 2002.

[161] C. B. Chiu, E. C. G. Sudarshan, and B. Misra. Time evolution of unstable quantum states and a resolution of zeno's paradox. *Phys. Rev. D*, 16(2):520–529, Jul 1977.

[162] L.-M. Duan and G.-C. Guo. *Phys. Rev. A*, 58:3491, 1998.

[163] P. Zanardi and F. Rossi. *Phys. Rev. B*, 59:8170, 1999.

[164] A. Beige, D. Braun, B. Tregenna, and P. L. Knight. *Phys. Rev. Lett.*, 85:1762, 2000.

[165] Q. A. Turchette, C. J. Hood, W. Lange, H. Mabuchi, and H. J. Kimble. *Phys. Rev. Lett.*, 75:4710, 1995.

[166] C. Monroe, D. M. Meekhof, B. E. King, W. M. Itano, and D. J. Wineland. *Phys. Rev. Lett.*, 75:4714, 1995.

[167] A. Rauschenbeutel, G. Nogues, P. Bertet S. Osnaghi, M. Brune, J. M. Raimond, and S. Haroche. *Phys. Rev. Lett.*, 83:5166, 1999.

[168] E. Knill, R. Laflamme, and G. J. Milburn. *Nature*, 409:46, 2001.

[169] K. J. Resch, J. S. Lundeen, and A. M. Steinberg. *Phys. Rev. Lett.*, 89:037904, 2002.

[170] T. B. Pittman, M. J. Fitch, B. C. Jacobs, and J. D. Franson. *Phys. Rev. A*, 68: 032316, 2003.

[171] J. L. O'Brien, G. J. Pryde, A. G. White, T. C. Ralph, and D. Branning. *Nature*, 426:264, 2003.

[172] D. Leibfried, B. DeMarco, V. Meyer, M. Barrett D. Lucas, J. Britton, W. M. Itano, B. Jelenković, C. Langer, T. Rosenband, and D. J. Wineland. *Nature*, 422:412, 2003.

[173] T. Yamamoto, Yu. A. Pashkin, O. Astafiev, Y. Nakamura, and J. S. Tsai. *Nature*, 425:941, 2003.

[174] P. Kok, W. J. Munro, K. Nemoto, T. C. Ralph, J. P. Dowling, and G. J. Milburn. *Rev. Mod. Phys.*, 79:135, 2007.

[175] D. Bouwmeester, J.-W. Pan, K. Mattle, M. Eibl, H. Weinfurter, and A. Zeilinger. Experimental quantum teleportation. *Nature*, 390:575–579, Dec 1997.

[176] C. Z. Peng, T. Yang, X. H. Bao, J. Zhang, X. M. Jin, F. Y. Feng, B. Yang, J. Yang, J. Yin, Q. Zhang, N. Li, B. L.Tian, and J. W. Pan. *Phys. Rev. Lett.*, 94:150501, 2005.

[177] T.-Y. Chen, J. Zhang, J.-C. Boileau, X.-M. Jin, B. Yang, Q. Zhang, T. Yang, R. Laflamme, and J. W. Pan. *Phys. Rev. Lett.*, 96:150504, 2006.

[178] W. Tittel, J. Brendel, H. Zbinden, and N. Gisin. *Phys. Rev. Lett.*, 84:4737, 2000.

[179] S.L. Braunstein and H.J. Kimble. *Phys. Rev. A*, 61:042302, 2000.

[180] M. W. Mitchell, J. S. Lundeen, and A. M. Steinberg. *Nature*, 429:161, 2004.

[181] I. Marcikic, H. de Riedmatten, W. Tittel, H. Zbinden, and N. Gisin. Long-distance teleportation of qubits at telecommunication wavelengths. *Nature*, 421 (6922):509–513, January 2003.

[182] S. Bose, P. L. Knight, M. B. Plenio, and V. Vedral. *Phys. Rev. Lett.*, 83:5158, 1999.

[183] S.-B. Zheng and G.-C. Guo. *Phys. Rev. A*, 73:032329, 2006.

[184] L.-M. Duan and H. J. Kimble. *Phys. Rev. Lett.*, 90:253601, 2003.

[185] T. Di, A. Muthukrishnan, M. O. Scully, and M. S. Zubairy. *Phys. Rev. A*, 71: 062308, 2005.

[186] M. Riebe, H. Häffner, C. F. Roos, W. Hänsel, J. Benhelm, G. P. T. Lancaster, T. W. Körber, C. Becher, F. Schmidt-Kaler, D. F. V. James, and R. Blatt. *Nature*, 429:734, 2004.

[187] M. D. Barrett, J. Chiaverini, T. Schaetz, J. Britton, W. M. Itano, J. D. Jost, E. Knill, C. Langer, D. Liebfried, R. Ozeri, and D. J. Wineland. *Nature*, 429: 737, 2004.

[188] N. A. Gershenfeld and I. L. Chuang. *Science*, 275:350, 1997.

[189] P. G. Kwiat, J. R. Mitchell, P. D. D. Schwindt, and A. G. White. Grover's search algorithm: an optical approach. *J. Mod. Opt.*, 47:257, 2000.

[190] D. Cory, A. Fahmy, and T. Havel. *Proc. Nat. Acad. Sci*, 94:1634, 1997.

[191] Isaac L. Chuang, Neil Gershenfeld, and Mark Kubinec. Experimental implementation of fast quantum searching. *Phys. Rev. Lett.*, 80(15):3408–3411, Apr 1998.

[192] L. DiCarlo, J. M. Chow, J. M. Gambetta, Lev S. Bishop, B. R. Johnson, D. I. Schuster, J. Majer, A. Blais, L. Frunzio, S. M. Girvin, and R. J. Schoelkopf. Demonstration of two-qubit algorithms with a superconducting quantum processor. *Nature*, advanced online publication:–, June 2009.

[193] E. Urban, T. A. Johnson, T. Henage, L. Isenhower, D. D. Yavuz, T. G.Walker, and M. Saffman. Observation of rydberg blockade between two atoms. *Nat. Phys.*, 5:110, 2009.

[194] A. Gilchrist, A. G. White, and W. J. Munro. *Phys. Rev. A*, 66:012106, 2002.

[195] H. Azuma. *Phys. Rev. A*, 68:022320, 2003.

[196] H. Azuma. *Phys. Rev. A*, 70:012318, 2004.

[197] J. D. Franson, B. C. Jacobs, and T. B. Pittman. *Phys. Rev. A*, 70:062302, 2004.

[198] O. Hosten, M. T. Rakher, J. T. Barreiro, N. A. Peters, and P. G. Kwiat. *Nature*, 439:949, 2006.

[199] D. Boschi, S. Branca, F. De Martini, L. Hardy, and S. Popescu. Experimental realization of teleporting an unknown pure quantum state via dual classical and einstein-podolsky-rosen channels. *Phys. Rev. Lett.*, 80(6):1121–1125, Feb 1998.

[200] Jian-Wei Pan, Matthew Daniell, Sara Gasparoni, Gregor Weihs, and Anton Zeilinger. Experimental demonstration of four-photon entanglement and high-fidelity teleportation. *Phys. Rev. Lett.*, 86(20):4435–4438, May 2001.

[201] S. Olmschenk, D. N. Matsukevich, P. Maunz, D. Hayes, L.-M. Duan, and C. Monroe. Quantum teleportation between distant matter qubits. *Science*, 323(5913):486–489, 2009.

[202] W. H. Zurek. *Phys. Today*, 44:36, 1991.

[203] J. R. Friedman, V. Patel, W. Chen, S. K. Tolpygo, and J. E. Lukens. *Nature (London)*, 60:43, 2000.

[204] M. Arndt, O. Nairz, J. Vos-Andreae, C. Keller, G. van der. Zouw, and A. Zeilinger. *Nature (London)*, 401:680, 1999.

[205] C. Monroe, D. M. Meekhof, B. E. King, and D. J. Wineland. *Science*, 272:1131, 1996.

[206] C. A. Sackett, D. Kielpinski, B. E. King, C. Langer, V. Meyer, C. J. Myatt, M. Rowe, Q. A. Turchette, W. M. Itano, D. J. Wineland, and C. Monroe. Experimental entanglement of four particles. *Nature*, 404(6775):256–259, March 2000.

[207] J. R. Friedman, M. P. Sarachik, J. Tejada, and R. Ziolo. *Phys. Rev. Lett.*, 76: 3830, 1996.

[208] R. Rouse, S. Han, and J. E. Lukens. *Phys. Rev. Lett.*, 75:1614, 1995.

[209] P. Silvestrini, V. G. Palmieri, B. Ruggiero, and M. Russo. *Phys. Rev. Lett.*, 79: 3046, 1997.

[210] Y. Nakamura, Y. A. Pashkin, and J. S. Tsai. *Nature*, 398:786, 1999.

[211] M. H. Anderson, J. R. Ensher, M. R. Matthews, C. E. Wieman, and E. A. Cornell. *Science*, 269:198, 1995.

[212] C. C. Bradley, C. A. Sackett, J. J. Tollett, and R. G. Hulet. *Phys. Rev. Lett.*, 75:1687, 1995.

[213] K. B. Davis, M.-O. Mewes, M. R. Andrews, N. J. van Druten, D. S. Durfee, D. M. Kurn, and W. Ketterle. *Phys. Rev. Lett.*, 75:3969, 1995.

[214] F. Dalfovo, S. Giogini, L. P. Pitaevskii, and S. Stringari. *Rev. Mod. Phys.*, 71: 463, 1999.

[215] J. Higbie and D. M. Stamper-Kurn. *Phys. Rev. A*, 69:053605, 2004.

[216] M. Greiner, O. Mandel, T. Esslinger, T. W. Hänsch, and I. Bloch. *Nature (London)*, 415:39, 2002.

[217] J. I. Cirac, M. Lewenstein, K. Mølmer, and P. Zoller. *Phys. Rev. A*, 57:1208, 1998.

[218] T. L. Ho and C. V. Ciobanu. *Journal of Low Temperature Physics*, 135:257, 2004.

[219] A. Smerzi, S. Fantoni, S. Giovanazzi, and S. R. Shenoy. *Phys. Rev. Lett.*, 79: 4950, 1997.

[220] S. Raghavan, A. Smerzi, S. Fantoni, and S. R. Shenoy. *Phys. Rev. A*, 59:620, 1999.

[221] D. A. R. Dalvit, J. Dziarmaga, and W. H. Zurek. *Phys. Rev. A*, 62:013607, 2000.

[222] P. J. Y. Louis, P. M. R. Brydon, and C. M. Savage. *Phys. Rev. A*, 64:053613, 2001.

[223] G. J. Milburn, J. Corney, E. M. Wright, and D. F. Walls. *Phys. Rev. A*, 55: 4318, 1997.

[224] J. K. Chin, J. M. Vogels, and W. Ketterle. *Phys. Rev. Lett*, 90:160405, 2003.

[225] Yu. Kagan, A. E. Muryshev, and G. V. Shlyapnikov. *Phys. Rev. Lett.*, 81:933, 1997.

[226] R. H. Dicke. *Phys. Rev.*, 93:99, 1954.

[227] A. Imamoğlu, M. Lewenstein, and L. You. Inhibition of coherence in trapped bose-einstein condensates. *Phys. Rev. Lett.*, 78(13):2511–2514, Mar 1997.

[228] W. Zhang and D. F. Walls. *Phys. Rev. A*, 49:3799, 1994.

[229] V. Giovannetti, S. Lloyd, and L. Maccone. *Science*, 306:1330, 2004.

[230] P. Carruthers and M. M. Nieto. *Rev. Mod. Phys.*, 40:411, 1968.

[231] M. Born and E. Wolf. *Principles of Optics.* Pergamon and Oxford, 1975.

[232] C. M. Caves. *Phys. Rev. D*, 23:1693, 1981.

[233] R. S. Bondurant and J. H. Shapiro. *Phys. Rev. D*, 30:2548, 1984.

[234] Y. P. Huang and M. G. Moore. On-demand generation of entanglement of atomic qubits via optical interferometry. *Phys. Rev. A*, 77(3):032349, 2008.

[235] R. A. Campos, Christopher C. Gerry, and A. Benmoussa. *Phys. Rev. A*, 68: 023810, 2003.

[236] Ole Steuernagel and Stefan Scheel. *J. Opt. B: Quantum Semiclass. Opt.*, 6:S66, 2004.

[237] K. Eckert *et al. Phys. Rev. A*, 73:013814, 2006.

[238] D. Denot, T. Bschorr, and M. Freyberger. *Phys. Rev. A*, 73:013824, 2006.

[239] L. Pezzé and A. Smerzi. *Phys. Rev. Lett.*, 100:073601, 2008.

[240] Christopher C. Gerry and Adil Benmoussa. *Phys. Rev. A.*, 65:033822, 2002.

[241] P. Walther, J.-W. Pan, M. Aspelmeyer, R. Ursin, S. Gasparon, and A. Zeilinger. *Nature (London)*, 429:158, 2004.

[242] T. Kim, J. Dunningham, and K. Burnett. *Phys. Rev. A*, 72:055801, 2005.

[243] K. Eckert, P. Hyllus, D. Bruß, U. V. Poulsen, M. Lewenstein, C. Jentsch, T. Müller, E. M. Rasel, and W. Ertmer. *Phys. Rev. A*, 73:013814, 2006.

[244] Z. Hradil and J. Řeháček. *Phys. Lett. A*, 334:267, 2005.

[245] Alistair S. Lane, Samuel L. Braunstein, and Carlton M. Caves. *Phys. Rev. A*, 47:1667, 1993.

[246] Thomas B. Bahder and Paul A. Lopata. *Phys. Rev. A*, 74:051801(R), 2006.

[247] Carlton M. Caves, Christopher A. Fuchs, and Rüdiger Schack. *Phys. Rev. A*, 65:022305, 2002.

[248] T. Kim and *et al. Phys. Rev. A*, 57:4004, 1998.

[249] Y. P. Huang and M. G. Moore. *Phys. Rev. A*, 73:023606, 2006.

[250] L. Pezzé and A. Smerzi. *quant-ph/0508158*, 2005.

[251] J. M. McGuirk, G. T. Foster, J. B. Fixler, M. J. Snadden, and M. A. Kasevich. *Phys. Rev. A*, 65:033608, 2002.

[252] TheoryC. W. Helstrom. *Quantum Detection and Estimation.* Academic Press, New York, 1976.

[253] B. C. Sanders and G. J. Milburn. *Phys. Rev. Lett.*, 75:2944, 1995.

[254] V. Meyer, M. A. Rowe, D. Kielpinski, C. A. Sackett, W. M. Itano, C. Monroe, and D. J. Wineland. *Phys. Rev. Lett.*, 86:5870, 2000.

[255] L. Pezzé *et al.* *Phys. Rev. A*, 72:043612, 2005.

[256] G. A. Durkin and J. P. Dowling. *Phys. Rev. Lett.*, 99:070801, 2007.

[257] M. O Scully and M. S. Zubairy. *Quantum Optics.* Cambridge University Press, NewYork, USA, 1997.

[258] L. You, Maciej Lewenstein, and J. Cooper. *Phys. Rev. A*, 51(11):4712, 1995.

[259] B. Julsgaard, A. Kozhekin, and E. S. Polzik. *Nature*, 413:400, 2001.

[260] D. N. Matsukevich and A. Kuzmich. *Science*, 306:663, 2004.

[261] P. van Loock, T. D. Ladd, K. Sanaka, Kae Nemoto F. Yamaguchi, W. J. Munro, and Y. Yamamoto. *Phys. Rev. Lett.*, 96:240501, 2006.

[262] S. J. van Enk and H. J. Kimble. *Phys. Rev. A*, 63:023809, 2001.

[263] A. Kuhn, M. Hennrich, and G. Rempe. *Phys. Rev. Lett.*, 89:067901, 2002.

[264] W. T. M. Irvine, K. Hennessy, and D. Bouwmeester. *Phys. Rev. Lett.*, 96: 057405, 2006.

[265] X.-B. Zou, J. Kim, and H.-W. Lee. *Phys. Rev. A*, 63:065801, 2001.

[266] C. C. Gerry and R. A. Campos. *Phys. Rev. A*, 64:063814, 2001.

[267] H. Lee, P. Kok, N. J. Cerf, and J. P. Dowling. *Phys. Rev. A*, 65:030101(R), 2002.

[268] A. Micheli, D. Jaksch, J. I. Cirac, and P. Zoller. *Phys. Rev. A*, 67:013607, 2003.

[269] D. M. Greenberger, M. Horne, and A. Zeilinger. *Bell's Theorem and Quantum Theory and Conceptions of the Universe.* Kluwer and Dordrecht, 1989.

[270] J.-W. Pan, D. Bouwmeester, H. Weinfurter, and A. Zeilinger. *Phys. Rev. Lett.*, 80:3891, 1998.

[271] A. D. Boozer, A. Boca, R. Miller, T. E. Northup, and H. J. Kimble. *Phys. Rev. Lett.*, 97:083602, 2006.

[272] A. D. Boozer, A. Boca, R. Miller, T. E. Northup, and H. J. Kimble. *Phys. Rev. Lett.*, 98:193601, 2007.

[273] S. Pötting, E. S. Lee, W. Schmitt, I. Rumyantsev, B. Mohring, and P. Meystre. *Phys. Rev. A*, 62:060101(R), 2000.

[274] B. Misra and E. C. G. Sudarshan. *J. Math. Phys.*, 18:756, 1977.

[275] A. Peres. *Am. J. Phys.*, 48:931, 1980.

[276] E. Joos. *Phys. Rev. D*, 29:1626, 1984.

[277] W. M. Itano, D. J. Heingzen, J. J. Bollinger, and D. J. Wineland. *Phys. Rev. A*, 41:2295, 1990.

[278] S. H. Simon and P. M. Platzman. *Phys. Rev. A*, 61:052103, 2000.

[279] J. Ruseckas and B. Kaulakys. *Phys. Rev. A*, 73:052101, 2006.

[280] A. C. Elitzur and L. Vaidman. *Found. Phys.*, 23 (7):987, 1993.

[281] P. G. Kwiat, H. Weinfurter, T. Herzog, A. Zeilinger, and M. A. Kasevich. *Phys. Rev. Lett.*, 74:4763, 1995.

[282] P. Kwiat, H. Weinfurter, and A. Zeilinger. *Sci. Am.*, 2755:72, 1996.

[283] T. Tsegaye, E. Goobar, A. Karlsson, G. BjÖrk, M. Y. Loh, and K. H. Lim. *Phys. Rev. A*, 57:3987, 1998.

[284] A. G. White, J. R. Mitchell, O. Nairz, and P. G. Kwiat. *Phys. Rev. A*, 58:605, 1998.

[285] P. G. Kwiat, A. G. White, J. R. Mitchell, O. Nairz, G. Weihs, H. Weinfurter, and A. Zeilinger. *Phys. Rev. Lett.*, 83:4725, 1999.

[286] T. Rudolph. *Phys. Rev. Lett.*, 85:2925, 2000.

[287] T. C. Ralph, A. G. White, W. J. Munro, and G. J. Milburn. *Phys. Rev. A*, 65: 012314, 2002.

[288] T. C. Ralph, N. K. Langford, T. B. Bell, and A. G. White. *Phys. Rev. A*, 65: 062324, 2002.

[289] H. F. Hofmann and S. Takeuchi. *Phys. Rev. A*, 66:024308, 2002.

[290] Z. Zhao, A.-N. Zhang, Y.-A. Chen, H. Zhang, J.-F. Du, T. Yang, and J.-W. Pan. *Phys. Rev. Lett.*, 94:030501, 2005.

[291] K. J. Xu, Y. P. Huang, M. G. Moore, and C. Piermarocchi. Two-qubit conditional phase gate in laser-excited semiconductor quantum dots using the quantum zeno effect. *Physical Review Letters*, 103(3):037401, 2009.

[292] M. A. Nielsen, E. Knill, and R. Laflamme. *Nature*, 396:52, 1998.

[293] A. Kuzmich and E. S. Polzik. *Phys. Rev. Lett.*, 85:5639, 2000.

[294] A. Dantan, N. Treps, A. Bramati, and M. Pinard. *Phys. Rev. Lett.*, 94:050502, 2005.

[295] N. Takei, H. Yonezawa, T. Aoki, and A. Furusawa. *Phys. Rev. Lett.*, 94:220502, 2005.